

© 2009 by Natalie Erin Strand. All rights reserved.

THE RELATIONSHIP OF ACTIVE GALACTIC NUCLEI & QUASARS
WITH THEIR LOCAL GALAXY ENVIRONMENT

BY

NATALIE ERIN STRAND

B.S., The Pennsylvania State University, 2003
M.S., University of Illinois at Urbana-Champaign, 2005

DISSERTATION

Submitted in partial fulfillment of the requirements
for the degree of Doctor of Philosophy in Physics
in the Graduate College of the
University of Illinois at Urbana-Champaign, 2009

Urbana, Illinois

Doctoral Committee:

Professor John Stack, Chair
Associate Professor Robert Brunner, Director of Research
Associate Professor Brian Fields
Assistant Professor Leslie Looney

Abstract

We explore how the local environment is related to properties of active galactic nuclei (AGNs) of various luminosities. Recent simulations and observations are converging on the view that the extreme luminosity of quasars, the brightest of AGNs, is fueled in major mergers of gas-rich galaxies. In such a picture, quasars, the highest luminosity AGNs, are expected to be located in regions with a higher density of galaxies on small scales where mergers are more likely to take place. However, in this picture, the activity observed in low-luminosity AGNs is due to secular processes that are less dependent on the local galaxy density. To test this hypothesis, we compare the local photometric galaxy density on kiloparsec scales around spectroscopic type I and type II quasars to the local density around lower-luminosity spectroscopic type I and type II AGNs. To minimize projection effects and evolution in the photometric galaxy sample we use to characterize AGN environments, we place our random control sample at the same redshift as our AGNs and impose a narrow redshift window around both the AGNs and control targets. Our results support these merger models for bright AGN origins. We find that the brightest sources have overdensities that increase on the smallest scales compared to dimmer sources. In addition, we investigate the nature of the quasar and AGN environments themselves and find that the increased overdensity of early-type galaxies in the environments of bright type I sources suggests that they are located in richer cluster environments than dim sources. We measure increased environment overdensity with increased quasar black hole mass, consistent with the well-known $M_{\text{DMH}} - M_{\text{BH}}$ relationship, and find evidence for quenching in the environments of high accretion efficiency type I quasars.

*to my husband Joel
and
to my dad*

Acknowledgments

Many thanks are due to the people who have been a part of this project:

My advisor, Robert Brunner, who supported and challenged me throughout the process.

My group mates, especially Ashley Ross, Adam Myers, and Britt Lundgren, with whom I had conversations that provoked insight and understanding.

Reinabelle Reyes and Lei Hao, who generously provided data and willingly answered questions about it.

My husband Joel, my family, and my friends, who encouraged me, supported me, and prayed for me continually.

Most importantly, I praise my Rock and my Redeemer, who set me on this path and sustained me along the way.

Additionally, I acknowledge support from Microsoft Research, the University of Illinois, and NASA through grants NNG06GH156 and NB 2006-02049. I made extensive use of the storage and computing facilities at the National Center for Supercomputing Applications and thank the technical staff for their assistance in enabling this work.

Funding for the creation and distribution of the SDSS Archive has been provided by the Alfred P. Sloan Foundation, the Participating Institutions, the National Aeronautics and Space Administration, the National Science Foundation, the U.S. Department of Energy, the Japanese Monbukagakusho, and the Max Planck Society. The SDSS Web site is <http://www.sdss.org/>.

The SDSS is managed by the Astrophysical Research Consortium (ARC) for the Participating Institutions. The Participating Institutions are The University of Chicago, Fermilab, the Institute for Advanced Study, the Japan Participation Group, The Johns Hopkins University, the Korean Scientist Group, Los Alamos National Laboratory, the Max-Planck-Institute for Astronomy (MPIA), the Max-Planck-Institute for Astrophysics (MPA), New Mexico State University, University of Pittsburgh, University of Portsmouth, Princeton University, the United States Naval Observatory, and the University of Washington.

Table of Contents

Chapter 1	Introduction	1
1.1	A BRIEF HISTORY OF STRUCTURE FORMATION	1
1.2	ACTIVE GALACTIC NUCLEI	2
1.3	AGN ENVIRONMENTS	2
Chapter 2	The Data	5
2.1	OVERVIEW	5
2.2	SPECTROSCOPIC TARGETS	5
2.2.1	Active Targets	5
2.2.2	Normal (Quiescent) Galaxies	7
2.3	PHOTOMETRIC GALAXIES	9
Chapter 3	The Technique	16
3.1	COUNTING GALAXIES AROUND TARGETS	16
3.2	APPLYING A PHOTOMETRIC REDSHIFT CUT	17
3.3	QUANTIFYING REDSHIFT UPPER LIMITS	18
3.4	VOLUME-LIMITING	19
3.4.1	Spectroscopic Target Samples	19
3.4.2	Photometric Environment Galaxy Sample	19
Chapter 4	The Dependence on Redshift, Type, & Broad-Band Luminosity	25
4.1	OVERVIEW	25
4.2	TARGET REDSHIFT	25
4.3	TARGET TYPE	26
4.4	TARGET BROAD-BAND LUMINOSITY	27
4.5	BROAD-BAND LUMINOSITY, REDSHIFT, AND TYPE	28
4.6	CONCLUSIONS	30
Chapter 5	The Dependence on [OIII] Luminosity	41
5.1	OVERVIEW	41
5.2	TARGET TYPE	41
5.3	TARGET REDSHIFT	42
5.4	CONCLUSIONS	43
Chapter 6	The Dependence on Environment Galaxy Type	53
6.1	OVERVIEW	53
6.2	TARGET TYPE	53
6.2.1	Comparison to L^* Galaxies	54
6.3	TARGET LUMINOSITY	54
6.4	TARGET REDSHIFT	55
6.5	FOUR ENVIRONMENT GALAXY TYPES	55
6.6	CONCLUSIONS	56

Chapter 7	The Dependence on Black Hole Mass	74
7.1	OVERVIEW	74
7.2	QI LUMINOSITY	75
7.3	QI REDSHIFT	75
7.4	ENVIRONMENT GALAXY TYPE	75
7.5	ACCRETION EFFICIENCY	76
7.6	CONCLUSIONS	77
Chapter 8	The Dependence on Multiwavelength Properties	90
8.1	OVERVIEW	90
8.2	RADIO QUASARS	90
8.3	X-RAY QUASARS	91
8.4	CONCLUSIONS	92
Chapter 9	Conclusions & Future Work	103
Appendix A	Documentation for Bincounting Code Package	105
A.1	OVERVIEW	105
A.2	HEADER FILE: bincountsfuctions.h	105
A.3	GENERAL FUNCTIONS: bincountsfuctions.c	106
A.4	CREATE BINARY DATA FILES:	
	sortbydec.c and sortbydec_zphot.c	107
	A.4.1 Negative Random Data for Masking	107
	A.4.2 Environment Galaxy Data for Bincounting	107
A.5	MASK TARGET DATA: maskforbincount.c	108
A.6	COUNT ENVIRONMENT GALAXIES:	
	bincount_zphotandztype.c and bincount_zphot4types.c	108
	A.6.1 Bincounting with All Galaxies and Red-Blue Galaxy Separation	108
	A.6.2 Bincounting with Budavari et al. (2003) Galaxy Subgroups	109
A.7	BINCOUNTING ALGORITHM	110
Appendix B	Photometric Redshift Estimation for SDSS Quasars	111
B.1	INTRODUCTION	111
	B.1.1 Photometry and Colors	111
	B.1.2 Previous Photometric Redshift Work: Galaxies	111
	B.1.3 Previous Photometric Redshift Work: Quasars	112
B.2	DATA SAMPLE	112
B.3	TECHNIQUE	113
	B.3.1 Recreation of Weinstein et al. (2004) Algorithm	113
B.4	VARIATIONS ON W04 ALGORITHM	115
	B.4.1 Binning	115
	B.4.2 Statistic	115
	B.4.3 Magnitude Type	116
	B.4.4 Reddened Quasars	117
	B.4.5 Magnitude and Magnitude Error Limits	118
	B.4.6 Adding additional bands	118
	B.4.7 Weighting Functions	119
	B.4.8 Covariance between SDSS magnitude bands	121
	B.4.9 CZRs from SDSS DR3 Quasar Subpopulations	122
B.5	CATASTROPHIC FAILURE ANALYSIS	122
	B.5.1 Colors of catastrophic failure objects	122
	B.5.2 Spectra of catastrophic failure objects	123
	B.5.3 PDFs of catastrophic failure objects	123
B.6	CONCLUSIONS	124

Appendix C	Tables of Results for CZR Based Photometric Redshift Estimator	. 143
References	184
Curriculum Vitae of		
Natalie Erin Strand	189

Chapter 1

Introduction

1.1 A BRIEF HISTORY OF STRUCTURE FORMATION or A Bit of Cosmic Background

In the early universe, tiny density fluctuations appeared and continued to increase when massive particles began to govern the expansion of the universe (“matter era”) instead of the background blackbody radiation (“radiation era”). As the matter era progressed and the universe continued to expand and cool, massive particles began to be attracted to these fluctuations, increasing the density. When the variations in density were measured in the cosmic microwave background by such surveys as WMAP and its predecessors, it became clear that visible baryonic matter alone is not enough to explain the sizes of the density fluctuations. The presence of a significant fraction of nonbaryonic cold dark matter in the universe is the currently accepted solution to this problem (e.g., Spergel et al., 2003). The interaction of this dark matter with radiation is thought to be negligible, therefore, the dark matter could have begun clumping during the radiation era. Thus, by the time the matter era began, the clumps of dark matter could have reached larger densities than were possible for baryons alone. Baryonic matter fell into the potential wells caused by these enhanced density regions of dark matter, known as halos, eventually collapsing into the first globular clusters, galaxies, and galaxy clusters (e.g., White & Rees, 1978). The relative clustering strength of visible baryonic matter (e.g., in the form of galaxies) to the underlying dark matter distribution is known as bias.

In the cold dark matter paradigm, which accurately describes the observed universe, the physical structures that we see were formed hierarchically: the smallest structures combining to form larger structures. Gas clouds condense to form stars, and collections of stars form galaxies. Galaxies tend to clump together to form groups (less than about 50 galaxies with scales of $\lesssim 1$ Mpc) and clusters (larger numbers of galaxies in regions with scales $\gtrsim 1$ Mpc); the abundance of galaxies in a cluster determines its richness (Abell, 1958).

The first stars (known as Population III stars) are proposed to have been zero-metallicity and very massive, on the order of hundreds of solar masses, forming in regions of enhanced density. The reactions that fueled these stars enriched the interstellar medium with heavier metals, which became the building blocks for later (Population II and I) stars. When Population III stars collapsed, they retained a large fraction of their mass to form massive black holes, which are thought to be the progenitors of supermassive black holes at the centers of galaxies. Mergers of the massive halos containing the black holes and their surrounding gas resulted in the building up of larger and larger halos. The massive black holes sank to the center, combining to form supermassive black holes at the centers of the newly-forming galaxies (see, e.g., Ferrara, 1998; Madau & Rees, 2001; Volonteri et

al., 2003, and references therein).

1.2 ACTIVE GALACTIC NUCLEI

It is now generally accepted that every massive galaxy harbors a supermassive black hole (e.g. Kormendy & Richstone, 1995; Richstone et al., 1998). Some of these supermassive black holes are in the process of actively accreting material (Lynden-Bell, 1969), thereby causing the central regions of the galaxy to emit large amounts of radiation across the electromagnetic spectrum. These active galactic nuclei (AGNs) can easily be classified by luminosity; Seyfert galaxies are among the dimmest variety of AGNs, while the most luminous AGNs are known as quasars. The Unified Model of an AGN (see, e.g., Antonucci, 1993; Urry & Padovani, 1995, for a detailed review) consists of a central supermassive black hole surrounded by an accretion disk which is itself surrounded by dusty clouds or a dusty torus. The object also may have jets visible in X-ray, optical, and/or radio wavelengths that emerge perpendicular to the plane of the torus. Antonucci (1993) claims that properties of observed AGNs of all luminosities differ primarily due to the orientation angle of the quasar to the viewer. In this popular model, broad emission lines are seen in the spectrum of an object viewed at an angle that allows a more direct line-of-sight to the central engine. Objects viewed at a more oblique angle exhibit narrow emission lines, since radiation from the central source is being re-emitted by the surrounding dust along the direction of observation.

However, this observationally-driven model does not explicitly address the origin or evolution of AGNs. Currently proposed theories (see, e.g., Hopkins et al., 2005b) suggest that the brightest AGNs are fueled by dust and gas driven toward the galactic nucleus by mergers or interactions of galaxies, while secular mechanisms cause the activity in lower luminosity AGNs. Therefore, In this model, the amount of fuel available to the AGN plays a major role in the properties that we observe. The aim of this dissertation is to use studies of AGN environments to constrain the validity of theories for the activation and fueling of AGNs.

1.3 AGN ENVIRONMENTS

The local environments of AGNs and quasars provide valuable insights into the formation history and evolution of those sources (e.g., Ellingson et al., 1991). Quasar environments were first studied by Bahcall, Schmidt, & Gunn (1969), who used a sample of five quasars and concluded that quasars are associated with galaxy clusters. Yee & Green (1984) found that quasars reside in regions with higher galaxy density, and more recent work has confirmed that quasars are found in regions with densities consistent with galaxy groups or clusters of poor to moderate richness (Bahcall & Chokshi, 1991; Fisher et al., 1996; McLure & Dunlop, 2001; Wold et al., 2001; Coldwell et al., 2002; Barr et al., 2003). Although studies of several X-ray- and radio-selected samples have found evidence for a relationship between environment and AGN activity (e.g., Wurtz et al., 1997; Best, 2004; Söchting et al., 2004), the Sloan Digital Sky Survey (SDSS) is the first survey to allow meaningful studies of quasar environments, because it samples large numbers of both quasars and galaxies for redshifts $z \lesssim 0.5$. Using SDSS data, Serber et al. (2006) concluded that the density of photometric galaxies around quasars increases with decreasing angular scale, but is independent of redshift for $z \leq 0.4$.

They also provided evidence for a higher density of galaxies around more luminous quasars at scales less than $100 h^{-1}$ kpc, while at larger angular scales, the density appears to be largely independent of luminosity (c.f., Porciani & Norberg, 2006; da Angela et al., 2008; Myers et al., 2007).

The results of Serber et al. (2006) agree with other studies showing enhanced clustering of quasars on small scales. Djorgovski (1991) first linked the excess of quasar clustering on small scales to galaxy interactions. Studies of the small-scale clustering of quasars (e.g., binary and triplet quasars) also support the hypothesis that there is excess quasar clustering on scales of $\lesssim 100 h^{-1}$ kpc (Kochanek et al., 1999; Mortlock et al., 1999; Hennawi et al., 2006; Djorgovski et al., 2007; Myers et al., 2007).

An excess of quasar pairs on small scales naturally follows from a merger origin for quasar activity, whether these pairs simply trace biased groups where mergers are likely to occur (Hopkins et al., 2008) or are being excited in merging galaxies (Djorgovski, 1991; Myers et al., 2008). Hopkins et al. (2006) have developed a unified, merger-driven framework that naturally predicts that quasar environments should be highly biased (Hopkins et al., 2008). These simulations show that major mergers between gas-rich galaxies are the likely mechanisms to trigger bright quasar activity, and that this activity is a phase in the evolution of massive spheroidal galaxies (Hopkins et al., 2005b, 2008). In contrast, secular mechanisms (e.g. disk instabilities that feed cold gas onto the central black hole) may fuel the activity in most low-luminosity AGN, implying that the small-scale environments of these objects should have a smaller bias (Hopkins & Hernquist, 2006; Hopkins et al., 2008). Therefore, we would expect that objects driven by major mergers will have biased environments on small scales, whereas objects fueled by secular means will reside in less rich environments. Such a simplification hides many subtleties, however, as secular mechanisms such as harassment can probably only occur in slightly overdense environments. Further, for objects whose observed characteristics differ purely because of viewing angle or internal structure (Antonucci, 1993; Elvis, 2000), there should be no particular difference in local environment. This, of course, would only be the case if that structure is not correlated with fueling, as could occur, for instance, if more luminous quasars had strong winds. Therefore, it is important to understand the relationship between the physical properties of AGN and their local environment, which will in turn provide insight into what aspects of AGN properties are explained by formation history, fueling, or simply by structure and orientation.

In this dissertation, we address this merger hypothesis by studying the relationships between different types of AGNs and their environments. Our work improves upon previous studies of AGN environments in several ways. First, we use larger samples of background photometric galaxies, as well as more cleanly defined samples of spectroscopic AGNs of various luminosities. Additionally, we include cuts in photometric redshift space around spectroscopic targets and the random positions to which they are compared to minimize interloping foreground or background objects, as well as to marginalize any redshift evolution of the photometric galaxy sample. By using photometric redshift cuts, we obtain more realistic overdensity estimates and errors, and we are able to extend the study of quasar environments in the SDSS to $z \approx 0.5$. With our large samples, we are able to isolate specific characteristics of the AGNs to quantify physical relationships between the AGN and its local environment.

We assume a concordance cosmology $\Omega_M = 0.3$, $\Omega_\Lambda = 0.7$, $H_0 = 70 \text{ km s}^{-1} \text{ Mpc}^{-1}$ (with $h = 0.7$) in order to compare to results from previous studies. Our spectroscopic data is divided into four target samples: Type I and Type II quasars (e.g., AGNs with the highest intrinsic luminosity) and lower-luminosity Type I and Type II AGNs. The spectra of Type I AGNs and quasars are

characterized by broad emission lines ($\text{FWHM} > 1000 \text{ km s}^{-1}$; e.g., Hao et al., 2005a; Schneider et al., 2007), while the spectra of Type II AGN and quasars exhibit narrow emission lines (e.g., Hao et al., 2005a; Zakamska et al., 2003). From this point forward, for simplicity, we will generally use “AGN” to describe lower-luminosity objects and “quasar” to describe higher-luminosity objects.

Chapter 2

The Data

2.1 OVERVIEW

We study the environments of spectroscopic AGN targets by counting photometric galaxies within a $2.0 h_{70}^{-1}$ Mpc projected comoving distance of the target center (i.e., we consider a conical slice around the target rather than a spherical volume). The samples of Type I quasars (QIs), Type II quasars (QIIs), lower luminosity AGNs (AIs and AIIs), spectroscopic and photometric galaxies selected from the SDSS are described below. We mask the spectroscopic samples to eliminate objects within $2.0 h_{70}^{-1}$ Mpc of any of the following: the survey edge, an area masked out by SDSS¹, an area with seeing $> 1.5''$, or an area with r -band reddening $A_r \geq 0.2$ (Scranton et al., 2002; Ross et al., 2006).

Since our spectroscopic data are compiled from several sources, as detailed below, we have eliminated duplicate objects between the samples. If an object appears in both a lower-luminosity AGN sample and a quasar sample, the object is classified as a quasar (and thus removed from the AGN sample), since the quasar samples have lower luminosity limits imposed. If an object appears in both the QI and QII sample, we classify it as a QII, since Reyes et al. (2008) have imposed strict line width cuts on objects that enter their sample. Figure 2.1 shows the redshift distributions for the spectroscopic target samples, which are also summarized in Table 2.1.

2.2 SPECTROSCOPIC TARGETS

2.2.1 Active Targets

Quasars

Our samples of spectroscopic Type I quasar targets are drawn from the SDSS Fifth Data Release (DR5; Adelman-McCarthy et al., 2007) Quasar Catalog (Schneider et al., 2007), which includes K -corrected absolute i -band magnitudes for each object. The $0.11 \leq z \leq 0.5$ QI samples have $-26.4 \leq M_i \leq -22.0$. In addition to absolute magnitude information, the catalog provides a flag to distinguish between resolved and point source objects. The measured absolute broad-band luminosity of resolved sources will likely be contaminated by starlight from the host galaxy, so initially, when we divide the sample by absolute luminosity, we exclude those quasars with extended morphology for a sample (QI_{pt}) that contains 2,314 objects. In our analyses which use the [OIII] emission line

¹See http://www.sdss.org/dr5/products/images/use_masks.html; negative random positions (see Section A.4.1) provided by A. D. Myers, private communication

luminosity and black hole mass measurements (Chapters 5ff), we re-introduce the extended sources, because $L_{[\text{OIII}]}$ is due to AGN activity. The combined point + extended sample of QIs with good $[\text{OIII}]$ and M_{BH} measurements contains 3,793 objects.

For our initial analysis, we draw Type II quasar targets from the sample presented by Zakamska et al. (2003). After cutting the sample to match the high redshift limit of the main quasar sample and masking this sample as described above, we have 131 QILZ targets with $0.3 \leq z \leq 0.5$. In the subsequent stages of our analysis, we extend our sample by using QIIs from Reyes et al. (2008) (QII), which includes over 90% of the sources in the QILZ sample. After masking there are 348 QII targets with $0.11 \leq z \leq 0.5$.

Lower-Luminosity AGNs

We compare the quasar targets to lower-luminosity Type I and Type II AGN (AI and AII, respectively) from Hao (private communication) selected from SDSS DR5 spectroscopic galaxies according to the criteria laid out in Hao et al. (2005a). The classification of these galaxies as AGN depends on the strengths of the $[\text{O III}]$ and $\text{H}\beta$ lines (Hao et al., 2005a; Kauffmann et al., 2003); therefore our low-redshift limit is set to $z = 0.11$, as this is where the $[\text{O III}]$ ($\lambda\lambda 4959, 5007$) lines enter the r -band (Kauffmann et al., 2003), resulting in a more uniform classification. After masking as above, there are 1,464 Type I AGN and 3,329 Type II AGN following the criteria of Kewley et al. (2001). While we could have adopted the less stringent criteria of Kauffmann et al. (2003), we wish to be conservative in our sample selection in this analysis and minimize the contribution from non-accretion luminosity sources (Hao et al., 2005a). The lower-luminosity AGN samples have a redshift range of $0.11 \leq z \leq 0.33$, with the majority of sources at $z < 0.15$.

Combined Samples

We have matched all of the targets with Galactic extinction-corrected $[\text{OIII}]$ line fluxes (in addition, QI targets set been matched with $\text{H}\beta$ line and 5100\AA continuum fluxes from which black hole masses and Eddington accretion ratios have been calculated; see Chapter 7). Because we have $[\text{OIII}]$ flux measurements for all of our active spectroscopic targets, we can investigate the relationship between $L_{[\text{OIII}]}$ and environment overdensity for Type I AGN samples and Type II AGN samples. We convert the observed $[\text{OIII}]$ flux to luminosity by first correcting for extinction using Galactic dust maps (Schlegel, Finkbeiner, & Davis, 1998) with an $R_V = 3.1$ extinction law (Cardelli, Clayton, & Mathis, 1989) to find the extinction correction for the object's coordinates. The corrected flux is then converted to luminosity using the target's spectroscopic redshift and our assumed cosmology.

The Type I sample has 5,257 objects (QIs + AIs), and the Type II sample has 3,677 objects (QIIs + AIIs; the low redshift, lower luminosity AGNs dominate this sample) for a total of 8,934 targets when the samples are combined. We plot the $L_{[\text{OIII}]}$ distribution of the combined Type I and Type II samples in the inset of Figure 2.2. Upon comparing the $L_{[\text{OIII}]}$ distributions of the two samples in Figure 2.2, we see that the whole distribution composed of distinctly separate peaks for the two types. We plot the redshift distributions and show $L_{[\text{OIII}]}$ vs. redshift in Figure 2.3.

Note: Slight Discrepancy in AI and QI Flux Measurements

When we compare the [OIII] measurements for AI and QI objects that are present in both samples (from Hao and Reyes, respectively), we see in the upper panels of Figure 2.4 that there is a systematic offset where the QI measurement is brighter than the AI measurement. The offset is not due to differences in redshift. According to Reyes (private communication, 2009), the difference is likely due to an improvement in the spectrophotometric flux scale calibration between the SDSS data analyzed by Hao et al. (2005a) and the later SDSS data analyzed by Reyes et al. (2008). In this later data release (i.e., DR6), spectra are calibrated relative to the PSF magnitudes of reference stars on each plate rather than their fiber magnitudes. Reyes et al. (2008) comment on this change, noting that the measured fluxes using the new calibration are on average 38% higher.

Rather than attempting to recalibrate the Hao et al. (2005a) data, we instead make a “correction” based on the offset between AI and QI measured fluxes in the lower left panel of Figure 2.4. We estimate the correction by calculating a linear fit to the objects not on the QI flux = AI flux black dashed line, which is shown as a magenta dashed line. The correction is $AI_{\text{flux,corrected}} = \frac{11}{7}(AI_{\text{flux}} - 45.45)$. Using this correction, we recalculate the extinction-corrected [OIII] luminosity values for the AIs and plot them against the QI luminosity values in the lower right panel of Figure 2.4.

While there is definite improvement in the agreement of the luminosities, it is not a very accurate correction. However, it is sufficient to estimate the extent to which this difference might affect our environment analysis (specifically in the circumstances where we combine AI and QI data to make the TI sample or all four samples to make the TI+TII sample). When the correction is applied to the AI dataset used for our analysis (duplicates removed), there are now 288 objects with $\log(L_{[\text{OIII}]} / L_{\odot}) \geq 8.0$, whereas before the correction, there were 201 objects above that volume limit value. Assuming that the same correction can be made to the AIIs, we similarly recalculate the luminosity values for the AII sample and find 303 AIIs with $\log(L_{[\text{OIII}]} / L_{\odot}) \geq 8.0$, whereas before the correction, there were 208 objects above that volume limit value.

For both samples, the changes in the measured overdensities (using the technique described in Chapter 3) with this very rough correction are well within the error bars (which only include errors due to variation in the environment overdensity, not error in the measurement of the [OIII] line). We estimate that there may be a few percent change in our measurements due to these differences. For the purposes of this work, we will combine the AI and QI (AII and QII) samples without applying a flux correction, but when we tabulate the results, we will additionally report only QI values where appropriate.

2.2.2 Normal (Quiescent) Galaxies

In order to compare a representative non-active galaxy population to our AGN samples, we have constructed a spectroscopic galaxy target sample. We select primary SDSS DR5 objects that are spectroscopically classified as galaxies with extinction-corrected *i*-band magnitudes < 18.5 using the following query:

```
SELECT p.objID, s.ra, s.dec, s.z,  
       (p.modelMag_u-p.extinction_u) AS uMag,  
       p.modelMagErr_u AS uMagErr,
```

```

(p.modelMag_g-p.extinction_g) AS gMag,
p.modelMagErr_g AS gMagErr,
(p.modelMag_r-p.extinction_r) AS rMag,
p.modelMagErr_r AS rMagErr,
(p.modelMag_i-p.extinction_i) AS iMag,
p.modelMagErr_i AS iMagErr,
(p.modelMag_z-p.extinction_z) AS zMag,
p.modelMagErr_z AS zMagErr, p.flags, p.insideMask
FROM PhotoTag as p, specObj as s
WHERE s.SpecClass = 2 AND p.Objid = s.bestObjID AND
      (p.modelMag_i - p.extinction_i) < 18.5 AND
      s.z BETWEEN 0.077 and 0.41

```

that returns 380,678 rows.

We calculate absolute magnitudes for the spectroscopic galaxy sample, where the absolute magnitude in that band is given by

$$M_{band} = m_{band} - DM - K_{band} \quad (2.1)$$

where m_{band} is the extinction-corrected apparent magnitude and DM is the distance modulus, which is found from the luminosity distance D_L in units of Mpc:

$$DM = 5 \log_{10}(D_L) + 25 \quad (2.2)$$

The quantity K_{band} is the K-correction in the particular band for which the magnitude is calculated. It corrects for the fact that when sources are observed at different redshifts, the broad-band magnitude is sampling flux from different features in the galaxies’ rest frame spectra (Hogg et al., 2002). Thus, the K-correction depends on both redshift and the spectral type for each galaxy (e.g., Ellis, 1997). We use K-correction software “Kcorrect” created by Blanton et al. (2007). This software fits galaxy spectral energy distribution (SED) templates to the photometric information for an individual galaxy and uses the best fit SED to calculate the K-correction.

We used the standalone C-code provided in the Kcorrect package to calculate the template fitting coefficients and reconstruct magnitudes from these coefficients from the observed bandpasses to rest-frame bandpasses shifted by 0.1, since the SDSS main galaxy sample is primarily at $z = 0.1$ (see Blanton et al., 2007, for more details). The K-correction in a particular band is given by²

$$K_{band} = -2.5 \log_{10} \left(\frac{maggies_{band}}{maggies.z0_{band}} \right) \quad (2.3)$$

where “maggie” is referring to a linear measure of flux, related to an AB magnitude by $maggie = 10^{-0.4 \cdot m}$ (note that SDSS magnitudes are asinh magnitudes, or “luptitudes,” and their relationship to more traditional astronomical magnitudes is described in detail in Lupton, Gunn, & Szalay, 1999).

The galaxy targets are then masked in the same manner as the AGN targets. Additionally, in order to ensure that we have only non-active galaxies in this sample, we remove the galaxies that

²see <http://cosmo.nyu.edu/blanton/kcorrect/>

are classified as AGNs in the DR5 samples described previously as well as in the Kauffmann et al. (2003) DR4 AGN catalog³. In order to define a sample of L^* galaxies, we select only those galaxies with i -band magnitudes within 0.25 magnitudes of $M_i^* = -21.59$ (Blanton et al., 2003), resulting in a final sample of 8,618 spectroscopic galaxies with $0.11 \leq z \leq 0.24$.

2.3 PHOTOMETRIC GALAXIES

We use the local number of photometric galaxies to characterize the environments of the spectroscopic targets described previously. The photometric galaxies are drawn from the SDSS DR5 database by selecting all primary objects photometrically classified as galaxies with r -band extinction corrected magnitude in the range $14.0 \leq r \leq 21.0$ ⁴. All of these objects have been assigned photometric redshifts via a template-fitting technique (Csabai et al., 2003). The photometric galaxy sample including photometric redshifts and galaxy type information is acquired from the DR5 database using the following query:

```
SELECT p.objID, p.ra, p.dec,
       p.u, p.Err_u, p.g, p.Err_g, p.r, p.Err_r, p.i, p.Err_i,
       p.z, p.Err_z, p.extinction_u, p.extinction_g,
       p.extinction_r, p.extinction_i, p.extinction_z,
       p.type, p.type_u, p.type_g, p.type_r, p.type_i, p.type_z,
       p.flags, p.flags_u, p.flags_g, p.flags_r,
       p.flags_i, p.flags_z, p.psfMagErr_g, p.psfMagErr_r,
       p.psfMagErr_i, p.insideMask,
       z.chiSq, z.z, z.zErr, z.t, z.terr, z.kcorr_r,
       z.rest_ug, z.rest_gr, z.absMag_r
FROM PhotoPrimary AS p LEFT OUTER JOIN
     photoz as z ON p.objID = z.objID
WHERE ((p.dered_g < 23.0) OR (p.dered_r < 23.0)
       OR (p.dered_i < 23.0))
       AND ((p.type_g = 3) OR (p.type_r = 3) OR (p.type_i = 3))
```

which returned 163,507,385 objects.

We accept galaxies in the clean r -band galaxy sample if they pass the following requirements:

- *type*: $type_r = 3$ (classified as a galaxy by the DR5 photometric pipeline)
- *extinction corrected magnitude*: $14.0 \leq r - extinction_r \leq 21.0$
- *flags*⁵:

³The AGNs in the Kauffmann et al. (2003) DR4 AGN catalog are selected on slightly less stringent criteria than the Kewley et al. (2001) criteria used by Hao et al. (2005a). We use the most conservative AGN classification to define our low-luminosity active galaxy samples, but here we eliminate a broader set of galaxies which could be considered active for our non-active galaxy sample.

⁴Note that Serber et al. (2006) used an r -band limit on their photometric galaxies rather than i -band as stated in their paper (W. Serber and R. Scranton, private communication).

⁵as defined by <http://cas.sdss.org/astro/en/help/docs/realquery.asp#flags>

```

((flag_r & BINNED1)!=0) and
((flag_r & NOPROFILE)==0) and
((flag_r & PEAKCENTER)==0) and
((flag_r & NOTCHECKED)==0) and
((flag_r & PSF_FLUX_INTERP)==0) and
((flag_r & SATURATED)==0) and
((flag_r & BAD_COUNTS_ERROR)==0) and
((flag_r & BRIGHT)==0) and
(((flag_r & DEBLEND_NOPEAK)==0) or
(float(psfErr_r)<=0.2)) and
(((flag_r & INTERP_CENTER)==0) or
((flag_r & COSMIC_RAY)==0)) and
((flag_r & DEBLENDED_AS_MOVING)==0)

```

The full r -band galaxy sample contains 28,856,324 objects. While we do not make explicit redshift cuts on the photometric galaxy sample, our technique effectively limits the sample to $0.06 \leq z \leq 0.55$.

Table 2.1: Summary of spectroscopic target data sets used for AGN environment analysis

Name	Type	# Objects	Range	Reference
QI _{pt} ¹	Type I quasars	2314	$0.11 < z < 0.5$	Schneider et al. (2007)
QI ²	Type I quasars	3793	$0.11 < z < 0.5$	Schneider et al. (2007)
QILZ ⁴	Type II quasars	131	$0.3 < z < 0.5$	Zakamska et al. (2003)
QII ³	Type II quasars	348	$0.11 < z < 0.5$	Reyes et al. (2008)
AI ⁵	Type I AGNs	1464	$0.11 < z < 0.33$	Hao et al. (2005a)
AII ⁶	Type II AGNs	3329	$0.11 < z < 0.33$	Hao et al. (2005a)
L* ⁷	L* galaxies	8618	$0.11 < z < 0.24$	SDSS CAS

¹ point sources only; used in Paper I

² point + extended sources; [OIII], H β , continuum luminosity measurements from Reyes, private communication (2008); includes only objects with both good [OIII] and M_{BH} measurements; duplicates removed

⁴ used in Paper I

⁵ selected from SDSS DR5 galaxies; [OIII] measurements from Hao, private communication (2008); duplicates removed

⁶ selected from SDSS DR5 galaxies; [OIII] measurements from Hao, private communication (2008); Kewley et al. (2001) AGN definition; duplicates removed

⁷ AGN matches removed

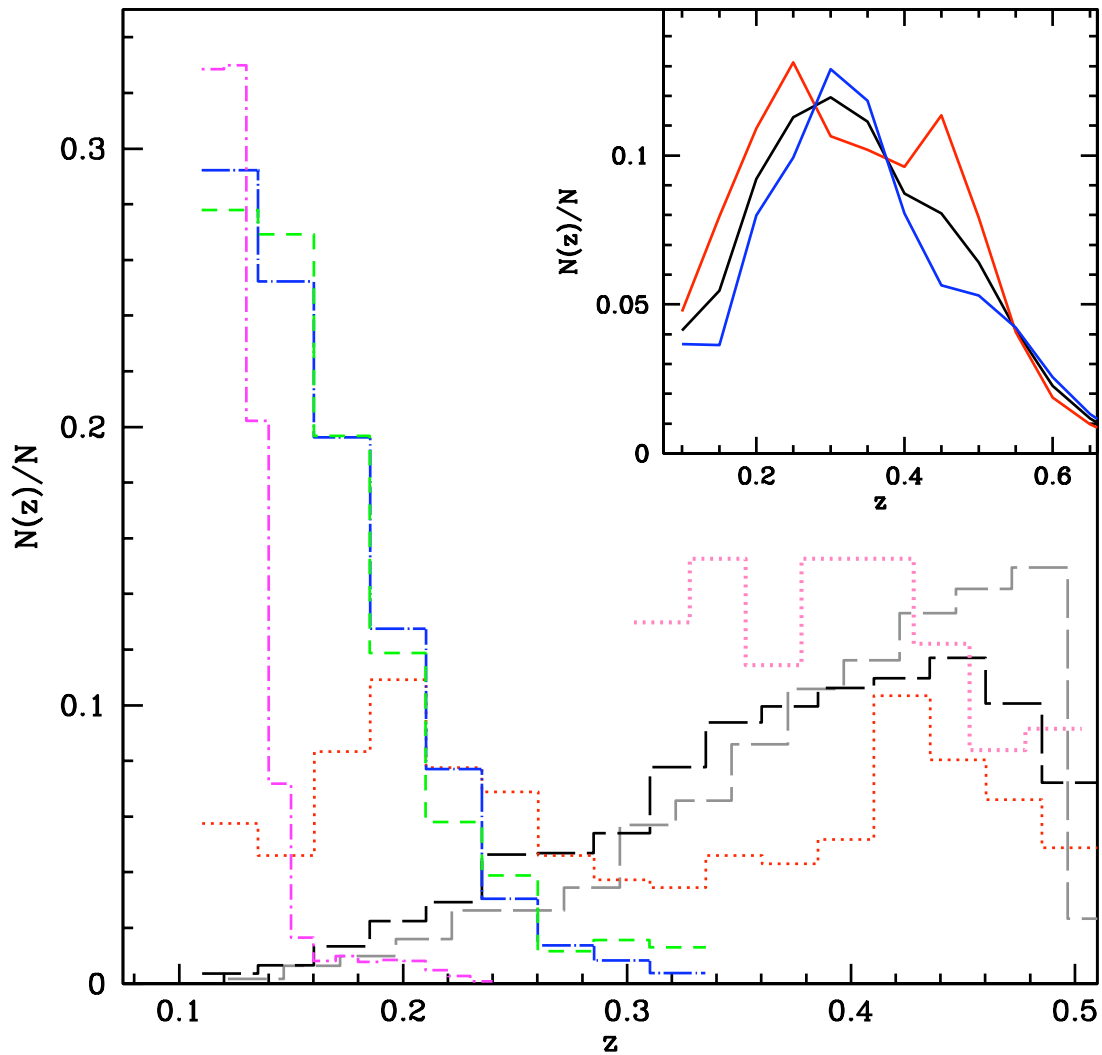


Figure 2.1— Normalized redshift distributions of each of the spectroscopic target samples. QI_pt: long gray dashed (2,314). QI: long black dashed (3,793). QII_Z: pink dotted (131). QII_R: red dotted (348). AI: short green dashed (1,464). AII: long blue dash dotted (3,329). L^* galaxies: short magenta dash dotted (8,618). *Inset*: Normalized redshift distribution of photometric galaxies. The solid black curve shows the distribution of all 28,851,353 galaxies, the solid red curve shows the distribution of the 12,150,909 early-type galaxies, and the solid blue curve shows the normalized of the 16,700,444 late-type galaxies.

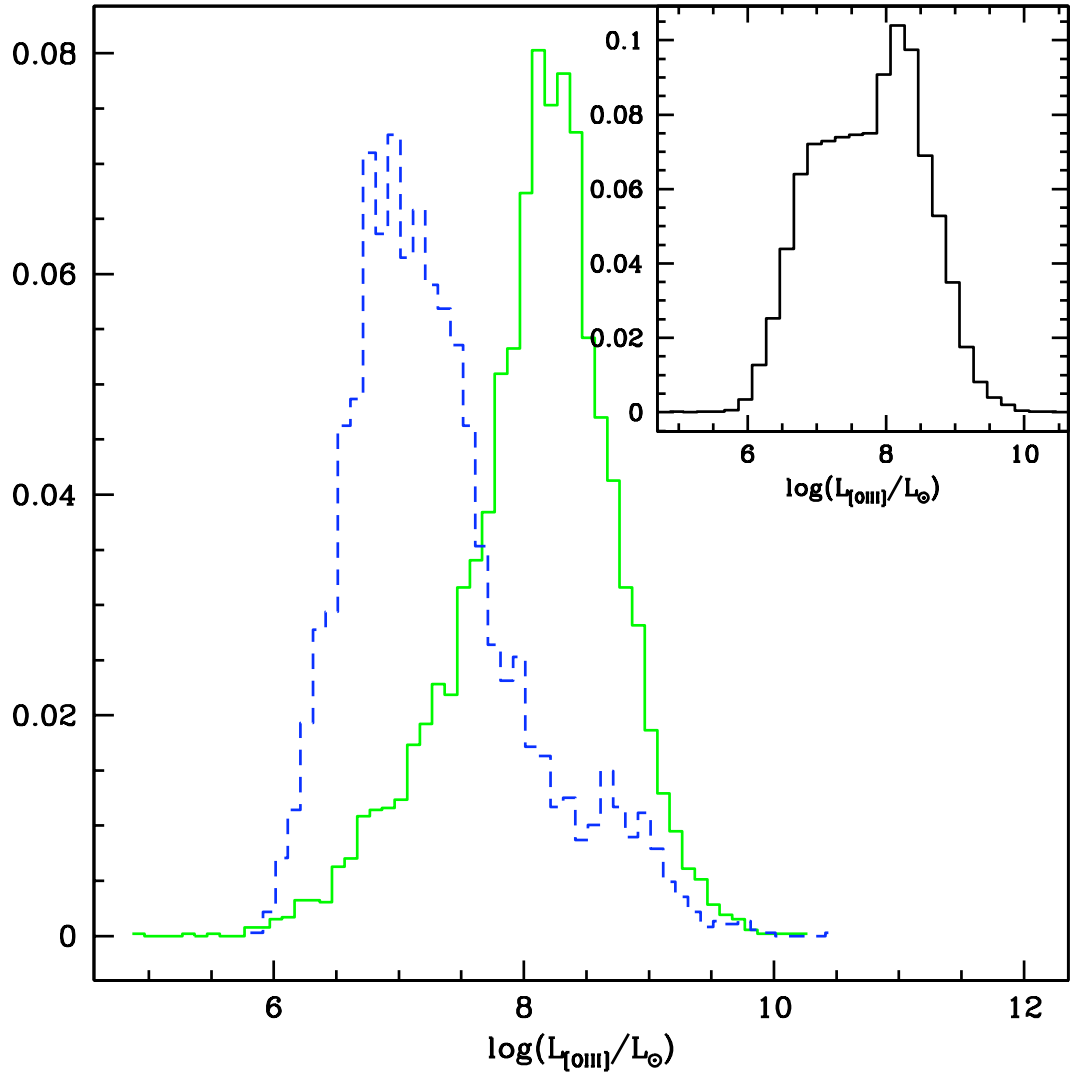


Figure 2.2— Normalized $L_{[\text{OIII}]}$ distribution for 5,257 Type I (green solid line) and 3,677 Type II (blue dashed line) targets. $L_{[\text{OIII}]}$ values have been corrected for Galactic extinction. *Inset:* Normalized $L_{[\text{OIII}]}$ distribution for all types of spectroscopic targets combined (8,934 objects).

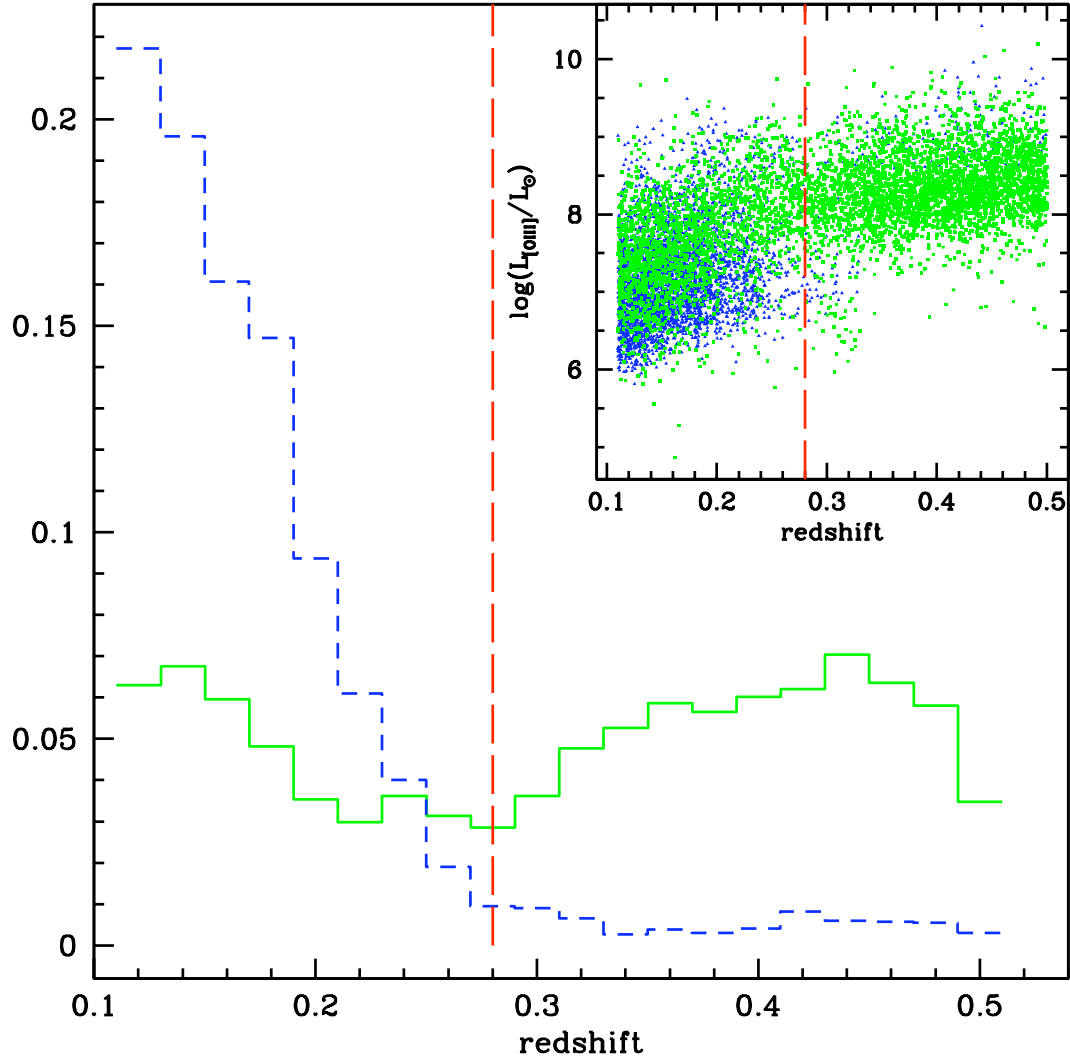


Figure 2.3— Normalized redshift distribution of the 5,257 Type I (green solid line) and 3,677 Type II (blue dashed line) targets. *Inset:* $L_{\text{[OIII]}}$ vs. z for Type I (green squares) and Type II (blue triangles) target samples. The dashed red vertical line in both plots shows $z = 0.28$, which divides the two main clusters of points.

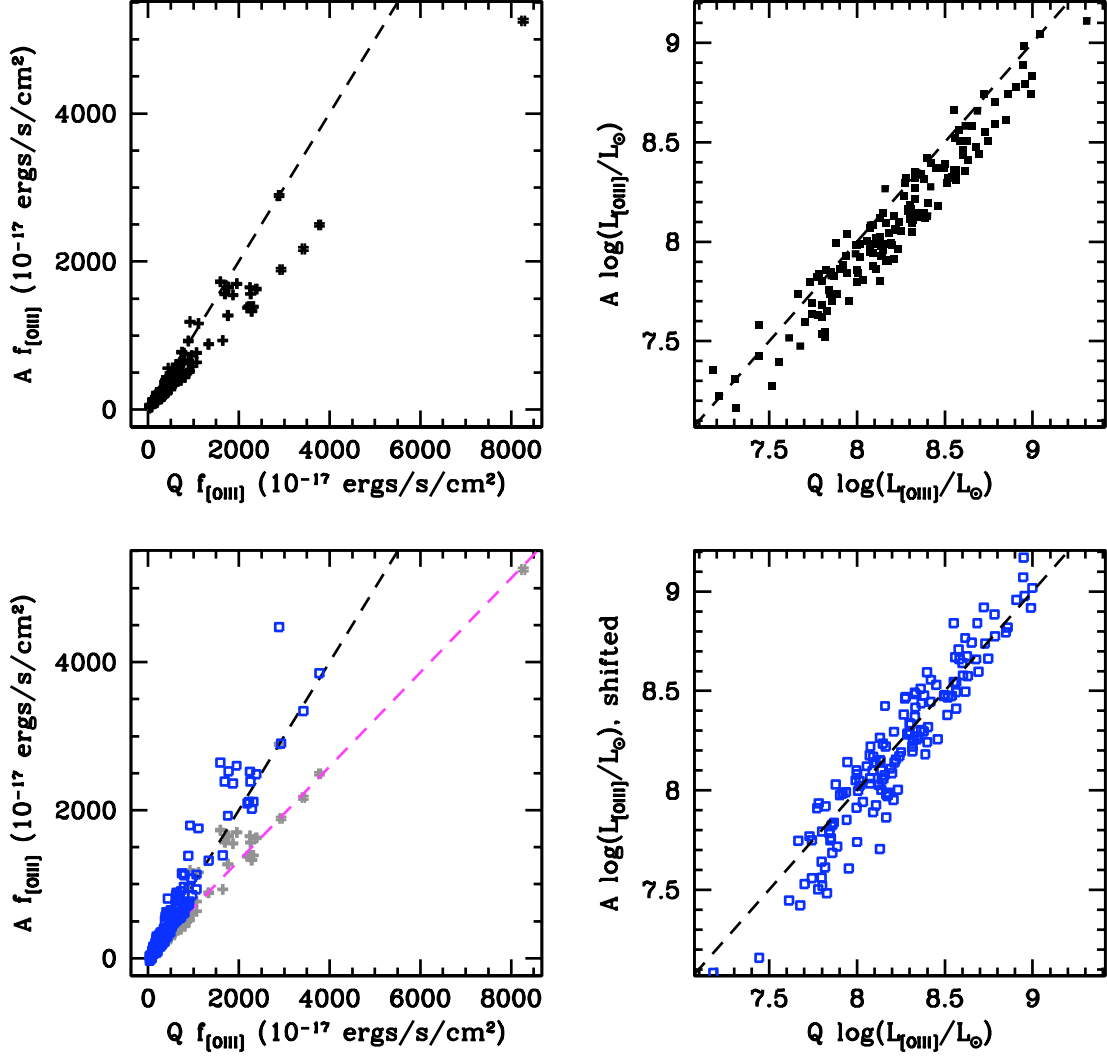


Figure 2.4— *Upper panels:* Comparison of $f_{[OIII]}$ (left) and $L_{[OIII]}$ (right) for QI objects that had duplicates in the AI sample (note: these objects are removed from the AI sample in all other figures). The measured fluxes are systematically lower in the AI catalog (measured by Hao et al., 2005a) compared to the QI catalog (measured by Reyes et al., 2008), and thus the luminosities calculated for the AIs are lower. *Lower left:* A correction of the form $AI_{\text{flux,corrected}} = \frac{11}{7}(AI_{\text{flux}} - 45.45)$ (magenta dashed line) is applied to original AI fluxes. Blue points show the shifted AI fluxes based on this correction; gray points are the original flux values. *Lower right:* Blue points show the extinction-corrected luminosities calculated from the “corrected” fluxes in the lower left panel.

Chapter 3

The Technique

3.1 COUNTING GALAXIES AROUND TARGETS

We count the number of photometric galaxies within a comoving radius of $2.0 h_{70}^{-1}$ Mpc of each spectroscopic target (e.g., spectroscopic quasar, AGN, or spectroscopic galaxy), excluding any galaxies that are within $25 h_{70}^{-1}$ kpc of the target. At $z < 0.4$, $25 h_{70}^{-1}$ kpc corresponds to an angular size of $> 3.3''$, which is approximately twice the average seeing in DR5 (Adelman-McCarthy et al., 2007). At angular scales smaller than this, deblending begins to complicate the reliable detection and measurement of faint galaxies.

We generate a large number of random positions in the DR5 footprint area for each redshift increment of 0.001 in our redshift range. We mask these random positions in the same manner as we masked the spectroscopic targets, requiring at least 1,000 random positions that are more than $2.0 h_{70}^{-1}$ Mpc away from the survey edge or a masked area for each redshift value. We count the number of photometric galaxies within a designated comoving distance around random positions and calculate the mean cumulative number of counts for that redshift increment as

$$R_i = \frac{\sum_z R_z}{N_z} \quad (3.1)$$

Here, N_z is the number of random positions R_z at a given redshift increment z . We calculate the error corresponding to the mean random counts as

$$e_{R_i}^2 = \frac{N_z}{N_z - 1} (\overline{R_i^2} - \overline{R_i}^2) = \sigma_{R_i}^2 \quad (3.2)$$

which is the variance on the mean random counts at a given redshift increment z .

The cumulative bincounts C_i around spectroscopic targets are matched with the mean cumulative random bincounts R_i (and error e_{R_i}) at the redshift increment closest to the target's redshift. We calculate a mean overdensity δ_{bin} in a particular scale, redshift, or absolute magnitude bin as

$$\delta_{bin} = \frac{\frac{1}{N} \sum_i C_i}{\frac{1}{N} \sum_i R_i} - 1 = \frac{\overline{C_{bin}}}{\overline{R_{bin}}} - 1 = \frac{C_{bin}}{R_{bin}} - 1 \quad (3.3)$$

where C_i is the counts around each target in the bin, R_i is the mean counts around random positions at the corresponding redshift, and there are N total targets in the bin. The error on the overdensity

is determined via error propagation:

$$e_{\delta_{bin}}^2 = \frac{e_{C_{bin}}^2}{R_{bin}^2} + \frac{C_{bin}^2}{R_{bin}^4} e_{R_{bin}}^2 \quad (3.4)$$

where $e_{C_{bin}} = \sqrt{C_{bin}}$ and $e_{R_{bin}}^2 = \sum_i^N e_{R_i}^2$.

We will refer to the quantity of $\frac{C_{bin}}{R_{bin}}$ as the *mean density*; this quantity is used to compare our results to those of Serber et al. (2006). In order to compare the environments of our various spectroscopic populations, however, we use the *mean overdensity*, $\frac{C_{bin}}{R_{bin}} - 1$, which is related to the underlying dark matter distribution and can be more directly related to correlation analyses (e.g., Padmanabhan et al., 2008).

Appendix A summarizes the C code written to perform the bincounting and masking.

3.2 APPLYING A PHOTOMETRIC REDSHIFT CUT

One of the difficulties in using photometric galaxy samples for overdensity measurements is the issue of projection effects, where foreground or background objects contaminate a measurement. We use photometric redshifts that are assigned to the photometric galaxies to minimize this complication. We apply a photometric redshift cut on the galaxies so that only those galaxies which satisfy $|z_{target} - z_{photogal}| \leq \delta z$ are counted in each bin. Crucially, the same δz cut is applied to both the spectroscopic targets and the random positions to which they are compared, which, as noted above, are also placed at the same redshift as the spectroscopic targets. We therefore minimize contamination by most galaxies outside of the δz interval. Additionally, by calculating our spectroscopic-photometric and random-photometric counts in the same $z \pm \delta z$ bin, we marginalize redshift evolution in the photometric galaxy sample outside of that $z \pm \delta z$ bin. We make the reasonable assumption that there is no redshift evolution in the photometric galaxy sample over this small δz interval. We have not accounted for the changes in photometric redshift accuracy as a function of magnitude and redshift, which we also assume are negligible over these redshift ranges.

We verify that the projection effect issue is mitigated by the δz cut without introducing systematics by calculating overdensities for random positions with the same redshift distribution as the QI_pt sample. We find that the overdensities of photometric galaxies around random positions is consistent with zero on all scales with and without the photometric redshift cut. We use the value $\delta z = 0.05$, which is large enough to encompass the effective rms error of the photometric redshifts ($\Delta z_{rms} = 0.04$ for $r < 18$; Budavari et al., 2003), for all further analysis. We have tested other values of δz and find that they give consistent results, albeit with larger uncertainties for narrower cuts, which is consistent with the expectations of Poissonian sampling.

To compare directly to the results of Serber et al. (2006), who did not apply any such redshift cut, we calculate the mean density of photometric galaxies around QI_pt targets with $-24.2 \leq M_i \leq -22.0$ and $0.08 \leq z \leq 0.4$. At a scale of $250 h_{70}^{-1}$ kpc, the density of photometric galaxies around quasars is 1.41 ± 0.033 and around L^* galaxies is 1.15 ± 0.005 without the δz cut. However, applying the δz cut decreases the random background noise, and with this cut we measure an environment density of 2.11 ± 0.096 around quasars and 1.74 ± 0.020 around L^* galaxies at the same scale. In order to confirm that we have not added any systematics by using the δz cut, we compare the relative densities of

QL-pt environments to L^* galaxy environments. The relative density of photometric galaxies around quasars to that around L^* galaxies is 1.22 ± 0.029 without the δz cut. The relative density does not appreciably change when the δz cut is used, and we find the relative density to be 1.22 ± 0.057 .

The true physical effect of the δz cut is shown in the comparison of mean *overdensities*. At the same scale of $250 h_{70}^{-1}$ kpc, the relative overdensity around quasars compared to around L^* galaxies is 2.67 ± 0.236 without the δz cut, but is 1.51 ± 0.137 with the δz cut. Because we have removed projection effects, the relative overdensities are lower when the δz cut is used; however, the errors on the mean densities with the δz cut have increased. We believe these larger errors are more physically relevant: with no δz cut, objects not actually correlated with the target will reduce Poissonian error estimates. Therefore, all subsequent analysis and figures include the $\delta z = 0.05$ cut.

3.3 QUANTIFYING REDSHIFT UPPER LIMITS

We use the δz cut to extend our redshift range to include spectroscopic targets with redshifts $z \geq 0.4$ without concern that foreground objects will contaminate the overdensity measurements; however caution must be exercised at these higher redshifts because the number of photometric galaxies at these higher redshifts is falling off quickly. In Figure 3.1, we present the mean counts around random positions at each redshift increment of 0.001 in $0.11 \leq z \leq 0.6$ including the δz cut. The number of galaxies expected to be counted within $2.0 h_{70}^{-1}$ Mpc and the δz cut decreases quickly as the angular size of this radius shrinks with redshift and the number of photometric galaxies in the entire sample decreases. If we assume that the photometric galaxies follow a Poisson distribution, the expected signal-to-noise ratio within the $2.0 h_{70}^{-1}$ Mpc area is $\sqrt{R_i}$, where R_i is the mean number of galaxies counted within that area at a particular redshift. We compare the expected signal-to-noise ratio to the standard deviation on the mean counts with redshift in Figure 3.2. At low redshifts it is clear that the expected error (due to true physical variations in the galaxy distribution) overwhelms the Poisson error, but at higher redshifts, the Poisson error has a larger contribution. We require a signal-to-noise of at least 2, which means that it is necessary to set an upper limit on redshift of $z = 0.5$ when the photometric galaxy sample is used as a whole. However, we also subdivide the photometric galaxy sample by type, and in order to keep our signal-to-noise above 2, we must decrease the upper redshift limit when smaller background samples are used. Table 3.1 lists the redshift limits and expected signal-to-noise values for each of the background galaxy samples that we use in our analysis.

In Figure 3.3, we confirm the necessity of an upper limit by determining the probability of counting at least one galaxy in $2 h_{70}^{-1}$ Mpc if the environment galaxies are assumed to follow a Poisson distribution. At $z = 0.4$, it is certain that at least one environment galaxy of any type will be detected, and probability of finding an early-type (late-type) galaxy is 0.996 (0.992). At $z = 0.5$, the probability of finding at least one environment galaxy is 0.988; probability of finding an early-type (late-type) galaxy is 0.881 (0.896). At $z = 0.6$, the probability of finding at least one environment galaxy is much lower at 0.649; the probabilities of finding an early-type or late-type galaxy are further reduced to 0.300 and 0.498, respectively.

3.4 VOLUME-LIMITING

The spectroscopic and photometric data samples used in this analysis have been selected from magnitude-limited surveys and parent samples. Therefore, because the apparent magnitude limit is constant for all redshifts, there is a systematic increase in minimum (intrinsic) luminosity of objects detected with redshift due to the inverse-square law for electromagnetic radiation. To remove this evolution in minimum luminosity, one selects a volume-limited sample by determining the intrinsic luminosity corresponding to the (apparent) magnitude limit at the maximum redshift and allowing only those sources that are brighter than this luminosity into the sample. Such a sample minimizes systematics due to redshift-dependent properties such as galaxy type (e.g., Budavari et al., 2003)

3.4.1 Spectroscopic Target Samples

Primarily, we will use the extinction-corrected $L_{[\text{OIII}]}$ measurement to create volume-limited samples of spectroscopic targets. Based on Figure 2.3, we select targets with $\log(L_{[\text{OIII}]} / L_{\odot}) \geq 8.0$ for a volume-limited sample to $z = 0.5$. When we restrict the redshift to $z \leq 0.28$ ($z \leq 0.3$), we lower the luminosity limit to $\log(L_{[\text{OIII}]} / L_{\odot}) \geq 6.75$. Table 3.2 summarizes the various volume-limits that will be implemented throughout the analysis.

3.4.2 Photometric Environment Galaxy Sample

We test the usefulness of a volume-limited photometric galaxy sample by creating a sample with $z \leq 0.45$ and $M_r > -20.55$ (hereafter referred to as the V4 volume limit).

We compare the cumulative overdensity of targets as a function of redshift using no photometric galaxy cuts, the $\delta z = 0.05$ cut, the V4 limit, and both the V4 and δz cuts (see Figure 3.4, which uses QI_{pt} sources with $-24.2 \leq M_i \leq -22.0$). We find that applying just the V4 volume-limit has a negligible effect on the measured overdensity of the target environments. Applying the $\delta z = 0.05$ cut has a strong effect as it eliminates most of the projection effects of background and foreground galaxies. Combining the $\delta z = 0.05$ cut with the V4 background sample increases the overdensities measured but also increases the measurement noise. The increase of overdensity when using the V4 background sample is due to the fact that only brighter galaxies are being counted, and it is well known that brighter galaxies cluster more strongly (e.g. Norberg et al., 2002; Hogg et al., 2003; Blanton et al., 2005).

Our goal is to marginalize over the photometric redshift distribution of the background galaxy sample, which is accomplished with the δz cut; adding the volume limit increases the noise without improving the overdensity measurement. Therefore, in general, we will not use volume-limited background galaxy samples.

Table 3.1: Redshift limits based on Poisson signal-to-noise.

Galaxy Sample	Redshift Limit	Expected S/N	$P > 0$ counts
all	0.5	2.09	0.988
early	0.4	2.33	0.996
late	0.4	2.21	0.992
Ell	0.28	2.48	0.998
Sbc	0.28	2.20	0.992
Scd	0.28	2.14	0.990
Irr	0.28	3.50	1.0

Table 3.2: Volume-limited spectroscopic samples.

Sample	Redshift	Luminosity	# Objects
TI+TII	$0.11 \leq z \leq 0.5$	$\log(L_{[\text{OIII}]} / L_{\odot}) \geq 8.0$	3781
TI	$0.11 \leq z \leq 0.5$	$\log(L_{[\text{OIII}]} / L_{\odot}) \geq 8.0$	3229
TII	$0.11 \leq z \leq 0.5$	$\log(L_{[\text{OIII}]} / L_{\odot}) \geq 8.0$	552
TI+TII	$0.11 \leq z \leq 0.28$	$6.75 \leq \log(L_{[\text{OIII}]} / L_{\odot}) \leq 8.0$	2944
TI	$0.11 \leq z \leq 0.28$	$6.75 \leq \log(L_{[\text{OIII}]} / L_{\odot}) \leq 8.0$	894
TII	$0.11 \leq z \leq 0.28$	$6.75 \leq \log(L_{[\text{OIII}]} / L_{\odot}) \leq 8.0$	2050
TI+TII	$0.11 \leq z \leq 0.4$	$\log(L_{[\text{OIII}]} / L_{\odot}) \geq 8.0$	2229
TI	$0.11 \leq z \leq 0.4$	$\log(L_{[\text{OIII}]} / L_{\odot}) \geq 8.0$	1791
TII	$0.11 \leq z \leq 0.4$	$\log(L_{[\text{OIII}]} / L_{\odot}) \geq 8.0$	438
QI	$0.11 \leq z \leq 0.5$	$\log(L_{[\text{OIII}]} / L_{\odot}) \geq 8.0$	3030
QI	$0.11 \leq z \leq 0.4$	$\log(L_{[\text{OIII}]} / L_{\odot}) \geq 8.0$	1592
AI	$0.11 \leq z \leq 0.15$	$\log(L_{[\text{OIII}]} / L_{\odot}) \geq 6.5$	621
AII	$0.11 \leq z \leq 0.15$	$\log(L_{[\text{OIII}]} / L_{\odot}) \geq 6.5$	1222

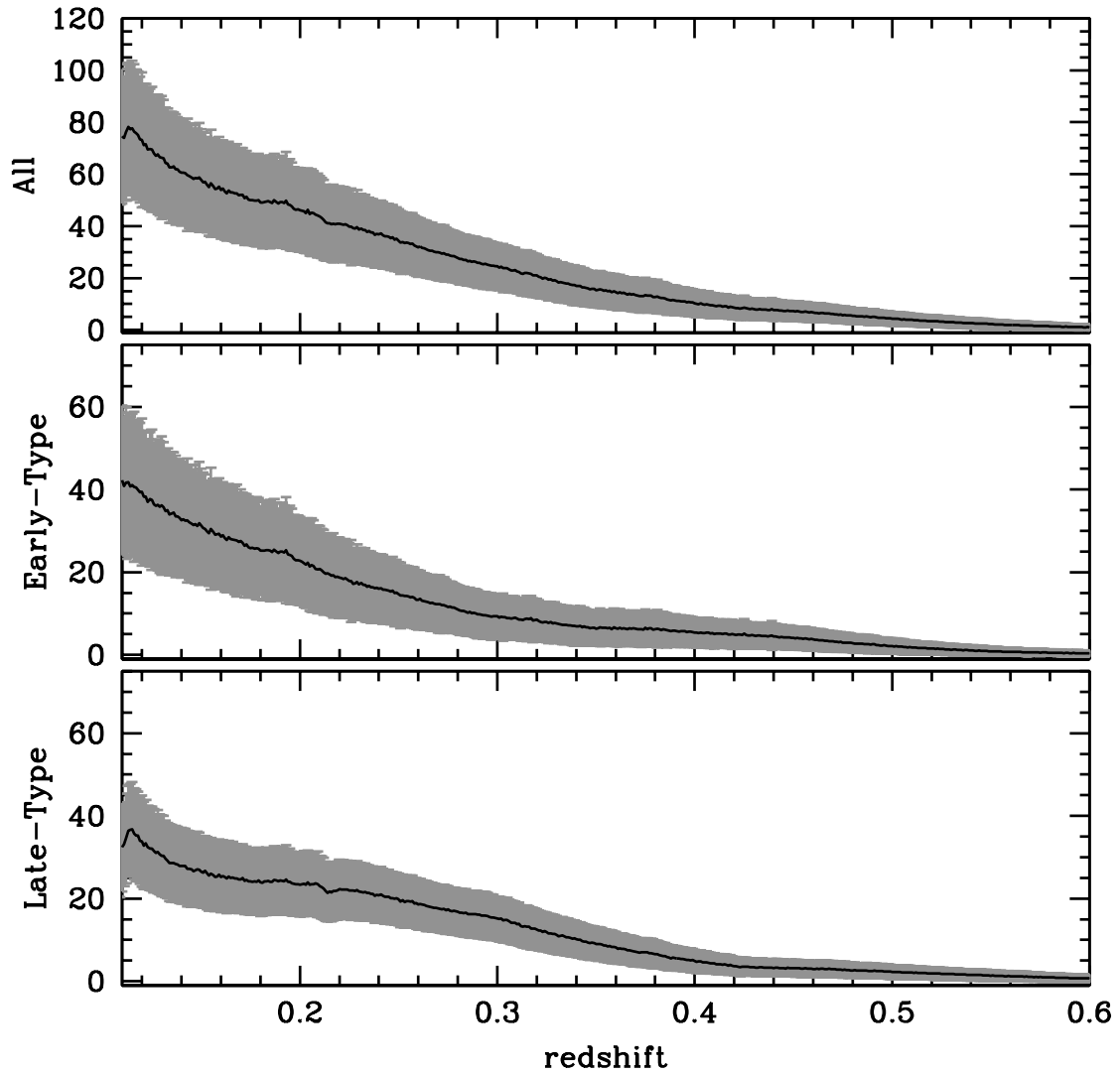


Figure 3.1— Expected galaxy counts in $2.0 h_{70}^{-1}$ Mpc radius vs. redshift. The black line corresponds to the mean number of counts around random targets, the grey area corresponds to the standard deviation from this mean (*Note*— at least 1000 random targets contribute to the mean at each 0.001 in redshift).

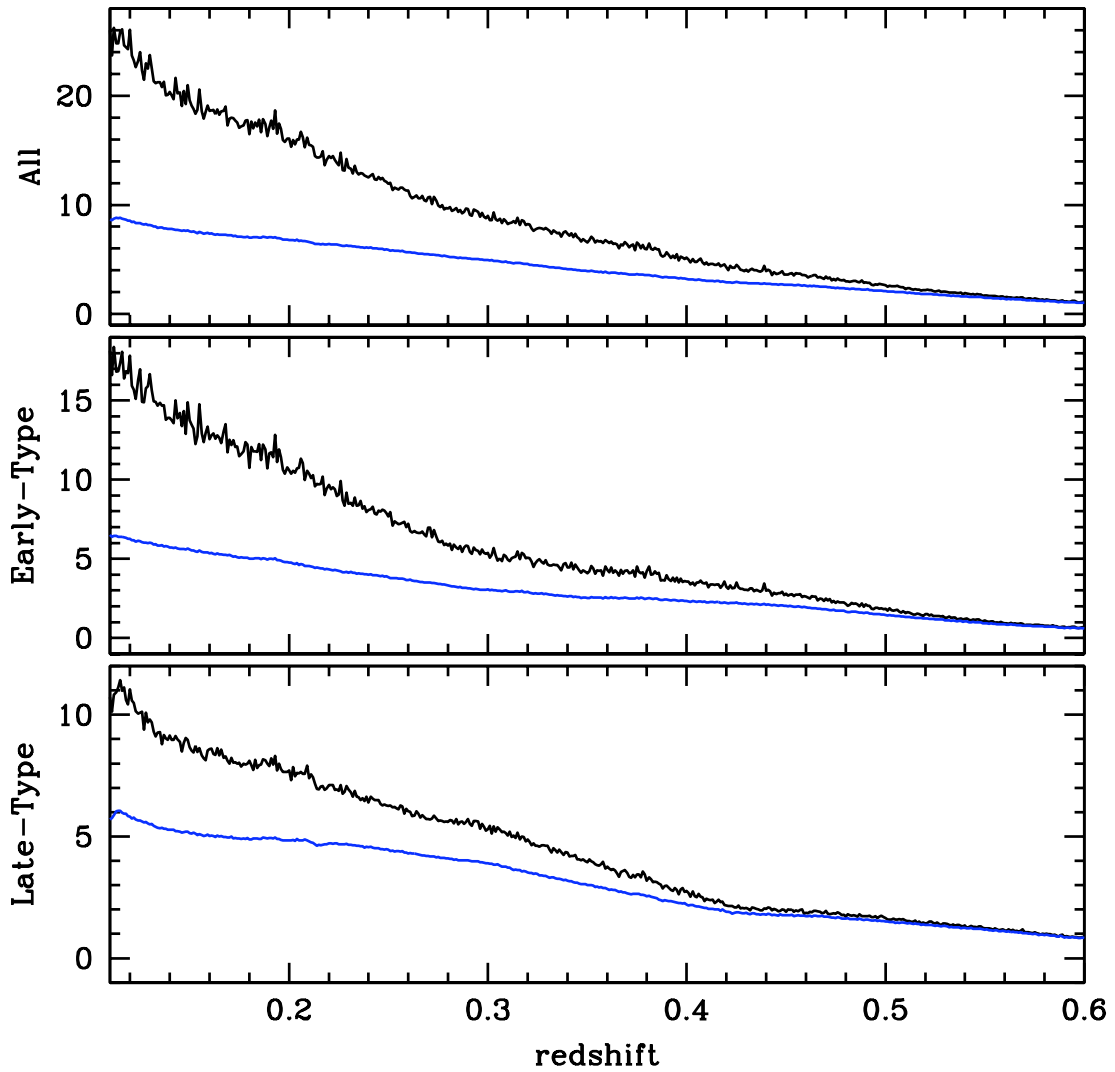


Figure 3.2— Comparison of the standard deviation on the mean number of counts around random targets (black) to the Poisson error ($= \sqrt{\text{mean counts}}$; blue).

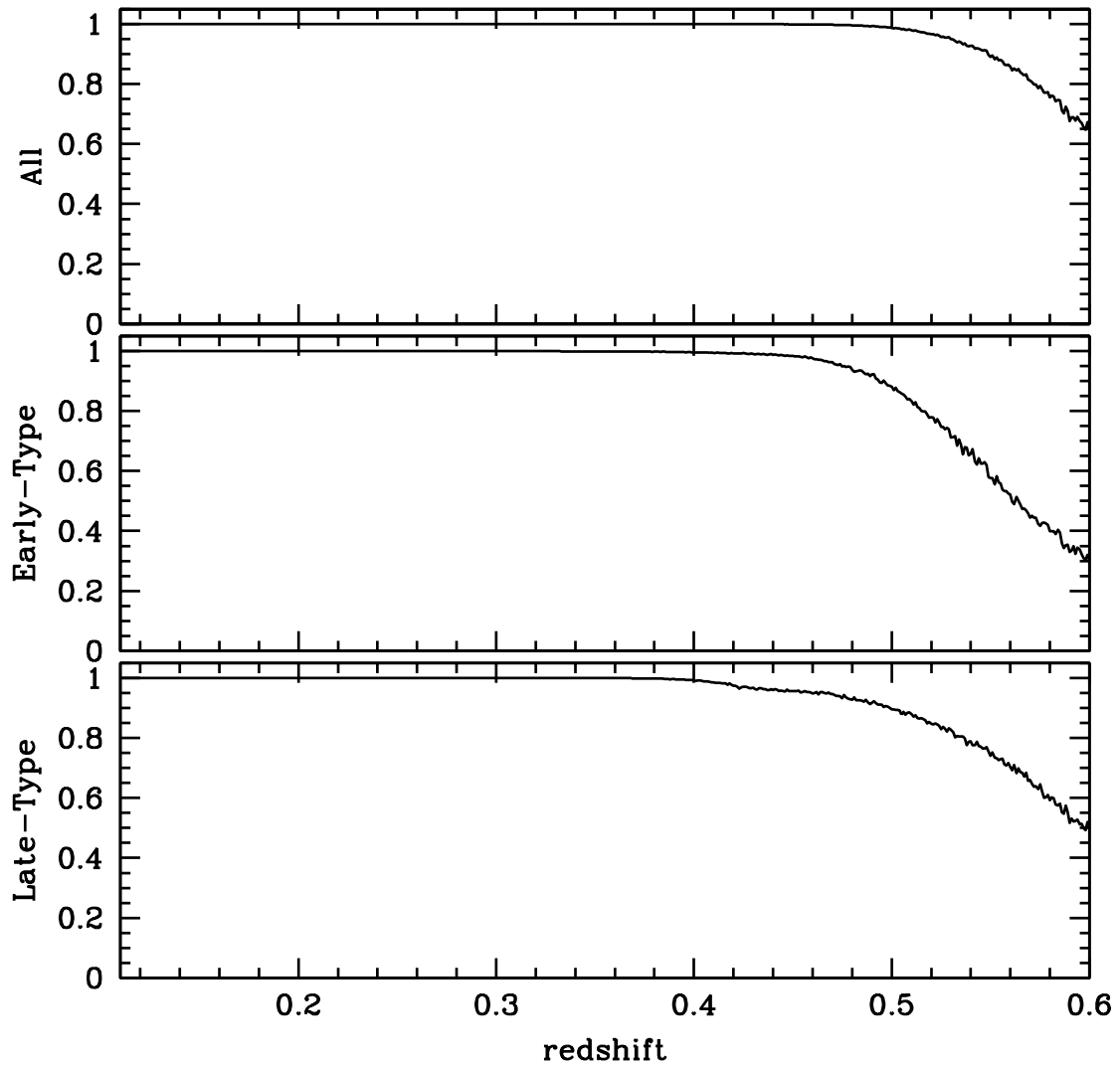


Figure 3.3— Probability of finding more than zero counts if the environment galaxies can be approximated as having a Poissonian distribution.

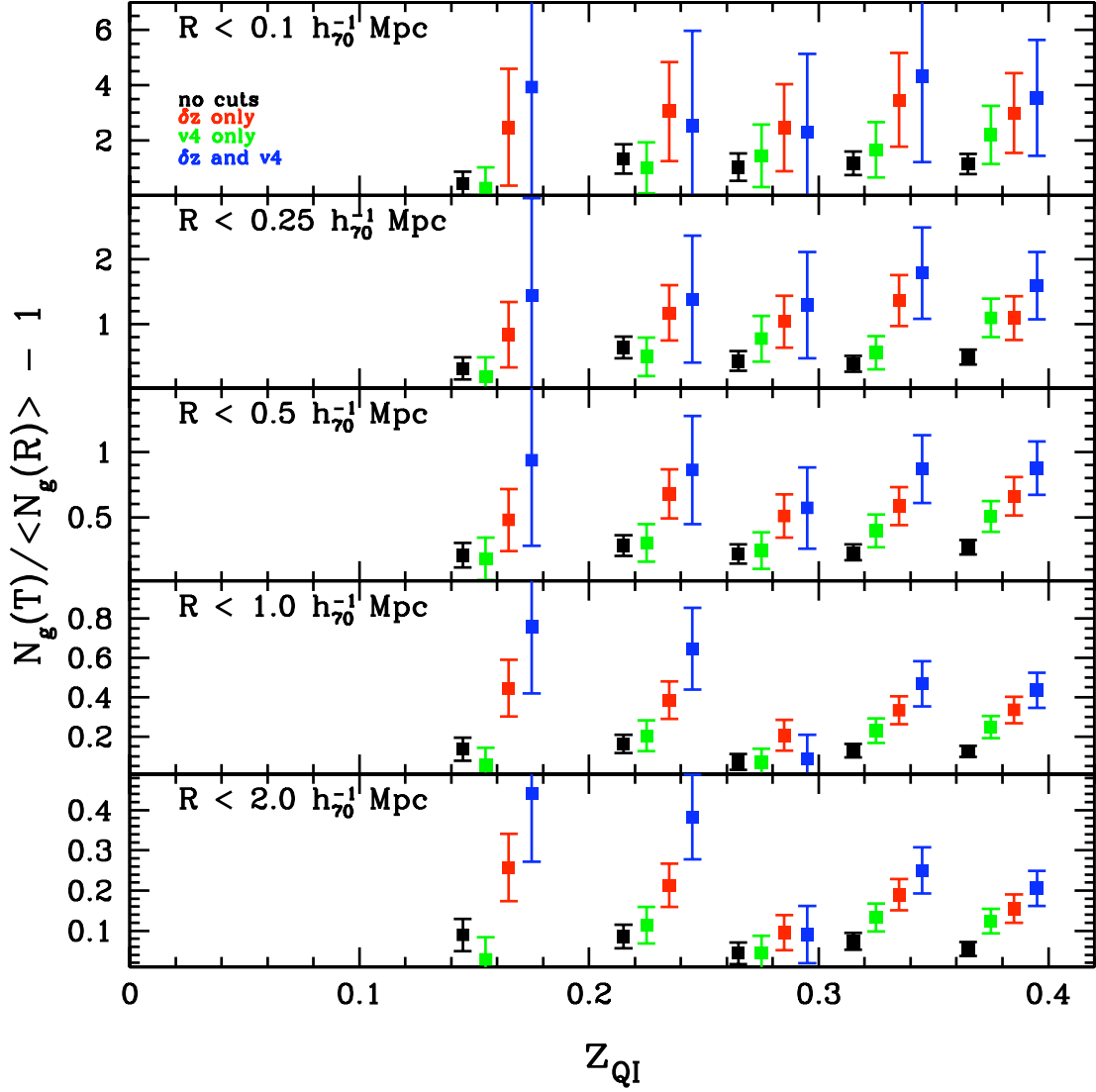


Figure 3.4— Cumulative overdensity vs. redshift for $0.11 \leq z \leq 0.4$ QI_pt sources with $-24.2 \leq M_i \leq -22.0$ using no cuts (black), only $\delta z = 0.05$ cut (red), only V4 sample photometric galaxy sample (green), and both V4 photometric galaxy sample and $\delta z = 0.05$ (blue).

Chapter 4

The Dependence on Redshift, Type, & Broad-Band Luminosity

4.1 OVERVIEW

We now begin our analysis of the environments of AGNs and quasars using the galaxy counting technique established in the previous chapter. Here we explore how the local environment of the targets is related to their redshift, type, and broad-band luminosity. This work was originally published as Strand et al. (2008); since its publication, however, we have modified our upper limits in redshift (see Section 3.3). The updated results, which are qualitatively unchanged, are presented in this chapter.

In Figure 4.1, we present the mean cumulative overdensity of photometric galaxies as a function of scale for the QL_pt, QIL_Z, AI, and AII spectroscopic samples. There are clear differences: Type II objects are in more overdense environments than Type I objects for both higher luminosity AGN (i.e. quasars) and lower luminosity AGN, and quasars are in the most overdense environments at all scales. Within a scale of $\approx 150 h_{70}^{-1}$ kpc, QIL_Zs have an environment 1.3 times more overdense than that of QL_pts, albeit with large errors, while the AIIs have an environment 1.4 times more overdense than AIs. At the same scale, the QL_pts have environments more overdense than AIs by a factor of 1.8, and QIL_Zs have environments 1.6 times more overdense than AIIs. Moving out to the scale of $\approx 1 h_{70}^{-1}$ Mpc, the QIL_Zs again have an environment 1.3 more overdense than the environment of QL_pts, and the QL_pts are in environments 1.4 times more overdense than AIs.

The differences between the target samples' environment overdensities could be an effect of AGN type, however, and the intertwined effects of AGN luminosity and redshift will certainly play into these differences. In this chapter, we explore how type, redshift and broad-band luminosity influence the measured differences in AGN environments.

4.2 TARGET REDSHIFT

We first isolate the effects of redshift and investigate the redshift dependence of AGN environments. Figure 4.2 shows the mean cumulative overdensity as a function of redshift for different spectroscopic targets, which provides marginal evidence for redshift evolution in the environment overdensity of QL_pts. The magenta dashed line shows the linear weighted least-squares fit to the QL_pt environment overdensity data with redshift at different maximum radii; the fitting parameters for these lines is given in Table 4.1. The rightmost column of the table gives the χ^2 probability for each fit using the relevant degrees of freedom. While these fits indicate a slight redshift dependence, we also try a zero-slope linear fit and find that the zero-slope fit, i.e., no redshift dependence, is also a good fit to the data and in the case of the $1 h_{70}^{-1}$ Mpc scale, slightly more likely. In contrast, weighted least-squares

fits for AIs and AIIIs (which are not shown in Figure 4.2, but the parameters are listed in Table 4.1) show that there is evolution with redshift (especially for AIIIs). This conclusion is strengthened by the fact that zero-slope fits are increasingly poor characterizations of the overdensity with redshift relationship as the scale decreases. The average QII_Z environment overdensity, which is placed at the average redshift of the sample, is consistent with the QI_pt overdensity values at all scales. We note that both larger samples and higher redshift measurements will be necessary to place strong constraints on the functional form of QI environment overdensity evolution with redshift. However, if the QI environment overdensity is indeed independent of redshift, this implies that the significant differences in environment seen in Figure 4.1 are caused primarily by luminosity and type effects, rather than the influence of redshift evolution.

In the top panel of Figure 4.3, we show the evolution of the mean cumulative overdensity of photometric galaxies in the environments of QI_pt, AI and AII samples. It is important to recall that we have placed the random points at the same redshift as the spectroscopic targets, and that we have imposed δz cuts on the photometric galaxies (as described in Section 3.2) in order to minimize the effect of redshift evolution in the photometric galaxy sample. Therefore we can compare objects in different redshift bins. Figure 4.3 demonstrates that higher redshift QI_pts are in environments 1.29 times more overdense than the lower redshift quasars on scales $\lesssim 500 h_{70}^{-1}$ kpc, while at larger scales, there appears to be little-to-no redshift evolution. However, there is scale-dependent redshift evolution evident on scales $\lesssim 1.0 h_{70}^{-1}$ Mpc for the AIIIs, shown in the lowest panel. The AIs begin to exhibit more noticeable redshift evolution at scales $\lesssim 300 h_{70}^{-1}$ kpc, where the environments of lower redshift AIs are 1.16 times less dense than those of the higher redshift AIs.

We see therefore that there is some evidence for a change in local environment as a function of redshift, all else being held constant. However, we have not yet taken AGN luminosity into account. Even in the same redshift range, selection effects due to the magnitude-limited samples may come into play, which we investigate in Sections 4.4 and 4.5.

4.3 TARGET TYPE

In Figure 4.4, we identify three redshift ranges where there is overlap between our AGN samples and explore whether differences in type are reflected in the relative overdensity. The top panel shows the overdensity as a function of scale for both types of higher-luminosity AGNs (i.e. quasars) in the range $0.3 \leq z \leq 0.5$, and for both types of lower-luminosity AGNs in two redshift ranges, $0.11 \leq z \leq 0.15$ and $0.15 < z \leq 0.33$. The dividing redshift value of $z = 0.15$ is chosen to roughly equalize the number of lower-luminosity AGNs in each redshift range. The lower three panels show the ratio of Type II environment overdensity to Type I environment overdensity in the three redshift ranges. Again, we are able to compare objects in different redshift ranges because we have imposed δz cuts on the photometric galaxies around both the spectroscopic targets and the random positions to which they are compared in order to account for any redshift evolution in the photometric galaxy sample and to minimize projection effects.

QII_Zs have higher overdensity environments than QI_pts with little scale dependence: at $R \approx 1.0 h_{70}^{-1}$ Mpc, the overdensity of QII_Z environments is a factor of 1.4 greater than the overdensity of QI_pt environments, and at the smaller scale of $R \approx 250 h_{70}^{-1}$ kpc, the QII_Z environments have 1.2 times the overdensity of QI_pt environments. However, the large errors due to the small number

of QII-Zs prevent us from drawing strong conclusions.

Type II environment overdensity is again consistently about a factor of 1.3 higher on all scales than the Type I environment overdensity for AIs and AIIIs in the redshift range $0.15 < z \leq 0.33$. In the lower redshift range of $0.11 \leq z \leq 0.15$, however, the AII and AI environment overdensities have a ratio consistent with unity until scales $R < 200 h_{70}^{-1}$ kpc, where the ratio increases to 1.3. This result agrees with previous work that concluded that Type II Seyfert galaxies are more likely to have close neighbors than Type I Seyferts at very low redshifts (Koulouridis et al., 2006).

Because we see increased overdensity for AIIIs compared to AIs on small scales in overlapping redshift ranges, we can conclude that in Figure 4.1, the differences seen in environment overdensity between the AGN types are not primarily due to redshift evolution. However, we have not ruled out the effects of AGN luminosity. The AI and AII samples are selected from magnitude-limited spectroscopic galaxy samples, which will be dominated by intrinsically more luminous sources at higher redshift. The AI sample could be more affected by this magnitude limit, as the broad emission lines contribute more significantly to the overall flux in a given band and therefore the two AGN populations could have different average intrinsic luminosities.

4.4 TARGET BROAD-BAND LUMINOSITY

Unlike Type I quasars, which are targeted largely based on their strong nuclear luminosity (Schneider et al., 2007), the lower luminosity AGN we use were selected from objects classified as galaxies by the SDSS selection algorithms (Hao et al., 2005a). The broad-band flux of these sources will be dominated by host galaxy starlight and/or flux from star formation, etc., which has little or no association with the nuclear luminosity. Therefore, we first focus on the point-source QIs only (QI-pt) for our analysis of the relationship between absolute magnitude and environment, as the QI sample spans the entire redshift range we study, and with this long redshift baseline we are best able to disentangle redshift and luminosity effects on environment overdensity.

In order to verify that the observed evidence for evolution of environment overdensity is not due to the $i \leq 19.1$ ($z \lesssim 3.0$) limit imposed on QI selection in the SDSS (Schneider et al., 2007), we performed several tests in which we vary the apparent magnitude limit of the data. We considered two quasar samples limited to $i \leq 18.9$ and to the $i \leq 19.1$ SDSS limit. The two magnitude-limited samples were each subdivided into two luminosity bins. We first compared environment overdensity measurements of bright or dim quasars in each of the magnitude-limited samples and found no appreciable difference. Additionally, no difference was observed when different absolute magnitude values were used to define the bright and dim samples. In order to ensure that there is no difference between environments of quasars with $i > 19.1$, which were selected by the high-redshift targeting algorithm, and the rest of the apparent magnitude-selected sample, we performed similar tests comparing the environment overdensity of the entire quasar sample to that of the subset of quasars with $i \leq 18.9$ or $i > 19.1$. In all cases, there was no appreciable change in the observed overdensity.

We compare the environment overdensities of QI-pt in two luminosity bins to the other target samples without redshift cuts in Figure 4.5. The threshold value $M_i = -23.0$ is chosen to give roughly equal numbers of QI-pt sources in each luminosity bin: there are 1,136 (1,178) quasars with $-26.4 \leq M_i \leq -23.0$ ($-23.0 < M_i \leq -22.0$). The average magnitude of the brighter (fainter) bin is $\overline{M}_i = -23.60$ ($\overline{M}_i = -22.60$).

QII_Zs and the brighter QI_pt sources are located in similarly overdense environments consistently at all scales, while the dimmer QI_pts are located in environments slightly less overdense than the QII_Zs. At a scale $R \approx 500 h_{70}^{-1}$ kpc, the cumulative overdensity of QII_Z environment is 1.14 times that of the brighter QI_pts, but 1.18 times as the dimmer QI_pts. At the scale of $R \approx 1.0 h_{70}^{-1}$ Mpc, QII_Zs have environment overdensities 1.3 times the environment overdensity of brighter QI_pts but 1.3 times that of dimmer QI_pts. Again we note that the large error bars nearly overlap with unity and prevent strong conclusions.

The more luminous QI_pts are located in environments more overdense than AIs, while there is less difference in the overdensities of dimmer QI_pts and AIs. The environment overdensity ratio increases with decreasing scale for both brighter and dimmer QI_pts. At a scale $R \approx 500 h_{70}^{-1}$ kpc, brighter QI_pt environments have an overdensity 1.5 times the overdensity of AI environments with significance $2, 2\sigma$, and dimmer QI_pt environments have an overdensity 1.4 times the overdensity of AI environments with significance 2.2σ . At $R \approx 150 h_{70}^{-1}$ kpc, the environments of brighter QI_pts are 2.2 times as overdense (2.4σ), and the environments of dimmer QI_pts are 1.9 times as overdense as the environments of AIs (2.2σ).

The ratio of QI_pts to AIs increases for both bright and dim quasars with decreasing scale, but less dramatically as the ratio to AIs. The ratio between dimmer QI_pts and AIs is approximately consistent with unity for scales $150 h_{70}^{-1}$ kpc $< R \leq 2.0 h_{70}^{-1}$ Mpc; the ratio between brighter QI_pts and AIs is 1.2 (1.2σ) for scales $R \approx 500 h_{70}^{-1}$ kpc. On smaller scales, both ratios increase. At scales $R \approx 150 h_{70}^{-1}$ kpc, the ratio of brighter QI_pts to AIs is 1.6 (1.7σ), and the ratio of dimmer QI_pts to AIs is 1.3 (1.3σ). This scale dependency could be evidence for the merger origin of quasars, since one would expect to see a higher density of environment galaxies at small scales where merger events are likely to take place (Hopkins et al., 2008).

4.5 BROAD-BAND LUMINOSITY, REDSHIFT, AND TYPE

We combine our analysis of type, redshift and broad-band luminosity effects on environment overdensity in Figures 4.6, 4.7, and 4.8. Our δz cuts on the photometric galaxies around the spectroscopic targets as well as around the random positions to which they are compared (as described in Section 3.2) allow us to make meaningful comparisons of objects in different redshift ranges. In Figure 4.6, QII_Zs are compared to QI_pts in the redshift range $0.3 \leq z \leq 0.5$. We divide the QI_pts into bright (1,039; $\overline{M}_i = -23.60$) and dim (980; $\overline{M}_i = -22.60$, about 2.5 times fainter) samples of roughly equal numbers at $M_i = -23.0$.

Comparing the lower panel of Figure 4.6 to the top ratio panel of Figure 4.4 shows the dramatic part luminosity plays compared to evolution alone. The environment of QII_Zs is similar to the signature of brighter QI_pts for the smallest scales. The similarity of environments at small scales suggests that the differences observed between brighter Type I quasars and Type II quasars are due to a non-environmentally driven mechanism such as orientation or internal structure effects. This in turn implies that Type II quasars are not a different cosmological population from these brighter Type I quasars.

However, the QII_Z environments are slightly more overdense, albeit with large errors, than those

of dimmer QI_pts on scales $R \leq 2.0 h_{70}^{-1}$ Mpc that we measure. The different characteristics of the environments of the dimmer QI_pt population from the QII_Z population are most likely due to intrinsic luminosity differences rather than redshift differences. We see consistent overdensity ratios on all scales and do not see small scale effects, therefore we conclude that the difference in environment overdensity between the brighter and dimmer quasars is primarily due to mass effects. More luminous AGN are expected to have higher mass black holes (e.g., Magorrian et al., 1998; Marconi & Hunt, 2003), which are in turn correlated with more massive dark matter halos (e.g., Ferrarese & Merritt, 2000; Gebhardt et al., 2000; Tremaine et al., 2002). Selection effects in the magnitude-limited photometric galaxy sample could also play into the difference in overdensity between the brighter and dimmer QI_pts. The redshift distribution of QI_pts in the brighter ($M_i \leq -23.25$) bin is slightly different from that of the dimmer ($M_i > -23.25$) bin even over the redshift range of $0.3 \leq z \leq 0.5$ (the brighter quasars have a mean redshift of 0.43, and the dimmer quasars have a mean redshift of 0.40). The galaxies seen in the environments of brighter (higher redshift) quasars will tend themselves to be brighter, and consequently more massive, and therefore cluster more strongly than the dimmer environment galaxies (Maddox et al., 1990; Zehavi et al., 2002). This, however, should not be a major effect.

Figure 4.7 compares the environments of QI_pts in two luminosity bins to the environments of AIs and AIIIs in the redshift range $0.15 < z \leq 0.33$. We use $M_i = -22.65$ as the threshold value for brighter and dimmer quasars in this lower redshift range to equalize the number in each luminosity bin. The 222 brighter (228 dimmer) QI_pts have a mean magnitude of $\overline{M}_i = -23.39$ ($\overline{M}_i = -22.32$, about 2.4 times fainter than the brighter sample). We note that these QI_pt samples are more than four times smaller than the QI_pt samples in the higher redshift range, thus the measurements (and resulting interpretation) will be less precise.

The top panel of Figure 4.7 shows that at all scales, the environments of dimmer QI_pts are more overdense than those of brighter QI_pts. It appears that the situation has been reversed from Figure 4.6, where the environments of dimmer quasars were less overdense than the environments of brighter quasars. However, the range of luminosity at this lower redshift range of $0.15 < z \leq 0.33$ is much smaller than for the higher range of $0.3 \leq z \leq 0.5$. The overall absolute magnitude distribution of these QI_pts is skewed toward the faint end, thus the dividing value $M_i = -22.65$ is very close to the quasar-Seyfert divide of $M_i \approx -22.5$ as defined by Hao et al. (2005b). Significant variation in overdensities was seen when different magnitude cuts were imposed, with the dimmer quasars consistently having higher overdensities by varying margins. The dramatic sensitivity of results on the bright/dim dividing value emphasize that for low luminosities and redshifts, broad-band absolute magnitudes are a poor proxy for AGN luminosity. The measured flux is more likely to be affected by galaxy starlight, star formation, etc. at this faint end. Therefore, any attempt to use broadband magnitudes to correlate nuclear luminosity with environment will be skewed.

With these caveats in mind, we compare the QI_pts to lower-luminosity AIs and AIIIs in the lower two panels of the figure. Dimmer QI_pt environments have overdensities greater than the AIs, but the environments of brighter QI_pts and the AIs have about the same amplitude on all scales. The lower ratio panel shows the ratio of bright and dim QI_pts to AIIIs. The brighter quasars have environments with slightly lower overdensity than AIIIs; the environments of dimmer QI_pts are only slightly more overdense than the environments of AIIIs, but are consistent within the error bars.

In Figure 4.8 we focus on QI_pts alone to investigate the evolution of the environment overdensity

of brighter and dimmer objects. We have chosen two luminosity intervals of one magnitude in width and compare the environment overdensities of brighter to dimmer objects in three redshift intervals. ΔM_1 corresponds to the dimmer luminosity interval of $-23.0 < M_i \leq -22.0$ and contains 1,174 QI_pts, and the brighter luminosity interval ΔM_2 is $-24.0 < M_i \leq -23.0$, containing 924 QI_pts. Table 4.2 gives the number of quasars as well as the mean magnitude in each redshift and magnitude bin.

In the two lower redshift bins $0.15 < z \leq 0.3$ and $0.3 < z \leq 0.4$, there is little difference in the environment overdensity of brighter and dimmer quasars with little-to-no scale dependence. However, in the highest redshift interval of $0.4 < z \leq 0.5$, brighter quasars are shown to be located in slightly more overdense environments than the dimmer quasars. At scale of $R \approx 1.0 h_{70}^{-1}$ Mpc, the brighter quasars are located in environments with overdensity 1.5 times that of the dimmer quasars. The brighter quasars have environments with overdensity 1.4 times the overdensity of dimmer quasar environments at a scale of $R \approx 250 h_{70}^{-1}$ kpc, and then the ratio begins to drop toward unity at the innermost scales. However, the large errors are nearly consistent with unity on all scales we measure.

It appears, therefore, that there is again slight evidence for some redshift evolution of QI_pt environments, but it is mainly manifested at the highest redshift range, which also has the largest error bars. This emphasizes the need for additional studies of the environments around higher redshift Type I quasars. We caution that the increased overdensity at higher redshift be affected by the change in mean luminosity of the dimmer quasar sample with increasing redshift (see Table 4.2). While the bright quasar luminosity hardly changes between the three redshift intervals, the mean dim quasar luminosity changes by 0.23 magnitudes. Therefore we cannot draw strong conclusions, but reiterate the need for higher precision and higher redshift measurements of quasar environments.

4.6 CONCLUSIONS

We have shown in this chapter that QII_Zs are shown to have similar environments as brighter Type I quasars in the same redshift range on all scales that we study, which suggests the observational differences in Type I and Type II quasars are driven by orientation and/or structure and not by cosmological evolution. Evidence that dimmer quasars and lower-luminosity AGN are located in environments with similar overdensity might suggest that dimmer quasars could be a transition population between low-luminosity AGN (likely fueled in dry mergers, close encounters, or secular processes) and high-luminosity AGN (likely fueled in major mergers). Rather than disparate populations of merger-fueled and secularly fueled AGN, there may be a continuum of galaxy interactions from major mergers to close encounters or harassment that cause AGN luminosity differences. Alternatively, a mix of mergers and secular processes could drive the AGN population near the quasar-Seyfert divide ($M_i \approx -22.5$; Hao et al., 2005b). We have compared the AGN samples without redshift cuts, but we note that in Section 4.2 we demonstrated that evolution of quasar environments with redshift is negligible.

The significant difference in the environments of bright QI_pts and the environments of both AIs and AIIs could imply that these populations have different fueling mechanisms. A weak link between nearby neighbors of narrow-line AGN and their nuclear activity (Li et al., 2006, 2008) implies that it is likely internal mechanisms rather than merger activity that gives rise to the AGN activity in the low-luminosity sources. The scale dependency in the relative environment overdensities of bright

QI_{pt} overdensities and lower-luminosity AGN could be evidence for the merger origin of bright QIs, since mergers are expected to be more likely in regions with a higher local density of galaxies (Hopkins et al., 2008).

Finally, there is marginal evidence for redshift evolution of Type I quasar environments on all scales, especially for $0.4 \leq z \leq 0.5$, not noted in previous studies. However, this evolution is not the primary explanation for the environment overdensity differences seen between Type I quasars and Type II quasars, and between Type I AGN and Type II AGN. In order to place strong constraints on the functional form of this redshift evolution, it is necessary to acquire higher precision measurements and higher redshift measurements.

Table 4.1: Linear weighted least-squares fit parameters for QI_pt, AI, and AII environment data in Figure 4.2.

R_{max}	slope	intercept	χ^2	$P(\chi^2, \nu)$
QI_pt				
2.0 h_{70}^{-1} Mpc	0.161 ± 0.152 0.0	0.107 ± 0.057 0.165 ± 0.013	8.91 10.02	0.1787 0.1874
1.0 h_{70}^{-1} Mpc	0.237 ± 0.286 0.0	0.237 ± 0.104 0.321 ± 0.024	6.14 6.83	0.4077 0.4468
0.5 h_{70}^{-1} Mpc	0.830 ± 0.622 0.0	0.358 ± 0.219 0.641 ± 0.055	1.43 3.21	0.9640 0.8649
0.15 h_{70}^{-1} Mpc	4.49 ± 2.79 0.0	0.382 ± 0.927 1.82 ± 0.249	1.15 3.75	0.9793 0.8081
AI				
2.0 h_{70}^{-1} Mpc	0.152 ± 0.268 0.0	0.096 ± 0.045 0.121 ± 0.011	2.32 2.64	0.6771 0.7553
1.0 h_{70}^{-1} Mpc	0.555 ± 0.472 0.0	1.52 ± 0.077 0.240 ± 0.018	2.13 3.51	0.7119 0.6219
0.5 h_{70}^{-1} Mpc	1.35 ± 0.964 0.0	0.222 ± 0.155 0.434 ± 0.034	3.93 5.90	0.4156 0.3161
0.15 h_{70}^{-1} Mpc	7.28 ± 3.60 0.0	-0.164 ± 0.551 0.929 ± 0.114	0.661 4.77	0.9560 0.4446
AII				
2.0 h_{70}^{-1} Mpc	0.610 ± 0.198 0.0	0.053 ± 0.032 0.150 ± 0.007	7.20 16.7	0.1257 0.0051
1.0 h_{70}^{-1} Mpc	1.37 ± 0.353 0.0	0.072 ± 0.057 0.288 ± 0.012	11.7 26.9	0.0197 < 0.0001
0.5 h_{70}^{-1} Mpc	3.50 ± 0.743 0.0	-3.32 ± 0.117 0.537 ± 0.024	8.90 31.1	0.0636 < 0.0001
0.15 h_{70}^{-1} Mpc	10.8 ± 2.98 0.0	-0.332 ± 0.451 1.27 ± 0.087	2.71 15.9	0.6075 0.0071

Table 4.2: Details for data used in Figure 4.8.

Redshift	$-24.0 < M_i \leq -23.0$			$-23.0 < M_i \leq -22.0$		
Range	#	\overline{M}_i	\overline{z}	#	\overline{M}_i	\overline{z}
$0.15 < z \leq 0.3$	82	-23.38	0.241	195	-22.45	0.248
$0.3 < z \leq 0.4$	233	-23.40	0.361	472	-22.51	0.355
$0.4 < z \leq 0.5$	609	-23.38	0.457	507	-22.68	0.447

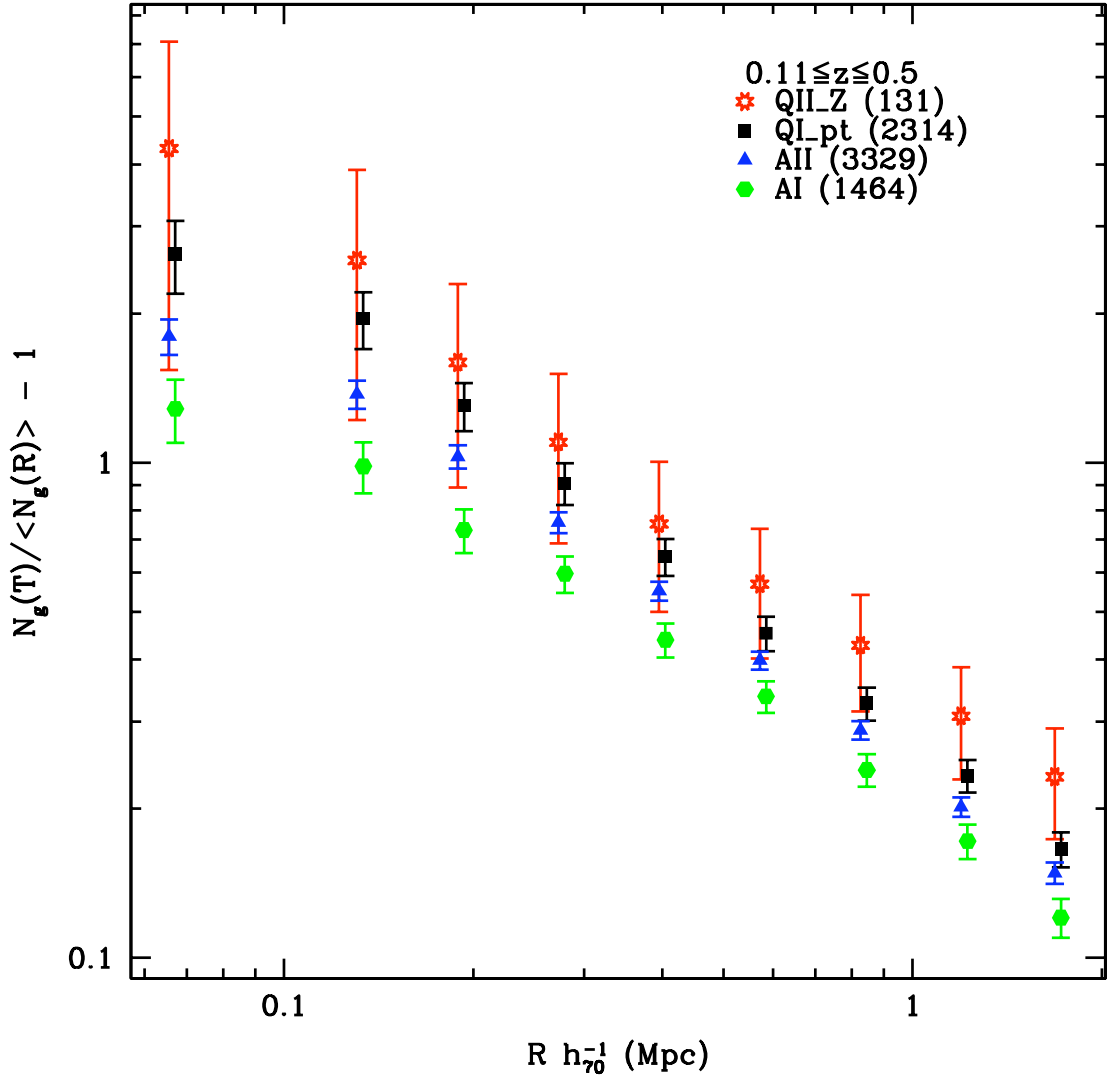


Figure 4.1— Mean cumulative overdensity of photometric galaxies as a function of comoving scale around spectroscopic targets. Solid black squares represent QI_pts, open red starred points represent QII_Zs, solid blue triangles represent AIIs, and solid green hexagons represent AIs. Points have been slightly offset horizontally for clarity.

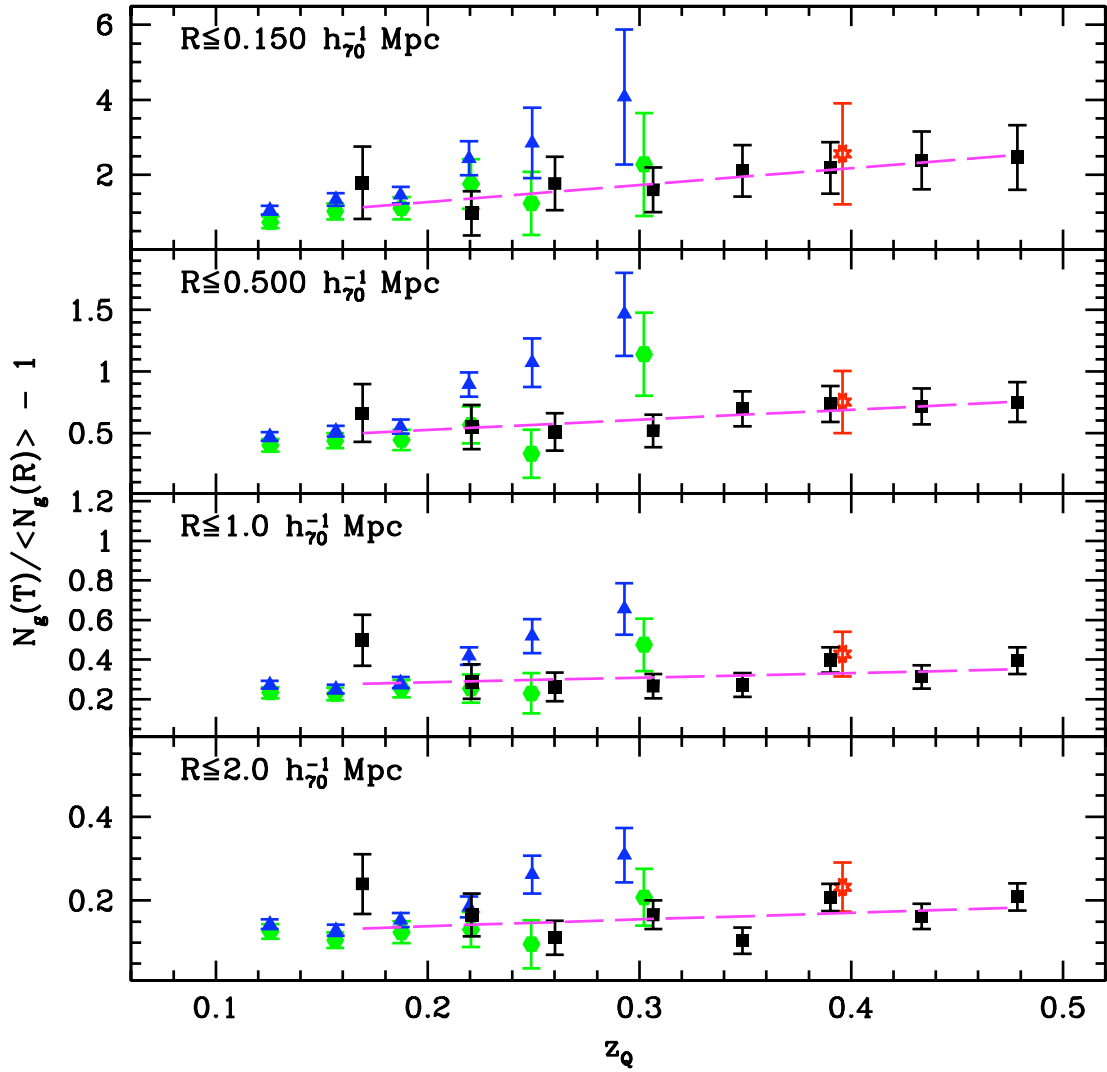


Figure 4.2— Mean cumulative overdensity vs. redshift for spectroscopic targets. Symbols correspond to those used in Figure 4.1. The magenta dashed lines are linear weighted least-squares fits for the QI_pt sample; the parameters for these lines are given in Table 4.1.

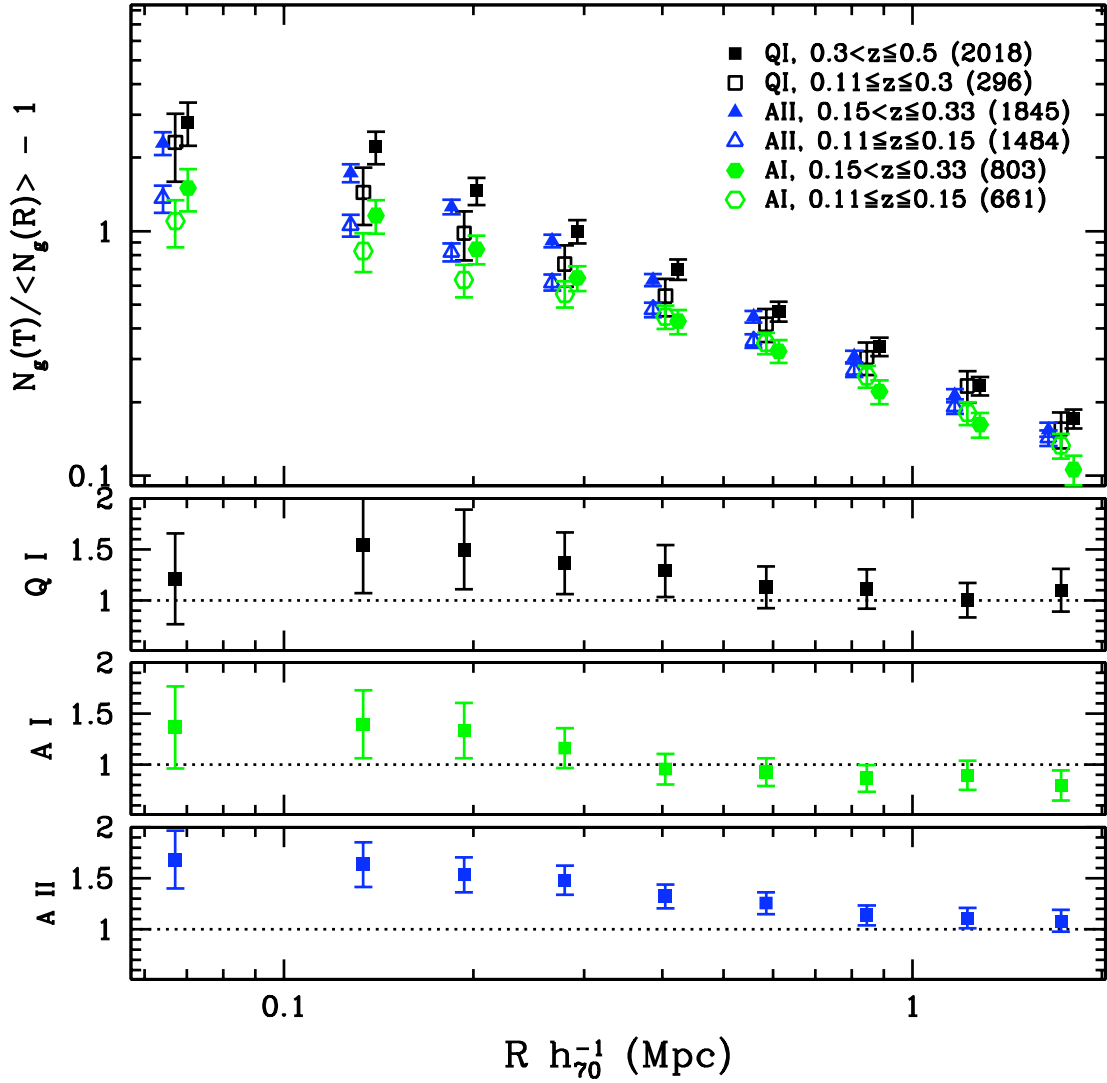


Figure 4.3— Upper panel: Mean cumulative overdensity of photometric galaxies around quasars and lower-luminosity AGN as a function of scale and redshift. Points have been slightly offset horizontally for clarity. Top lower panel: Ratio of environment overdensity of higher-redshift QI_pts to that of lower-redshift QI_pts. Middle lower panel: Ratio of environment overdensity of higher-redshift AIs to that of lower-redshift AIs. Bottom lower panel: Ratio of environment overdensity of higher-redshift AIIIs to that of lower-redshift AIIIs.

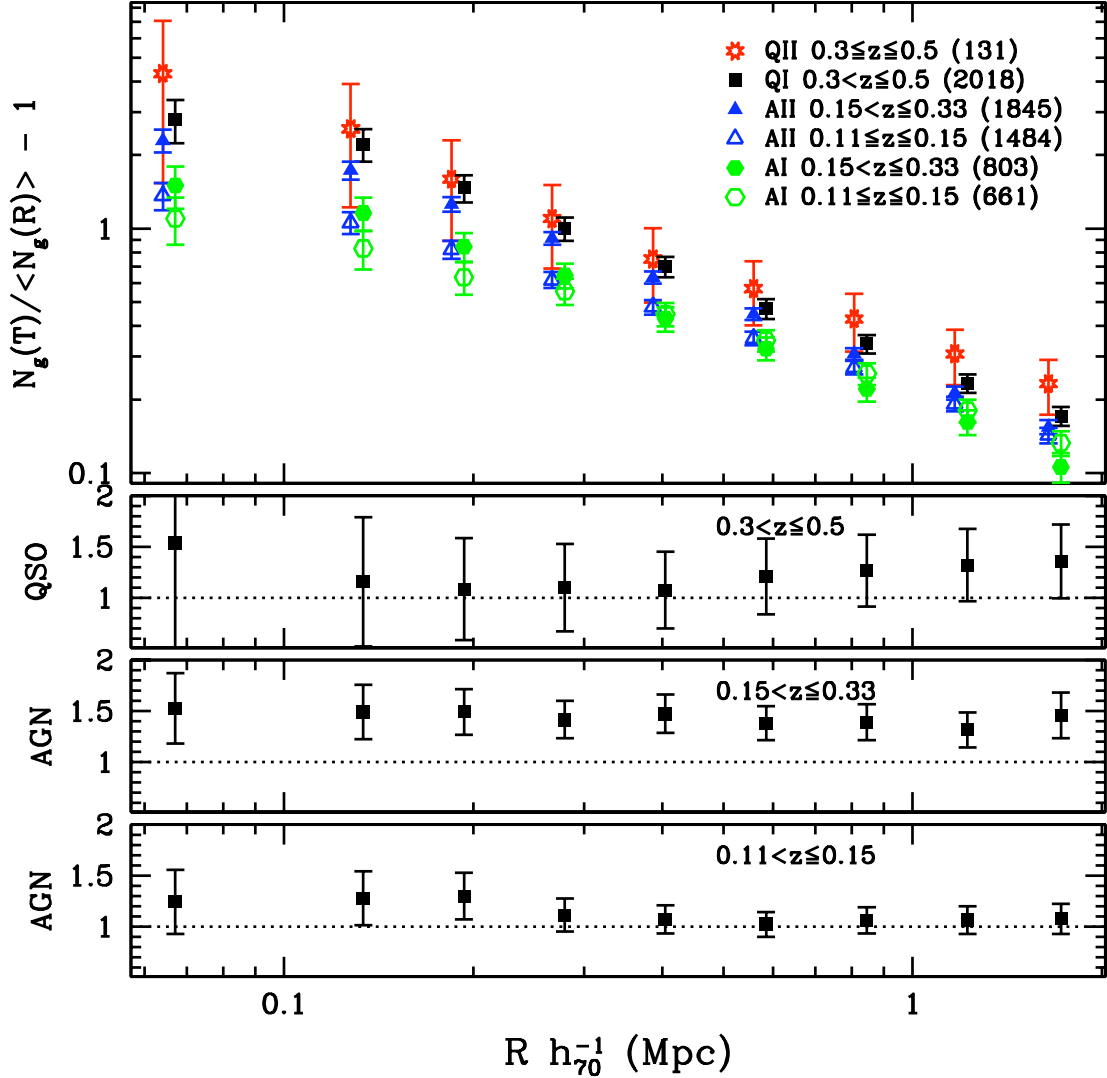


Figure 4.4— Upper panel: Mean cumulative overdensity of photometric galaxies around quasars and lower-luminosity AGN as a function of scale and redshift. Points have been slightly offset horizontally for clarity. Top lower panel: Ratio of environment overdensity of QII.Zs to that of QI.Lpts in the redshift range $0.3 \leq z \leq 0.5$. Middle lower panel: Ratio of environment overdensity of AII to that of AI in the redshift range $0.15 < z \leq 0.33$. Bottom lower panel: Ratio of environment overdensity of AII to that of AI in the redshift range $0.11 < z \leq 0.15$.

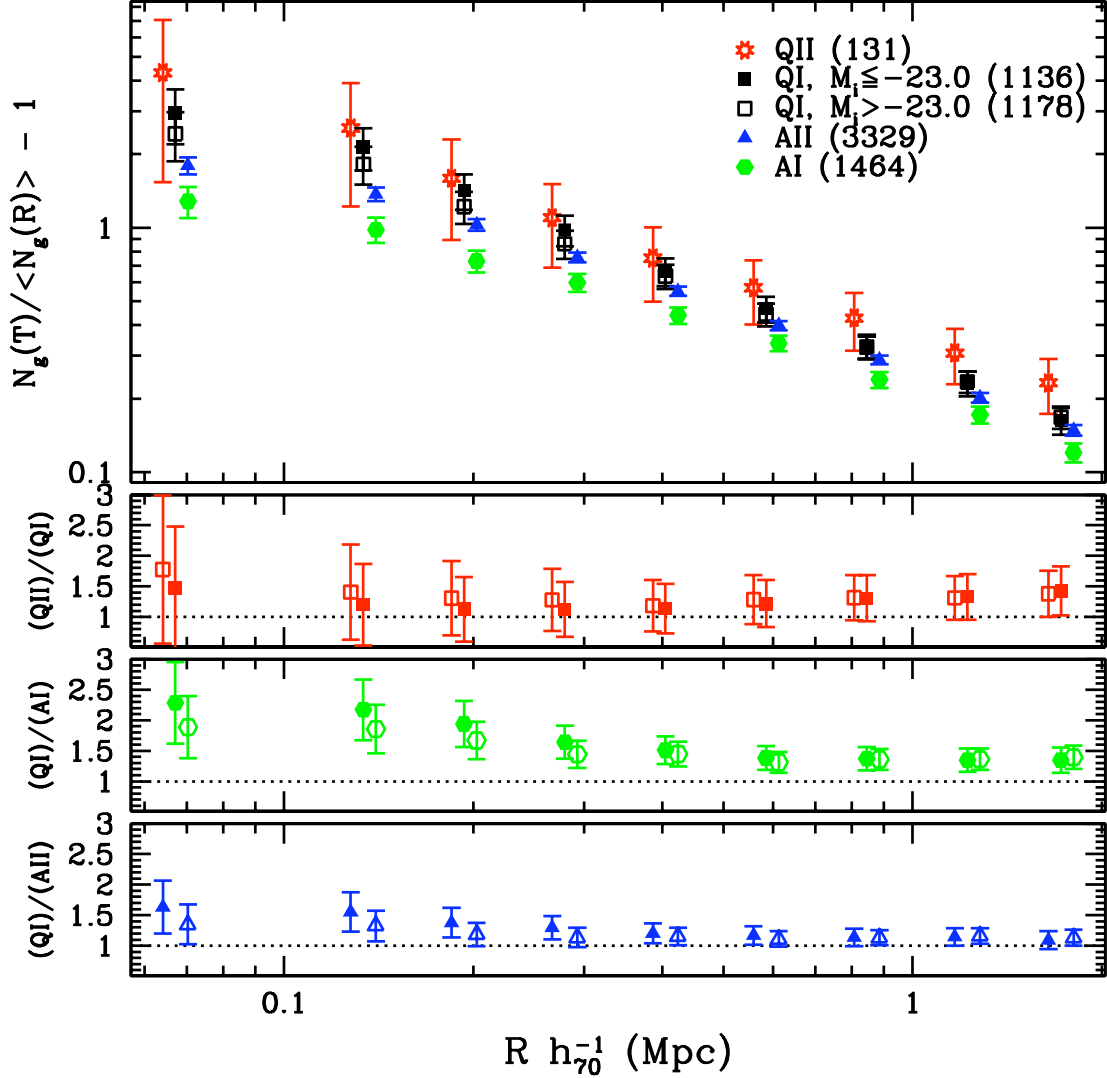


Figure 4.5— Top panel: Mean cumulative overdensity of photometric galaxies around QI_pts split by luminosity; low luminosity AGN; and QII_Zs. Bright quasars have absolute magnitude $-26.4 \leq M_i \leq -23.0$ and dim quasars have absolute magnitude $-23.0 < M_i \leq -22.0$. Top lower panel: ratio of QII_Zs environment overdensity to bright (solid points) and dim (open points) QI_pt environment overdensities. Middle lower panel: ratio of bright (solid points) and dim (open points) QI_pt environment overdensities to AI environment overdensity. Bottom lower panel: ratio of bright (solid points) and dim (open points) QI_pt environment overdensities to AII environment overdensity. No redshift limits have been imposed.

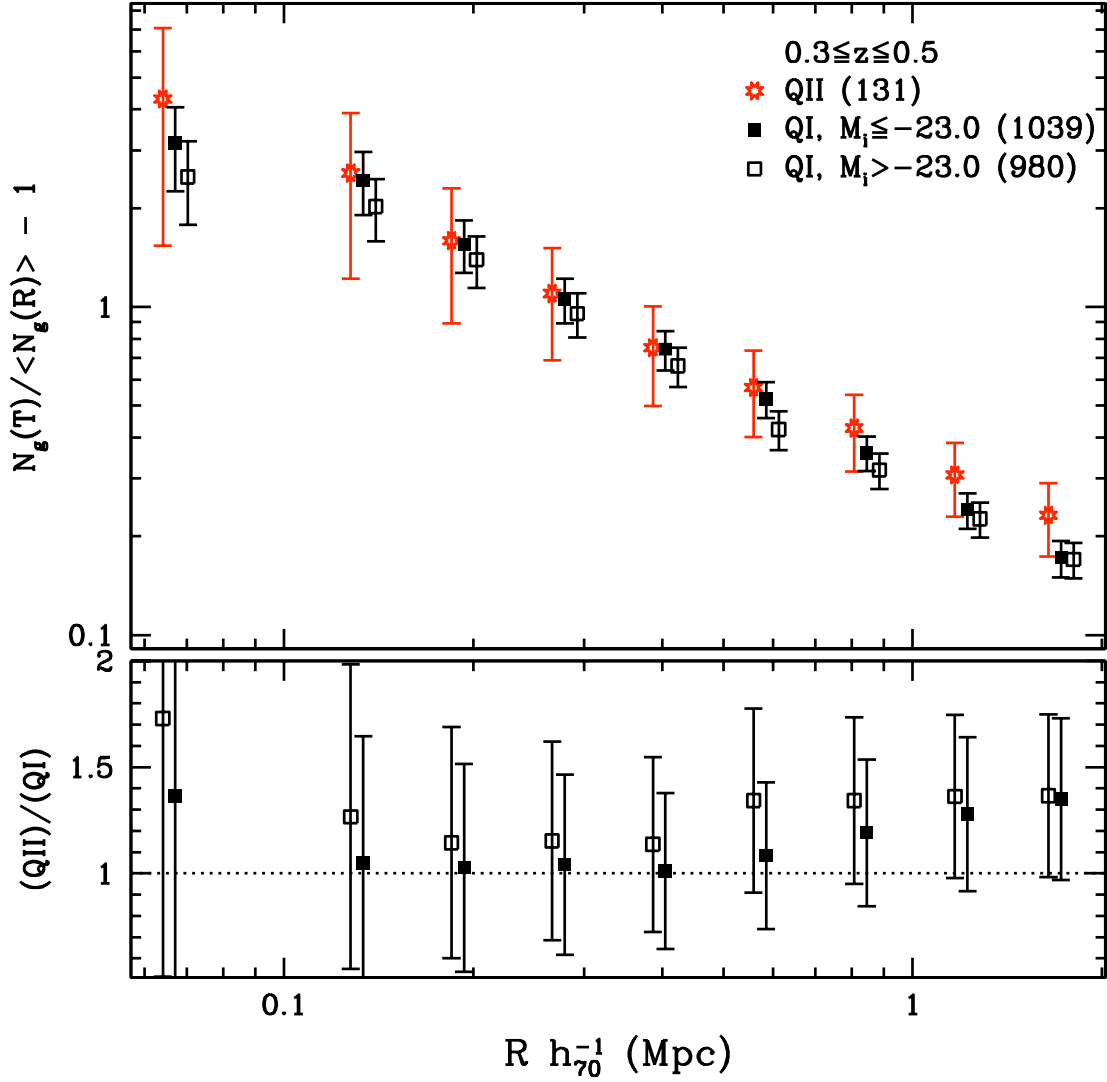


Figure 4.6— Upper panel: Mean cumulative overdensity of photometric galaxies around QII_Zs and QI_pts in the redshift range $0.3 \leq z \leq 0.5$. The QI_pts in this redshift range have been divided at $M_i = -23.0$ so that the luminosity bins contain approximately equal numbers of QI_pts. Lower panel: Ratio of environment overdensities of QII_Zs to brighter and dimmer QI_pts in this redshift range. Points in both panels have been slightly offset horizontally for clarity.

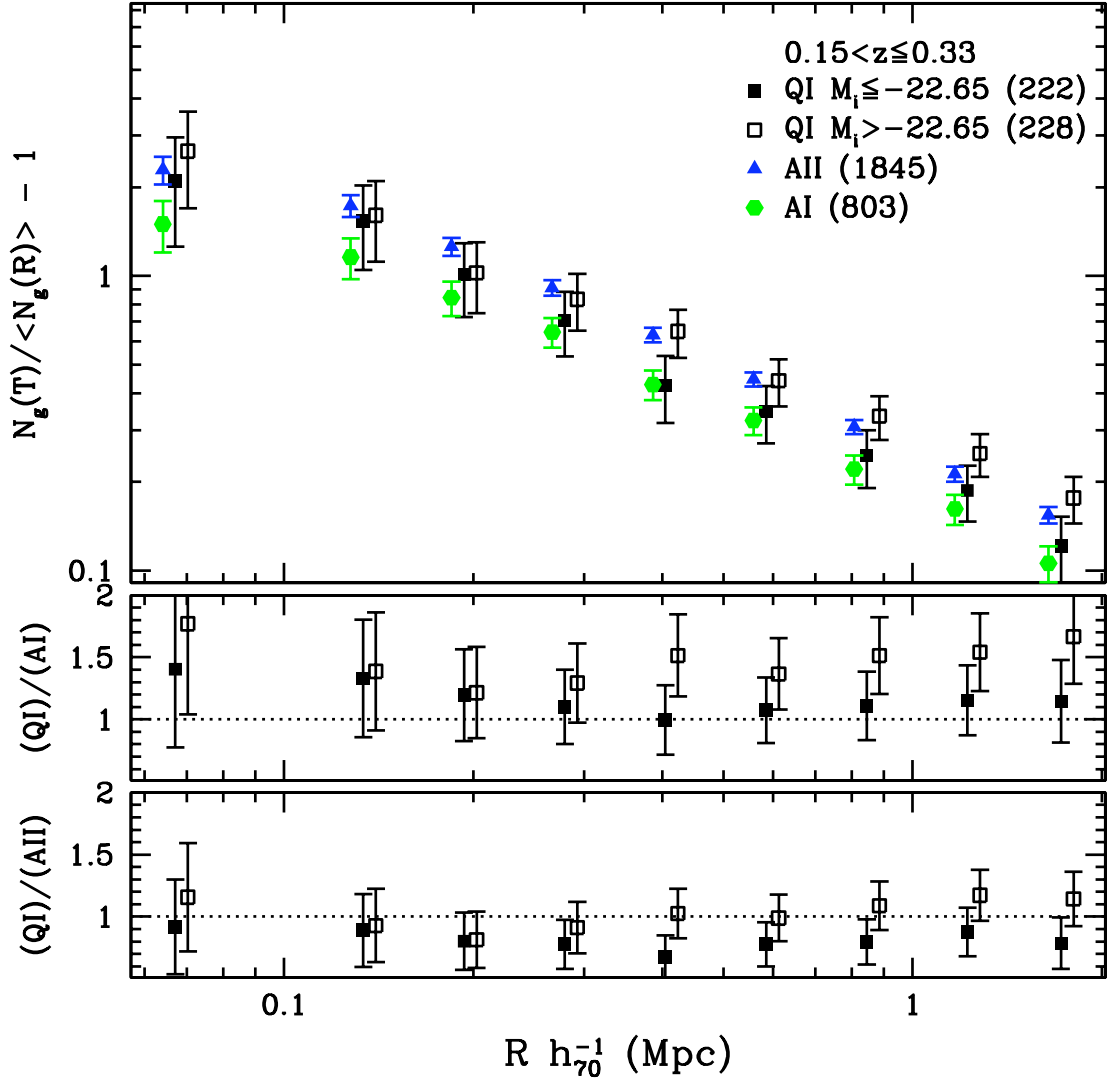


Figure 4.7— Upper panel: Mean cumulative overdensity of photometric galaxies around QI_pts and AIs and AII in the redshift range $0.15 < z \leq 0.33$. The QI_pts in this redshift range have been divided at $M_i = -22.65$ so that the luminosity bins contain approximately equal numbers of QI_pts. Lower panels: Ratio of environment overdensities of brighter and dimmer QI_pts to AIs and AII in this redshift range. Points in both panels have been slightly offset horizontally for clarity.

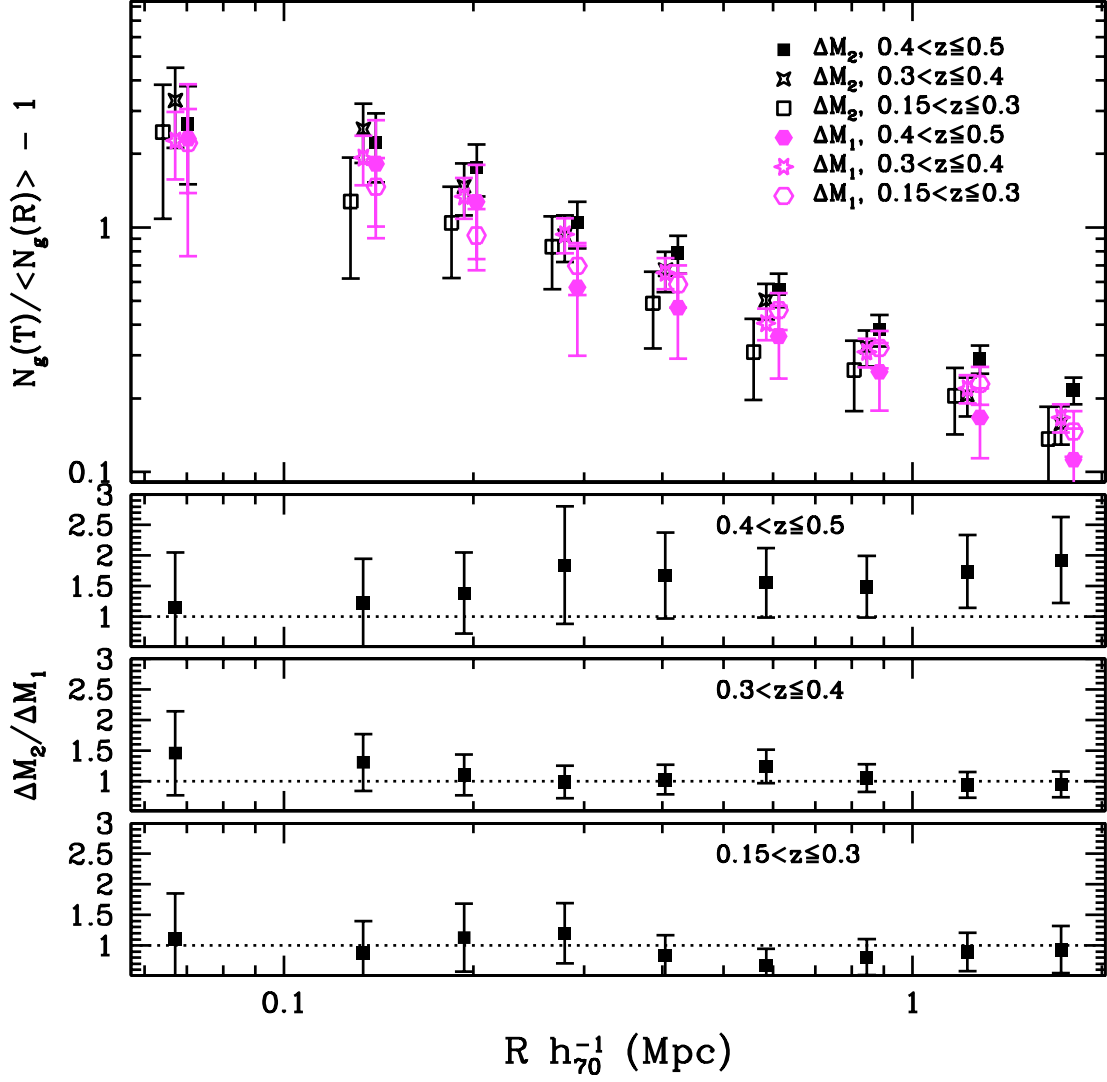


Figure 4.8— Mean cumulative overdensity of photometric galaxies around QI_pnts with redshift for two luminosity bins, where $\Delta M_1 : -23.0 < M_i \leq -22.0$ and $\Delta M_2 : -24.0 < M_i \leq -23.0$. Lower panels: Ratio of ΔM_2 to ΔM_1 quasar environment overdensities in the three redshift ranges.

Chapter 5

The Dependence on [OIII] Luminosity

5.1 OVERVIEW

In the previous chapter, we discussed that broad-band magnitudes were not a good proxy for the nuclear luminosity of AGNs and quasars, especially for lower-luminosity AGNs, due to possible contamination by stellar light from the host galaxy. In this section, we use the observed luminosity of the [OIII] λ 5007 emission line ($L_{[\text{OIII}]}$) to better quantify the AGN power (Kauffmann et al., 2003; Heckman et al., 2004; Hao et al., 2005a). The [OIII] λ 5007 line arises from the narrow-line region of the AGN (Reyes et al., 2008; Li et al., 2008) and is negligibly effected by emission due to star-formation (Kauffmann et al., 2003). Because the line will be present in both Type I and Type II AGNs and quasars, we can more effectively compare the nuclear luminosity of the different types of quasars and AGNs.

In Figure 5.1, we limit the combined $0.11 \leq z \leq 0.5$ AGN sample to $\log(L_{[\text{OIII}]} / L_{\odot}) \geq 8.0$ to make one large, volume-limited sample of 3,781 sources. We divide the sample into two luminosity bins at $\log(L_{[\text{OIII}]} / L_{\odot}) \geq 8.4$, which gives an approximately equal number of objects in each luminosity bin. It is clear that at scales $R \leq 1.0 h_{70}^{-1}$ Mpc, targets with higher [OIII] luminosity are located in environments more overdense than targets with lower [OIII] luminosity (upper panel). Table 5.1 summarizes the relative environment overdensity for bright and dim targets at $R \approx 500 h_{70}^{-1}$ kpc. At a scale of $R \approx 500 h_{70}^{-1}$ kpc, the brighter AGNs reside in environments that have overdensity 1.24 times the overdensity of the dimmer AGNs, with a significance of 1.7σ ; at $R \approx 2 h_{70}^{-1}$ Mpc, the ratio is 0.99 with significance $< 1\sigma$, and at $R \approx 150 h_{70}^{-1}$ kpc, the ratio is 1.4 with significance 1.7σ . From this we see evidence that the ratio of bright AGN environment overdensity to dim AGN environment overdensity is dependent on scale. Throughout this chapter, we will explore in greater detail the relationship between environment overdensity and [OIII] luminosity.

5.2 TARGET TYPE

We divide the $L_{[\text{OIII}]}$ volume-limited sample into Type I and Type II sources (recall that an object is characterized as Type I or Type II based on the width of its emission lines). There are 3,229 Type I (TI) sources and 552 Type II (TII) sources with $0.11 \leq z \leq 0.5$ and $\log(L_{[\text{OIII}]} / L_{\odot}) \geq 8.0$. We show overdensity vs. scale and $L_{[\text{OIII}]}$ for TIs and TIIs in Figure 5.2 and 5.3, respectively. It is noteworthy that the scale dependency in the ratio of overdensities (which can also be interpreted as a measurement of the relative bias) remains evident for the TIs, but from Figure 5.3, it appears that the scale dependency is not present for the TIIs.

We quantify the scale dependency of the overdensity- $L_{[\text{OIII}]}$ relationship by calculating a linear least-squares fit to cumulative overdensity vs. $L_{[\text{OIII}]}$ at several fixed scales (see Figure 5.4). The fit parameters for overdensity vs. $L_{[\text{OIII}]}$ at $150 h_{70}^{-1}$ kpc, $500 h_{70}^{-1}$ kpc, $1 h_{70}^{-1}$ Mpc, and $2 h_{70}^{-1}$ Mpc are summarized in Table 5.2. As expected, there is an increase in slope at smaller scales for the TI target sample. Though less dramatic than for TIs, we still see evidence for a slight scale dependency of TII environment overdensity.

The $\log(L_{[\text{OIII}]} / L_{\odot}) \geq 8.0$ volume limit is a fairly bright one and removes the majority of our lower-luminosity AGNs (AI and AII) from consideration. If we instead select targets with $z \leq 0.28$ (see dividing line in Figure 2.3), we can use a lower limit of $\log(L_{[\text{OIII}]} / L_{\odot}) > 6.75$ to create the volume-limited samples; we additionally restrict the objects in the sample to have $\log(L_{[\text{OIII}]} / L_{\odot}) \leq 8.0$, resulting in 894 TIs and 2,050 TIIs. At these low redshifts and luminosities, the AI and AII dominate the samples. We again calculate least-squares fits to the overdensity vs. $L_{[\text{OIII}]}$ relationship at four scales (Table 5.2) and find that there is very little change in slope with scale for both samples. In fact, with the exception of the $R = 150 h_{70}^{-1}$ kpc measurement for TIs (where the error bars are very large and a zero-slope line would be an acceptable fit), the slope at any given scale is close to zero.

In contrast, if we instead look at the high-luminosity ($\log(L_{[\text{OIII}]} / L_{\odot}) > 8.0$) targets at these low redshifts, we see that the scale dependence appears again especially for the TI sources. When we select TI and TII targets with $\log(L_{[\text{OIII}]} / L_{\odot}) \geq 8.0$ and $z > 0.28$ (4317 and 271 objects, respectively), the QI and QII objects dominate the samples. Due to the very small number of TII objects in this sample, it is difficult to draw strong conclusions, but any scale dependency is small in the relationship between overdensity and luminosity for TIIs. Overdensity vs. $L_{[\text{OIII}]}$ fits for this sample are presented in Table 5.2, and the increase in slope with decreasing scale is again seen for TIs. Thus we can conclude that there is a scale-dependent relationship between environment overdensity and luminosity for the brightest sources, especially those classified as Type I.

5.3 TARGET REDSHIFT

Using the $L_{[\text{OIII}]}$ volume-limited samples and without making any additional luminosity cuts, we investigate the effect of redshift on environment overdensity by plotting cumulative overdensity vs. redshift and calculating fits. Table 5.3 gives the least-squares fitting parameters corresponding to the fits in Figure 5.5 (only the fit for the combined TI and TII sample is shown in the figure). It appears that there is some redshift evolution of overdensity, and that this evolution depends on scale, especially for TIs. The small sample size of the TIIs gives rise to very large error bars, so we cannot draw conclusions for this sample.

Because we have a larger sample of TIs with the $\log(L_{[\text{OIII}]} / L_{\odot}) \geq 8.0$ volume-limit, we can subdivide each luminosity bin from Figure 5.2 into two redshift bins at $z = 0.28$. Figure 5.6 shows the overdensity vs. scale, $L_{[\text{OIII}]}$, and redshift for TIs. It appears that there is slight evidence for redshift evolution in the brighter objects. The scale dependency seen in the ratio of environment overdensity of bright to dim TIs is seen in the $z > 0.28$ redshift bin but is harder to discern in the low redshift bin, where the ratio is consistent with unity on all scales. However, the subset of TIs with $\log(L_{[\text{OIII}]} / L_{\odot}) \geq 8.0$ and $0.11 \leq z \leq 0.28$ is small, so we must be cautious in our conclusions. The scale dependency at high redshifts and not low redshifts could signal mass evolution with redshift in our sample which we have not yet accounted for. Chapter 7 will discuss the relationship between

black hole mass and QI environment overdensity.

5.4 CONCLUSIONS

To summarize, we see that the environments of the brightest sources (i.e., those with at least $\log(L_{[\text{OIII}]} / L_{\odot}) \geq 8.4$) have greater overdensity with greater luminosity compared to dimmer sources (with at least $\log(L_{[\text{OIII}]} / L_{\odot}) \geq 8.0$), and that there is a slight scale dependency observed, especially for bright TIs at scales $R \leq 150 h_{70}^{-1}$ kpc. Since at \sim Mpc scales we are seeing approximately equal environment overdensity for bright and dim TIs, we can conclude that the halo mass is not dependent on luminosity. However, on smaller scales, higher luminosity sources have higher overdensity, implying that the halos in which they reside are occupied differently than the lower-luminosity (but still $\log(L_{[\text{OIII}]} / L_{\odot}) \geq 8.0$) sources.

The weak or absent luminosity dependence of environment overdensity on \gtrsim Mpc scales provides support for the results of simulations by Lidz et al. (2006), which showed that galaxy merger models predict that there is a weak dependency of clustering of quasars on luminosity at larger scales. The luminosity independence of quasar clustering has implications for understanding the lifetime and luminosity “cycle” of quasars (e.g., Hopkins et al., 2005a; Adelberger & Steidel, 2006; Lidz et al., 2006; Myers et al., 2006). While the brightest observed quasars are likely radiating at their peak, the dimmer end of the quasar luminosity function is a combination of quasars that are building up to their peak luminosity (and possibly obscured by the material that powers them) or fading away as the material available for accretion is ejected by outflows from the central engine. Thus, bright and dim sources can have similar clustering at larger scales because halo mass is not necessarily dependent the luminosity, which changes over the lifetime of the quasar with accretion efficiency. However, at smaller scales, we measure a higher galaxy overdensity in the environments of bright sources compared to dimmer sources which increases with decreasing scale. The scale-dependency of the environments on these small scales is tell-tale evidence for the merger origin of these bright AGNs (e.g., Djorgovski, 1991; Hennawi et al., 2006; Hopkins et al., 2008; Myers et al., 2008), as mergers are expected to occur with greater frequency in regions with higher galaxy density (e.g., Lacey & Cole, 1993).

For AGNs with lower $L_{[\text{OIII}]}$ (i.e., $6.75 \leq \log(L_{[\text{OIII}]} / L_{\odot}) \leq 8.0$), we do not see scale dependency or even much increase in overdensity with luminosity even at the smallest scales, which supports the predictions for less biased environments of low-luminosity AGNs in a secular-fueling model (e.g., Hopkins & Hernquist, 2006; Hopkins et al., 2008).

Table 5.1: Overdensity ratios comparing environments of bright ($\log(L_{[\text{OIII}]} / L_{\odot}) > 8.4$) and dim ($8.0 \leq \log(L_{[\text{OIII}]} / L_{\odot}) \leq 8.4$) targets at scale $R \approx 500 h_{70}^{-1}$ kpc.

Sample	bright/dim	significance
TI+TII	1.24 ± 0.147	1.66σ
TI	1.30 ± 0.172	1.74σ
TI, $0.11 \leq z \leq 0.28$	1.09 ± 0.244	$< 1\sigma$
TI, $0.28 < z \leq 0.5$	1.40 ± 0.232	1.71σ
TII	1.10 ± 0.287	$< 1\sigma$
QI	1.25 ± 0.179	1.41σ
QI, $0.11 \leq z \leq 0.28$	0.971 ± 0.269	$< 1\sigma$
QI, $0.28 < z \leq 0.5$	1.40 ± 0.232	1.71σ

Table 5.2: Linear least-squares fit parameters for overdensity vs. $L_{\text{[OIII]}}$ at four different scales using all AGNs combined, TIs, and TIIIs. (See also Figure 5.4).

scale (h_{70}^{-1} Mpc)	All AGNs				Type I AGNs				Type II AGNs			
	slope	intercept	χ^2	slope	intercept	χ^2	slope	intercept	χ^2	slope	intercept	χ^2
	$\log(L_{\text{[OIII]}}/L_{\odot}) \geq 8.0, 0.11 \leq z \leq 0.28$											
2.0	0.027 ± 0.012	-0.063 ± 0.102	0.404	0.004 ± 0.009	0.133 ± 0.072	0.152	0.074 ± 0.053	-0.462 ± 0.449	2.18			
1.0	0.098 ± 0.019	-0.518 ± 0.159	0.317	0.094 ± 0.037	-0.487 ± 0.311	0.869	0.104 ± 0.033	-0.572 ± 0.278	0.286			
0.5	0.226 ± 0.035	-1.31 ± 0.296	0.241	0.266 ± 0.054	-1.62 ± 0.458	0.389	0.155 ± 0.080	-0.782 ± 0.679	0.427			
0.15	0.911 ± 0.189	-5.95 ± 0.159	0.332	1.12 ± 0.182	-7.61 ± 1.53	0.195	0.526 ± 0.433	-2.99 ± 3.67	0.703			
	$6.75 < \log(L_{\text{[OIII]}}/L_{\odot}) \leq 8.0, 0.11 \leq z \leq 0.28$											
2.0	0.011 ± 0.012	0.063 ± 0.091	10.1	0.042 ± 0.011	-0.195 ± 0.088	3.16	0.001 ± 0.014	0.140 ± 0.100	6.51			
1.0	0.002 ± 0.016	0.256 ± 0.115	5.67	0.052 ± 0.023	-0.155 ± 0.079	4.17	-0.011 ± 0.021	0.368 ± 0.155	5.64			
0.5	-0.010 ± 0.031	0.584 ± 0.230	5.82	0.082 ± 0.035	-0.176 ± 0.268	2.76	-0.030 ± 0.031	0.758 ± 0.222	2.99			
0.15	0.050 ± 0.108	0.873 ± 0.798	5.12	0.292 ± 0.141	-1.21 ± 1.07	3.70	0.049 ± 0.077	1.01 ± 0.553	1.30			
	$\log(L_{\text{[OIII]}}/L_{\odot}) > 8.0, 0.11 \leq z \leq 0.28$											
2.0	0.033 ± 0.012	-0.107 ± 0.088	2.04	0.052 ± 0.017	-0.281 ± 0.133	1.81	0.027 ± 0.025	-0.050 ± 0.183	4.41			
1.0	0.037 ± 0.018	-0.003 ± 0.140	1.77	0.074 ± 0.025	-0.332 ± 0.195	1.33	0.026 ± 0.025	0.093 ± 0.185	1.58			
0.5	0.045 ± 0.027	0.174 ± 0.203	0.955	0.139 ± 0.054	-0.627 ± 0.418	1.57	0.006 ± 0.038	0.500 ± 0.279	0.929			
0.15	0.318 ± 0.082	-1.14 ± 0.614	0.545	0.681 ± 0.116	-4.24 ± 0.895	0.468	0.142 ± 0.179	0.313 ± 1.32	1.30			
	$\log(L_{\text{[OIII]}}/L_{\odot}) > 8.0, 0.28 < z \leq 0.5$											
2.0	-0.003 ± 0.020	1.95 ± 0.169	2.25	0.007 ± 0.016	0.107 ± 0.134	1.17	-0.082 ± 0.027	0.918 ± 0.238	0.523			
1.0	0.040 ± 0.047	-0.003 ± 0.394	3.31	0.066 ± 0.038	-0.232 ± 0.314	1.73	-0.146 ± 0.062	1.68 ± 0.533	0.696			
0.5	0.126 ± 0.139	-0.366 ± 1.16	5.07	0.221 ± 0.129	-1.17 ± 1.07	3.54	-0.400 ± 0.309	4.17 ± 2.70	2.82			
0.15	0.731 ± 0.426	-4.11 ± 3.35	2.03	1.18 ± 0.417	-7.86 ± 3.43	1.62	-1.07 ± 0.994	11.01 ± 8.80	1.21			

Table 5.3: Linear least-squares fit parameters for overdensity vs. redshift at four different scales using all AGNs combined, TIs, and TIIs with $\log(L_{[\text{OIII}]} / L_{\odot}) \geq 8.0$. (See also Figure 5.5).

scale (h_{70}^{-1} Mpc)	All AGNs			Type I AGNs			Type II AGNs		
	slope	intercept	χ^2	slope	intercept	χ^2	slope	intercept	χ^2
2.0	0.005	0.165	0.4714	0.002	0.162	1.860	0.143	0.145	2.551
1.0	0.259	0.239	1.656	0.278	0.226	2.431	0.490	0.213	0.3509
0.5	0.734	0.404	1.087	0.751	0.400	1.974	0.243	0.492	0.7431
0.15	3.03	0.946	0.0703	3.04	0.954	0.1613	1.92	1.13	0.1421

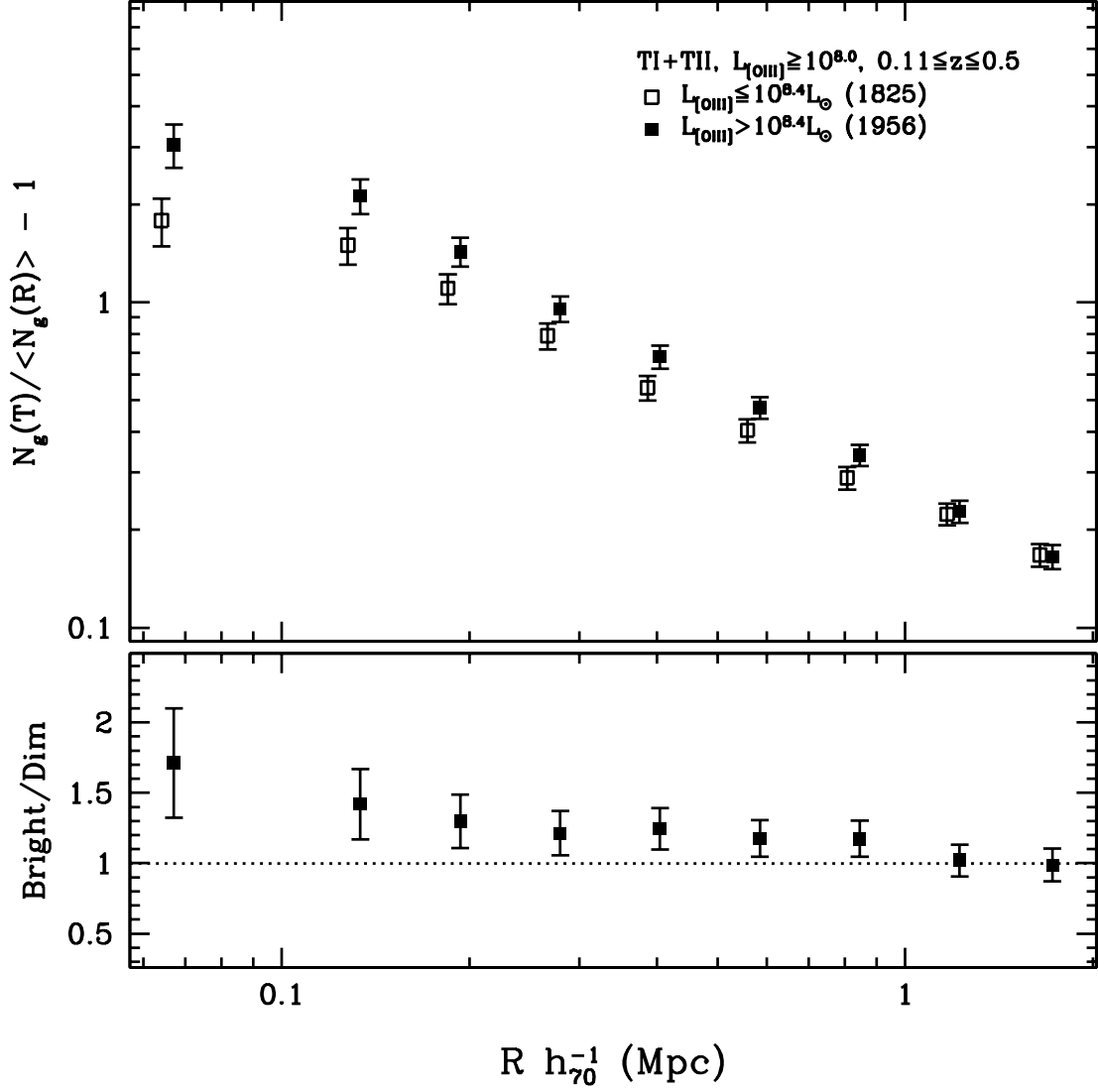


Figure 5.1— *Upper panel:* Mean cumulative environment overdensity vs. scale and $L_{[\text{OIII}]}$ for TI+TII targets with $\log(L_{[\text{OIII}]} / L_{\odot}) \geq 8.0$. *Lower panel:* Ratio of high luminosity AGN environment overdensity to low luminosity AGN environment overdensity.

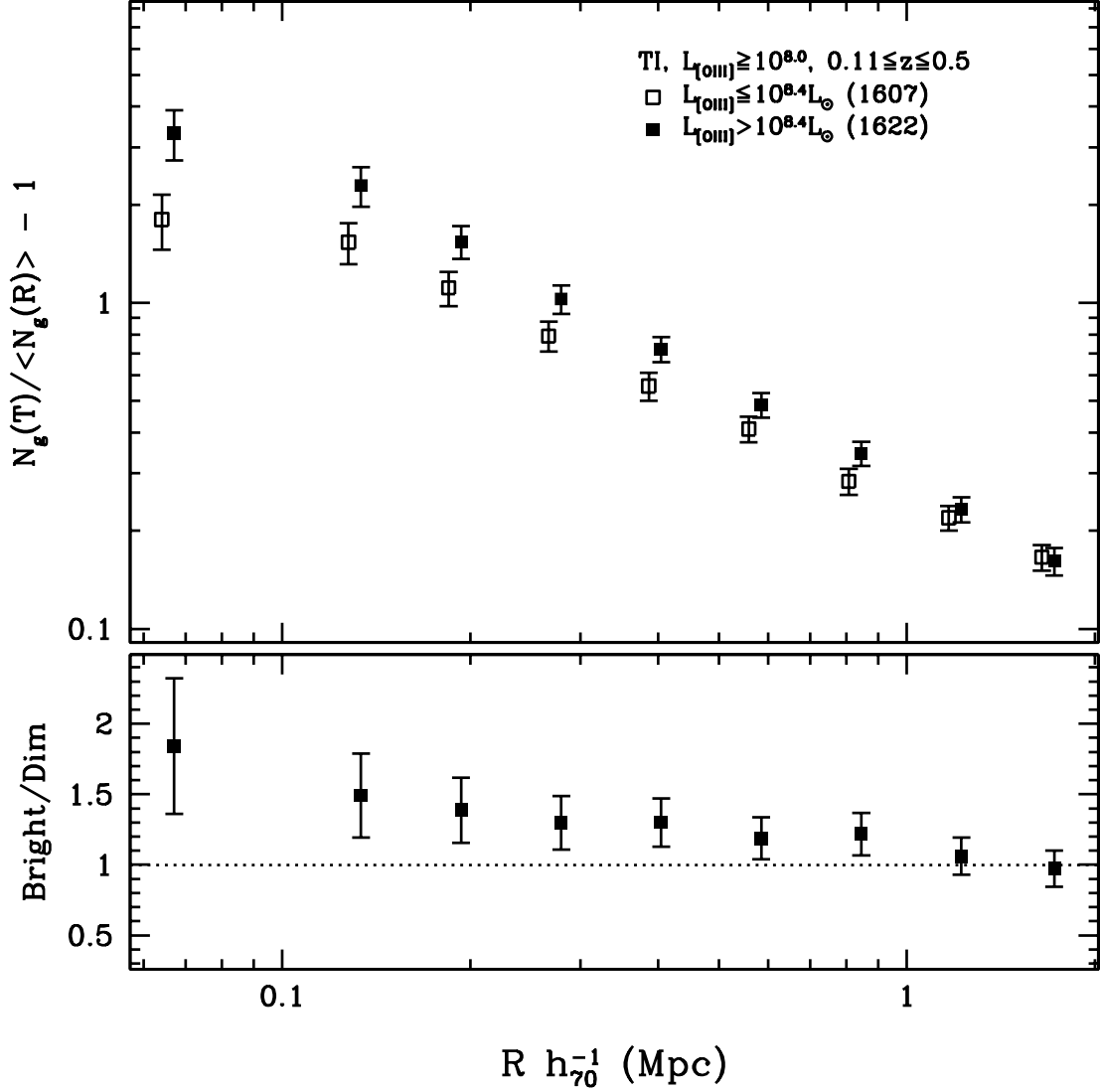


Figure 5.2— *Upper panel:* Mean cumulative environment overdensity vs. scale and $L_{[\text{OIII}]}$ for TI targets with $\log(L_{[\text{OIII}]} / L_{\odot}) \geq 8.0$. *Lower panel:* Ratio of high luminosity AGN environment overdensity to low luminosity AGN environment overdensity.

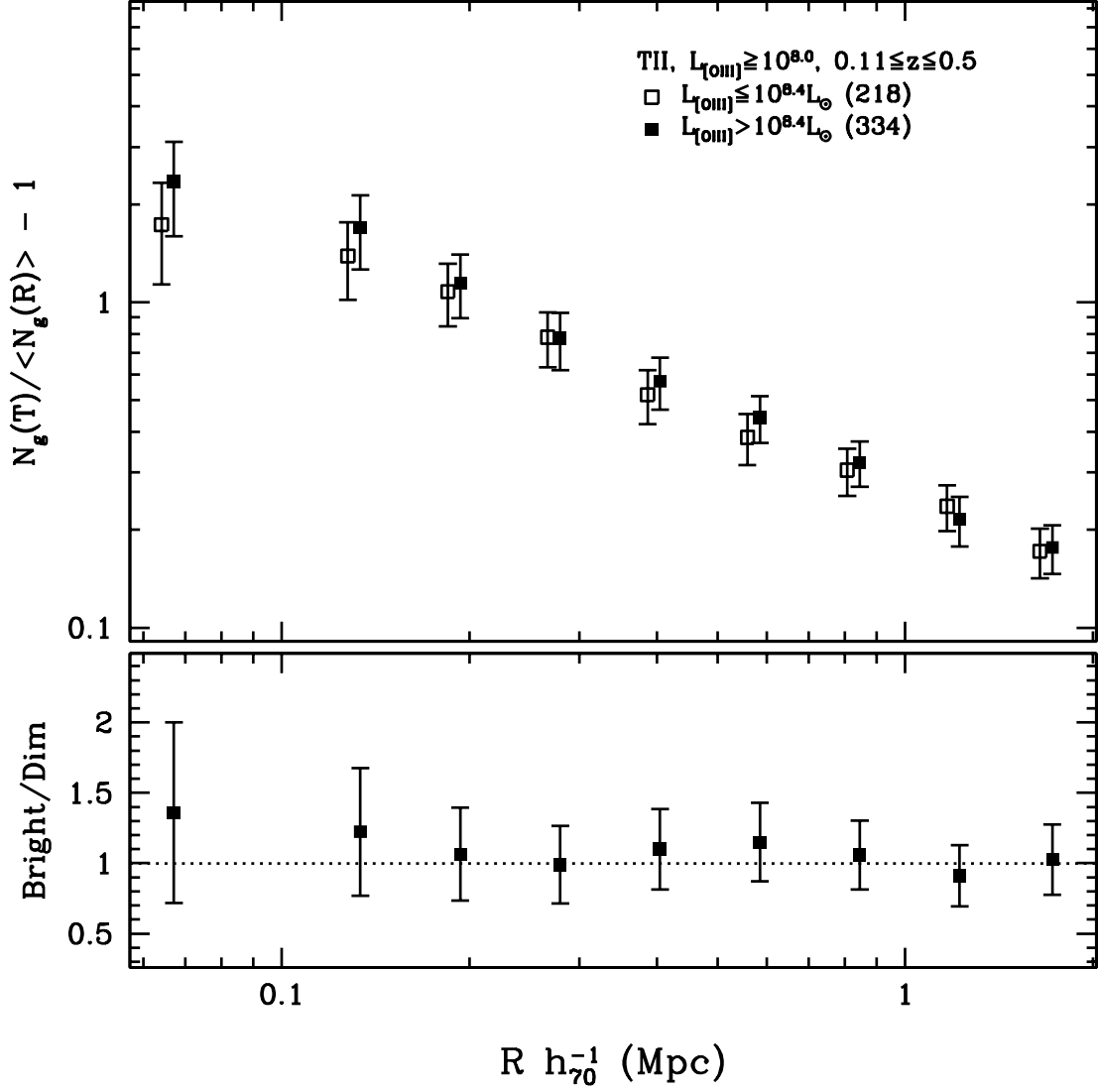


Figure 5.3— *Upper panel*: Mean cumulative environment overdensity vs. scale and $L_{[\text{OIII}]}$ for TII targets with $\log(L_{[\text{OIII}]} / L_{\odot}) \geq 8.0$. *Lower panel*: Ratio of high luminosity AGN environment overdensity to low luminosity AGN environment overdensity.

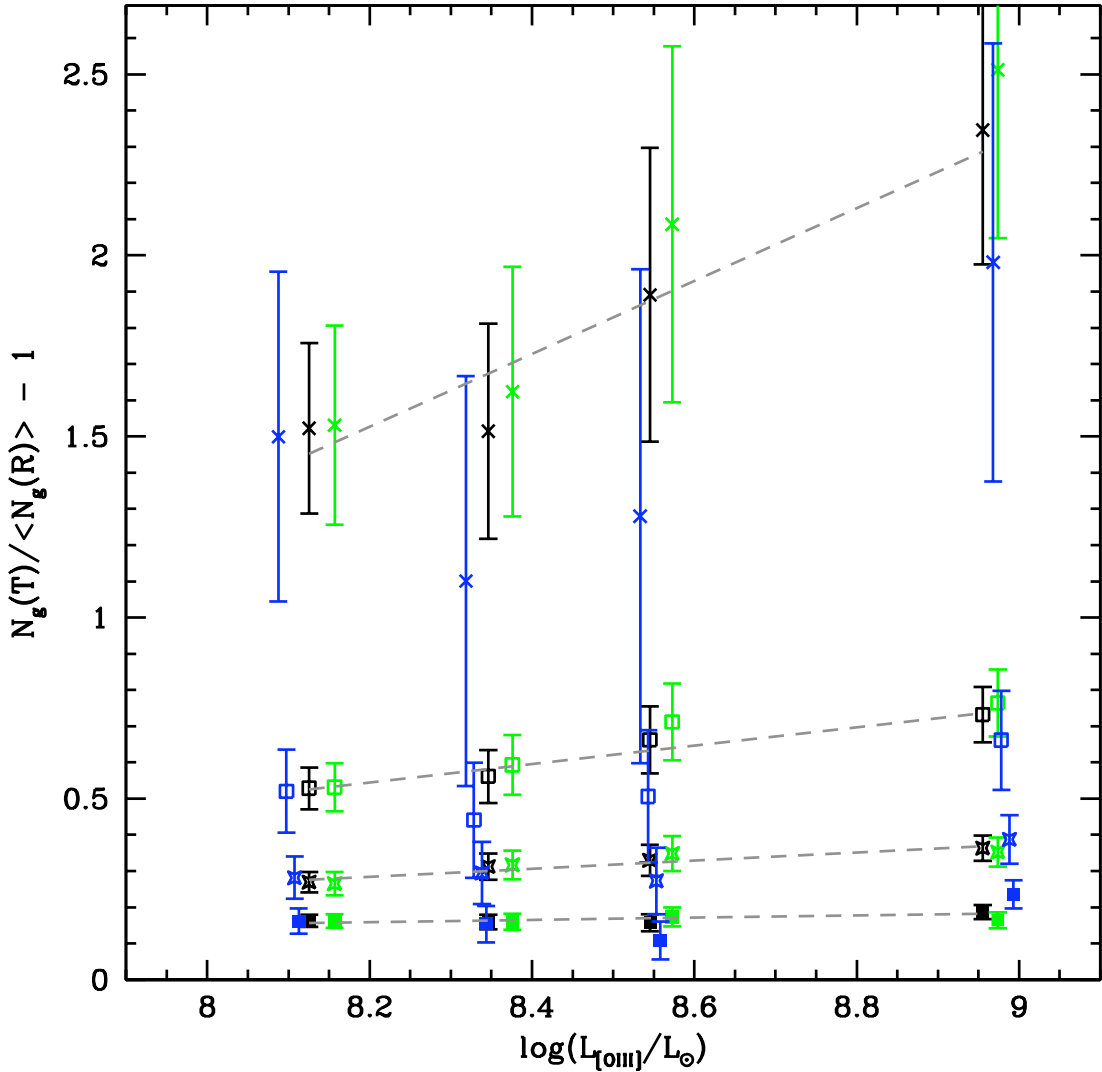


Figure 5.4— Mean cumulative environment overdensity vs. redshift and scale for all targets (black points), Type I targets (green points), and Type II targets (blue points) with $0.11 \leq z \leq 0.5$ and $\log(L_{[\text{OIII}]} / L_{\odot}) \geq 8.0$. The solid square points show overdensity vs. redshift for $R \approx 2 h_{70}^{-1}$ Mpc, starred points for $R \approx 1 h_{70}^{-1}$ Mpc, open squares for $R \approx 500 h_{70}^{-1}$ kpc, and crosses for $R \approx 150 h_{70}^{-1}$ kpc. The linear least-squares fits to the combined target sample data for each of these scales are given by the dashed lines; The fit parameters for each of the samples are summarized in Table 5.2. Points are shifted from their average $L_{[\text{OIII}]}$ bin value (horizontal axis) by a small amount for clarity.

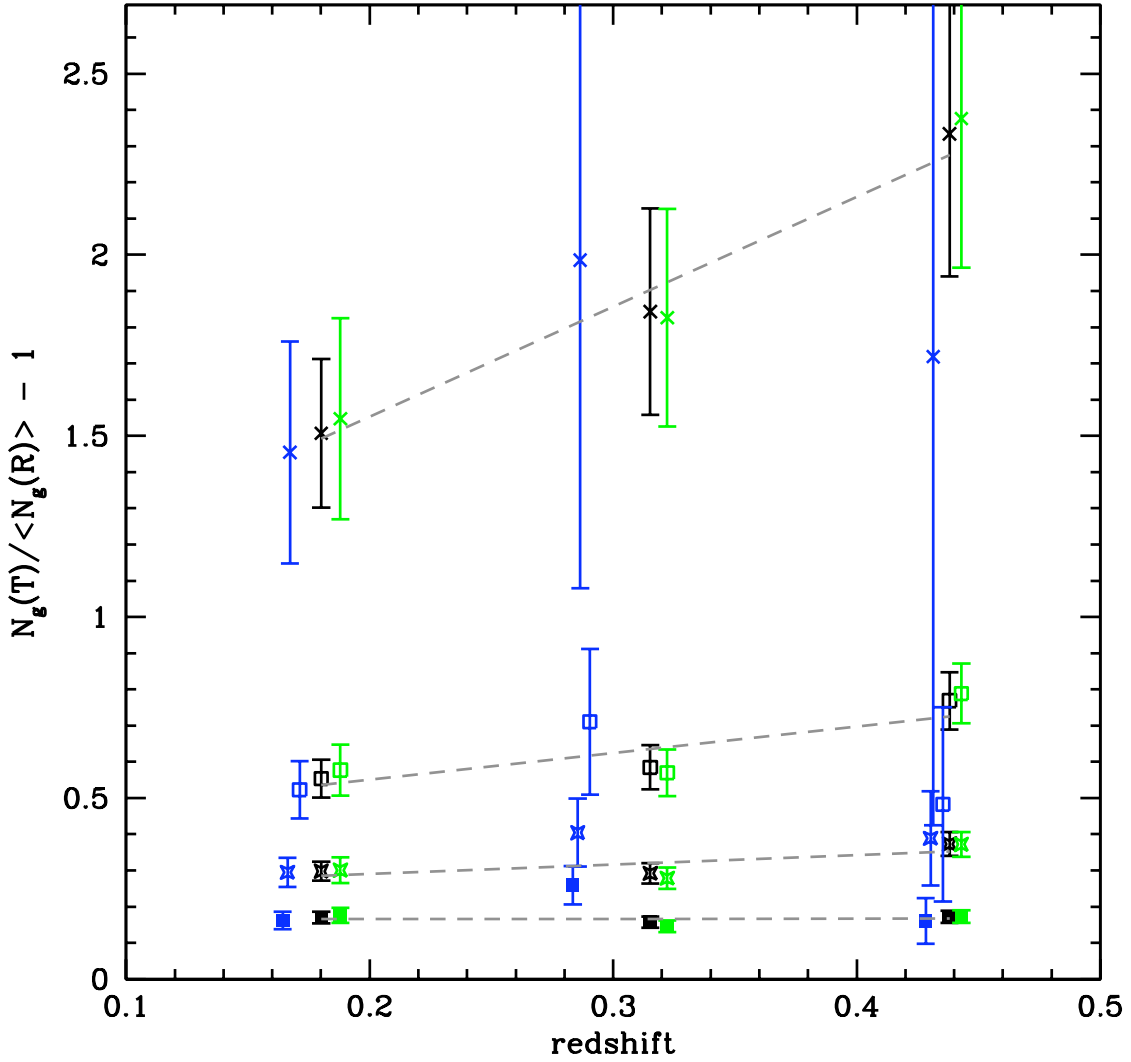


Figure 5.5— Mean cumulative environment overdensity vs. redshift and scale for all targets (black points), Type I targets (green points), and Type II targets (blue points) with $\log(L_{[\text{OIII}]} / L_{\odot}) \geq 8.0$. The solid square points show overdensity vs. redshift for $R \approx 2 h_{70}^{-1}$ Mpc, starred points for $R \approx 1 h_{70}^{-1}$ Mpc, open squares for $R \approx 500 h_{70}^{-1}$ kpc, and Xes for $R \approx 150 h_{70}^{-1}$ kpc. The linear least-squares fits to the combined target sample data for each of these scales are given by the dashed lines; The fit parameters for each of the samples are summarized in Table 5.3. Points are shifted from their average z bin value (x-axis) by a small amount for clarity.

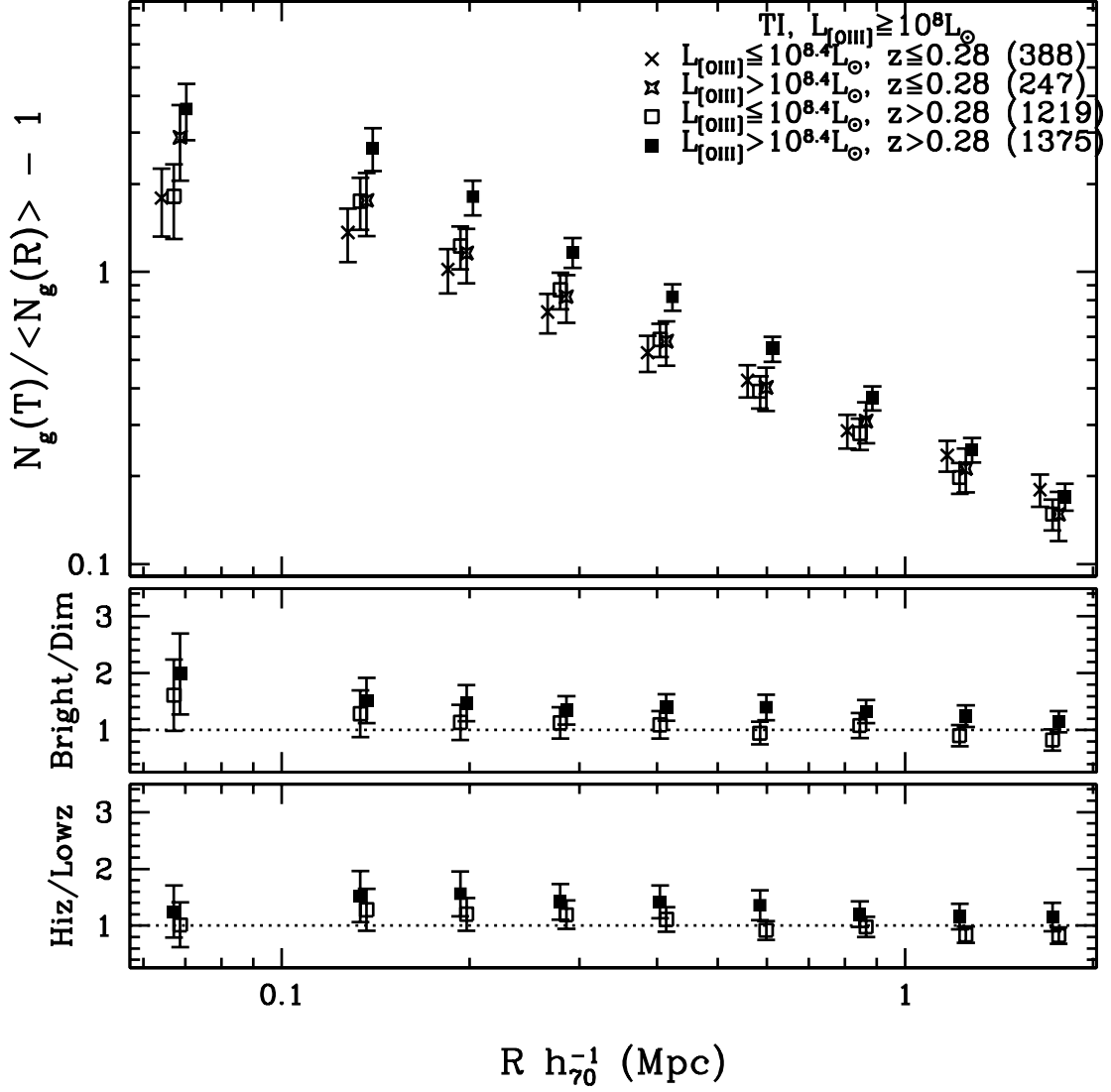


Figure 5.6— Mean cumulative environment overdensity vs. scale, $L_{[\text{OIII}]}$, and redshift for TI targets with $\log(L_{[\text{OIII}]} / L_{\odot}) \geq 8.0$. *Middle panel:* ratio of environment overdensities of bright TIs to dim TIs for $z \leq 0.28$ (open points), and $z > 0.28$ (filled points) targets. *Lower panel:* ratio of overdensities for high-redshift TIs to low-redshift TIs for bright (filled points) and dim (open points) targets.

Chapter 6

The Dependence on Environment Galaxy Type

6.1 OVERVIEW

We now focus on the characteristics of the galaxies in the environment of AGNs to provide additional insight into the relationship between the AGN and its environment. The composition of AGN environments can be related to galaxy formation models for clues about their location in or proximity to groups or clusters. The photometric galaxy catalog from which our environment galaxy sample is derived contains a parameter t that provides an estimate of the galaxy spectral type. The type classification is based on the spectral energy distribution of the template galaxy used to estimate the photometric redshift. Following Budavari et al. (2003), we first use the separation that $t < 0.3$ is an early-type (red) galaxy, and late-type (blue) galaxies have $t \geq 0.3$ (in Section 6.5, we will further subdivide the environment galaxies into Coleman, Wu, & Weedman, 1980, hereafter CWW, spectral types). As discussed in Section 3.3, subdividing our environment galaxy sample limits the maximum redshift at which we have a reasonable probability of counting galaxies. Thus, when we divide the environment sample into two environment galaxy types, we use a redshift range of $0.11 \leq z \leq 0.4$.

We use the same $\log(L_{[\text{OIII}]} / L_{\odot}) \geq 8.0$ combined sample of AGNs in Figure 6.1, where we compare the overdensity of early-type environments to the overdensity of late-type environments. At all scales, we see that the AGNs reside in environments more densely populated with early-type environment galaxies. In Table 6.1, we give the ratio of early-type environment galaxy overdensity to late-type environment galaxy overdensity at a scale $R \approx 500 h_{70}^{-1}$ kpc. Throughout this chapter, we will expand on the details of the relationship between overdensity of different types of galaxies and AGN type, luminosity, and redshift.

6.2 TARGET TYPE

First, we explore whether the type of the target is related to the composition of its environment. Figures 6.2 and 6.3 show the overdensity vs. scale and environment galaxy type for the TI and TII samples with $\log(L_{[\text{OIII}]} / L_{\odot}) \geq 8.0$, respectively. By comparing the overdensity values for the two types (see Table 6.2), we see that the lower early/late ratio for TIIs is due to the fact that the difference between early-type overdensity between TI and TII AGNs increases with decreasing scale: at $1.0 h_{70}^{-1}$ Mpc, the early-type overdensity around TI (TII) targets is 0.41 ± 0.04 (0.38 ± 0.06), and at $500 h_{70}^{-1}$ kpc, the overdensity has more than doubled for TIs (0.85 ± 0.08), but has not quite doubled for TIIs (0.69 ± 0.11). The late-type overdensities show only slight differences between TI and TIIs; thus the difference in overdensity ratios is due to lower overdensities of early-type galaxies in the

environments of TIIs.

6.2.1 Comparison to L^* Galaxies

At low redshifts, we can compare the environments of $\log(L_{[\text{OIII}]} / L_{\odot}) \geq 6.5$ AIs and AIIIs to the environments of L^* galaxies: it is in the range $0.11 \leq z \leq 0.15$ that the vast majority of our L^* galaxies are located. Figure 6.4 and Table 6.3 shows the comparison of environments using all environment galaxies, and early- and late-type environment galaxies individually. We find that these lower-luminosity AGN environments are approximately consistent with the L^* galaxy environments, but there is a slight excess at the smallest scales, which is seen especially the comparison of late-type environment galaxy overdensities. The late-type excess is especially noticeable in the smallest scales of AII environments where at $150 h_{70}^{-1}$ kpc, the ratio of late-type overdensity around AIIIs to L^* galaxies is 1.45 ± 0.28 with a significance of $\sim 2\sigma$. The slight excess of gas-rich late-type galaxies in the nearby environment of AGNs compared to the L^* galaxies could be evidence that the AGNs are affecting star formation in the nearby galaxies, or that they may accrete gas from outside their host galaxies (Coldwell et al., 2003, 2006; Koulouridis et al., 2006).

6.3 TARGET LUMINOSITY

Now that we have established that there is a difference in environment galaxy composition due to target type, we investigate the relationship between target luminosity and the types of galaxies in the environment in order to further understand the luminosity dependency we saw in Chapter 5. In Figure 6.5, we divide the ($L_{[\text{OIII}]}$ volume-limited) TI sample by luminosity at $\log(L_{[\text{OIII}]} / L_{\odot}) = 8.4$ to quantify the relationship of the early- or late-type environment galaxy overdensity to the luminosity of the targets. We observe a scale dependency in the early-type environment galaxy overdensity for bright TIs to dim TIs (red points in the middle panel of Figure 6.5). However, the bright/dim overdensity ratio for the late-type environment galaxies has virtually no scale dependency. Additionally, the ratios of early-type to late-type overdensity for bright or dim TIs (lower panel of Figure 6.5) have no notable change with scale, and the ratios at scale $R \approx 500 h_{70}^{-1}$ kpc are shown in Table 6.1.

Though the overdensity errors are larger due to the smaller sample size, we make the same luminosity division for TIIs in Figure 6.6. For these targets, there are no obvious scale dependencies in any of the ratios, and in fact, the early- to late-type overdensity ratios are virtually the same for bright and dim TII targets.

We compare the early- and late-type overdensity values for bright and dim TIs and TIIs in Table 6.4. For both the bright and dim samples, TIs and TIIs have very similar late-type galaxy overdensities in their environments. However, the bright TIs have increasing early-type galaxy overdensities with decreasing scale. Thus the difference that we have observed (e.g., in Chapter 5) in the TI and TII environments is most likely caused by this increase in early-type overdensity around bright targets at smaller scales.

6.4 TARGET REDSHIFT

Next, we examine whether there are redshift effects influencing the composition of TI source environments, recalling that in Chapter 4 we saw some evidence for redshift evolution in QI environments, but that the redshift effects were minor compared to those of luminosity. In Figure 6.7, we divide the TI sample at $z = 0.28$ (see Figure 2.3) and find that there is evidence for redshift evolution in the early-type overdensity in the environment of TIs, especially on the smallest scales (red points in the middle panel). In contrast, there is virtually no redshift evolution in the late-type overdensity. Redshift evolution in the background galaxy sample is marginalized because we are comparing counts around targets to counts around random at the same redshift with the δz cut. Therefore, the variation is in the composition of the small-scale environment of AGNs with redshift, specifically that there is a larger percent of early-type galaxies in higher redshift environments.

There is sufficient data in the volume-limited TI sample for us to make cuts on both redshift and luminosity and measure the early- and late-type overdensities in the subsamples. We plot this information in two figures for readability: Figure 6.8 shows the effects on early-type overdensity when the TI sample is divided on luminosity and redshift, and Figure 6.9 shows the effects on late-type overdensity using the same redshift and luminosity divisions. Additionally, the overdensities are compared in Table 6.5. In the lower panel of Figure 6.8, we see that there is redshift evolution in the early-type overdensity for both bright and dim TIs, but the redshift effects are slightly more pronounced for brighter TIs. At $R \approx 500 h_{70}^{-1}$ kpc, the environment overdensity ratio of bright high redshift to bright low redshift TIs is 1.76 ± 0.47 (significance 1.6σ), and for dim TIs, the ratio is 1.28 ± 0.33 (significance $\sim 1\sigma$). In contrast, we see that there is essentially no redshift evolution in the late-type overdensity around both bright (0.98 ± 0.37 , significance $> 1\sigma$) and dim (0.79 ± 0.31 , significance $> 1\sigma$) TIs in the lower panel of Figure 6.9. However, in the middle panels of both figures, we find that the bright overdensity to dim overdensity ratio has similar behavior for both high- and low-redshift TIs (including some evidence for scale-dependency for the early-type environment galaxies similar to what is seen in Figure 6.5). Therefore, we again conclude that although there is redshift evolution present in the early-type environment overdensities, the effect of target luminosity is more important.

6.5 FOUR ENVIRONMENT GALAXY TYPES

Finally, we take advantage of additional subdivisions using the photometric galaxy type parameter t that correspond to four galaxy types based on the CWW spectral templates. Following the divisions chosen by Budavari et al. (2003), we define $t < 0.02$ to be Ell type, $0.02 \leq t < 0.3$ is approximately CWW Sbc type, $0.3 \leq t < 0.65$ is approximately CWW Scd type, and $t \geq 0.65$ is approximately CWW Irregular type. Because we are further subdividing the environment galaxies, the average expected counts of any given type will be lower within $2 h_{70}^{-1}$ Mpc, so it is best to use a maximum redshift of $z = 0.28$ (see Section 3.3). Figures 6.10, 6.11, and 6.12 show the overdensity with scale and environment galaxy types for TI+TIIs, TIs, and TIs, respectively. The overdensities at $R \approx 500 h_{70}^{-1}$ kpc are compared in Table 6.6. We especially note that at these low redshifts, the Sbc type galaxies dominate the environments. Although the CWW templates are based on observations of nearby galaxies classified by morphology (e.g., for the Sbc type: M51, NGC 470, NGC 1659, and NGC

2903; Coleman, Wu, & Weedman, 1980) we interpret the calculated spectral energy distributions as containing information about the star formation history of galaxies in a particular class. Galaxies with more young stars are bluer, while galaxies with older stars appear redder. The Sbc type galaxy is representative of a galaxy with less recent star formation than Scd or Irr type galaxies and is therefore considered “early-type” in the broader definition we use in our work.

6.6 CONCLUSIONS

Given our results, we speculate that bright TIs are located nearby to or in galaxy clusters (see also, e.g., Barr et al., 2003; Söchting et al., 2004) because of the high overdensity of early-type galaxies in their environments. Early-type galaxies are known to cluster more strongly than late-type galaxies (e.g., Willmer et al., 1998; Zehavi et al., 2002), to be located closer to the centers of galaxy clusters (e.g., Dressler, 1980; Aguerri et al., 2007), and compose a predominant fraction of the galaxies in more massive halos (e.g. Zehavi et al., 2005).

Bright and dim TIIs are found to be in environments with fewer early-type galaxies. If the difference between TIs and TIIs is merely observation angle, the difference in their environments could be evidence that we are observing these narrow-line targets at a different stage of evolution, closer to the interaction of gas-rich (late-type) galaxies that triggered the activity in the nucleus, perhaps in the outskirts of interacting galaxy clusters (Söchting et al., 2004). The lower early-type overdensity could also be evidence that the clusters in which the TIIs are located are poorer.

According to the merger model, the active galactic nucleus is shrouded in gas and dust (only narrow-line emission will be observed) immediately following the interaction of massive gas rich galaxies, which also may trigger local star formation activity Li et al. (2008). In time, however, the feedback from the active nucleus blows out the gas and dust, revealing its bright center (now seen as a Type I source) and eventually quenching the nuclear activity and local star formation (e.g., Di Matteo et al., 2005; Hopkins et al., 2008). Our observation of a higher overdensity of Sbc type galaxies around our sources, especially TIs, could be evidence that this feedback also affects nearby galaxies outside of the host galaxy, quenching or suppressing star formation in nearby galaxies (e.g., Croton et al., 2006).

Table 6.1: Ratio of early-type environment galaxy overdensity to late-type environment galaxy overdensity at scale $R \approx 500 h_{70}^{-1}$ kpc. Targets have $0.11 \leq z \leq 0.4$ and $\log(L_{[\text{OIII}]} / L_{\odot}) \geq 8.0$.

Sample	early/late	significance
TI+TII	2.07 ± 0.282	3.80σ
TI	2.24 ± 0.358	3.47σ
TII	1.70 ± 0.446	1.58σ
QI	2.24 ± 0.393	3.16σ
TI, $\log(L_{[\text{OIII}]} / L_{\odot}) \leq 8.4$	2.09 ± 0.468	2.33σ
TI, $\log(L_{[\text{OIII}]} / L_{\odot}) > 8.4$	2.44 ± 0.556	2.59σ
TII, $\log(L_{[\text{OIII}]} / L_{\odot}) \leq 8.4$	1.76 ± 0.653	1.17σ
TII, $\log(L_{[\text{OIII}]} / L_{\odot}) > 8.4$	1.65 ± 0.612	1.07σ
QI, $\log(L_{[\text{OIII}]} / L_{\odot}) \leq 8.4$	2.06 ± 0.529	2.00σ
QI, $\log(L_{[\text{OIII}]} / L_{\odot}) > 8.4$	2.42 ± 0.580	2.45σ

Table 6.2: Comparison of early- and late-type environment galaxy overdensities at several scales (see also Figures 6.2 and 6.3).

scale (h_{70}^{-1} Mpc)	Early-Type		Late-Type			
	TI	TII	TI/TII	TI	TII	TI/TII
2.0	0.213 ± 0.019	0.208 ± 0.031	1.027 ± 0.176	0.119 ± 0.012	0.140 ± 0.021	0.853 ± 0.157
1.0	0.410 ± 0.035	0.377 ± 0.055	1.088 ± 0.184	0.202 ± 0.023	0.245 ± 0.039	0.825 ± 0.160
0.5	0.850 ± 0.078	0.687 ± 0.113	1.237 ± 0.234	0.379 ± 0.049	0.403 ± 0.082	0.940 ± 0.227
0.15	2.304 ± 0.346	1.755 ± 0.447	1.313 ± 0.388	1.249 ± 0.219	1.277 ± 0.357	0.978 ± 0.323

Table 6.3: Comparison environment overdensities of $0.11 \leq z \leq 0.15$ AI, AII, and L^* galaxies at several scales (see also Figure 6.4).

Scale (h_{70}^{-1} Mpc)	All Environment Galaxies				
	AI	AII	Lstar	AI/Lstar	AII/Lstar
2.0	0.136 ± 0.016	0.145 ± 0.012	0.175 ± 0.005	0.775 ± 0.095	0.828 ± 0.070
1.0	0.260 ± 0.027	0.277 ± 0.019	0.297 ± 0.008	0.876 ± 0.093	0.933 ± 0.069
0.50	0.448 ± 0.050	0.481 ± 0.036	0.477 ± 0.014	0.941 ± 0.108	1.009 ± 0.081
0.15	0.885 ± 0.157	1.101 ± 0.123	0.865 ± 0.043	1.023 ± 0.189	1.273 ± 0.155
	Early-Type Environment Galaxies				
2.0	0.142 ± 0.021	0.154 ± 0.015	0.198 ± 0.006	0.717 ± 0.108	0.775 ± 0.080
1.0	0.301 ± 0.037	0.321 ± 0.027	0.358 ± 0.011	0.841 ± 0.107	0.897 ± 0.079
0.5	0.576 ± 0.074	0.560 ± 0.052	0.586 ± 0.020	0.984 ± 0.130	0.956 ± 0.094
0.15	1.051 ± 0.233	1.230 ± 0.178	1.057 ± 0.064	0.994 ± 0.228	1.164 ± 0.183
	Late-Type Environment Galaxies				
2.0	0.128 ± 0.016	0.135 ± 0.012	0.148 ± 0.005	0.864 ± 0.113	0.910 ± 0.084
1.0	0.213 ± 0.028	0.226 ± 0.020	0.226 ± 0.008	0.941 ± 0.130	1.000 ± 0.097
0.5	0.300 ± 0.056	0.388 ± 0.042	0.349 ± 0.016	0.858 ± 0.166	1.111 ± 0.131
0.15	0.696 ± 0.200	0.954 ± 0.160	0.647 ± 0.053	1.077 ± 0.322	1.475 ± 0.275
number	621	1222	8036		

Table 6.4: Comparison of early- and late-type environment galaxy overdensities at several scales for bright and dim TI and TII targets (see also Figures 6.5 and 6.6).

scale (h_{70}^{-1} Mpc)	Early-Type		Late-Type			
	TI	TII	TI/TII	TI	TII	TI/TII
	$8.0 \leq \log(L_{\text{[OIII]}}/L_{\odot}) \leq 8.4$					
2.0	0.220 ± 0.025	0.183 ± 0.041	1.201 ± 0.299	0.123 ± 0.016	0.159 ± 0.030	0.777 ± 0.179
1.0	0.379 ± 0.045	0.357 ± 0.073	1.062 ± 0.252	0.180 ± 0.029	0.248 ± 0.054	0.726 ± 0.197
0.5	0.740 ± 0.097	0.661 ± 0.150	1.120 ± 0.293	0.354 ± 0.064	0.375 ± 0.110	0.942 ± 0.325
0.15	1.751 ± 0.381	1.544 ± 0.555	1.134 ± 0.477	1.135 ± 0.274	1.246 ± 0.481	0.911 ± 0.415
	$\log(L_{\text{[OIII]}}/L_{\odot}) > 8.4$					
2.0	0.204 ± 0.028	0.240 ± 0.047	0.847 ± 0.203	0.113 ± 0.019	0.117 ± 0.030	0.966 ± 0.297
1.0	0.455 ± 0.055	0.403 ± 0.084	1.130 ± 0.272	0.233 ± 0.036	0.242 ± 0.057	0.963 ± 0.269
0.5	1.012 ± 0.131	0.721 ± 0.174	1.403 ± 0.383	0.415 ± 0.078	0.436 ± 0.123	0.950 ± 0.321
0.15	3.130 ± 0.666	2.033 ± 0.738	1.540 ± 0.648	1.407 ± 0.359	1.312 ± 0.533	1.072 ± 0.514

Table 6.5: Comparison of early- and late-type environment galaxy overdensities at several scales for bright and dim TI targets in two redshift ranges (see also Figures 6.8 and 6.9).

scale (h_{70}^{-1} Mpc)	Early-Type			Late-Type		
	$0.11 \leq z \leq 0.28$	$0.28 < z \leq 0.4$	highz/lowz	$0.11 \leq z \leq 0.28$	$0.28 < z \leq 0.4$	highz/lowz
	$8.0 \leq \log(L_{\text{OIII}}/L_{\odot}) \leq 8.4$					
2.0	0.217 ± 0.032	0.226 ± 0.036	1.039 ± 0.227	0.144 ± 0.022	0.091 ± 0.024	0.635 ± 0.192
1.0	0.375 ± 0.058	0.388 ± 0.069	1.035 ± 0.244	0.200 ± 0.039	0.148 ± 0.045	0.739 ± 0.266
0.5	0.679 ± 0.118	0.869 ± 0.168	1.280 ± 0.333	0.385 ± 0.084	0.303 ± 0.099	0.787 ± 0.308
0.15	1.442 ± 0.421	2.404 ± 0.795	1.667 ± 0.735	1.291 ± 0.371	0.885 ± 0.398	0.685 ± 0.366
number	388	594		388	594	
	$\log(L_{\text{OIII}}/L_{\odot}) > 8.4$					
2.0	0.170 ± 0.041	0.245 ± 0.038	1.437 ± 0.409	0.129 ± 0.028	0.097 ± 0.025	0.753 ± 0.252
1.0	0.361 ± 0.075	0.573 ± 0.080	1.590 ± 0.398	0.262 ± 0.052	0.203 ± 0.049	0.776 ± 0.241
0.5	0.756 ± 0.162	1.330 ± 0.210	1.758 ± 0.468	0.420 ± 0.110	0.409 ± 0.110	0.975 ± 0.366
0.15	2.189 ± 0.719	4.296 ± 1.231	1.963 ± 0.855	1.372 ± 0.496	1.443 ± 0.519	1.052 ± 0.536
number	247	562		247	562	

Table 6.6: Comparison of four types (CWW) of environment galaxy overdensities at scale $R \approx 500 h_{70}^{-1}$ kpc. Targets have $\log(L_{[\text{OIII}]}/L_{\odot}) \geq 8.0$ and $0.11 \leq z \leq 0.28$ (see also Figures 6.10 through 6.12).

Galaxy Type	TI+TII	TI	TII
Ell	0.611 ± 0.088	0.644 ± 0.116	0.563 ± 0.136
Sbc	0.785 ± 0.104	0.791 ± 0.134	0.776 ± 0.165
Scd	0.447 ± 0.084	0.437 ± 0.107	0.463 ± 0.134
Irr	0.385 ± 0.065	0.373 ± 0.082	0.357 ± 0.099

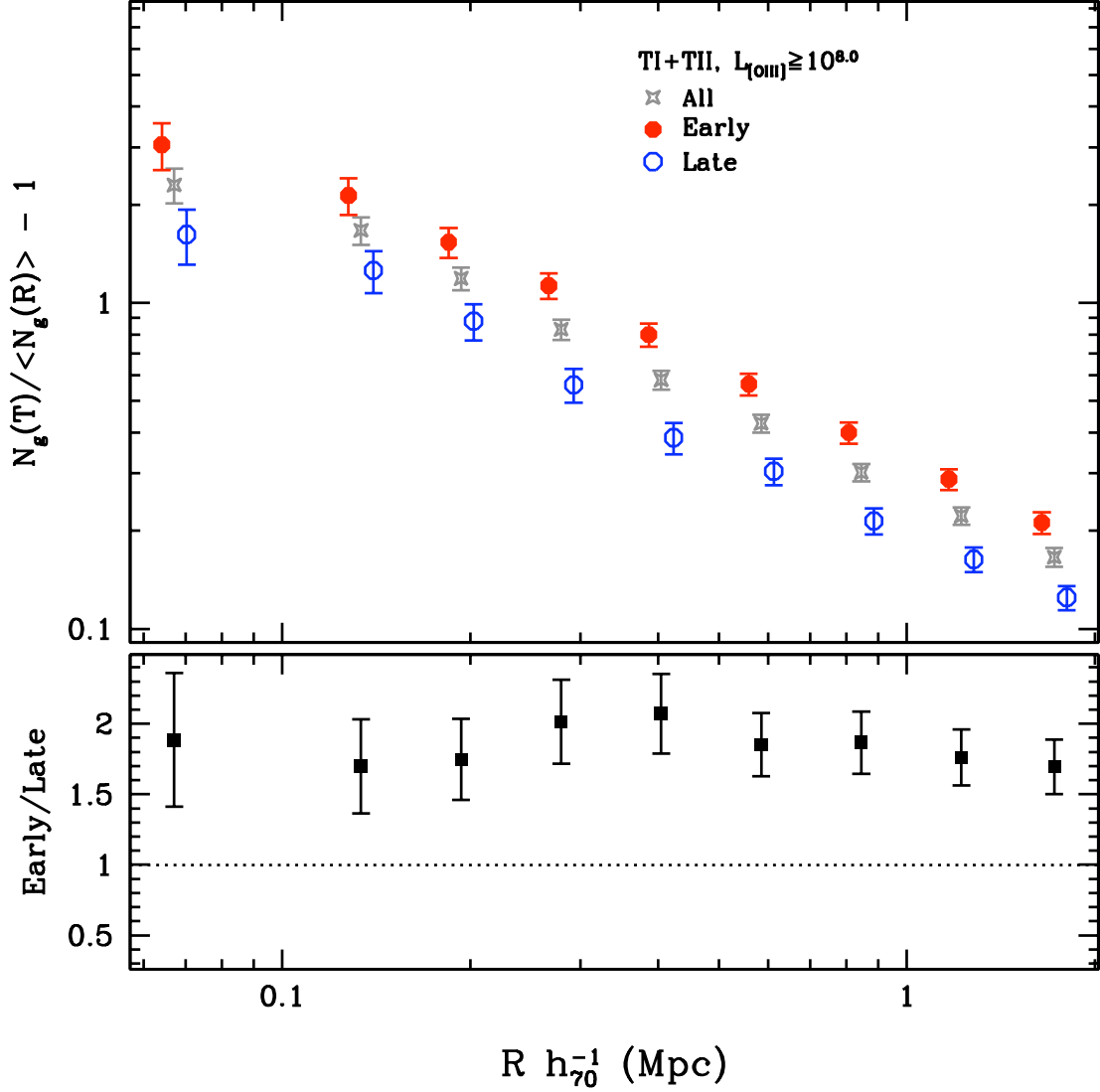


Figure 6.1— Mean cumulative environment overdensity vs. scale and environment galaxy type for all targets with $0.11 \leq z \leq 0.4$ and $\log(L_{[\text{OIII}]}/L_{\odot}) \geq 8.0$. *Lower panel:* Ratio of early-type environment overdensity to late-type environment overdensity.

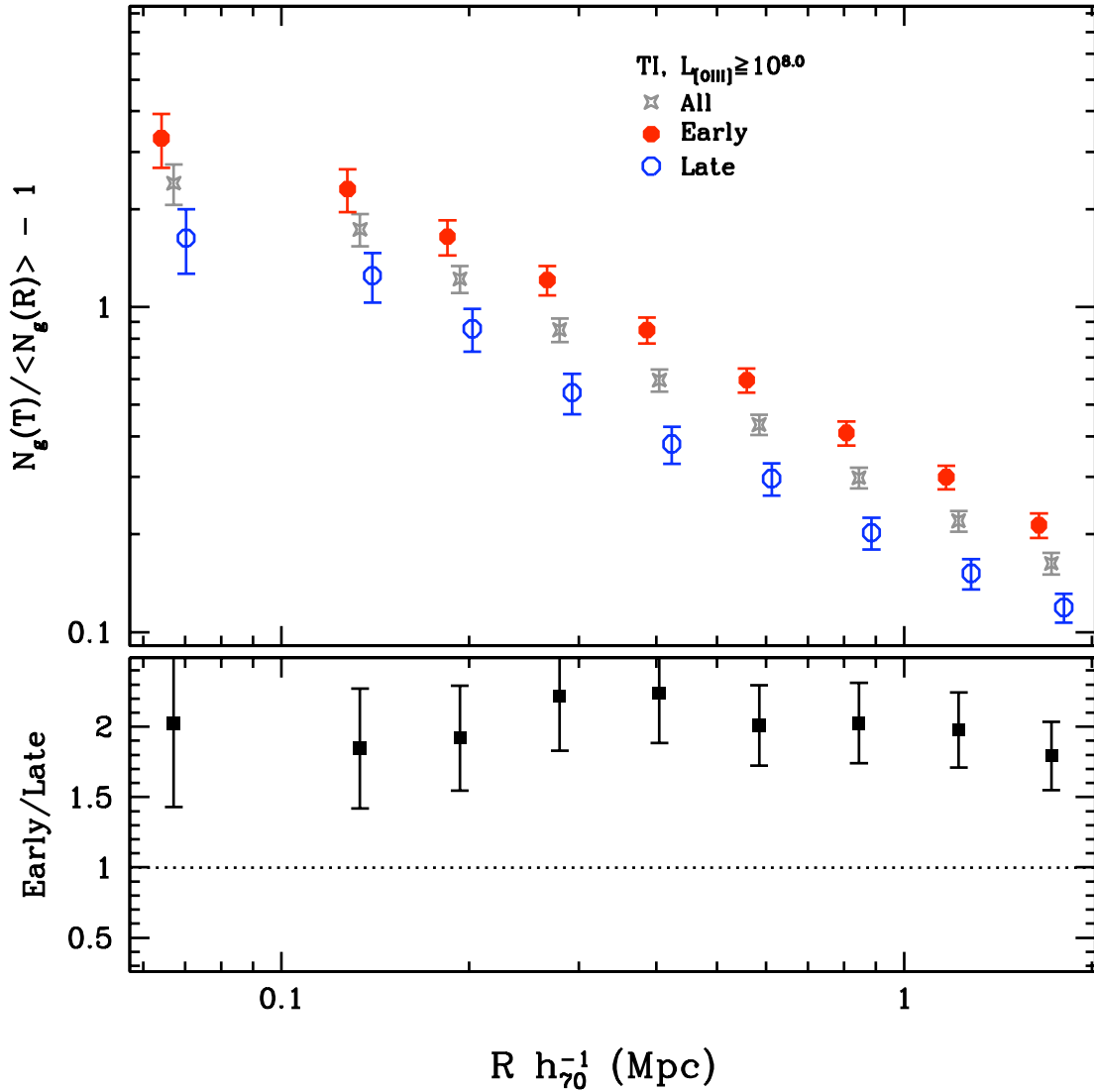


Figure 6.2— Mean cumulative environment overdensity vs. scale and environment galaxy type for TIs with $0.11 \leq z \leq 0.4$ and $\log(L_{[\text{OIII}]} / L_{\odot}) \geq 8.0$. *Lower panel:* Ratio of early-type environment overdensity to late-type environment overdensity.

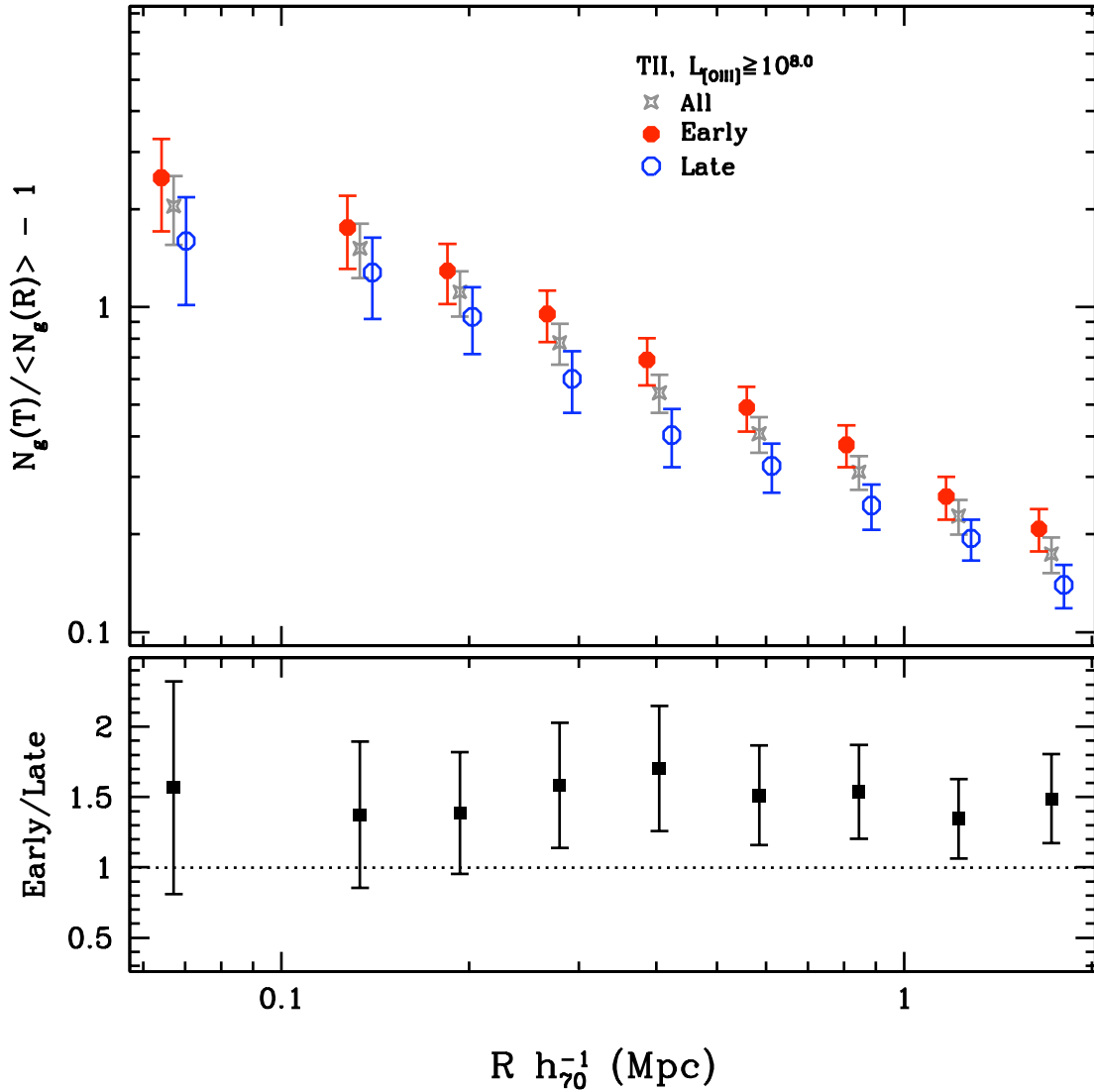


Figure 6.3— Mean cumulative environment overdensity vs. scale and environment galaxy type for TII with $0.11 \leq z \leq 0.4$ and $\log(L_{[\text{OIII}]} / L_{\odot}) \geq 8.0$. *Lower panel:* Ratio of early-type environment overdensity to late-type environment overdensity.

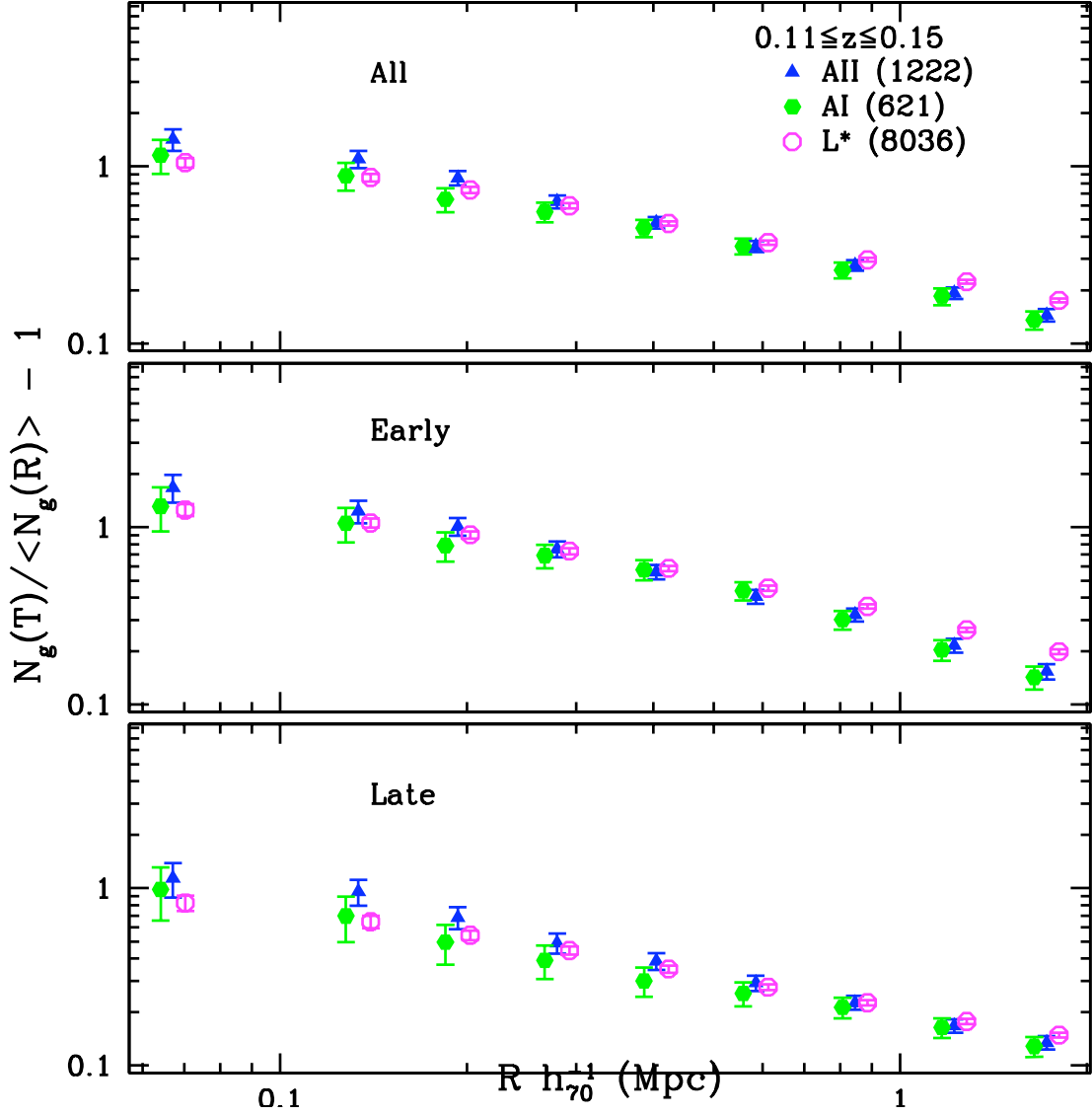


Figure 6.4— Mean cumulative environment overdensity vs. scale for AIs, AIIIs, and L^* galaxies with all environment galaxies; and early- and late-type environment galaxies alone. All targets have $0.11 \leq z \leq 0.15$, and the AGN targets have $\log(L_{[\text{OIII}]} / L_{\odot}) \geq 6.5$. See Table 6.3 for numerical overdensity values and comparisons.

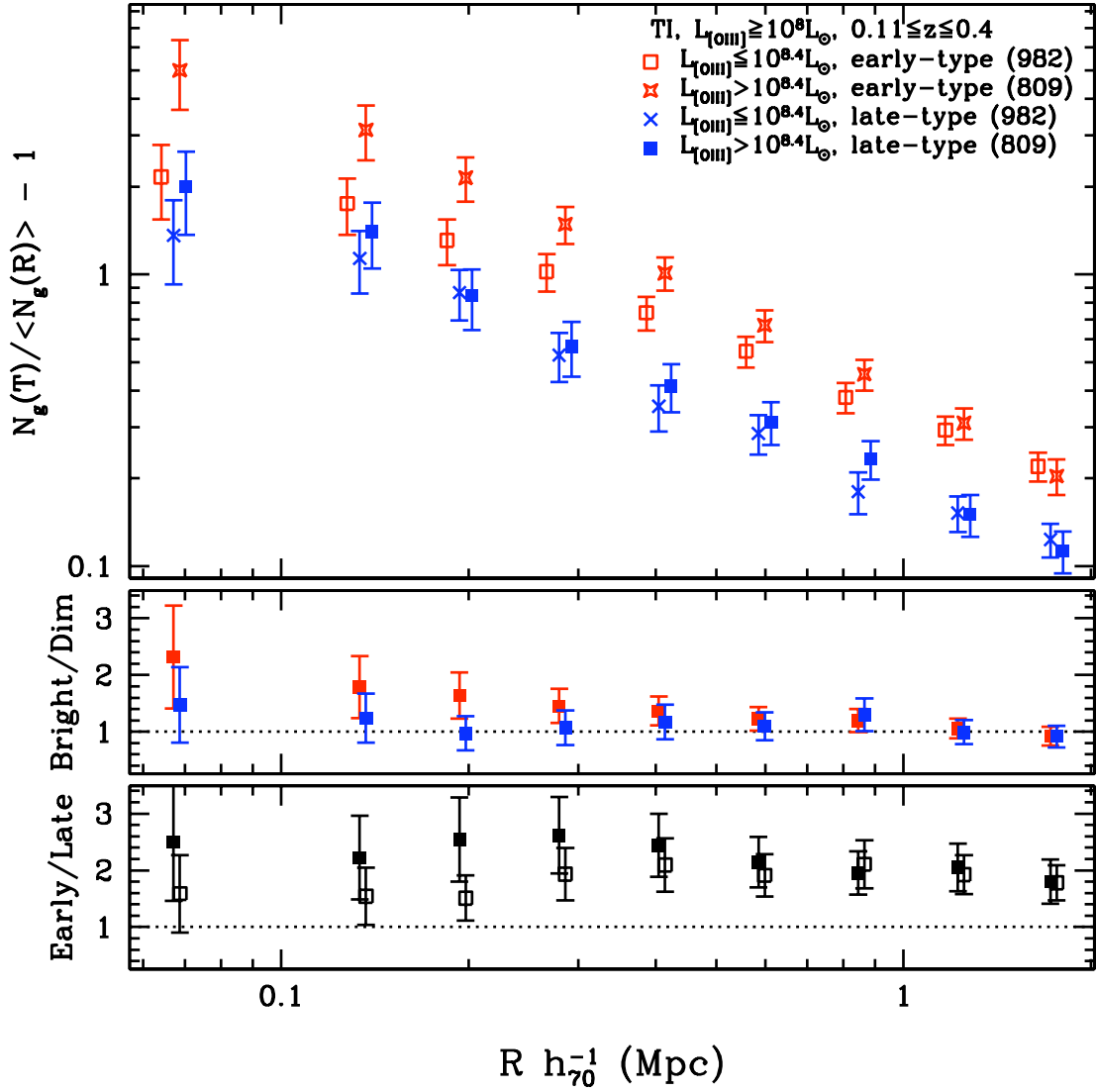


Figure 6.5— *Upper panel*: Mean cumulative environment overdensity vs. scale, $L_{[\text{OIII}]}$ and environment galaxy type for $0.11 \leq z \leq 0.4$ TI targets with $\log(L_{[\text{OIII}]} / L_{\odot}) \geq 8.0$. *Middle panel*: Ratio of early- or late-type environment overdensity around bright targets to that around dim targets (red, blue points respectively). *Lower panel*: Ratio of early-type overdensity to late-type overdensity around bright (solid points) and dim (open points) targets.

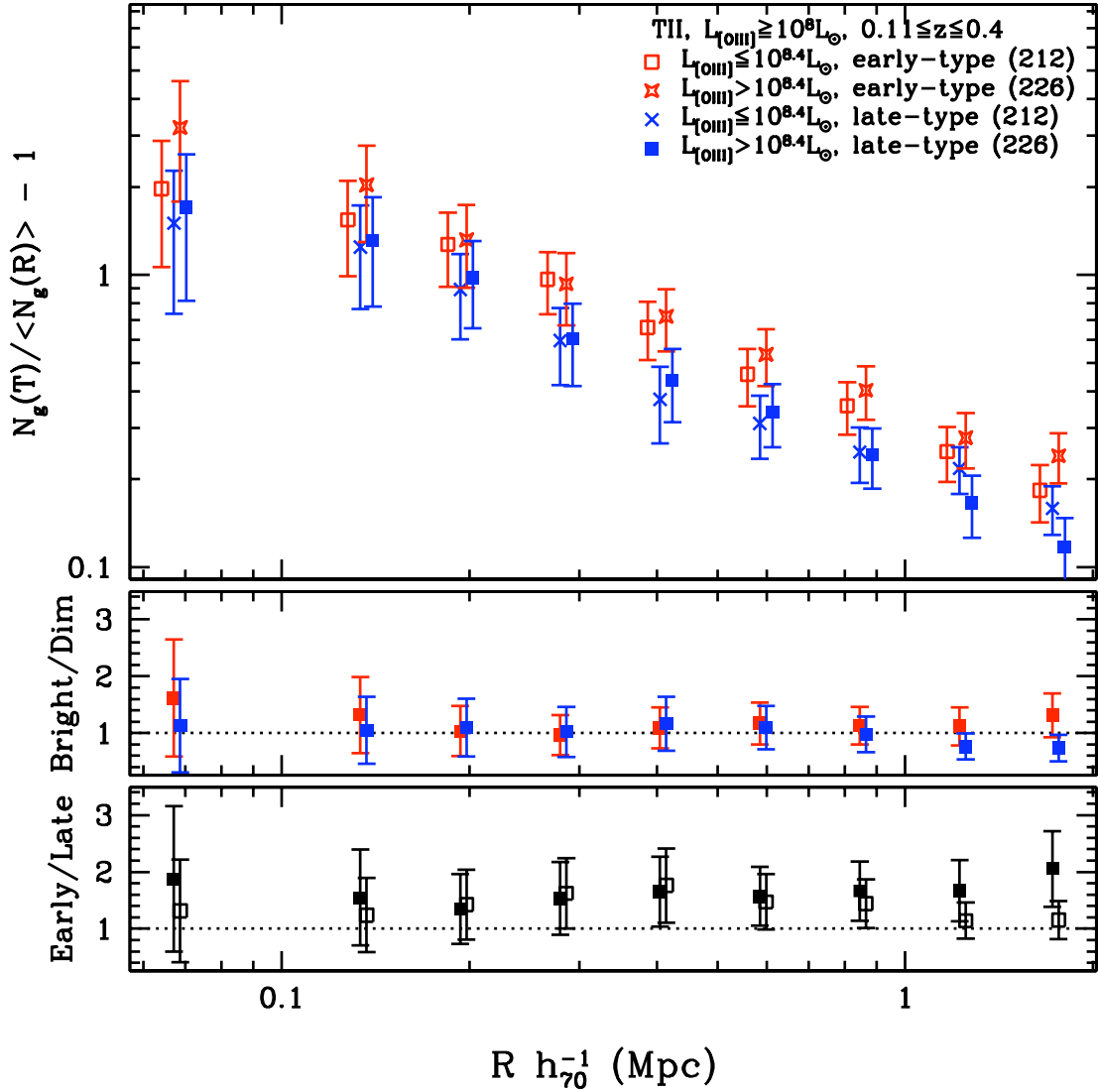


Figure 6.6— *Upper panel*: Mean cumulative environment overdensity vs. scale, $L_{[\text{OIII}]}$ and environment galaxy type for $0.11 \leq z \leq 0.4$ TII targets with $\log(L_{[\text{OIII}]} / L_{\odot}) \geq 8.0$. *Middle panel*: Ratio of early- or late-type environment overdensity around bright targets to that around dim targets (red, blue points respectively). *Lower panel*: Ratio of early-type overdensity to late-type overdensity around bright (solid points) and dim (open points) targets.

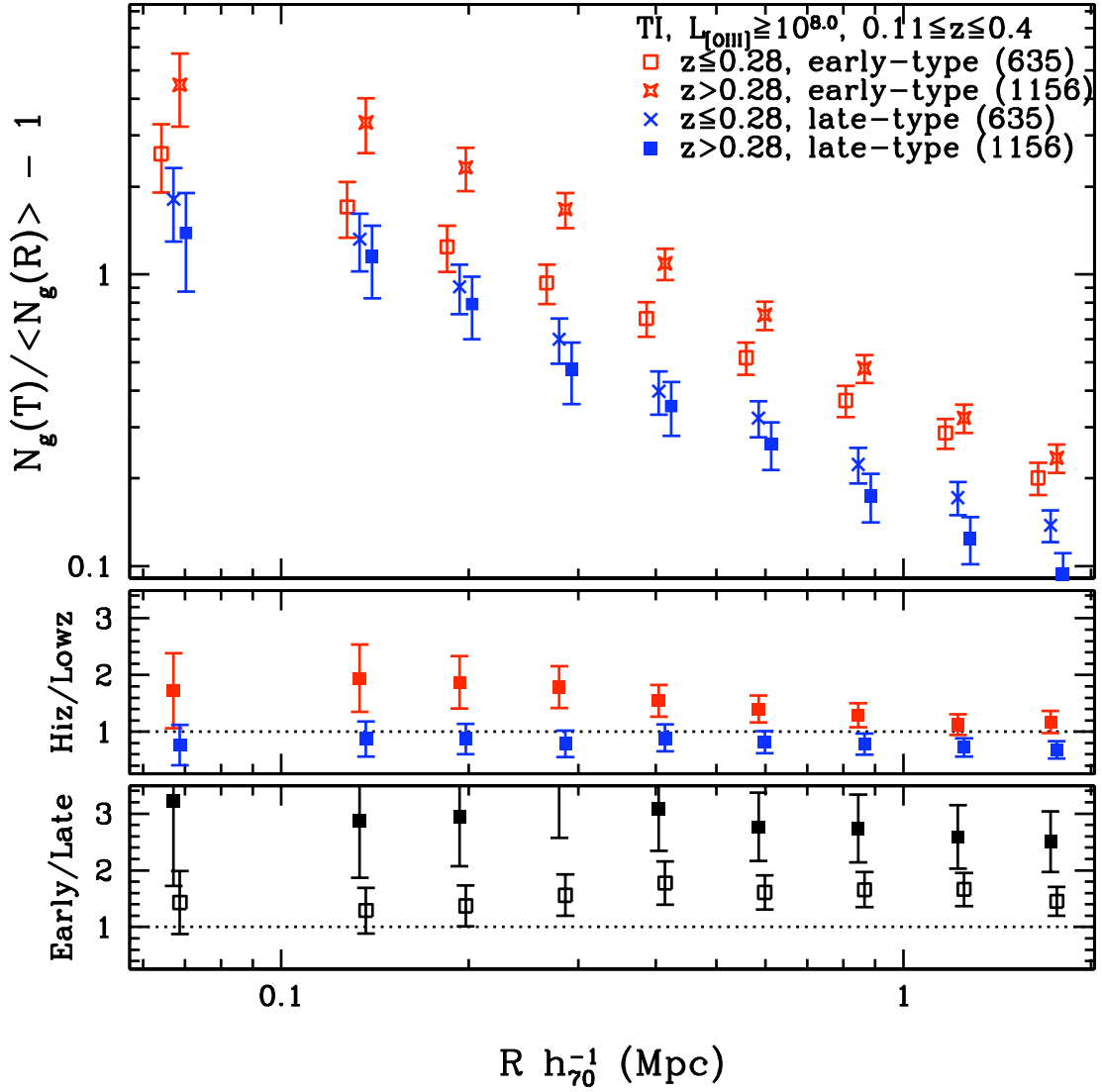


Figure 6.7— Mean cumulative environment overdensity vs. scale, redshift and environment galaxy type for TI targets with $\log(L_{\text{[OIII]}}/L_{\odot}) \geq 8.0$. *Middle panel:* ratio of high redshift environment overdensity to low-redshift environment overdensity of early-type galaxies (red points) and late-type galaxies (blue points). *Lower panel:* ratio of early-type galaxy overdensity to late-type galaxy overdensity for high redshift (solid points) and low redshift (open points) TIs.

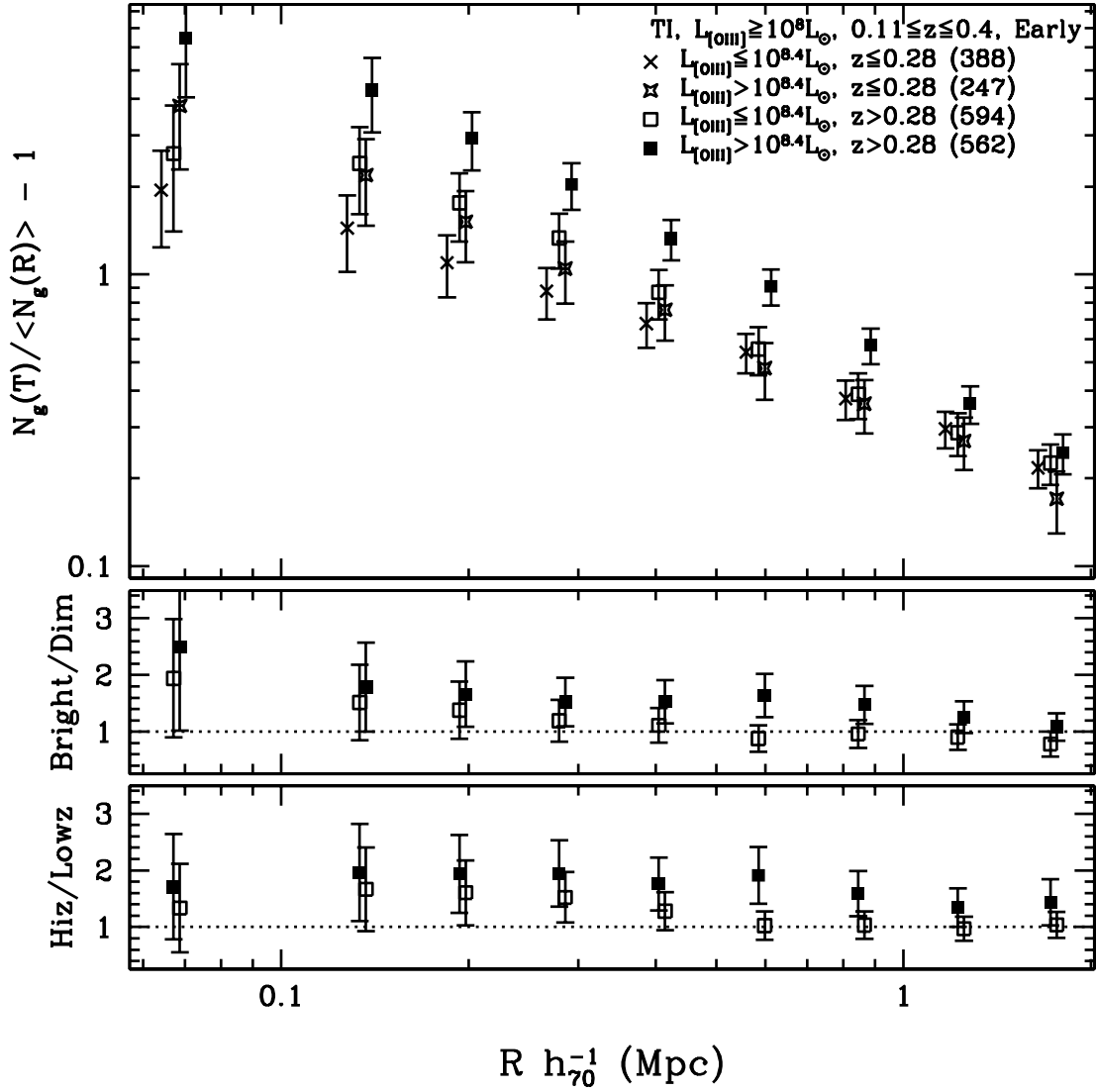


Figure 6.8— Mean cumulative environment overdensity of early-type galaxies vs. scale, $L_{[\text{OIII}]}$, and redshift for TI targets with $\log(L_{[\text{OIII}]} / L_{\odot}) \geq 8.0$. *Middle panel*: ratio of environment overdensities of bright TIs to dim TIs for $z \leq 0.28$ (open points), and $z > 0.28$ (filled points) targets. *Lower panel*: ratio of overdensities for high-redshift TIs to low-redshift TIs for bright (filled points) and dim (open points) targets.

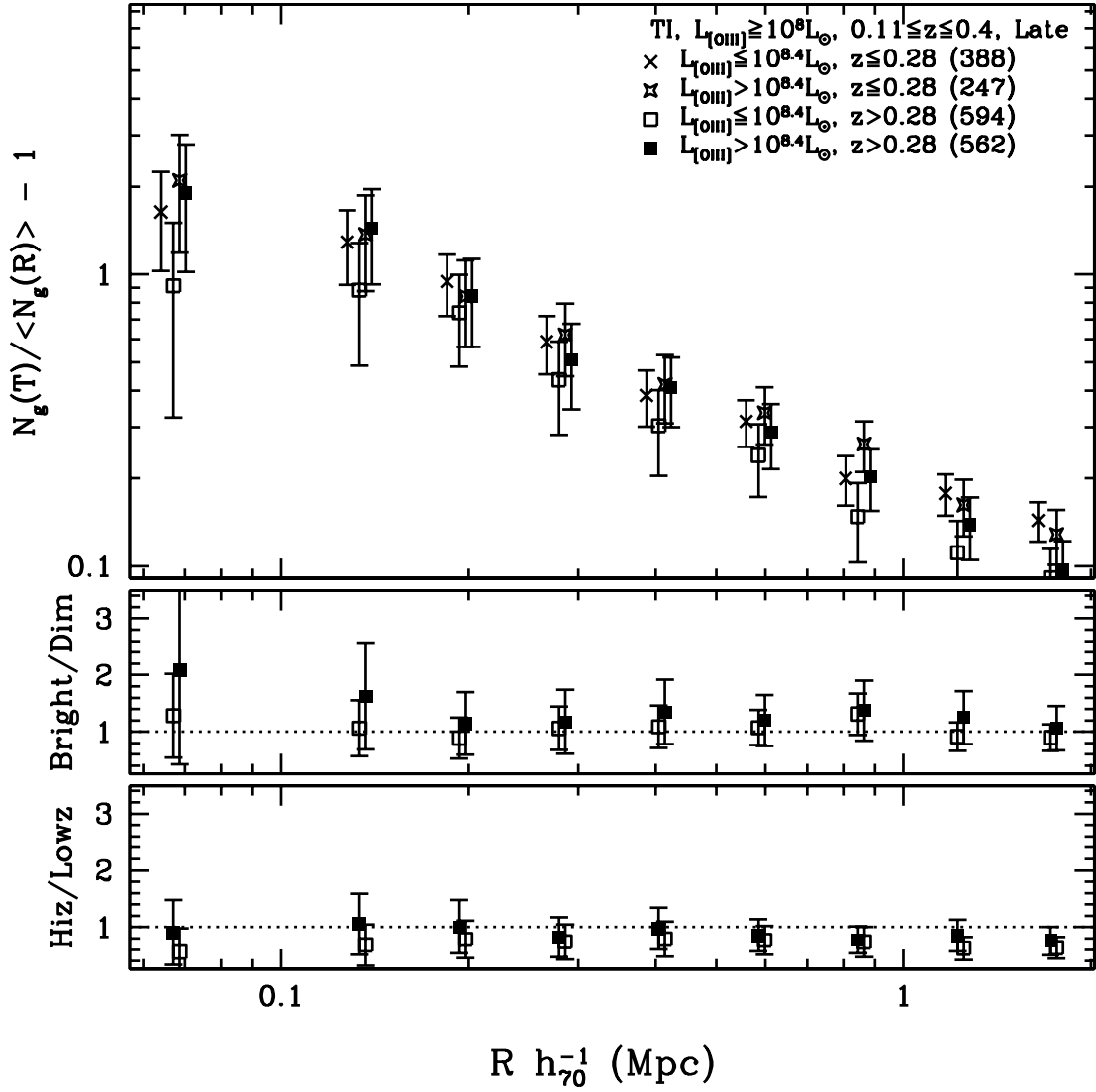


Figure 6.9— Mean cumulative environment overdensity of late-type galaxies vs. scale, $L_{[\text{OIII}]}$, and redshift for TI targets with $\log(L_{[\text{OIII}]} / L_{\odot}) \geq 8.0$. *Middle panel*: ratio of environment overdensities of bright TIs to dim TIs for $z \leq 0.28$ (open points), and $z > 0.28$ (filled points) targets. *Lower panel*: ratio of overdensities for high-redshift TIs to low-redshift TIs for bright (filled points) and dim (open points) targets.

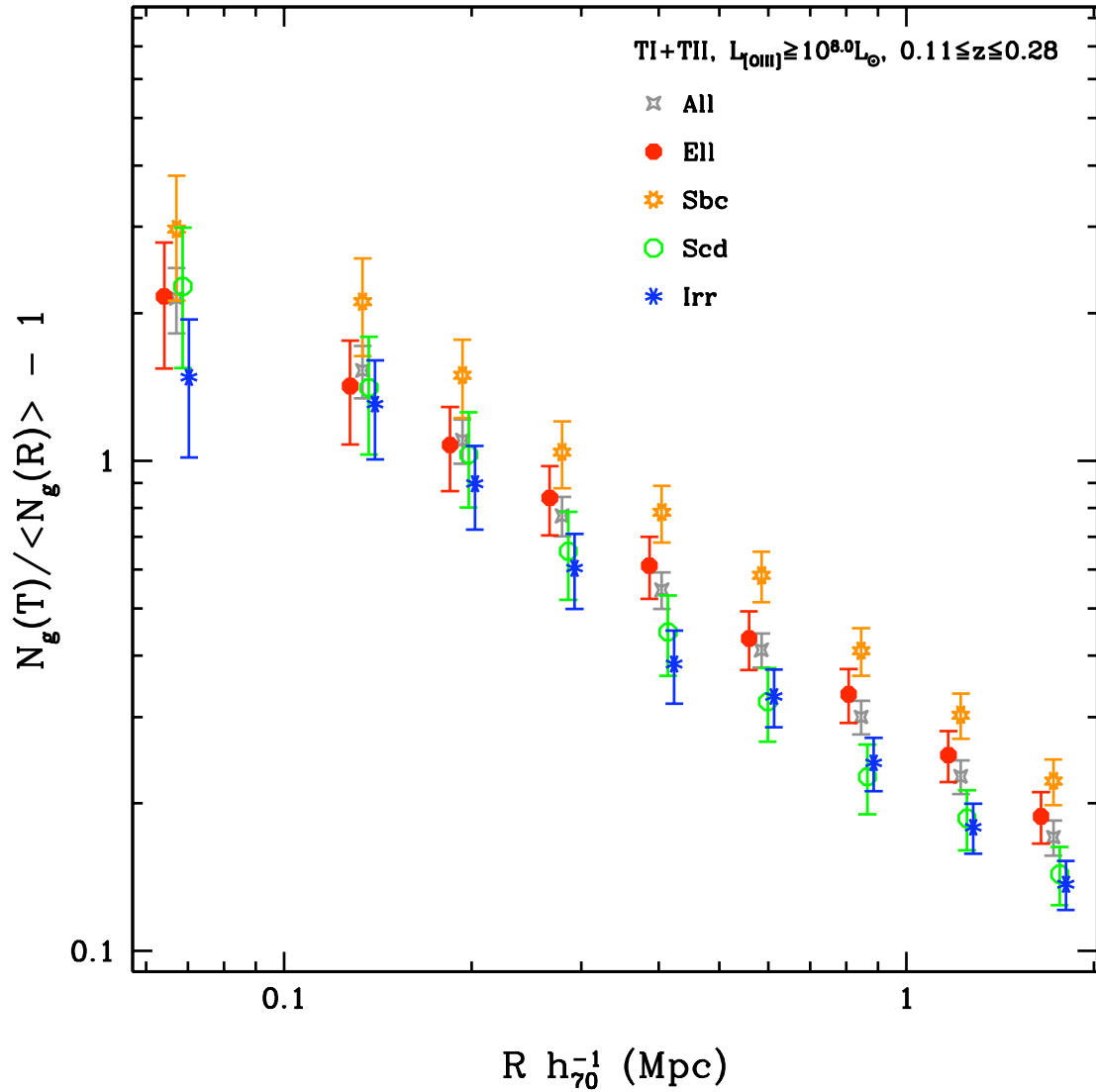


Figure 6.10— Mean cumulative environment overdensity vs. scale and environment galaxy type for all targets with $0.11 \leq z \leq 0.28$ and $\log(L_{\text{[OIII]}}/L_{\odot}) \geq 8.0$.

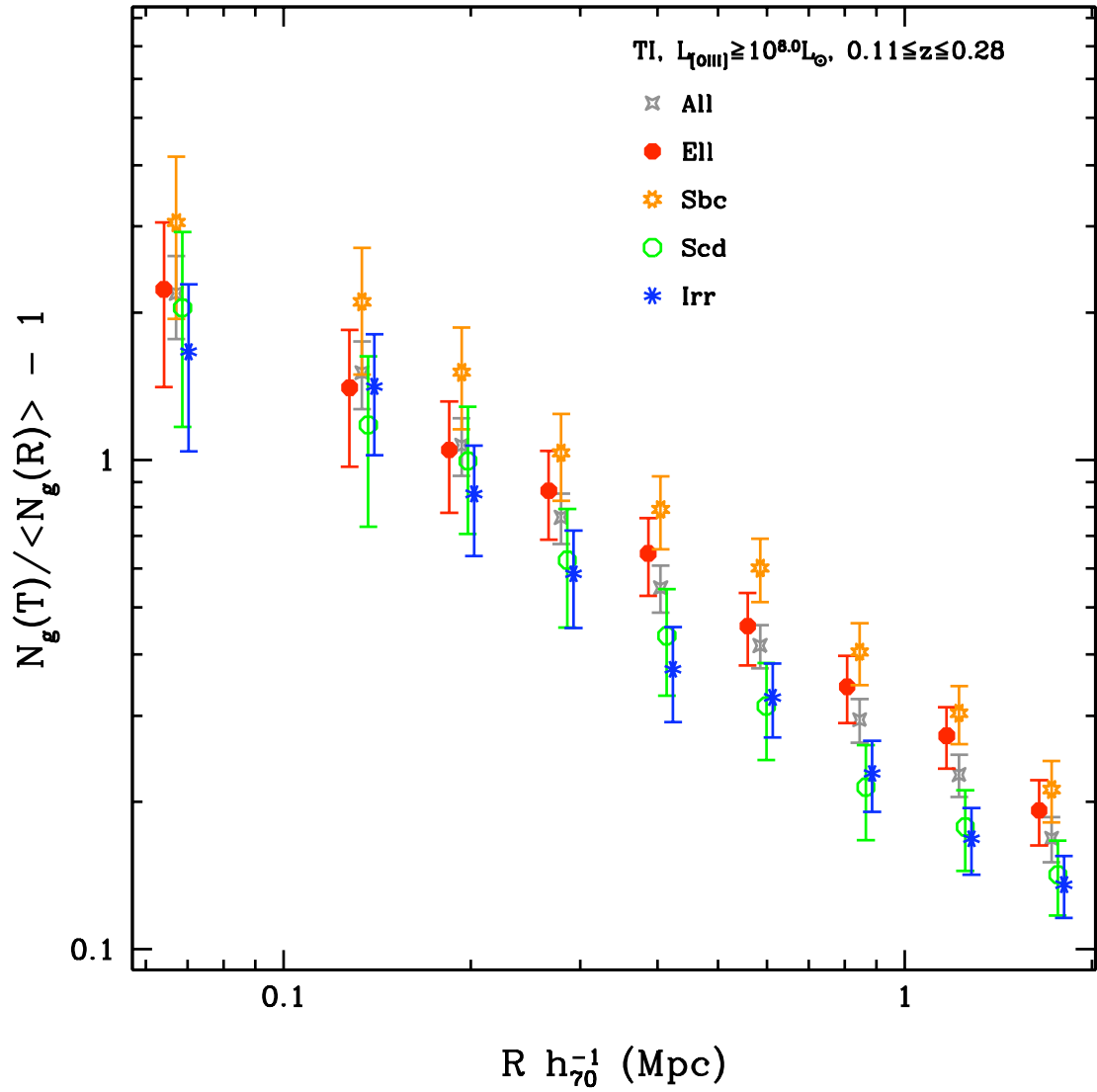


Figure 6.11— Mean cumulative environment overdensity vs. scale and environment galaxy type for TIs with $0.11 \leq z \leq 0.28$ and $\log(L_{[\text{OIII}]} / L_{\odot}) \geq 8.0$.

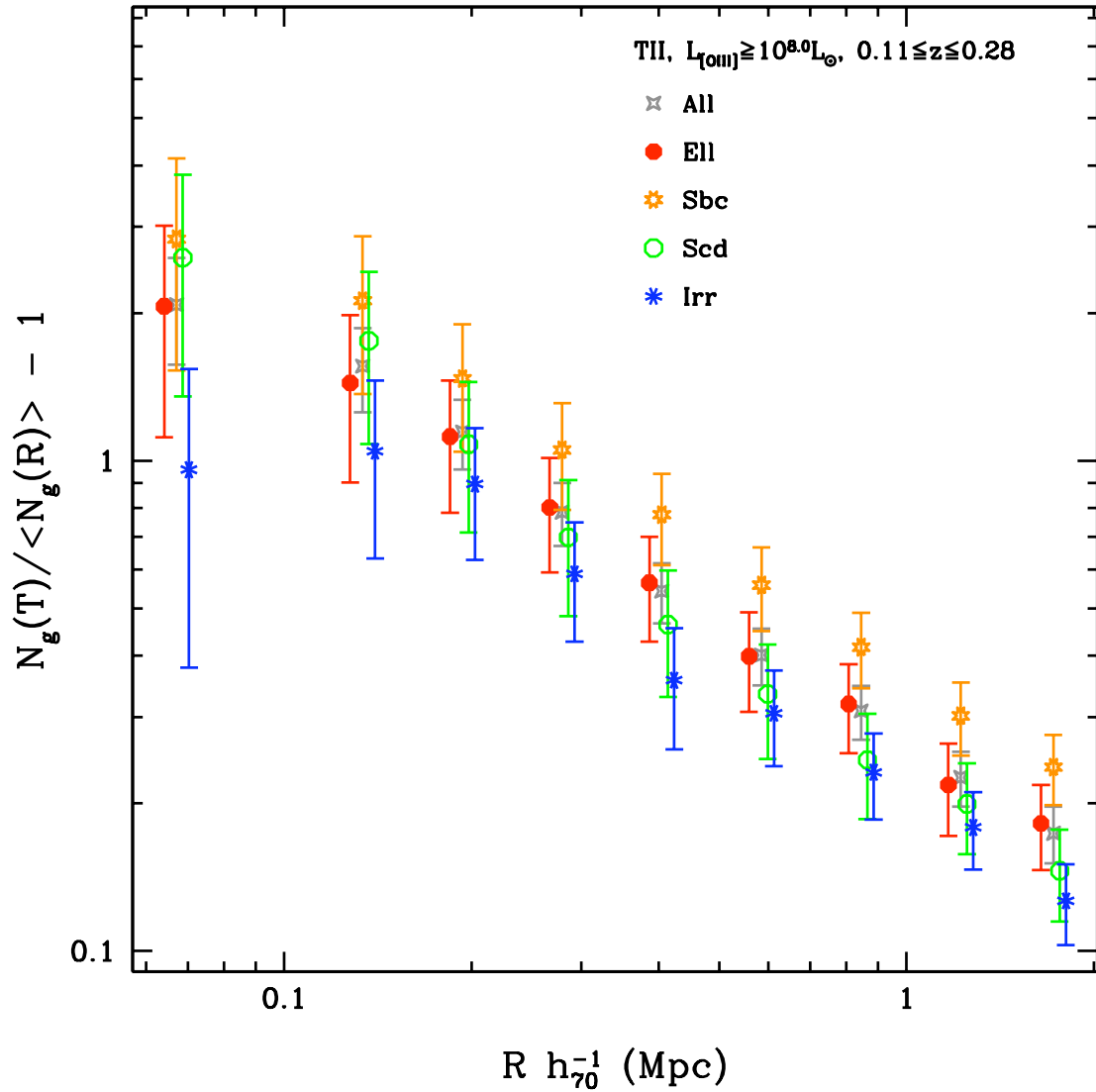


Figure 6.12— Mean cumulative environment overdensity vs. scale and environment galaxy type for Type II AGNs with $0.11 \leq z \leq 0.28$ and $\log(L_{[\text{OIII}]} / L_{\odot}) \geq 8.0$.

Chapter 7

The Dependence on Black Hole Mass

7.1 OVERVIEW

We calculate black hole masses M_{BH} for QIs using Equation 1 from Shen et al. (2008):

$$\log\left(\frac{M_{\text{BH,vir}}}{M_{\odot}}\right) = a + b \log\left(\frac{\lambda L_{\lambda}}{10^{44} \text{ ergs s}^{-1}}\right) + 2 \log\left(\frac{\text{FWHM}}{\text{km s}^{-1}}\right) \quad (7.1)$$

where FWHM is the full-width at half-maximum measurement of the H_{β} emission line and L_{λ} is the luminosity of the quasar continuum spectrum at $\lambda = 5100\text{\AA}$ (see Shen et al., 2008, for details on line measurement procedures; line measurements provided by R. Reyes, private communication, 2008). We see no evolution of H_{β} FWHM and continuum 5100\AA luminosity measurements in our redshift range of $0.11 \leq z \leq 0.5$, therefore the black hole mass distribution for the sample is also independent of redshift. As in previous chapters, we will apply a volume-limit to ensure that the objects we consider have $\log(L_{[\text{OIII}]} / L_{\odot}) \geq 8.0$. For simplicity, we will use “mass” interchangeably with M_{BH} throughout the chapter, unless explicitly noted otherwise.

Cumulative overdensity vs. scale and M_{BH} is plotted for this $L_{[\text{OIII}]}$ volume-limited QI sample in Figure 7.1 (see also Table 7.1 for the ratio of high-mass black hole environment overdensity to low-mass black hole environment overdensity at $R \approx 500 h_{70}^{-1}$ kpc). The dividing value of $\log(M_{\text{BH}}/M_{\odot}) = 8.25$ is chosen to give roughly equal subsamples of quasars in each mass bin. It is quite clear that at scales $R \gtrsim 100 h_{70}^{-1}$ kpc, the environments of quasars with more massive black holes are more overdense than the less massive ones, which reflects the well-known correlation between black hole mass and dark matter halo mass, the so-called $M - \sigma$ or $M_{\text{DMH}} - M_{\text{BH}}$ relation (e.g., Ferrarese & Merritt, 2000; Gebhardt et al., 2000; Tremaine et al., 2002). At scales $\lesssim 100 h_{70}^{-1}$ kpc, small numbers combined with an decreasing angular radius with redshift make strong conclusions difficult. The ratio of environment overdensity of high mass QIs to low mass QIs increases with increasing radius: at $R \approx 150 h_{70}^{-1}$ kpc, the ratio of environment overdensity for higher mass QIs to lower mass QIs is 1.24 ± 0.27 , at $R \approx 500 h_{70}^{-1}$ kpc the ratio is 1.30 ± 0.19 , and at $R \approx 1.0 h_{70}^{-1}$ Mpc it is 1.61 ± 0.22 . Thus, higher mass QIs are in environments that are more overdense than those of their lower mass counterparts to larger radii.

We quantify the relationship between overdensity and M_{BH} in Figure 7.2, where the linear least-squares fits for each of the scales are given in Table 7.2. Here we see that at small scales, QI environment overdensity increases with increasing M_{BH} as shown by the increasingly nonzero slope in the relationship of overdensity with M_{BH} . At the scale $\approx 150 h_{70}^{-1}$ kpc, the relationship has the form $\text{overdensity} = 0.59 \log(M_{\text{BH}}/M_{\odot}) - 2.9$, while at the largest scale of $2 h_{70}^{-1}$ Mpc, the slope is close

to zero, meaning that there is very little variation in overdensity with M_{BH} . In the following sections, we will isolate specific physical attributes of the QIs to identify their influence on the relationship between QI M_{BH} and environment overdensity.

7.2 QI LUMINOSITY

We first subdivide the mass bins by $L_{[\text{OIII}]}$ in Figure 7.3. We see that the ratio of overdensity around high mass to low mass QIs increases with increasing scale in the lower panel similar to what is seen in the lower panel of Figure 7.1, though the effect is not quite as strong for the dim quasars. The middle panel shows the ratio of bright QI environment overdensities to dim QI environment overdensities for high mass and low mass targets. The scale-dependency seen here is consistent with our results for TIs in Chapter 5. That the ratios for the two mass bins have similar values at all scales is evidence that the effect of $L_{[\text{OIII}]}$ dominates M_{BH} in the relationship between the QI and its environment.

Again, we quantify the relationship of overdensity with M_{BH} and $L_{[\text{OIII}]}$ in Figure 7.4. Table 7.2 lists the linear least-squares fits for the two samples at four different scales. The brighter QIs show the dependency of increasing environment overdensity for increasing scale that was evident in Figure 7.2, but the dimmer QIs show a much less dramatic scale dependency, where the change in slope between scales of $2.0 h_{70}^{-1}$ Mpc to $150 h_{70}^{-1}$ kpc is only about 0.1 compared to 0.6 for the brighter QIs.

7.3 QI REDSHIFT

The redshift distributions of the high and low mass QI samples are approximately the same, thus we can conclude that the overdensity differences we have observed are not an effect of a systematic difference in the two samples. However, we now investigate whether those environment differences are an effect of redshift evolution. We divide each of the two mass bins into two redshift bins; the dividing redshift value of $z = 0.4$ gives roughly equal numbers of QIs in each redshift bin before dividing by mass. As shown in Figure 7.5, the redshift evolution is not strong for quasars with high- or low-mass black holes: on all scales the ratio of environment overdensity for higher redshift QIs to lower redshift QIs is consistent with unity (middle panel), which supports the redshift independence of the $M - \sigma$ relationship (e.g., Shields et al., 2003). However, in the lower panel, it is interesting to note that the overdensity ratio for high-mass QIs to low-mass QIs at low-redshifts increases slightly with increasing scale, while the high-redshift quasars have a high-mass to low-mass overdensity ratio that is consistent with unity for nearly all scales (see also Table 7.1).

7.4 ENVIRONMENT GALAXY TYPE

Finally, we explore the nature of the environment galaxies themselves. Figure 7.6 shows the environment overdensity of early- and late-type galaxies around QIs in the redshift range $0.11 \leq z \leq 0.4$ (note that the redshift range has been restricted as discussed in Section 3.3) divided into two mass bins. High mass QIs have a noticeably higher overdensity of early-type galaxies in their environments compared to low mass QIs. The early/late overdensity ratio increases with decreasing scale for high-mass quasars from a ratio value of 2.0 ± 0.4 (2.7σ) at $R \approx 2.0 h_{70}^{-1}$ Mpc to 2.6 ± 0.9 (1.6σ)

at $R \approx 150 h_{70}^{-1}$ kpc, but for low-mass quasars, this ratio is scale-independent (middle panel). In the lower panel, the high-mass to low-mass overdensity ratio for early-type galaxies remains scale independent with higher-mass QIs in an environment at $R \approx 500 h_{70}^{-1}$ kpc with 1.58 ± 0.33 times more early-type galaxies than the environment of lower-mass QIs (with significance 1.7σ). However, the late-type overdensity for high-mass QIs seems to increase compared to the late-type overdensity for low-mass QIs with increasing scale, though not with large statistical significance. Thus the increase in high mass/low mass ratio with increasing scale may be due to a slight change in late-type overdensity in the environments of QIs.

7.5 ACCRETION EFFICIENCY

Following Li et al. (2008), we use the ratio $L_{[\text{OIII}]} / M_{\text{BH}}$ as an indicator of the AGN accretion efficiency of the supermassive black hole at the center of the QI. We see no evolution of the distribution of $L_{[\text{OIII}]} / M_{\text{BH}}$ over our redshift range, and as before we apply a volume limit and use only QIs with $\log(L_{[\text{OIII}]} / L_{\odot}) \geq 8.0$

We first observe that the environment overdensities of high efficiency and low efficiency QIs are similar in Figure 7.7. The dividing value of $\log(L_{[\text{OIII}]} / M_{\text{BH}}) = 0.225$ is at the center of the distribution of efficiency ratios for the sample and gives approximately equal numbers of objects in each bin. If we use the calibration of $L_{\text{bol}} / L_{[\text{OIII}]} \approx 3500$ (Heckman et al., 2004), this ratio corresponds to the QI accreting at approximately 18% of the Eddington accretion rate (i.e., the rate at which the inward gravitational pull on infalling material balances the outward radiation pressure caused by the accretion process). On the outermost scales $R \gtrsim 500 h_{70}^{-1}$ kpc, however, it appears that lower efficiency QIs have an environment that is a slightly more overdense compared to the higher efficiency QIs. In Figure 7.8, we divide the accretion efficiency bins into two redshift bins at $z = 0.4$. We see that at all scales there is no significant evidence for redshift evolution (middle panel), and that the ratio of environment overdensities for high efficiency QIs to low efficiency QIs is consistent between the two redshift bins. Thus, any small amount of redshift evolution has negligible effect on environment overdensity when it is compared in terms of accretion efficiency. We tabulate the overdensity ratios of high efficiency to low efficiency QIs at scale $R \approx 500 h_{70}^{-1}$ kpc in Table 7.3.

The accretion efficiency as determined by $L_{[\text{OIII}]} / M_{\text{BH}}$ is high with bright $L_{[\text{OIII}]}$ or with low M_{BH} . In an attempt to isolate these conditions, we first divide the sample on $L_{[\text{OIII}]}$ and calculate the overdensities for high- and low-efficiency QIs in each $L_{[\text{OIII}]}$ bin, as is shown in Figure 7.9. Here we see that low-luminosity, high efficiency QIs have the highest environment overdensity. Brighter QIs have higher environment overdensity than dimmer QIs, whether they have high or low accretion efficiency (middle panel). This effect is scale dependent, increasing with decreasing scale, just as we saw in Section 5.2. Low-efficiency QIs have a slightly higher bright/dim overdensity ratio compared to high-efficiency QIs: at $R \approx 500 h_{70}^{-1}$ kpc, the bright/dim ratio for low (high) efficiency QIs is 1.41 ± 0.27 (1.18 ± 0.26) with significance $\approx 1.5\sigma$ ($< 1\sigma$). At all scales (and with no scale dependency), both bright and dim low-efficiency QIs have environments with slightly higher overdensity than high-efficiency QIs (lower panel).

Next, we divide the sample on M_{BH} and compare the overdensities around high- and low-efficiency QIs in Figure 7.10. At all scales, the overdensity ratio of high-efficiency to low-efficiency environments is consistent with unity regardless of mass (lower panel). However, there is evidence that

the environment of high-mass QIs compared to low-mass QIs increases with increasing scale (middle panel); this trend, too, is regardless of the efficiency category of the QI.

When we separate the background galaxies by type in Figure 7.11 (again restricting the sample to have $0.11 \leq z \leq 0.4$), we see that the early-type overdensity in the environments of both high- and low-efficiency QIs is consistent with unity on all scales except the largest measures, and here the early-type overdensity is slightly higher around low-efficiency QIs with a significance of $\approx 1.5\sigma$ (lower panel). The late-type overdensity ratio is also consistent with unity, though at the innermost scales, high-efficiency QIs may have an increased overdensity of late-type galaxies in their environments. On all scales, the ratios of early-type to late-type galaxies around high- and low-efficiency quasars are consistent within the error bars (middle panel). At $R \approx 500 h_{70}^{-1}$ kpc, the ratio around high-efficiency QIs is 1.98 ± 0.5 (significance of $\approx 2\sigma$), and the ratio around low-efficiency QIs is 2.51 ± 0.61 (significance of $\approx 2.5\sigma$).

7.6 CONCLUSIONS

We are not surprised to see that there is an increased overdensity of galaxies in the vicinity of more massive black holes. This result is consistent with the $M_{\text{DMH}} - M_{\text{BH}}$ relationship (e.g., Ferrarese & Merritt, 2000; Gebhardt et al., 2000; Tremaine et al., 2002) in which there is a correlation between the mass of a galaxy’s black hole and the mass of the dark matter halo containing the quasar’s host galaxy. Since clustering of halos increases with increasing halo mass, we see higher mass objects located in environments with higher galaxy density. The fact that we observe QIs with higher black hole mass in environments that are more overdense than those of their lower mass counterparts to larger radii may imply that QIs of different black hole mass are located in galaxy clusters of varying richness, where QIs with higher M_{BH} may be located in richer clusters with higher halo mass. Indeed, we see that the lower-mass QIs have an increased overdensity of late-type galaxies in their environments at smaller scales compared to the environments of higher-mass QIs. This could be the signature of the morphology-density relation seen in local clusters: regions of increased galaxy density have a higher fraction of early-type galaxies and a correspondingly decreased fraction of late-type galaxies (e.g., Dressler, 1980).

When we classify the QIs based on accretion efficiency using the ratio $L_{[\text{OIII}]} / M_{\text{BH}}$, we see that low-efficiency QIs have a slightly higher environment overdensity compared to high-efficiency QIs. This effect is likely due to quenching: outflows from the central engine of the QI heat the surrounding intergalactic medium (IGM), which prevents the IGM from condensing to form galaxies (Scannapieco & Oh, 2003). QIs with more efficient accretion will have more powerful outflows; therefore, the galaxy overdensity is decreased around these sources compared to their lower-efficiency counterparts.

Table 7.1: Ratio of high mass black hole environment galaxy overdensity to low mass black hole environment galaxy overdensity for QIs at scale $R \approx 500 h_{70}^{-1}$ kpc. Targets have $0.11 \leq z \leq 0.5$ and $\log(L_{[\text{OIII}]} / L_{\odot}) \geq 8.0$.

Sample	high/low	significance
QI	1.30 ± 0.186	1.61σ
QI, $\log(L_{[\text{OIII}]} / L_{\odot}) > 8.4$	1.37 ± 0.278	1.34σ
QI, $\log(L_{[\text{OIII}]} / L_{\odot}) \leq 8.4$	1.13 ± 0.246	$< 1\sigma$
QI, $z > 0.4$	1.03 ± 0.259	$< 1\sigma$
QI, $z \leq 0.4$	1.40 ± 0.242	1.65σ
QI, $z \leq 0.4$, early	1.58 ± 0.334	1.72σ
QI, $z \leq 0.4$, late	1.13 ± 0.323	$< 1\sigma$

Table 7.2: Linear least-squares fit parameters for overdensity vs. M_{BH} at four different scales using QIs with $\log(L_{[\text{OIII}]} / L_{\odot}) \geq 8.0$ (see also Figure 7.2 and Figure 7.4).

scale (h_{70}^{-1} Mpc)	slope	intercept	χ^2
All QIs			
2.0	0.052 ± 0.033	-0.278 ± 0.277	3.80
1.0	0.142 ± 0.052	-0.873 ± 0.429	2.70
0.5	0.156 ± 0.064	-0.656 ± 0.535	0.862
0.15	0.564 ± 0.074	-2.76 ± 0.616	0.053
QIs $\log(L_{[\text{OIII}]} / L_{\odot}) > 8.4$			
2.0	0.082 ± 0.042	-0.535 ± 0.357	3.12
1.0	0.173 ± 0.034	-1.12 ± 0.283	0.563
0.5	0.270 ± 0.004	-1.57 ± 0.037	0.002
0.15	0.657 ± 0.288	-3.25 ± 2.41	0.315
QIs $\log(L_{[\text{OIII}]} / L_{\odot}) \leq 8.4$			
2.0	0.030 ± 0.039	-0.088 ± 0.318	2.17
1.0	0.096 ± 0.091	-0.510 ± 0.746	3.67
0.5	-0.034 ± 0.145	0.845 ± 1.19	2.12
0.15	0.121 ± 0.179	0.560 ± 1.47	0.182

Table 7.3: Ratio of high efficiency environment galaxy overdensity to low efficiency environment galaxy overdensity for QIs at scale $R \approx 500 h_{70}^{-1}$ kpc. Targets have $0.11 \leq z \leq 0.5$ and $\log(L_{[\text{OIII}]} / L_{\odot}) \geq 8.0$.

Sample	highEff/lowEff	significance
QI	0.895 ± 0.127	$< 1\sigma$
QI, $\log(L_{[\text{OIII}]} / L_{\odot}) > 8.4$	0.778 ± 0.145	1.53σ
QI, $\log(L_{[\text{OIII}]} / L_{\odot}) \leq 8.4$	0.934 ± 0.212	$< 1\sigma$
QI, $\log(M_{\text{BH}} / M_{\odot}) > 8.25$	1.05 ± 0.230	$< 1\sigma$
QI, $\log(M_{\text{BH}} / M_{\odot}) \leq 8.25$	1.04 ± 0.270	$< 1\sigma$
QI, $z > 0.4$	0.886 ± 0.222	$< 1\sigma$
QI, $z \leq 0.4$	0.895 ± 0.154	$< 1\sigma$
QI, $z \leq 0.4$, early	0.819 ± 0.169	1.07σ
QI, $z \leq 0.4$, late	1.04 ± 0.295	$< 1\sigma$

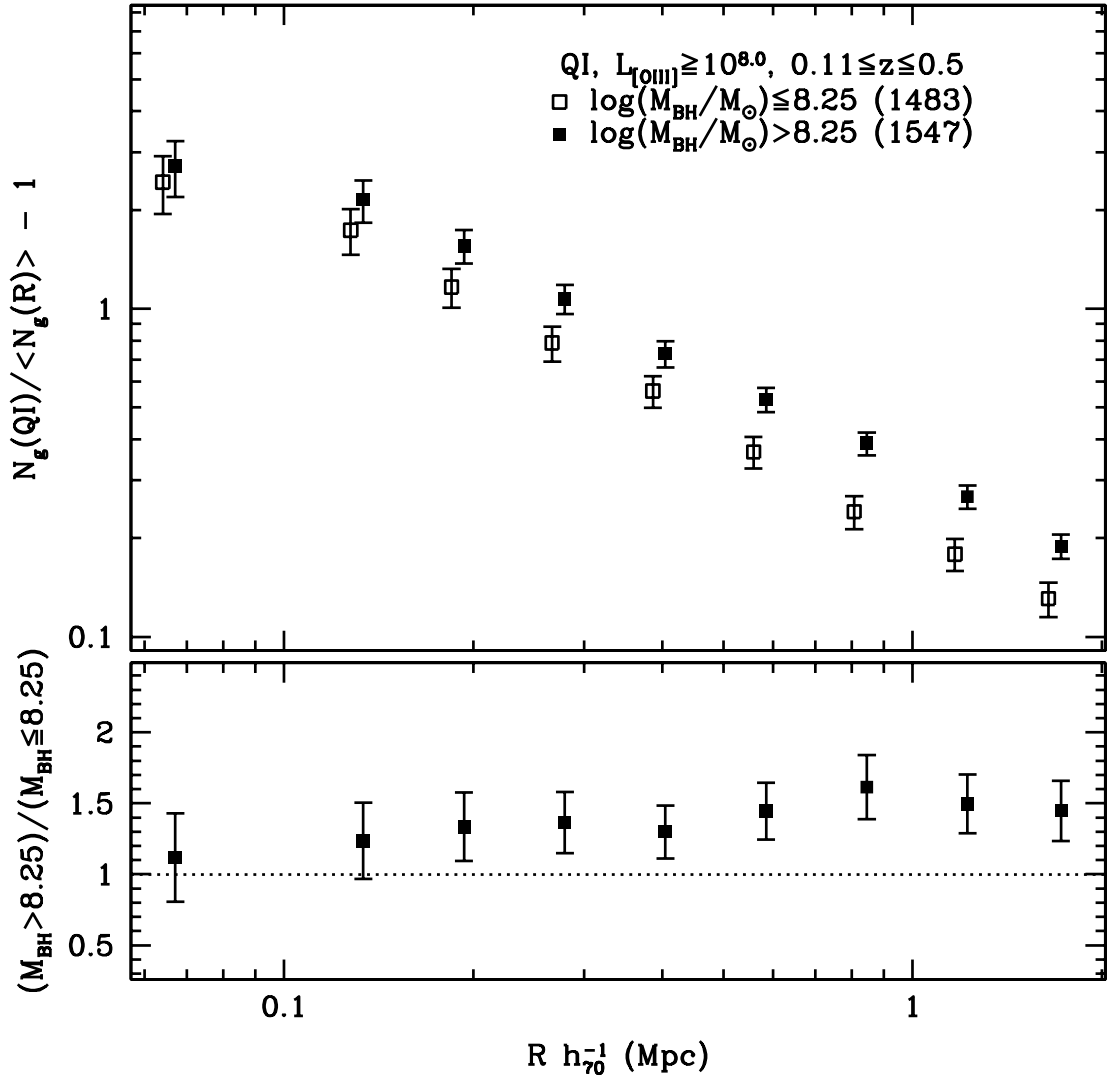


Figure 7.1— *Upper panel*: Mean cumulative overdensity vs. scale, M_{BH} for QIs with $\log(L_{[\text{OIII}]} / L_{\odot}) \geq 8.0$. *Lower panel*: Environment overdensity ratio for high mass QIs to low mass QIs.

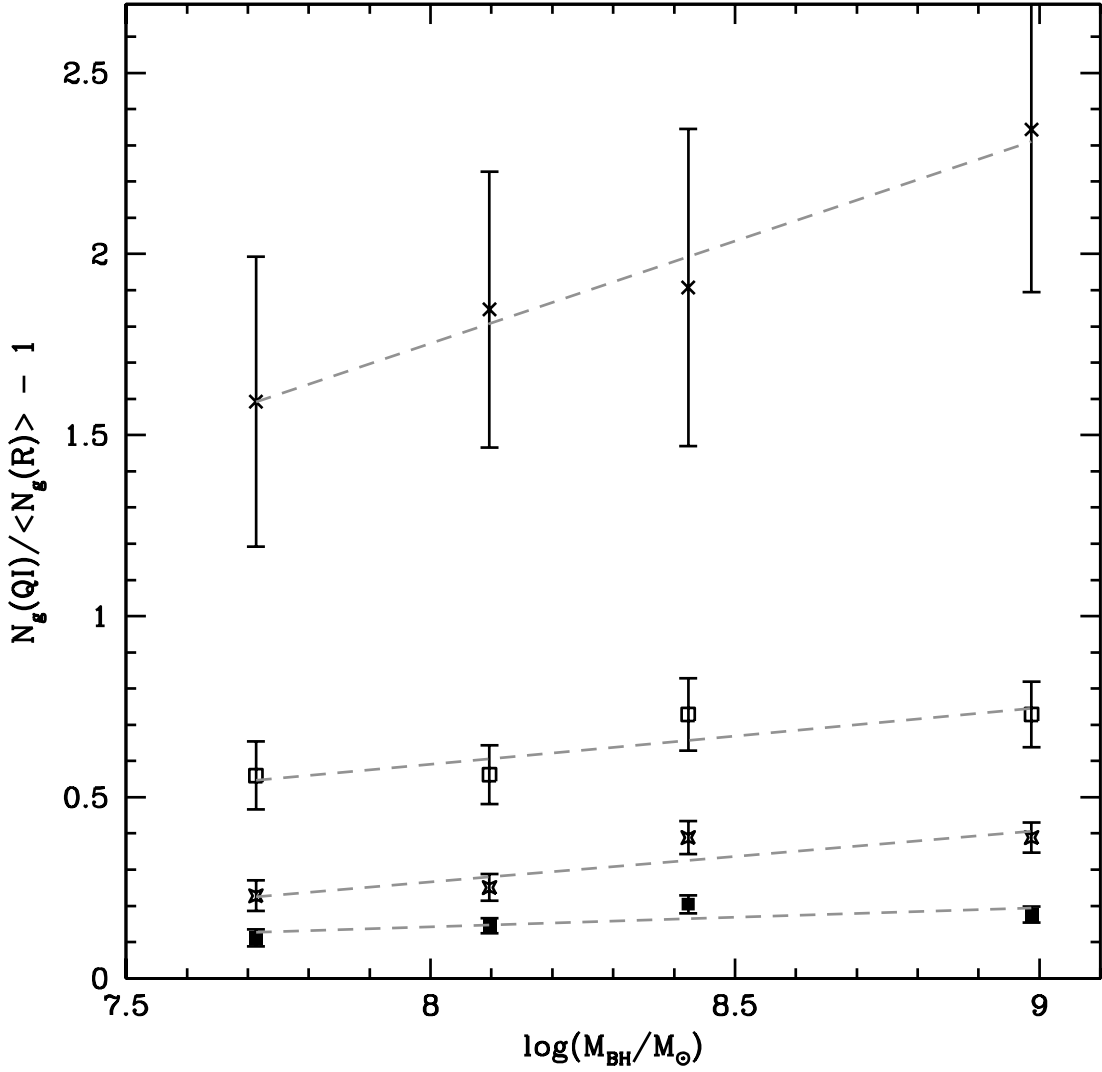


Figure 7.2— Mean cumulative environment overdensity vs. M_{BH} for QIs with $0.11 \leq z \leq 0.5$ and $\log(L_{[\text{OIII}]} / L_{\odot}) \geq 8.0$ at four scales: $R \approx 2 h_{70}^{-1}$ Mpc (solid squares), $R \approx 1 h_{70}^{-1}$ Mpc (starred squares), $R \approx 500 h_{70}^{-1}$ kpc (open squares), $R \approx 150 h_{70}^{-1}$ kpc (crosses). The linear least-squares fits to the combined target sample data for each of these scales are given by the dashed lines. The fit parameters are summarized in Table 7.2.

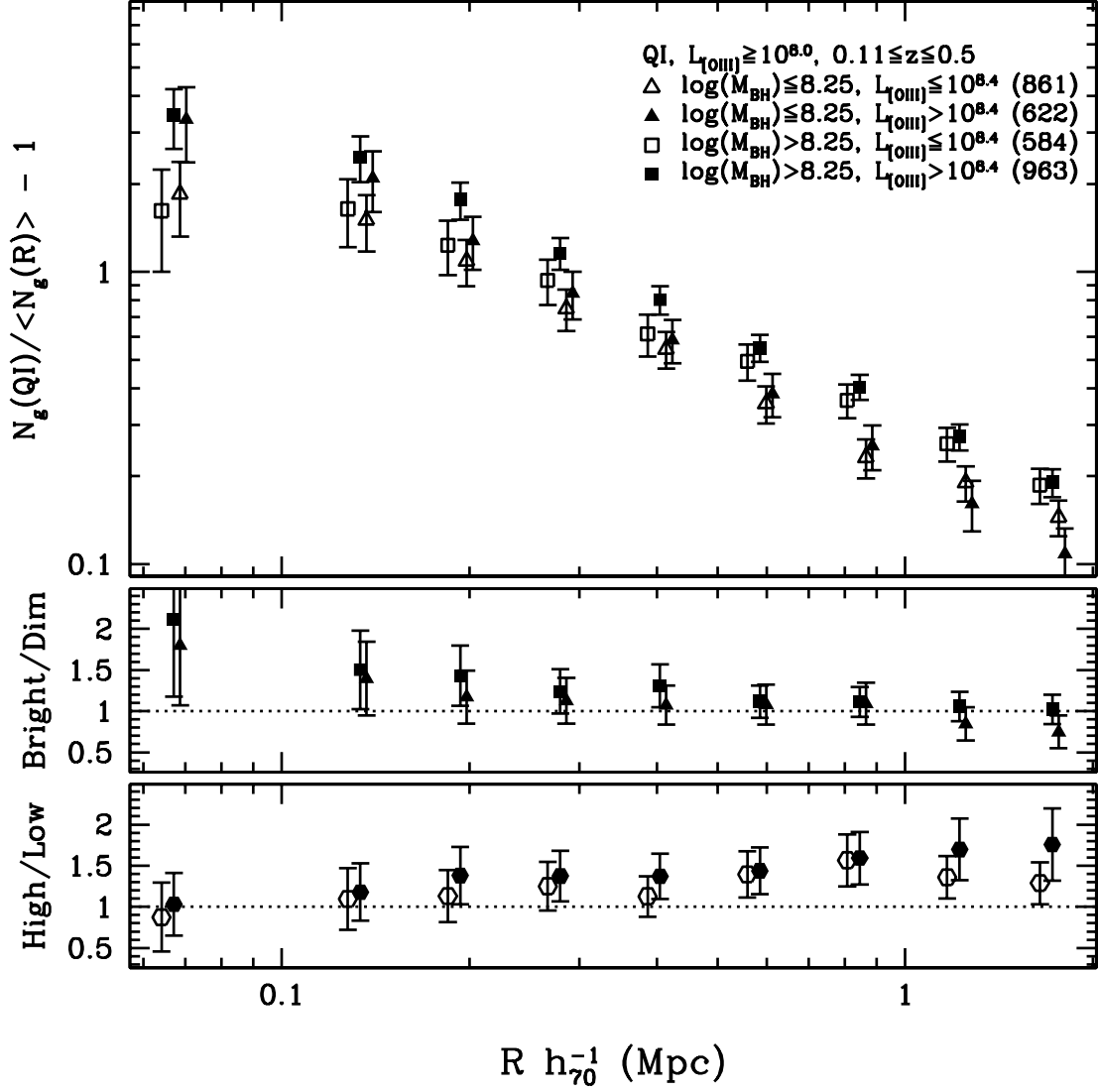


Figure 7.3— *Upper panel:* Mean cumulative overdensity vs. scale, M_{BH} and $L_{[\text{OIII}]}$ for QIs with $0.11 \leq z \leq 0.5$ and $\log(L_{[\text{OIII}]} / L_{\odot}) \geq 8.0$. *Middle panel:* Ratio of bright QI environment to dim QI environment for high mass (squares) and low mass (triangles) QIs. *Lower panel:* Ratio of high mass QI environment to low mass QI environment for bright (solid points) and dim (open points) QIs.

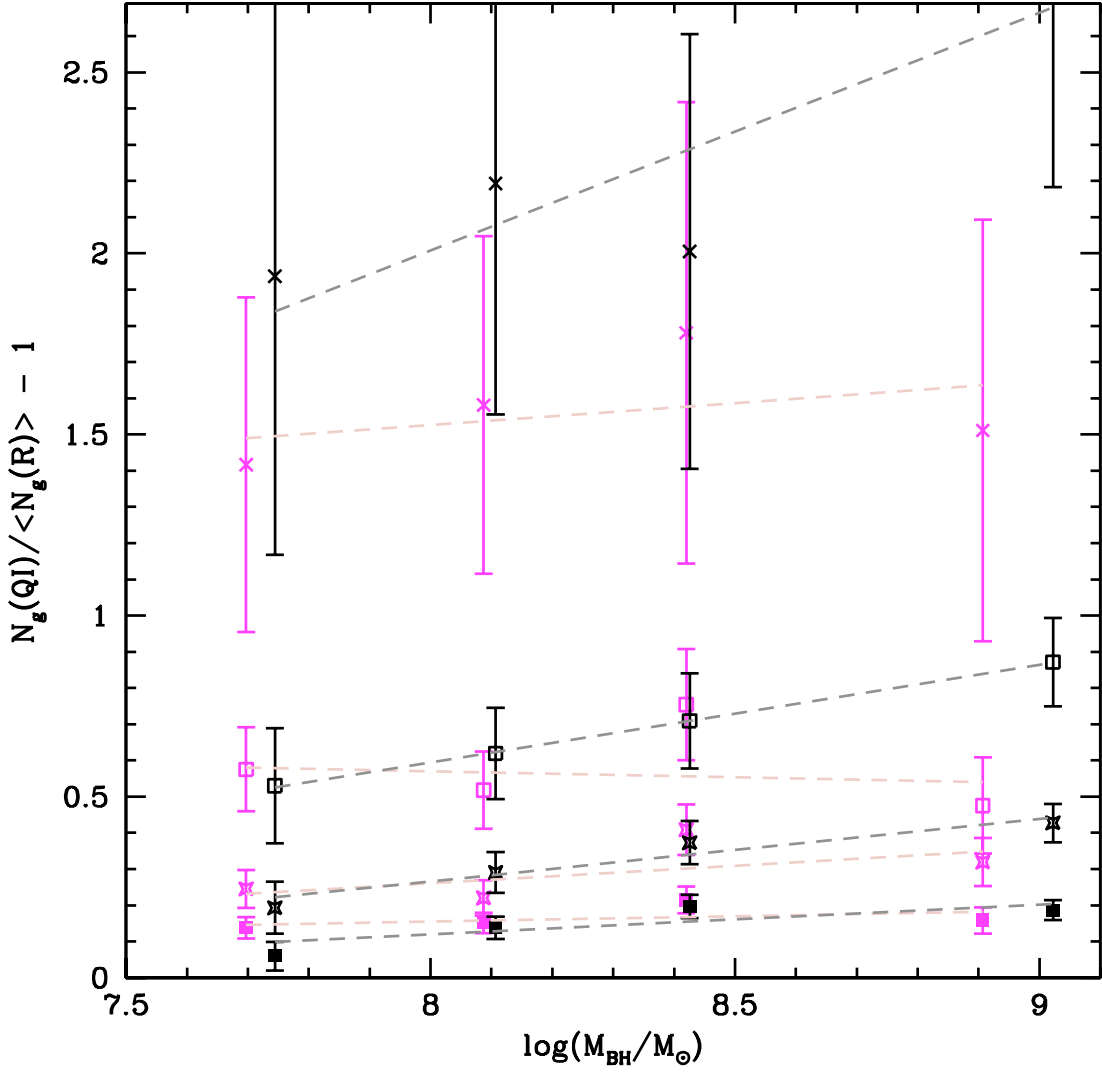


Figure 7.4— Mean cumulative environment overdensity vs. M_{BH} for bright (black points) and dim (magenta points) QIs with $0.11 \leq z \leq 0.5$ and $\log(L_{[\text{OIII}]} / L_{\odot}) \geq 8.0$ at four scales: $R \approx 2 h_{70}^{-1}$ Mpc (solid squares), $R \approx 1 h_{70}^{-1}$ Mpc (starred squares), $R \approx 500 h_{70}^{-1}$ kpc (open squares), $R \approx 150 h_{70}^{-1}$ kpc (crosses). The linear least-squares fits to the combined target sample data for each of these scales are given by the dashed lines. The fit parameters are summarized in Table 7.2.

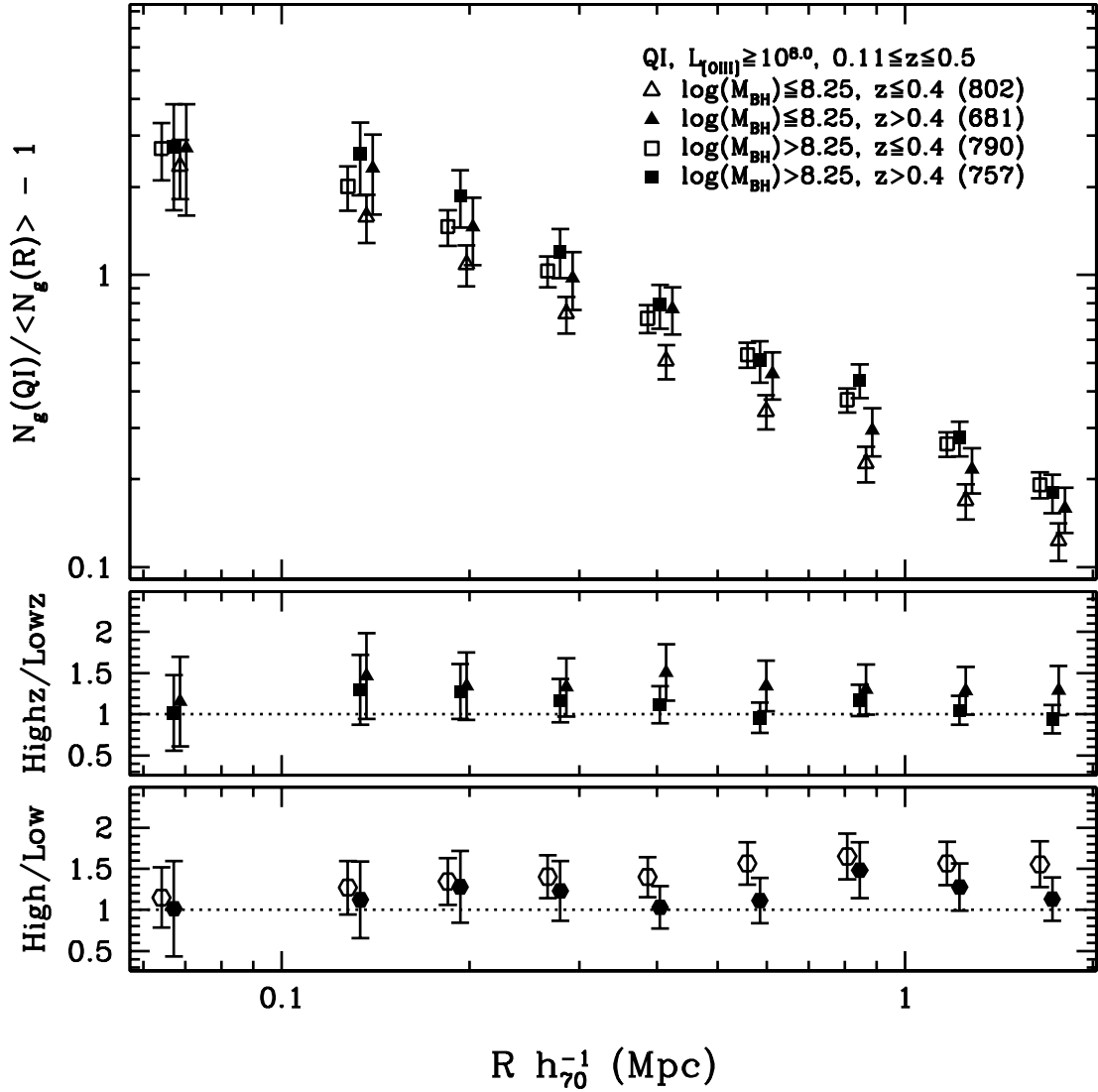


Figure 7.5— *Upper panel:* Mean cumulative overdensity vs. scale, M_{BH} and redshift for QIs with $0.11 \leq z \leq 0.5$ and $\log(L_{[\text{OIII}]} / L_{\odot}) \geq 8.0$. *Middle panel:* Ratio of high-redshift QI environment to low-redshift QI environment for high mass (squares) and low mass (triangles) QIs. *Lower panel:* Ratio of high mass QI environment to low mass QI environment for high-redshift (solid points) and low-redshift (open points) QIs.

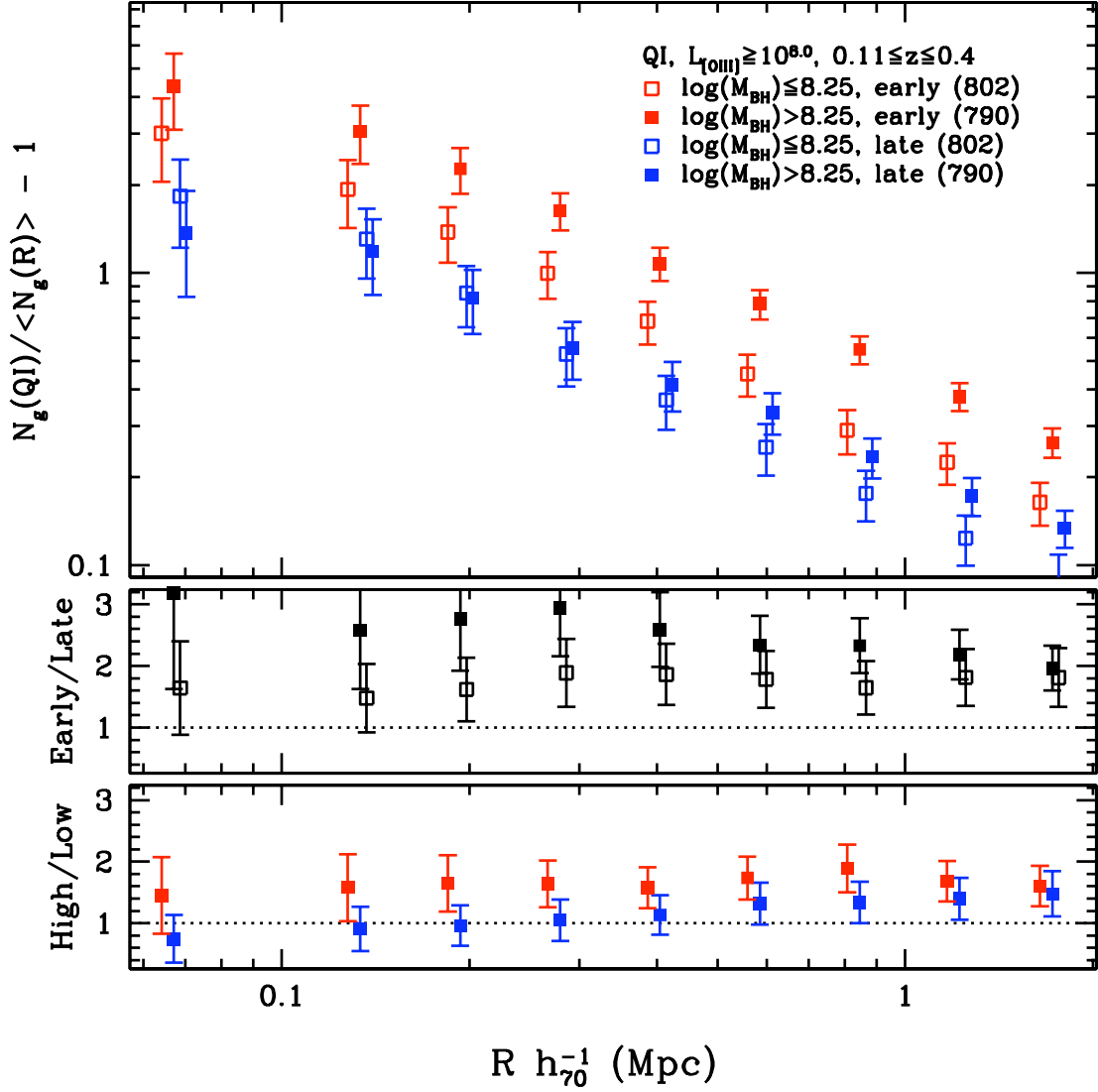


Figure 7.6— *Upper panel:* Mean cumulative overdensity vs. scale, M_{BH} and environment galaxy type for QIs with $0.11 \leq z \leq 0.4$ and $\log(L_{[\text{OIII}]} / L_{\odot}) \geq 8.0$. *Middle panel:* Ratio of early-type environment overdensity to late-type environment overdensity for high mass (solid) and low mass (open) QIs. *Lower panel:* Ratio of high mass QI environment to low mass QI environment for early-type (red) and late-type (blue) environments

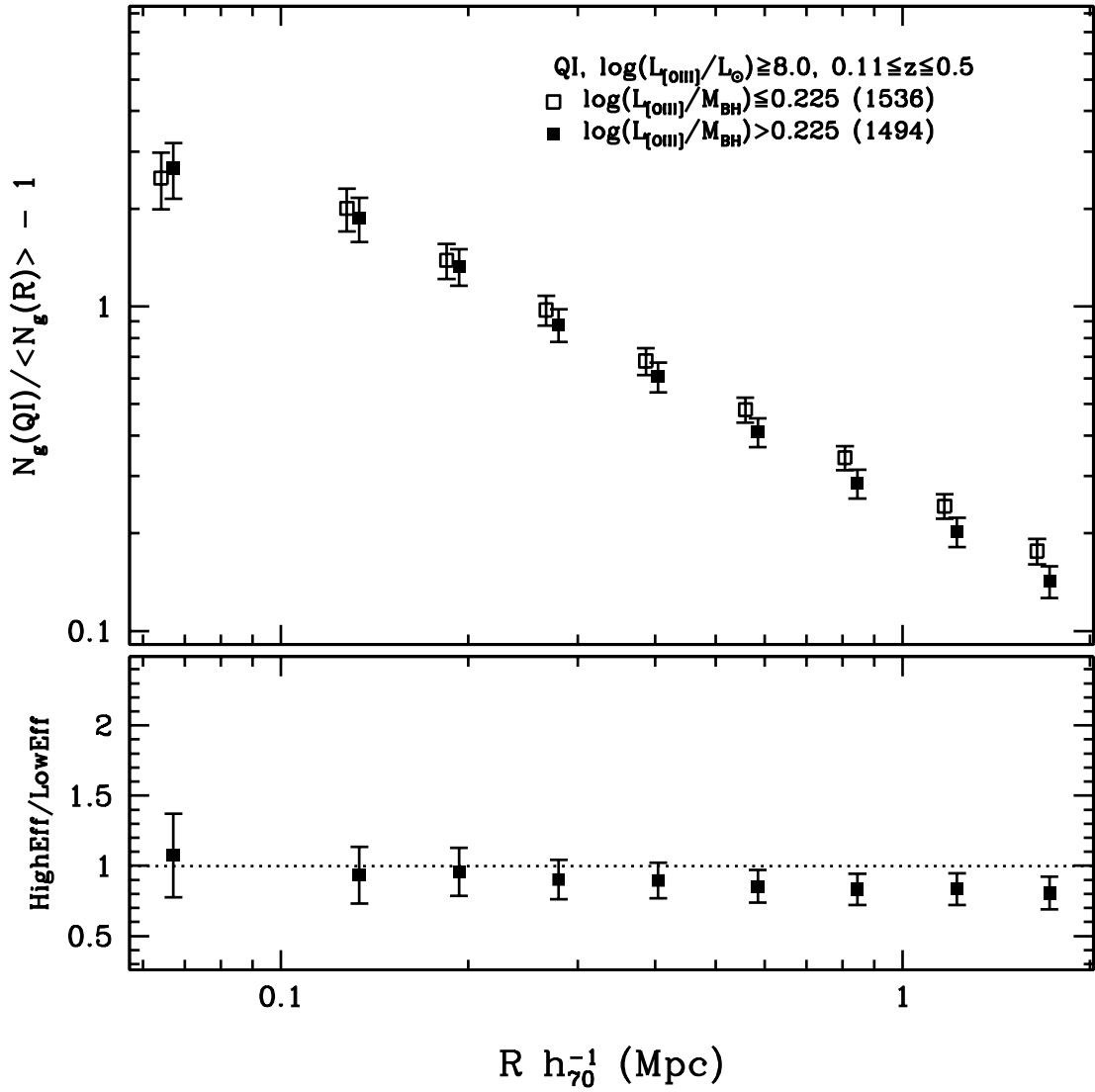


Figure 7.7— *Upper panel:* Mean cumulative overdensity vs. scale and $L_{[\text{OIII}]} / M_{\text{BH}}$ ratio for QIs with $\log(L_{[\text{OIII}]} / L_{\odot}) \geq 8.0$. *Lower panel:* Ratio of environment overdensity for higher efficiency QIs to the environment overdensity for lower efficiency QIs.

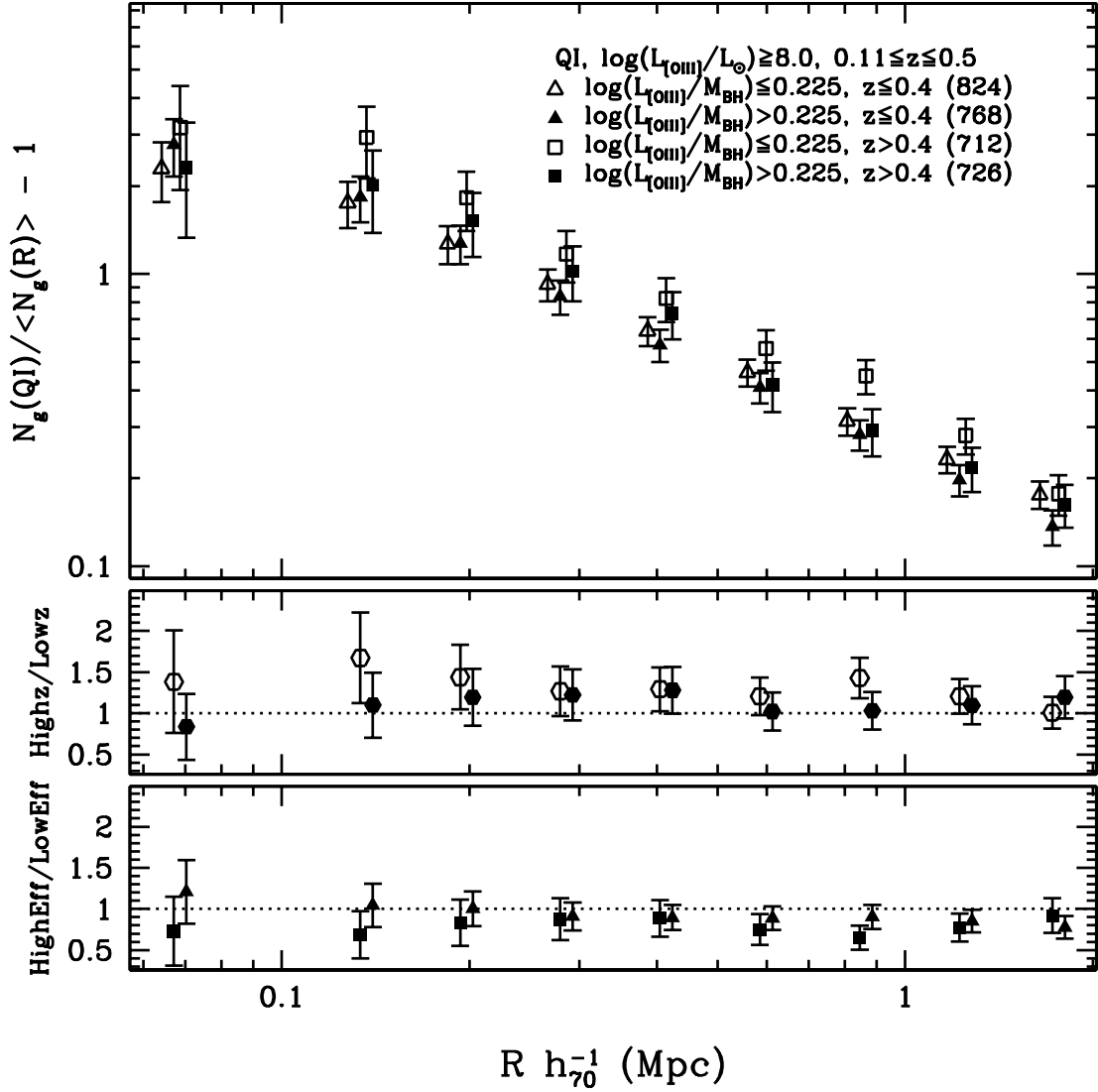


Figure 7.8— *Upper panel*: Mean cumulative overdensity vs. scale and $L_{[\text{OIII}]} / M_{\text{BH}}$ ratio for QIs with $\log(L_{[\text{OIII}]} / L_{\odot}) \geq 8.0$ in two different redshift bins. The dividing values are chosen for direct comparison to other figures. *Middle panel*: Ratio of environment overdensity of high redshift QIs to that of dim QIs for high efficiency (solid points) and low efficiency (open points) QIs. *Lower panel*: Ratio of high efficiency overdensity to low efficiency overdensity for high redshift (square) and low redshift (triangle) QIs.

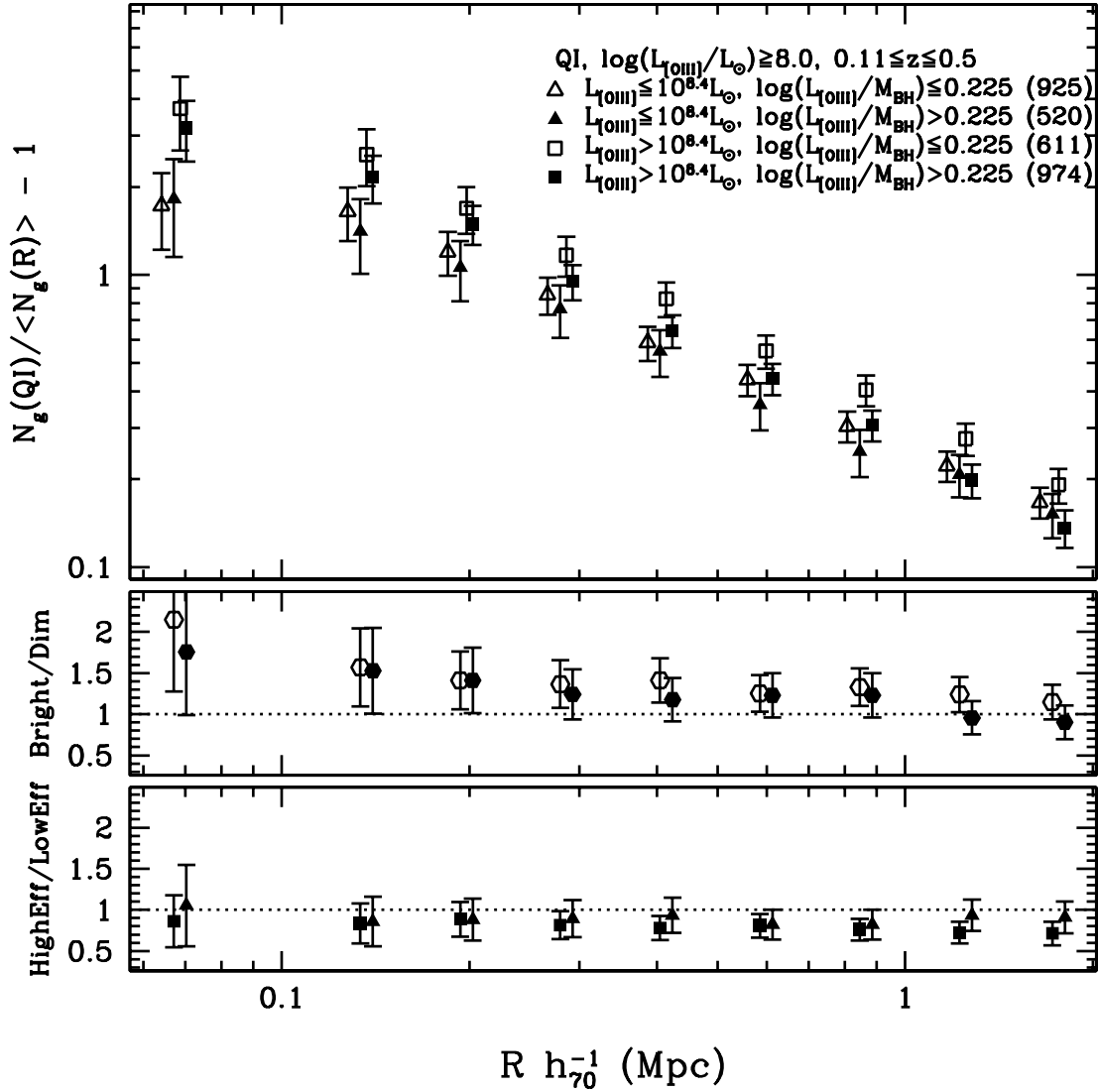


Figure 7.9— *Upper panel*: Mean cumulative overdensity vs. scale and $L_{[\text{OIII}]} / M_{\text{BH}}$ ratio for QIs with $\log(L_{[\text{OIII}]} / L_{\odot}) \geq 8.0$ in two different $L_{[\text{OIII}]}$ bins. The dividing values are chosen for direct comparison to other figures. *Middle panel*: Ratio of environment overdensity of bright QIs to that of dim QIs for high efficiency (solid points) and low efficiency (open points) QIs. *Lower panel*: Ratio of high efficiency overdensity to low efficiency overdensity for bright (square) and dim (triangle) QIs.

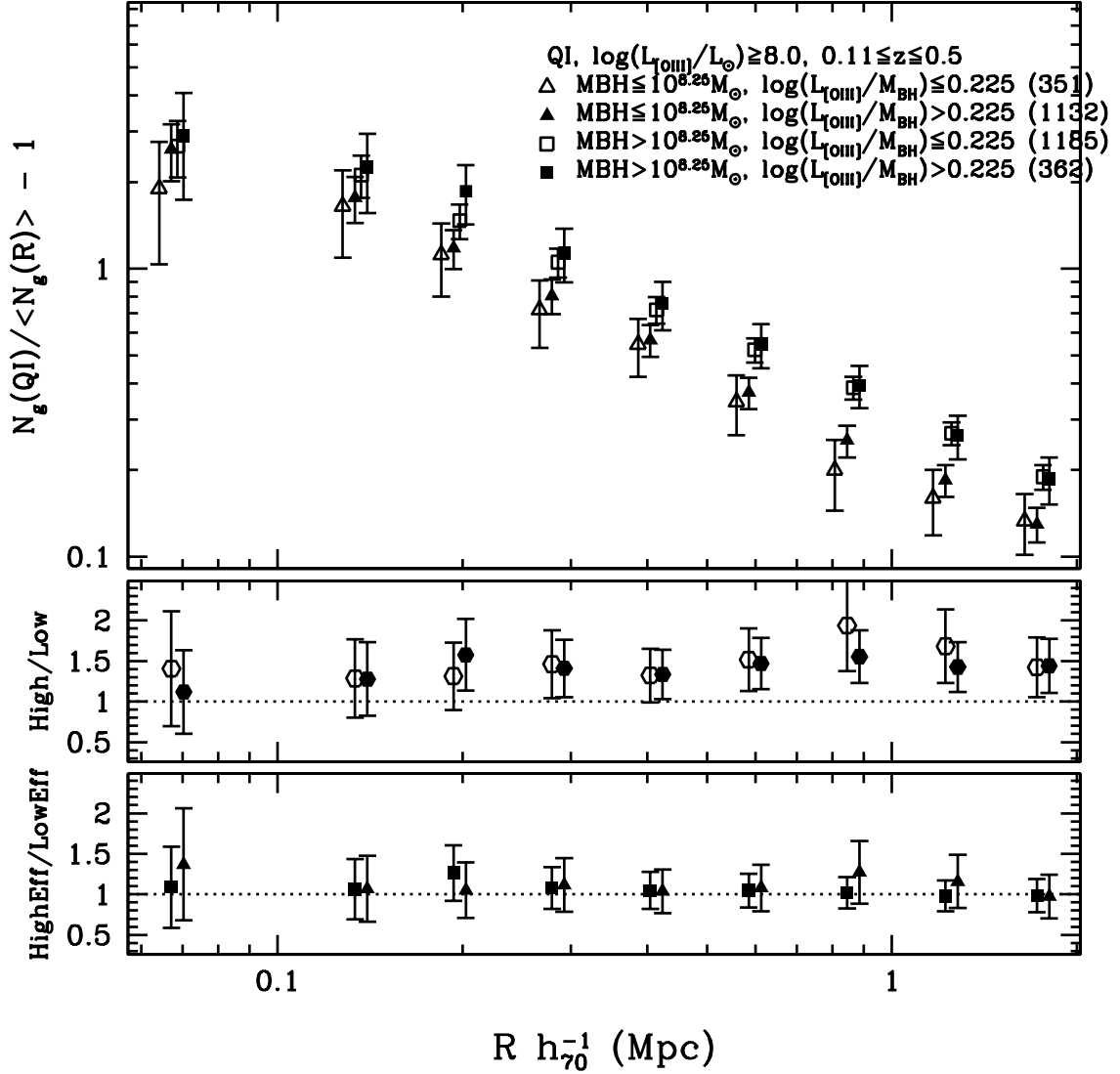


Figure 7.10— *Upper panel:* Mean cumulative overdensity vs. scale and $L_{[\text{OIII}]} / M_{\text{BH}}$ ratio for QIs with $\log(L_{[\text{OIII}]} / L_{\odot}) \geq 8.0$ in two M_{BH} bins. The dividing values are chosen for direct comparison to other figures. *Middle panel:* Ratio of environment overdensity of high-mass QIs to that of low-mass QIs for high efficiency (solid points) and low efficiency (open points) QIs. *Lower panel:* Ratio of high efficiency overdensity to low efficiency overdensity for high mass (square) and low mass (triangle) QIs.

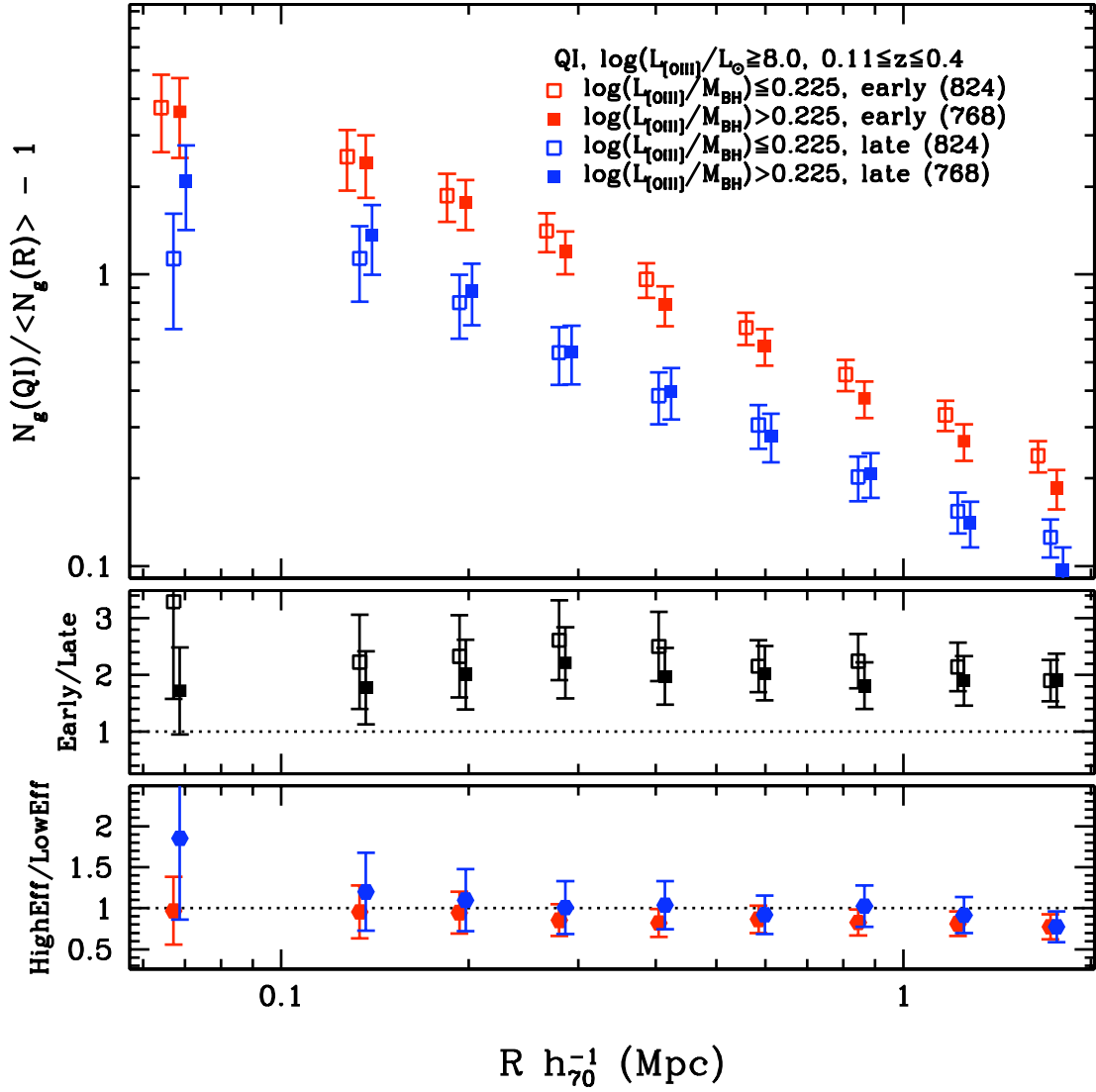


Figure 7.11— *Upper panel:* Mean cumulative overdensity vs. scale, $L_{\text{[OIII]}}/M_{\text{BH}}$ ratio, and environment galaxy type for QIs with $\log(L_{\text{[OIII]}}/L_{\odot}) \geq 8.0$ and $0.11 \leq z \leq 0.4$. *Middle panel:* Ratio of early-type environment overdensity to late-type environment overdensity for high efficiency (solid points) and low efficiency (open points) QIs. *Lower panel:* Ratio of high efficiency overdensity to low efficiency overdensity using early-type environments (red) and late type environments (blue) of QIs.

Chapter 8

The Dependence on Multiwavelength Properties

8.1 OVERVIEW

By investigating the environment overdensity of QIs with different multiwavelength properties, we can begin to determine whether the local environment of QIs is related to the conditions that produce radio or X-ray emission in quasars. In this chapter, we take advantage of the radio and X-ray information that has been cross-matched to QIs in the DR5 catalog (Schneider et al., 2007).

X-ray emission from quasars is tied to the process of material being accreted onto the central black hole. Thus, X-ray emission originates close to the black hole, and QIs with high X-ray luminosity must have enough material at hand to support the voracious accretion of their central sources. Radio emission can originate from the accretion process as well. But more often, radio emission is associated with synchrotron emission from jets produced by material thrown off from the accretion disk, collimated by magnetic field lines twisted by the rotation of the accretion disk. Radio emission in these lobes can extend far from the central source, even to Mpc scales (e.g., 3C 236; Willis & Strom, 1978), and therefore we should expect to see its influence on the local environment (e.g., Croton et al., 2006). Additionally, due to the geometry of radio jets, the orientation at which the quasar is observed will influence the radio-loudness measured.

8.2 RADIO QUASARS

The DR5 quasar catalog reports the FIRST peak flux density at 20 cm as an AB magnitude. The peak flux density is given by (Ivezic et al., 2002)

$$f_\nu = (3631 \text{ Jy}) \cdot 10^{\frac{ABmag}{-2.5}} \quad (8.1)$$

Then the luminosity density is calculated using

$$L_{2cm} = f_\nu \cdot \frac{4\pi \cdot D_L^2}{1+z} = f_\nu \cdot 4\pi \cdot (1+z) D_M^2 \quad (8.2)$$

Figure 8.1 shows the radio luminosity density and redshift distributions of the QI sample with $0.11 \leq z \leq 0.5$. In order to ensure that our samples are consistent, we first limit both the radio-detected and radio-undetected samples to $L_{[\text{OIII}]}$ limit of $\log(L_{[\text{OIII}]} / L_\odot) \geq 8.0$ (yellow dashed line in the lower left panel). The obvious flux limit in lower right panel necessitates a volume-limit in radio luminosity. Our limit of $\log(L_{2cm}) \geq 30.8$ (shown by the red dashed lines in the upper left and lower right panels) corresponds to the flux limit of the FIRST survey (Ivezic et al., 2002) at $z = 0.5$. The

final radio QI sample contains 215 sources, and the corresponding radio-undetected sample contains 2,569 QIs.

Figure 8.2 compares the overdensity of radio detected QIs to undetected QIs that are located in the FIRST survey area. In addition, overdensity values for these two samples are compared to the overdensity value for the entire QI sample combined at scale $R \approx 500 h_{70}^{-1}$ kpc in Table 8.1. We see very slightly increased overdensity for radio detected QIs compared to undetected QIs with significance $\gtrsim 1\sigma$ only at scales $R \gtrsim 1.0 h_{70}^{-1}$ Mpc; at $R \approx 1.0 h_{70}^{-1}$ Mpc, the ratio of overdensity in the environment of radio-detected QIs to that in the environment of radio-undetected QIs is 1.37 ± 0.29 (significance 1.3σ).

Although the error bars in Figure 8.3 are very large, we do see clear evidence that the radio detected QIs have a higher overdensity of early-type environment galaxies (at $R \approx 500 h_{70}^{-1}$ kpc, overdensity = 1.23 ± 0.418) and a lower overdensity of late-type environment galaxies (overdensity = 0.143 ± 0.194) compared to the environments of QIs without radio detection (at the same scale, early- and late-type overdensities for undetected QIs are 0.890 ± 0.101 and 0.424 ± 0.063 , respectively). The higher incidence of early-type galaxies in the environments of radio-loud QIs supports the theory that they are located in richer cluster environments (e.g., Ellingson et al., 1991; Wold et al., 2000; McLure & Dunlop, 2001; Best, 2004).

8.3 X-RAY QUASARS

The DR5 quasar catalog contains the logarithm of the ROSAT All-Sky Survey (RASS) count rate (photons s^{-1}) in the broad band (0.1 - 2.4 keV) for each object. This count rate must be converted into rest-frame luminosity density for our analysis.

We use the PIMMS (v3.9b) software to determine the observed flux $f_{0.1-2.4keV}$ from the count rate in the 0.1 - 2.4 keV band with $\Gamma = 2.0$, $\alpha = -1.0$ and the corresponding nH (also given in the DR5 quasar catalog) for each object (Vignali et al., 2003).

Once the flux is calculated for the 0.1 - 2.4 keV band, we calculate the flux density at 2 keV f_{2keV} again using $\alpha = -1.0$:

$$f_{2keV} = f_{0.1-2.4keV} \cdot \frac{\nu_{2keV}^\alpha}{(\log(\nu_{2.4keV}) - \log(\nu_{0.1keV}))} \quad (8.3)$$

We calculate the rest frame luminosity density L_{2keV} from f_{2keV} as follows:

$$L_{2keV} = \frac{f_{2keV} \cdot 4\pi \cdot D_L^2}{(1+z)} = f_{2keV} \cdot 4\pi \cdot (1+z) D_M^2 \quad (8.4)$$

where D_L is the luminosity distance and D_M is the transverse comoving distance.

Figure 8.4 shows the X-ray luminosity density and redshift distribution of the QI quasar sample with $0.11 \leq z \leq 0.5$. Again, we impose a lower $L_{[OIII]}$ limit of $\log(L_{[OIII]}/L_\odot) \geq 8.0$ on both the X-ray detected and X-ray undetected samples. Based on the minimum count rate required for inclusion in the RASS (e.g. Voges et al., 1999), also we impose a lower luminosity density limit of $\log(L_{2keV}) \geq 25.7$ for a volume-limited X-ray QI sample. There are 682 X-ray detected QIs and 2,168 X-ray undetected QIs in our final samples.

We compare the environment overdensity of X-ray detected QIs and non-detected QIs in Fig-

ure 8.5. At all scales, X-ray detected QIs are located in environments slightly more overdense than non-detected QIs (1.34 ± 0.21 times more overdense with significance 1.62σ at $R \approx 500 h_{70}^{-1}$ kpc). As shown in Figure 8.6, there does not appear to be strong redshift evolution of the X-ray detected QI environments, since the ratio of high-redshift X-ray QI overdensity to low-redshift X-ray QI overdensity is consistent with unity on all scales. We note that there is again evidence for slight redshift evolution in the X-ray undetected QIs, similar to that seen in Chapter 4.

The X-ray detected and undetected samples are divided into two bins by [OIII] luminosity at $\log(L_{[\text{OIII}]} / L_{\odot}) = 8.4$, the value used in all previous figures. We plot overdensity vs. scale and $L_{[\text{OIII}]}$ for these samples in Figure 8.7. We see that although the X-ray detected QIs have slightly higher overdensities at all scales than the undetected QIs (which is consistent with Figure 8.5), the ratio of [OIII] bright QIs to [OIII] dim QIs is about the same within the error bars for both the X-ray detected and undetected samples.

In Figure 8.8 we plot mean cumulative overdensity vs. scale for two bins in X-ray luminosity density. The mean cumulative overdensity around quasars with no RASS detection is plotted in gray for comparison. The dividing L_{2keV} value is chosen because it gives approximately equal numbers of X-ray QIs in each bin. On all scales, the brightest X-ray QIs have the highest environment overdensity, though the result is not statistically significant; at $R \approx 500 h_{70}^{-1}$ kpc, the ratio of overdensity for X-ray bright QIs to X-ray dim QIs is 1.26 ± 0.320 , with significance $< 1\sigma$. However, the overdensities of both X-ray QI samples are higher than the X-ray undetected QI overdensities on most scales. The brightest X-ray QIs have an overdensity 1.52 ± 0.301 times the overdensity of the undetected QIs with a significance 1.7σ at the scale $R \approx 500 h_{70}^{-1}$ kpc.

Finally, Figure 8.9 shows the early-type and late-type galaxy overdensity around X-ray detected and undetected QIs. In Table 8.1, we compare overdensity values at scale $R \approx 500 h_{70}^{-1}$ kpc for X-ray detected QIs to X-ray undetected QIs. Although the overdensity values for both early- and late-type environment galaxies are higher on all scales for X-ray detected QIs, it appears that the early- to late-type environment overdensity ratio is about the same and is scale-independent within the error bars.

8.4 CONCLUSIONS

We have shown some evidence for increased overdensity around radio QIs, but larger samples are required for greater statistical significance. We cannot make strong claims about the relationship between radio QIs and their environments due to our lack of knowledge of their radio morphology. This morphology information could allow us to differentiate radio emission due to accretion from radio emission due to jet activity.

The fact that QIs with higher X-ray luminosity are shown to have more densely populated environments is not surprising, given our previous results showing that TIs with bright $L_{[\text{OIII}]}$ are in the most overdense environments, since [OIII] $\lambda 5007$ emission line luminosity and hard ($2 - 10\text{KeV}$) X-ray luminosity have been shown to be strongly correlated (Heckman et al., 2005). We reiterate the need for larger samples of X-ray QIs in order to draw stronger conclusions about their relationship with their environments.

Table 8.1: Comparison of environment overdensity for various samples of QIs with $\log(L_{[\text{OIII}]} / L_{\odot}) \geq 8.0$ at scale $R \approx 500 h_{70}^{-1}$ kpc.

Sample	$z \leq 0.5$	$z \leq 0.4$, early	$z \leq 0.4$, late
all QI	0.644 ± 0.045	0.877 ± 0.090	0.391 ± 0.056
radio QI	0.706 ± 0.182	1.23 ± 0.418	0.143 ± 0.194
no radio QI	0.659 ± 0.051	0.890 ± 0.101	0.424 ± 0.063
X-ray QI	0.803 ± 0.102	1.22 ± 0.214	0.453 ± 0.118
no X-ray QI	0.599 ± 0.055	0.788 ± 0.109	0.354 ± 0.069

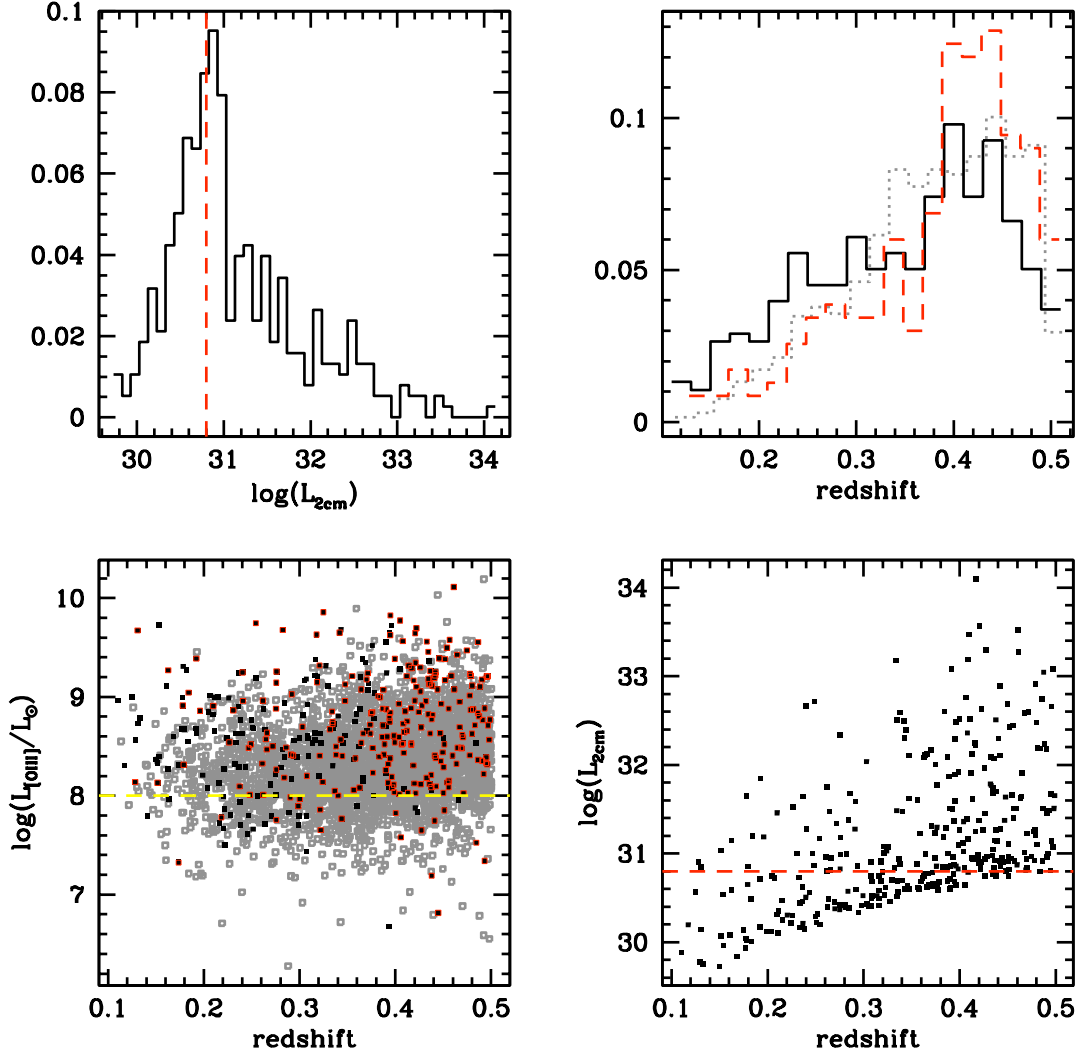


Figure 8.1— *Upper left*: distribution of radio luminosity for 378 QIs with FIRST detection and $0.11 \leq z \leq 0.5$. The dashed red line shows the radio luminosity volume-limit cutoff. *Upper right*: redshift distribution for 378 QIs with FIRST detection (solid black line) and 3253 QIs with no FIRST detection, but that are still in the FIRST survey area (dotted black line). The redshift distribution of the “volume-limited” sample, with $\log(L_{2cm}) \geq 30.8$ is shown with the dashed red line; 215 QIs. *Lower left*: $L_{[\text{OIII}]}$ vs. redshift for radio undetected QIs (grey); radio detected QIs (black), where those objects satisfying the radio volume-limit are outlined in red. The yellow dashed line shows the $L_{[\text{OIII}]}$ volume-limit that is applied. *Lower right*: Radio luminosity as a function of redshift for QIs with FIRST detection with $\log(L_{[\text{OIII}]} / L_{\odot}) \geq 8.0$. The dashed red line shows the radio luminosity volume-limit cutoff.

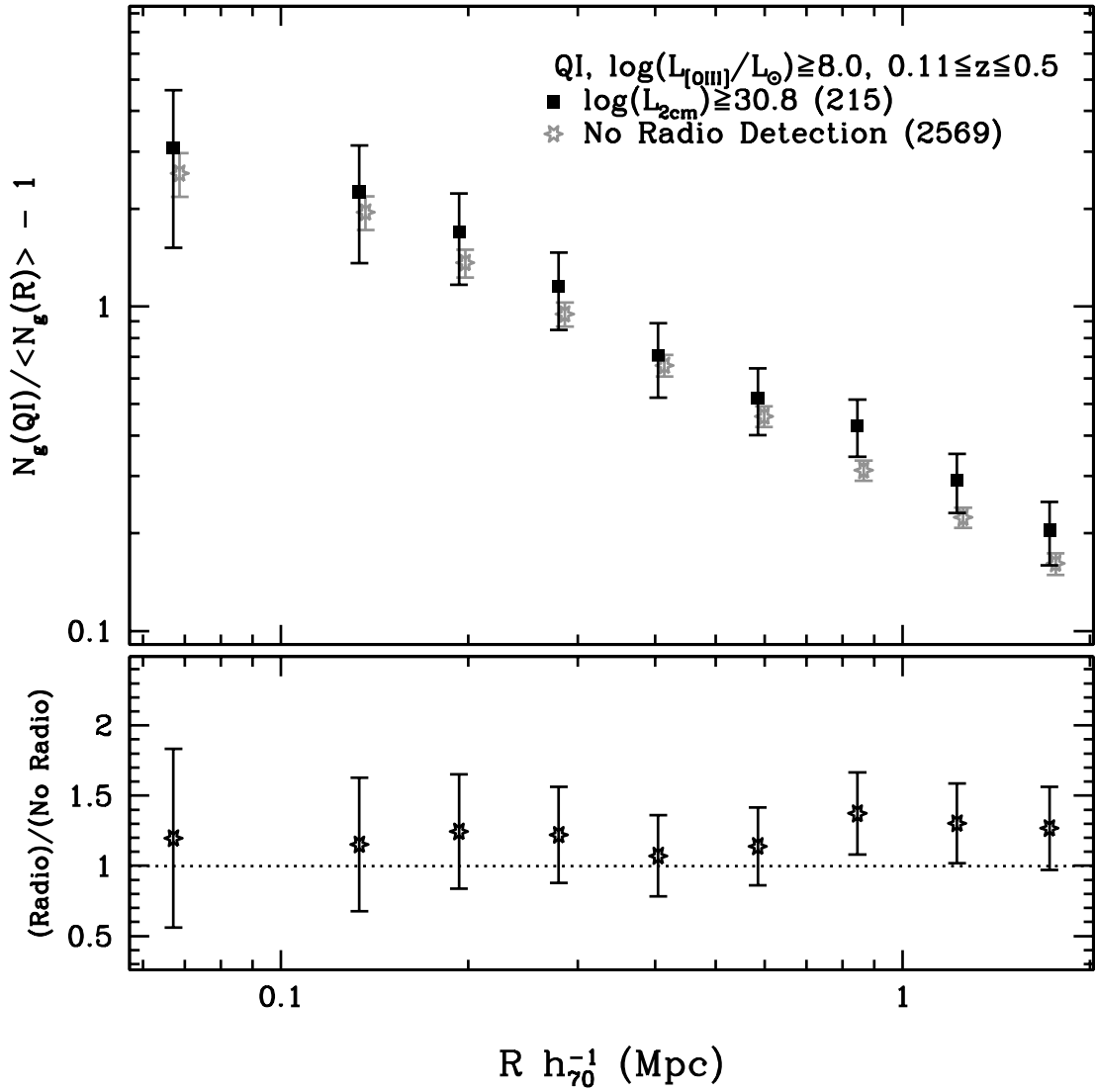


Figure 8.2— *Upper panel:* Mean cumulative overdensity vs. scale for $\log(L_{[\text{OIII}]}) \geq 8.0$ and $0.11 \leq z \leq 0.5$ QIs with and without detections in FIRST (radio detected QIs have $\log(L_{2\text{cm}}) \geq 30.8$). *Lower panel:* Overdensity ratio of FIRST-detected QIs to undetected QIs.

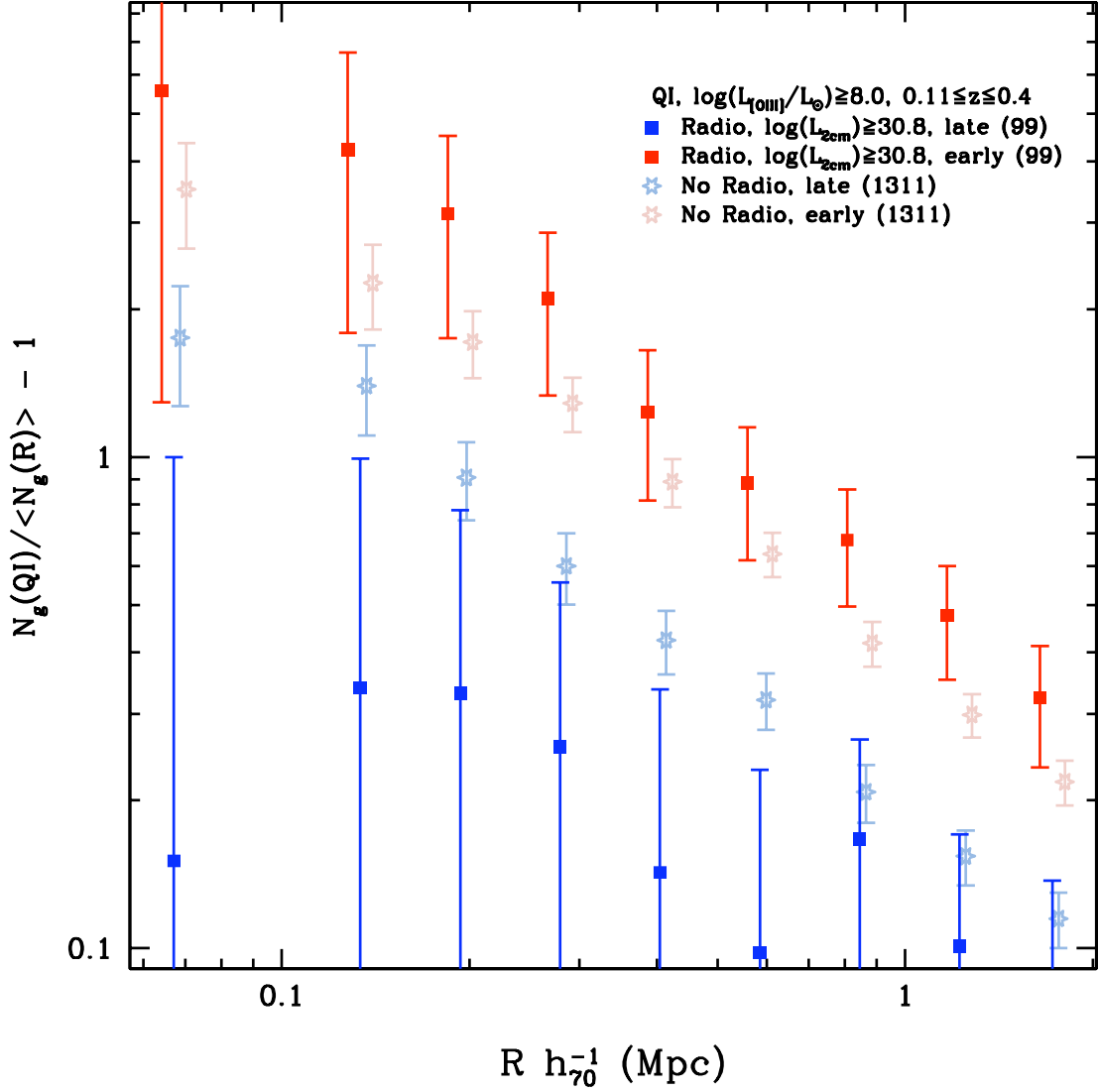


Figure 8.3— Mean cumulative overdensity vs. scale and environment galaxy type for $\log(L_{\text{[OIII]}}/L_{\odot}) \geq 8.0$ and $0.11 \leq z \leq 0.4$ QIs with and without detections in FIRST (radio detected QIs have $\log(L_{2\text{cm}}) \geq 30.8$).

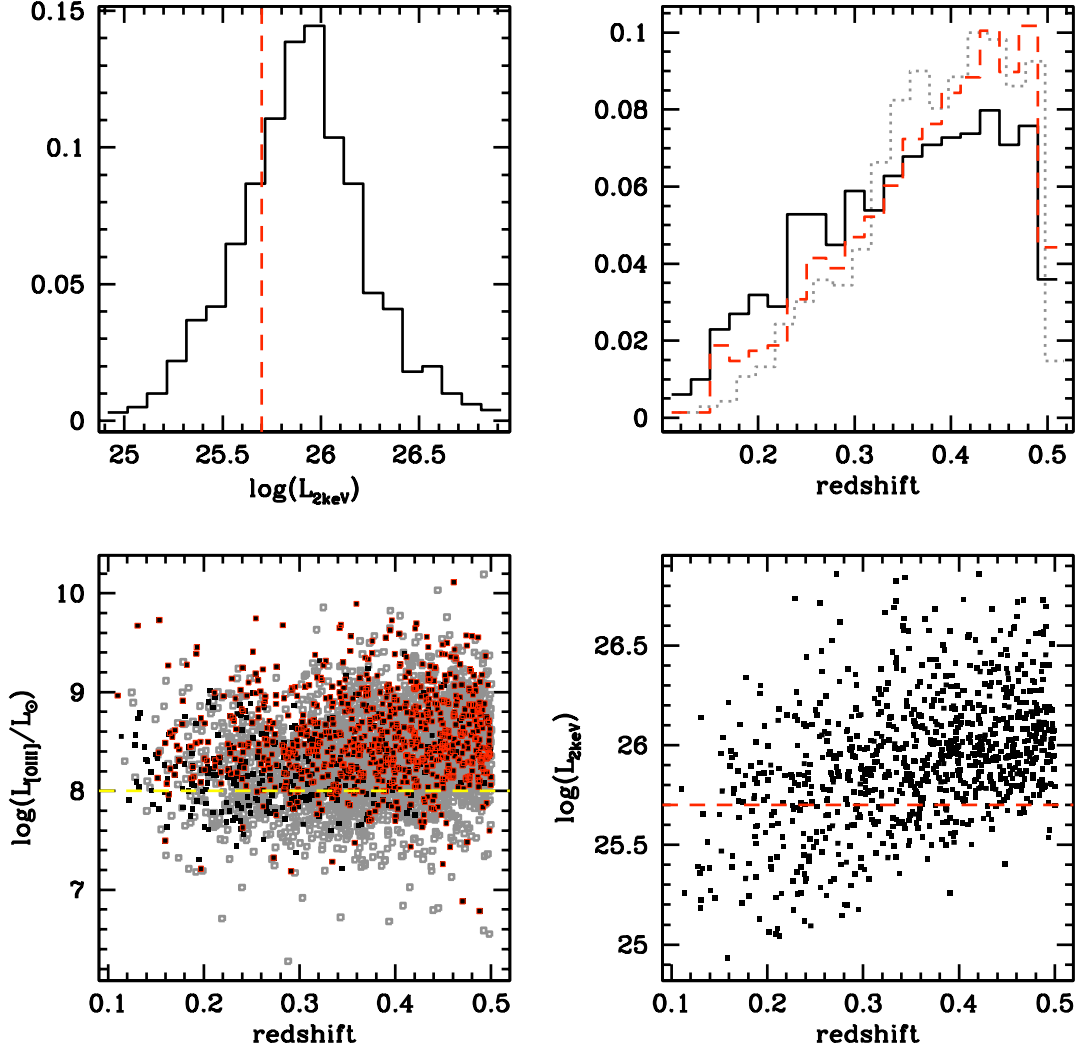


Figure 8.4— *Upper left*: distribution of X-ray luminosity for 1003 QIIs with RASS detection and $0.11 \leq z \leq 0.5$. The dashed red line shows the X-ray luminosity volume-limit cutoff. *Upper right*: redshift distribution for 1003 QIIs with RASS detection (solid black line) and 2790 QIIs with no RASS detection (dotted black line). The redshift distribution of the “volume-limited” sample, with $\log(L_{2\text{keV}}) \geq 25.7$ is shown with the dashed red line; 747 QIIs. *Lower left*: $L_{\text{[OIII]}}$ vs. redshift for X-ray undetected QIIs (grey); X-ray detected QIIs (black), where those objects satisfying the X-ray volume-limit are outlined in red. The yellow dashed line shows the $L_{\text{[OIII]}}$ volume-limit that is applied. *Lower right*: X-ray luminosity as a function of redshift for QIIs with RASS detection and $\log(L_{\text{[OIII]}}/L_{\odot}) \geq 8.0$. The dashed red line shows the X-ray luminosity volume-limit cutoff.

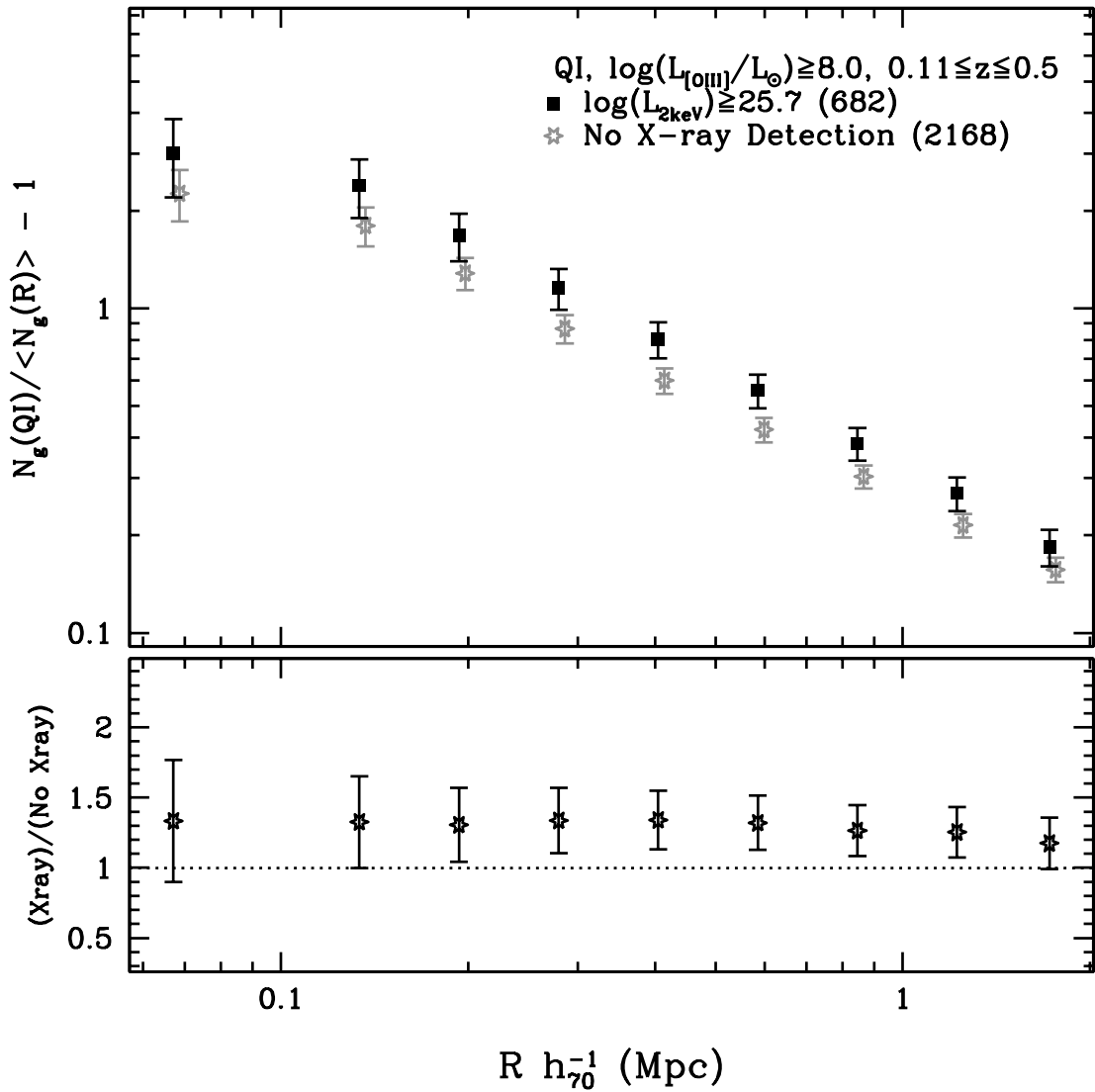


Figure 8.5— *Upper panel:* Mean cumulative overdensity vs. scale for $\log(L_{[\text{OIII}]} / L_{\odot}) \geq 8.0$ and $0.11 \leq z \leq 0.5$ QIs with and without detections in RASS (X-ray detected QIs have $\log(L_{2\text{keV}}) \geq 25.7$). *Lower panel:* Overdensity ratio of RASS-detected QIs to undetected quasars.

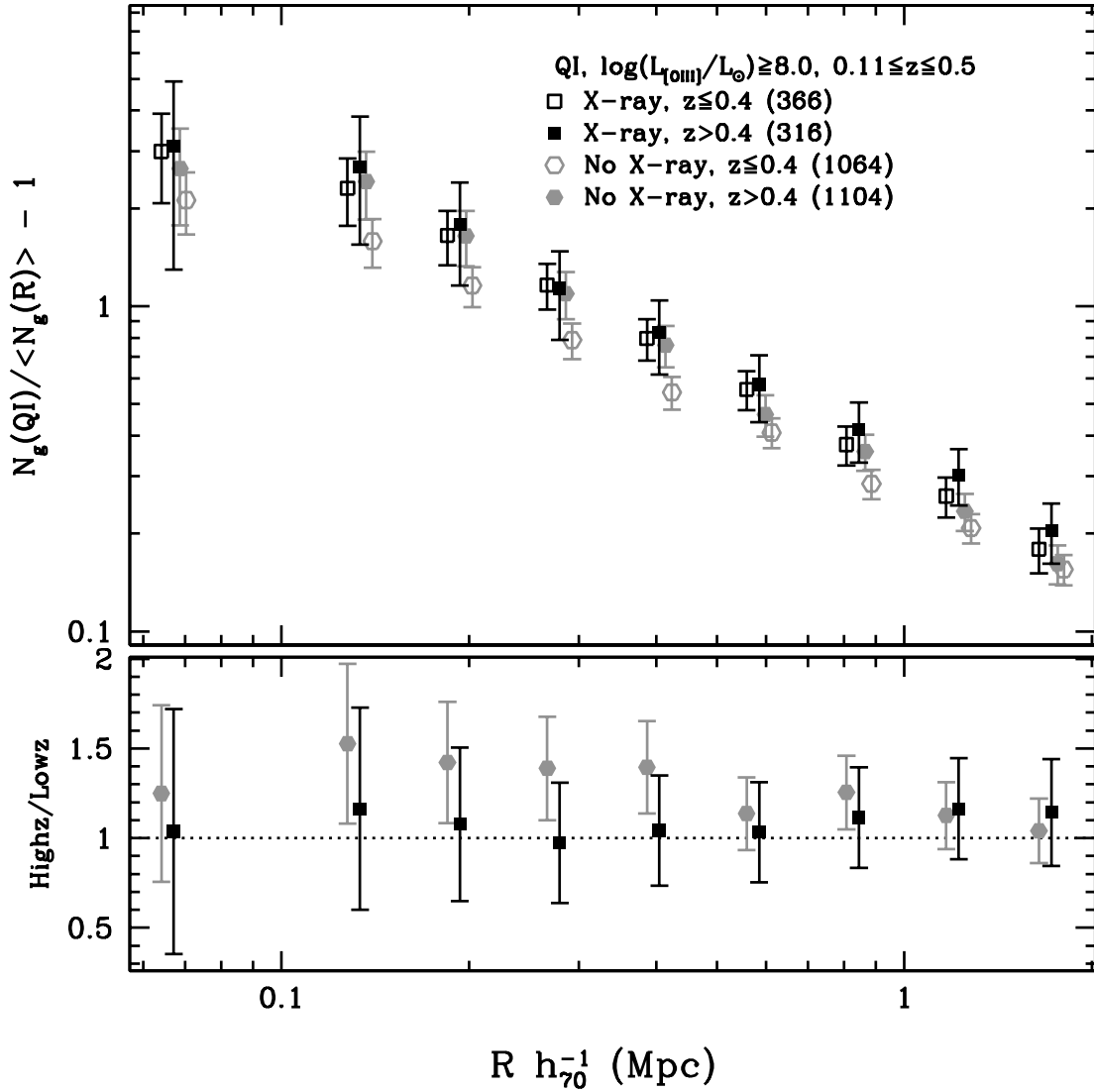


Figure 8.6— Upper panel: Mean cumulative overdensity vs. scale and redshift for $\log(L_{[\text{OIII}]}/L_{\odot}) \geq 8.0$ and $0.11 \leq z \leq 0.5$ QIs with and without detections in RASS (RASS detected QIs have $\log(L_{2\text{keV}}) \geq 25.7$). Lower panel: Overdensity ratio of $z > 0.4$ to $z \leq 0.4$ QIs

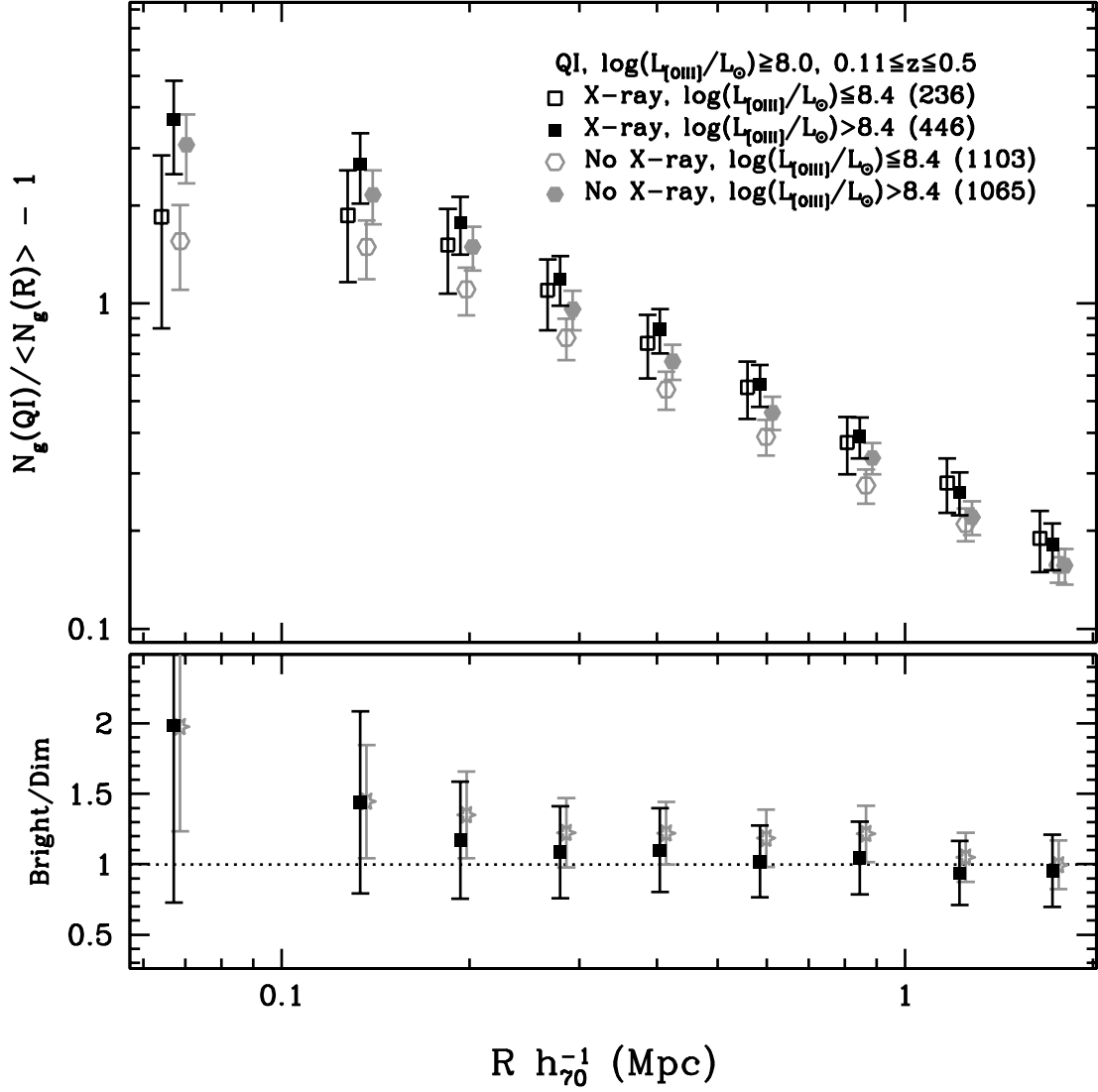


Figure 8.7— *Upper panel:* Mean cumulative overdensity vs. scale and $L_{[\text{OIII}]}$ for $\log(L_{[\text{OIII}]} / L_{\odot}) \geq 8.0$ and $0.11 \leq z \leq 0.5$ QIs with and without detections in RASS (X-ray detected QIs have $\log(L_{2\text{keV}}) \geq 25.7$). *Lower panel:* Overdensity ratio of bright $L_{[\text{OIII}]}$ to dim $L_{[\text{OIII}]}$ for X-ray detected and X-ray undetected QIs.

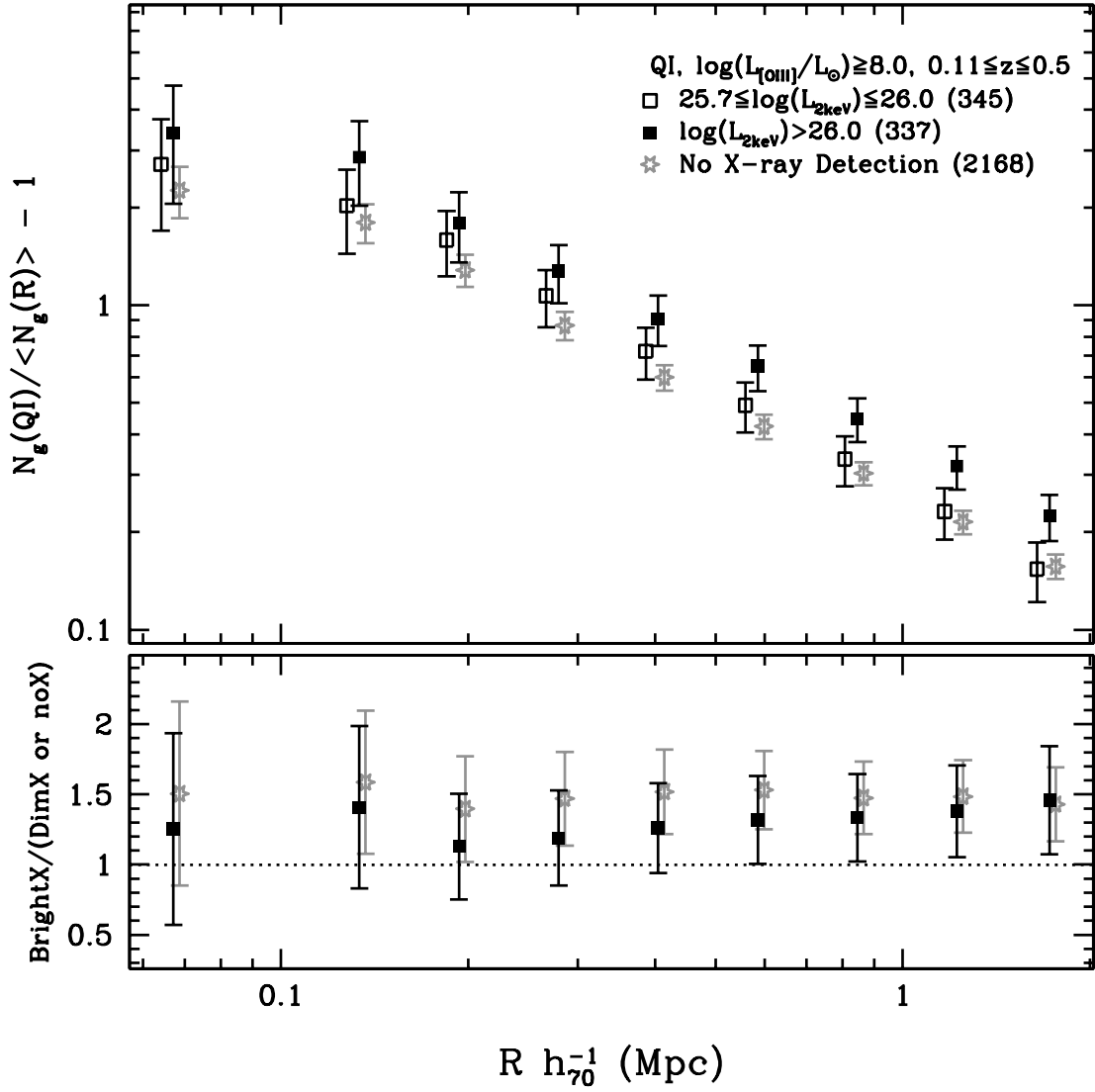


Figure 8.8— *Upper panel:* Mean cumulative overdensity vs. scale and X-ray luminosity for $\log(L_{\text{OIII}}/L_{\odot}) \geq 8.0$ and $0.11 \leq z \leq 0.5$ X-ray detected QIs volume-limited to $\log(L_{2\text{keV}}) \geq 25.7$. The gray starred points show the overdensity around QIs not detected by RASS for comparison. *Lower panel:* Solid black square points give the overdensity ratio of brighter X-ray QIs to dimmer X-ray QIs. The gray starred points show the ratio of brighter X-ray QIs to QIs undetected in RASS.

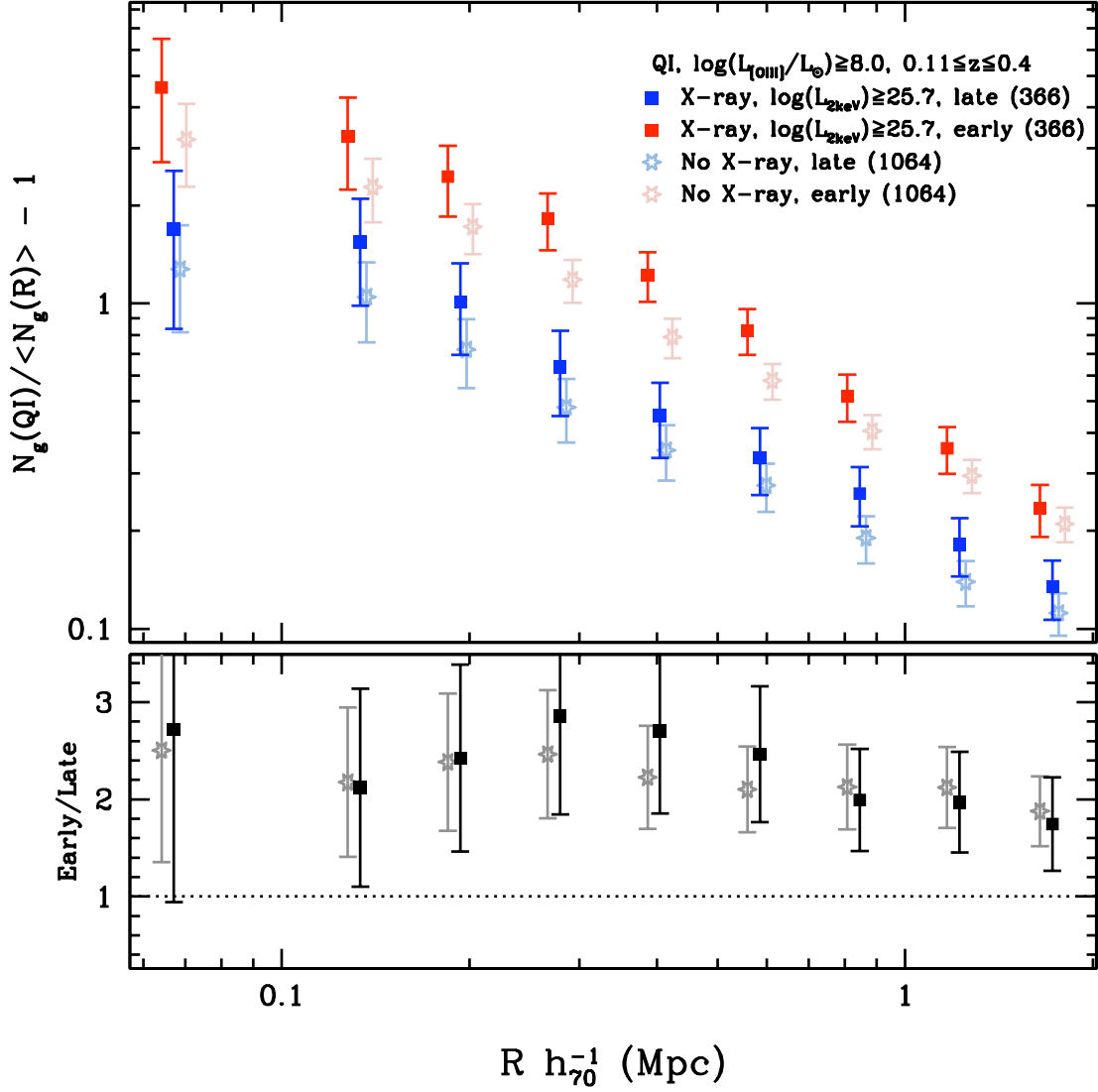


Figure 8.9— *Upper panel:* Mean cumulative overdensity vs. scale and environment galaxy type for $\log(L_{\text{[OIII]}}/L_{\odot}) \geq 8.0$ and $0.11 \leq z \leq 0.4$ QIs with and without detections in RASS (X-ray detected QIs have $\log(L_{2\text{keV}}) \geq 25.7$). *Lower panel:* Overdensity ratio of RASS-detected QIs to undetected QIs.

Chapter 9

Conclusions & Future Work

Our results support recently proposed merger models of quasar origin (Hopkins et al., 2008). On small scales, we measure an increased overdensity around the brightest sources that is scale-dependent, providing evidence that the fueling mechanisms for bright quasars are merger-related (Djorgovski, 1991; Hennawi et al., 2006; Myers et al., 2008; Lacey & Cole, 1993). Lower luminosity AGN do not show the increasing overdensity at smaller scales, leading us to conclude that they are fueled by mechanisms less dependent on the local galaxy environment (Li et al., 2006, 2008). On \sim Mpc scales, bright and dim quasars have approximately equal overdensities, which implies that they occupy dark matter halos of similar mass. This result is consistent with the predictions of the merger models that quasars of different luminosities are mainly similar objects radiating at different times in their evolution (Lidz et al., 2006; Hopkins et al., 2005a).

In addition, we investigate the nature of the quasar and AGN environments themselves. We find that type I sources are located in environments with a higher overdensity of early-type galaxies than late-type galaxies, and that brighter TIs have an increasing environment overdensity of early-type galaxies on small scales. A higher overdensity of early-type galaxies on small scales could be evidence that feedback affects nearby galaxies outside the host galaxy, quenching or suppressing star formation (Croton et al., 2006). Type II sources have a lower overdensity of early-type galaxies in their environments but similar overdensities of late-type galaxies. We speculate that TIIs are being observed at a different stage of their evolution compared to TIs and/or are in poorer clusters than TIs.

Additional information in our data set allows us to focus on the QIs alone and measure the relationship of QI black hole mass with environment overdensity. The increased overdensity with higher mass is consistent with the $M_{\text{DMH}} - M_{\text{BH}}$ relationship (Ferrarese & Merritt, 2000; Gebhardt et al., 2000; Tremaine et al., 2002). The change in the early-to-late type environment galaxy ratio for QIs supports the conclusion that QIs with higher M_{BH} are located in richer clusters (Zehavi et al., 2005). Additionally, we find that QIs with low accretion efficiency have a slightly higher environment overdensity compared to high efficiency QIs, which may be evidence of quenching due to accretion feedback (Scannapieco & Oh, 2003).

Finally, our exploration of QI environments and their relationship to QI multiwavelength properties enforced the need for larger samples with deeper radio and X-ray observations, which would allow us to sample a larger range of the radio and X-ray luminosity functions. Additionally, valuable insight about the relationship of radio sources with their environments could be gained with detailed radio morphology information. When we measure marginal evolution in the QI environment overdensity with redshift in the range $0.11 \leq z \leq 0.5$, we determine that it is not the primary factor influencing

the increased overdensity of QIs compared to the lower luminosity AGNs. However, whether there is significant evolution in quasar environments at higher redshifts can be determined by studying the environments of higher redshift quasars using data from deeper surveys such as the Cosmic Evolution Survey (COSMOS). The two-square-degree field studied by COSMOS has been imaged in the optical as well as across other wavelengths using a combination of space-based and ground-based telescopes.

Measurements of additional quasar properties will allow us to hone in even deeper on the links between quasars and their environments. For example, the Large Synoptic Survey Telescope (LSST) will measure quasar variability, which is known to be linked to physical properties of quasars and their fueling mechanisms (e.g., Wilhite et al., 2008). Studying how quasar variability is linked to quasar environments would help us to understand in more detail how the environment influences quasar fueling or vice versa.

Historically, investigations of quasar and AGN environments have been performed using galaxy-counting techniques similar to those we employ in this dissertation. However, now that large data sets are available, and we have the promise of even larger ones, it is becoming possible to transition studies of environments to use correlation and marked correlation analyses (e.g., Kauffmann & Haehnelt, 2002; Adelberger & Steidel, 2005; White & Padmanabhan, 2009). The advantage of correlation and cross-correlation measurements is that they can be more directly interpreted via models such as halo occupation distribution models (e.g., Cooray & Sheth, 2002) to constrain theories of structure formation.

Appendix A

Documentation for Bincounting Code Package

A.1 OVERVIEW

This appendix details the Bincounting Code (BC) package (written in C) developed as part of this dissertation to study the environments of AGNs and quasars in the Sloan Digital Sky Survey. This package includes code to make a binary file from environment galaxy data or negative random position data (for masking), mask target data using binary files containing negative random position data, and count environment galaxies within defined (comoving) radii of target objects using the binary environment galaxy data files.

A.2 HEADER FILE: `bincountsfunctions.h`

The header file contains definitions for all of the functions used in the BC package as well as global variable definitions.

- `H0` : value of h_0 , such that the Hubble constant $H_0 = 100 h_0 \text{ km s}^{-1}\text{Mpc}^{-1}$. Default value = 0.7.
- `MIND` : minimum distance in units of $h^{-1} \text{ Mpc}$ from the target coordinate within which objects will be counted. Default value = 0.025.
- `MAXD` : maximum distance in units of $h^{-1} \text{ Mpc}$ from the target coordinate within which objects will be counted. Default value = 10.0.
- `NUMBINS` : number of bins in which the objects are (differentially) counted. This value is used in the `binDistance` function to select the correct list of maximum bin edges. Default value = 14 for data used in overdensity vs. scale plots.
- `T1MAX` : photometric galaxy type classification cut (see Section A.6.2 for details). Galaxies with spectral-type parameter $t < 0.02$ correspond to the CWW Ell template (Budavari et al., 2003). Used for subdividing environment galaxies beyond the early/late division. Default value = 0.02.
- `T2MAX`: photometric galaxy type classification cut (see Section A.6.2 for details). Galaxies with spectral-type parameter $0.02 < t < 0.3$ approximately correspond to the CWW Sbc template (Budavari et al., 2003). Used for subdividing environment galaxies beyond the early/late division. Default value = 0.3.

- T3MAX: photometric galaxy type classification cut (see Section A.6.2 for details). Galaxies with spectral-type parameter $0.3 < t < 0.65$ approximately correspond to the CWW Scd template, and galaxies with $t > 0.65$ approximately correspond to the CWW Irr template (Budavari et al., 2003). Used for subdividing environment galaxies beyond the early/late division. Default value = 0.65.
- radians(x) : function to convert x to radians
- degrees(x) : function to convert x to degrees

We also define new object types that are used throughout the code:

- Coord : struct to contain only right ascension and declination of an object
- zphotCoord : struct to contain information about photometric galaxies. Contains right ascension and declination of object, as well as photometric redshift and spectral type parameter as defined by Budavari et al. (2003).
- zCoord : struct to contain information about targets. Contains right ascension, declination, and redshift of object. Also contains comoving distance corresponding to the object’s redshift and a string that identifies the object, as well as lists in which (differential) bincounts are stored.
- DecDic : “declination dictionary” created to speed up object searching in the bincounting code. See Section A.7 for details of its usage.

A.3 GENERAL FUNCTIONS: `bincountsfuctions.c`

This section contains functions that are used throughout the BC package.

- `mysort_ra` : given two Coord objects, sort them (Boolean) by their right ascension. Returns int: 1 if first coordinate is greater than second coordinate, 0 if coordinates are equal, and -1 if second coordinate is greater than first coordinate.
- `mysort_dec` : given two Coord objects, sort them (Boolean) by their declination. Returns int (see `mysort_ra`).
- `mysort_dec_photoz` : given two zphotCoord objects, sort (Boolean) by their declination. Returns int (see `mysort_ra`).
- `mysort_zphot_photoz` : given two zphotCoord objects, sort (Boolean) by their photometric redshift. Returns int (see `mysort_ra`).
- `minimum` : given two doubles, return double of lesser value.
- `angularDistance` : given right ascension and declination (doubles) of two points, use Haversine formula to calculate angular distance between them. Coordinates should be entered in degrees; output is in radians (double).
- `angDiamDistance` : given a zCoord object, calculate the angular diameter distance (double) corresponding to its comoving distance.

- `angle2Mpc` : given an angle in radians (double) and a `zCoord` object, returns the comoving distance in Mpc (double) corresponding to that angle at the redshift of the `zCoord` object.
- `Mpc2angle` : given a comoving distance in Mpc (double) and a `zCoord` object, returns the angle in radians (double) corresponding to that comoving distance at the redshift of the `zCoord` object.
- `binDistance` : given a physical distance (double) between a target and a photometric galaxy, find the bin (bin maxima correspond to value of `NUMBINS` global variable, see below) in which the galaxy falls and increment the counts in that bin (list of `bincounts` given as the second argument).
- `binZ` : function to create $N(z)$ for photometric galaxy samples.

The `binDistance` function uses the value of the `NUMBINS` global variable to determine the bin maxima to be used in the bincounting. The `binEdges` lists are defined at the beginning of the `bincountsfunctions.c` file.

A.4 CREATE BINARY DATA FILES:

`sortbydec.c` and `sortbydec_zphot.c`

A.4.1 Negative Random Data for Masking

In order to mask target data using the BC package, binary files with negative random position data must be created. These negative random data are points (right ascension, declination) that correspond to “bad” areas of the sky. The `sortbydec.c` program opens an ASCII file (no header line or other columns should appear in the file) with the negative random positions and sorts them by declination. The code outputs a binary file containing the exact number of objects in the input file and a binary file containing the negative random data sorted by declination.

Command line usage :

```
>> gcc -o sortbydec bincountsfunctions.c sortbydec.c -lm
>> sortbydec <catalogname> <binarydatafilename>
           <binarylinecountname> <approx#ofobjects>
```

The final argument is an approximate number of objects (long) contained in the catalog (must be greater than actual number) used to allocate enough memory for the code.

A.4.2 Environment Galaxy Data for Bincounting

The bincounting code also requires binary files containing the environment galaxy data. The input ASCII file of environment galaxy data must have the columns (and only these columns, with no header) right ascension, declination, redshift, and spectral type parameter. The code then outputs a binary file containing the exact number of objects in the input file and a binary file containing the

environment galaxy data sorted by declination.

Command line usage :

```
>> gcc -o sortbydec_zphot bincountsfunctions.c
      sortbydec_zphot.c -lm
>> sortbydec <catalogname> <binarydatafilename>
      <binarylinecountname> <approx#ofobjects>
```

The final argument is an approximate number of objects (long) contained in the catalog (must be greater than actual number) used to allocate enough memory for the code.

A.5 MASK TARGET DATA: maskforbincount.c

Target data can be masked using the binary files of negative random data with `maskforbincount.c`. This code reads in the entire catalog of negative randoms, then opens the file of targets and reads them in one at a time, determining whether there are negative random points within the maximum radius (as determined by the `binDistance` function) and writes out only those targets with zero negative random positions within that maximum radius.

Command line usage :

```
>> gcc -o maskforbincount bincountsfunctions.c
      maskforbincount.c -lm
>> maskforbincount <binarylinecountname> <binarydatafilename>
      <targetcatalogname> <outputfilename>
      <approx#oftargets>
```

The final argument is an approximate number of objects (long) contained in the target catalog (must be greater than actual number).

A.6 COUNT ENVIRONMENT GALAXIES:

`bincount_zphotandztype.c` and `bincount_zphot4types.c`

A.6.1 Bincounting with All Galaxies and Red-Blue Galaxy Separation

The code `bincount_zphotandztype.c` is used to count the number of environment objects within a specified distance and redshift interval from the target. There are three output files: the first gives the overall bincounts; the second, bincounts of only early-type galaxies; and the third, bincounts of only late-type galaxies. (Summing the bincounts given in the second two output files should give the counts in the first output file!)

Command line usage :

```
>> gcc -o bincount_zphotandztype bincountsfuctions.c
        bincount_zphotandztype.c -lm
>> bincount_zphotandztype <binarylinecountname>
        <binarydatafilename> <targetcatalogname>
        <outputfilename> <outputfilename_earlytype>
        <outputfilename_latetype> <approx#oftargets>
        <cumoption> <deltaz> <typesplit>
```

Command line arguments:

- linecount filename: binary file produced by sortbydec_zphot.c corresponding to environment object data file
- environment object filename: binary file produced by sortbydec_zphot.c
- target object filename: ASCII columns id, ra, dec, redshift, comovingdistance, no header line
- total output filename: will have columns id, bincountMaxR-thru-bincountMinR
- early-type output filename: will have columns id, bincountMaxR-thru-bincountMinR
- late-type output filename: will have columns id, bincountMaxR-thru-bincountMinR
- number of targets: integer (can be approx but must be > actual number)
- cum option: cum = 1 if cumulative counts, cum = 0 if differential counts, best if 0
- deltaz value: the environment objects must have a redshift within this separation from the target redshift to be counted in a radius bin
- type value split: value at which early and late type galaxies are to be separated. According to Budavari et al. (2003), the best value for this split is 0.3.

A.6.2 Bincounting with Budavari et al. (2003) Galaxy Subgroups

The process is almost identical to that of Section A.6.1, except there are further divisions imposed on the photometric galaxies in the environment. Additionally, the output files *do not* include a file that gives the total number of galaxies within each counting radius.

Galaxies with spectral-type parameter $t < 0.02$ (T1) correspond to the CWW Ell template; $0.02 < t < 0.3$ (T2) approximately correspond to the CWW Sbc template; $0.3 < t < 0.65$ (T3) approximately correspond to the CWW Scd template, and galaxies with $t > 0.65$ (T4) approximately correspond to the CWW Irr template (Budavari et al., 2003).

Command line usage :

```
>> gcc -o bincount_zphot4ztypes bincountsfuctions.c
        bincount_zphot4ztypes.c -lm
>> bincount_zphot4ztypes <binarylinecountname>
        <binarydatafilename> <targetcatalogname>
```

```
<T1outputfilename> <T2outputfilename>  
<T3outputfilename> <T4outputfilename>  
<approx#oftargets> <cumoption> <deltaz>
```

Command line arguments:

- linecount filename: binary file produced by `sortbydec_zphot.c` corresponding to environment object data file
- environment object filename: binary file produced by `sortbydec_zphot.c`
- target object filename: ASCII columns id, ra, dec, redshift, comovingdistance, no header line
- total output filename: will have columns id, bincountMaxR-thru-bincountMinR
- T1 output filename: will have columns id, bincountMaxR-thru-bincountMinR
- T2 output filename: will have columns id, bincountMaxR-thru-bincountMinR
- T3 output filename: will have columns id, bincountMaxR-thru-bincountMinR
- T4 output filename: will have columns id, bincountMaxR-thru-bincountMinR
- number of targets: integer (can be approx but must be $>$ actual number)
- cum option: cum = 1 if cumulative counts, cum = 0 if differential counts, best if 0
- deltaz value: the environment objects must have a redshift within this separation from the target redshift to be counted in a radius bin

A.7 BINCOUNTING ALGORITHM

Rather than do a brute-force run through the galaxies in order to find those that are in the defined nearby neighborhood of the target position, the bincounting code creates what we call a “Dec Dictionary” to index the objects by declination.

The pre-sorted environment galaxy binary data file (and corresponding linecount file) is read into the code. The galaxy list is divided into fifty equal increments, and the “Dec Dictionary” holds the index and declination of the object at the end of each of the increments. Thus, when a target object is read from the file, the code jumps to the increment closest to and less than the target’s declination minus the maximum distance set by MAXD.

The targets are read from the target data file one-by-one and a minimum and maximum RA and dec are calculated based on the maximum distance set by MAXD. Beginning at the object selected using the Dec Dictionary, each potential environment galaxy is tested to find if it falls within the maximum and minimum coordinate box. If it does, the full distance calculation is invoked and that distance is sent to the `binDistance` function for bincounting. The counts in each bin are printed to a file with the object’s ID, redshift, and coordinates.

Appendix B

Photometric Redshift Estimation for SDSS Quasars

B.1 INTRODUCTION

Electromagnetic radiation from a distant object loses energy in its transit through the universe due to the universe's expansion. This results in a net shift of the radiation toward the red end of the spectrum, an effect known as cosmological redshift. The most accurate way to find an object's redshift is to acquire its spectrum and measure how far known spectral lines are shifted from their vacuum wavelengths. However, it can be time-consuming to take spectra for large samples of objects, whereas photometric (or broad-band) measurements can be made much more efficiently. Therefore, large samples of objects with photometric redshift data can be available for use in cosmological calculations that until now have been restricted by sample size. For instance, large scale structure in the universe has been studied by using galaxies with photometric redshift information. Because quasars are more easily observed at higher redshifts than galaxies, accurate photometric redshift information for quasars is extremely valuable for probing large scale structure closer to the earliest times in the universe.

B.1.1 Photometry and Colors

Broadband filters on a telescope measure the observed flux within a certain wavelength range. Our data comes from the Sloan Digital Sky Survey (SDSS), which uses a dedicated telescope located at the Apache Point Observatory in New Mexico. The telescope measures flux through five broadband filters: u , g , r , i , and z with average weighted filter wavelengths of 3551, 4686, 6165, 7481, and 8931 Angstroms, respectively (York et al., 2000). A magnitude is calculated by taking a logarithm of the flux measured in a specific wavelength band (Lupton, Gunn, & Szalay, 1999). Colors are formally defined as the difference between two magnitudes, or equivalently, by the ratio of fluxes through the two different bands; this ratio is independent of redshift.

B.1.2 Previous Photometric Redshift Work: Galaxies

Photometric redshift estimation techniques were pioneered with galaxies and are particularly effective for galaxies because of distinctive breaks in their spectral energy distributions (SEDs), such as the 4000Å break. The concept was first introduced by Baum (1962), who measured multiple colors of galaxies and used them to estimate the location of the 4000Å break, thereby determining the galaxy's redshift, and Koo (1985) and Loh & Spillar (1986) expanded the technique to larger samples of galaxies. More recently, work by Brunner et al. (1997) and Connolly et al. (1999) matched broad-

band galaxy colors to colors estimated using galaxy SEDs generated from theoretical models with excellent results.

B.1.3 Previous Photometric Redshift Work: Quasars

The average lower-redshift quasar spectrum can be approximated by a power law, which alone would give an uninformative color-redshift relation. High redshift quasars have a distinctive break in their optical spectra at the Lyman- α forest, but this feature does not affect the quasar spectrum enough to use for redshift estimation until $z \gtrsim 3.0$. Fortunately, quasars have prominent emission and absorption features that affect the colors measured by broadband photometry (see detailed discussion in Richards et al., 2001a) enough to give the color-redshift relations shapes that are very often nondegenerate in our four-dimensional color space. Richards et al. (2001a) demonstrated that the empirical color-redshift relation (CZR) for quasars using four colors determined from the five SDSS broadband filters has structure that can be exploited to understand quasars themselves, as well as to predict photometric redshifts.

Photometric redshift estimation techniques for quasars have improved significantly from about 50% of quasars with photometric redshifts estimated within 0.3 of the actual spectroscopic redshift (Hatziminaoglou et al., 2000) to nearly 70% of quasars having estimated photometric redshifts within 0.2 of the spectroscopic redshift using a χ^2 minimization technique between observed colors and colors predicted by a CZR (Richards et al., 2001b). Using a probability density function (PDF) derived from a χ^2 distribution, Weinstein et al. (2004) reports a success rate of over 77% of quasars within 0.2 of the spectroscopic redshift. A benefit of this probability density function method is that it also gives the probability that the estimated redshift is correct (Weinstein et al., 2004). However, even with these improved results, there is need for still more improvement before these methods produce reliable photometric redshifts suitable for cosmological applications.

This chapter discusses our implementation of a number of improvements on the photometric redshift determination algorithm developed by Weinstein et al. (2004) in an attempt to achieve higher accuracy photometric redshift estimates.

B.2 DATA SAMPLE

We use the SDSS Third Data Release (DR3; Abazajian et al., 2005) Quasar Catalog created by Schneider et al. (2005). The 46,420 quasars in the catalog were selected from DR3 on the basis of their spectra containing at least one broad emission line or their being unquestionably broad absorption line quasars. The objects have luminosities $M_i > -22.0$ and a bright limit in the i -band of 15.0. Spectroscopic redshifts of quasars in the catalog range from 0.078 to 5.4135. Figure B.1 shows the redshift distribution of the sample.

The catalog contains only point-spread function (PSF) magnitudes, so we matched the quasars to the DR3 SpecPhotoAll Database by plate and fiber numbers to obtain the model magnitudes, fiber magnitudes, and Petrosian magnitudes for each of the objects in the catalog (these magnitude types will be discussed in more detail in Section B.4.3. One object from the DR3 Quasar Catalog does not have a match in the SpecPhotoAll database and is excluded from our calculations. While there are PSF magnitudes and errors measured in all bands for all remaining 46,419 objects, there are a few

objects that have “null” or “-9999” values for one or more magnitude and/or error measurements in the other magnitude types. Objects with any invalid field are therefore excluded from our calculations of color-redshift relations when we use those magnitudes.

B.3 TECHNIQUE

B.3.1 Recreation of Weinstein et al. (2004) Algorithm

Following the matrix method outlined in Weinstein et al. (2004, hereafter W04 algorithm), we calculate the color-redshift relation (CZR) and its associated “covariance matrices”. The method is summarized in the following subsections.

Removing reddened quasars

We follow the scheme of Weinstein (2002) to determine (and subsequently discard from the sample used to calculate the CZR) those quasars in the input sample which are anomalously red. First, the quasars are binned by redshift, and the discrete median colors in each bin are calculated. Next, the “normalized colors” (Richards et al., 2001a, W04) for $u - g$ and $g - r$ are calculated for every quasar in the input sample. The normalized color is defined as

$$(u - g)_{norm} = (u - g)_{measured} - (u - g)_{median} \quad (\text{B.1})$$

and

$$(g - r)_{norm} = (g - r)_{measured} - (g - r)_{median} \quad (\text{B.2})$$

where the median color is calculated at the quasar’s redshift. Since the quasar will likely not be exactly at a redshift bin center, a linear interpolation is made between the two bin centers that flank the quasar’s redshift to determine the median color used in the formula above.

When the normalized colors have been calculated for all the quasars in the sample, they are sorted from bluest to reddest (smallest to largest normalized color value). The “red limit” in $u - g$ and $g - r$ is defined as the 2.5th percentile of the $u - g$ normalized color $(u - g)_{2.5}$ and the 50th percentile of the $g - r$ normalized color $(g - r)_{50}$. A quasar is considered anomalously reddened if both of the following conditions are true (Weinstein, 2002):

$$(u - g)_{norm} > -(u - g)_{2.5} \quad (\text{B.3})$$

and

$$(g - r)_{norm} > (g - r)_{50} \quad (\text{B.4})$$

The DR3 quasar sample is plotted by color as a function of redshift in Figure B.2, and we show the distribution of reddened quasars.

Calculating CZR and Covariance Matrix Values

Once the reddened quasars have been identified and removed from the initial data set, the CZR and corresponding covariance matrices are calculated from the remaining non-reddened quasars.

Following W04, this means calculating the mean color in each redshift bin z :

$$M_z^j = \frac{1}{N_z} \sum_{q=1}^{N_z} x_{j,q} \quad (\text{B.5})$$

where x_j are the colors $u - g$, $g - r$, $r - i$, $i - z$ for each quasar q in the bin. Figure B.3 shows the mean CZR for the DR3 quasar data. (Later, we explore the use of the median or mode colors of each redshift bin to form the CZR.)

The components j, k of the CZR covariance matrix in each redshift bin z are (W04):

$$V_z^{jk} = \frac{1}{N_z - 1} \sum_{q=1}^{N_z} (x_{j,q} - M_z^j)(x_{k,q} - M_z^k) \quad (\text{B.6})$$

where N_z is the number of quasars in the redshift bin; i, j and k are colors; M_z is the vector of CZR colors in the redshift bin z as calculated in Equation B.5, and x_q is the vector of colors for quasar q in the bin.

Calculating Photometric Redshifts

A photometric redshift for an observed quasar is found using the CZRs and associated covariance matrices by first calculating the χ^2 distribution between the colors of the observed quasar and the colors of the CZR.

A color covariance matrix for the observed quasar is calculated from its measured magnitude errors:

$$V_o = \begin{pmatrix} \sigma_u^2 + \sigma_g^2 & -\sigma_g^2 & 0 & 0 \\ -\sigma_g^2 & \sigma_g^2 + \sigma_r^2 & -\sigma_r^2 & 0 \\ 0 & -\sigma_r^2 & \sigma_r^2 + \sigma_i^2 & -\sigma_i^2 \\ 0 & 0 & -\sigma_i^2 & \sigma_i^2 + \sigma_z^2 \end{pmatrix} \quad (\text{B.7})$$

Then, the value of the χ^2 distribution in the redshift bin z is given by:

$$\chi_z^2 = (X_o - M_z)^T (V_o + V_z)^{-1} (X_o - M_z) \quad (\text{B.8})$$

where X_o is the vector of color values for the observed quasar and M_z is the vector of CZR mean, median, or mode color values in bin z .

The probability distribution function (PDF) is found from this χ^2 distribution and the photometric redshift corresponds to the maximum of the PDF, which is calculated as follows:

$$P'_n = \frac{W_z \exp[-\frac{\chi_n^2}{2}]}{4\pi^2 |V_o + V_z|^{1/2}} \quad (\text{B.9})$$

The normalized PDF is

$$P_n = \frac{P'_n}{\sum_{n=1}^N P'_n} \quad (\text{B.10})$$

Here, W_z is a redshift-dependent weighting parameter. The weighting function used by W04 is the number distribution $N(z)$ of the CZR training dataset with redshift.

B.4 VARIATIONS ON W04 ALGORITHM

In this section, we discuss the variations we made to improve the W04 algorithm. In order to refine the CZR, we varied the binning and tested the use of median and mode statistics instead of the mean; explored the use of different magnitude types and adding additional bands; and imposed magnitude and/or magnitude error limits on the training data. We also explored the use of different weighting functions for calculating the PDF, as well as combining multiple PDFs to improve the redshift estimations. Table B.1 summarizes the variations that are made to the original W04 algorithm. The following subsections discuss the variations in more detail.

B.4.1 Binning

The W04 algorithm, as well as earlier work by Richards et al. (2001b), uses an overlapping binning scheme of the CZR training sample in which the bin centers are located at redshift intervals of 0.05. Bins with centers $z \leq 2.15$ have width 0.075, bins with centers $2.15 < z \leq 2.5$ have width 0.2, and bins with centers at $z > 2.5$ have width 0.5. They chose to use overlapping bins because their training data set was small; the larger bins increase the number of quasars, thus reducing noise. Because the sample from the DR3 Quasar Catalog is more than fifteen times larger than the sample used by Richards et al. (2001b), there is no need for overlapping bins. In addition, we can decrease the size of the bins and have smaller bins to higher redshifts, which increases the accuracy of the estimated photometric redshifts. With this in mind, we have developed a set of variations of bin widths. The binning schemes are summarized in Table B.2; note that the edge of the first bin always starts with $z = 0$. The first variation is based on the binning scheme of Richards et al. (2001b), where there are two different bin widths in two different redshift intervals (the change occurs at “division2”), but without overlap. In the next three variations, we continue to use only two redshift intervals, but change the bin width and the value of division2. In the last four variations, we increase the number of redshift intervals to three (the first change occurs at “division1”). This allows us to use the bin width of 0.05 below division1, where there is the smallest number of quasars in the training sample, and use even smaller bins in the interval between division1 and division2.

Table C.1 gives a comparison of results using different binning schemes. We isolate the low-redshift and high-redshift quasars (less than or greater than division2, respectively), in Tables C.2 and C.3. There is no drastic improvement in the estimation of quasar redshifts: any increased accuracy in the redshift estimate from decreasing the size of the bins is likely offset by a smaller number of training quasars in those bins, which will cause a decrease in accuracy of the CZR. To summarize, we find that a non-overlapping binning scheme does only slightly better than the O2 binning scheme.

B.4.2 Statistic

The W04 algorithm uses the mean of each color $u - g$, $g - r$, $r - i$, and $i - z$ within each redshift bin to form the CZR. Here we describe our results when a median (Richards et al., 2001a,b), and mode (Hopkins et al., 2004) of each color is used instead.

Discrete Statistics

The “discrete” median for each color is calculated by ordering the list of quasars by each color (smallest value to largest value) and choosing the central color in each of $u - g$, $g - r$, $r - i$, and $i - z$. A mode can be calculated from this median and the mean of the bin using the formula (Lupton, 1993):

$$\text{mode} = 3 \times \text{median} - 2 \times \text{mean} \quad (\text{B.11})$$

Hereafter, we refer to these statistics as the *discrete median* and *discrete mode*, respectively.

“Gaussian” Statistics

Since there are inherent errors in the color values (due to the magnitude errors in the measured data), we can alternatively treat the distribution of color in each bin as a continuum. The color distribution for the quasars in each redshift bin is calculated by approximating each quasars color as a Gaussian centered at the measured color with standard deviation equal to the color error (c.f. Hopkins et al., 2004). For a color $i - j$, where the measurement error for each magnitude is given by δm_i and δm_j , respectively, we define the color error for a single quasar as

$$\delta(m_i - m_j)^2 \equiv (\delta m_i)^2 + (\delta m_j)^2 \quad (\text{B.12})$$

The Gaussians for all the quasars in the bin are summed to determine the color distribution. The median of the distribution is at the 50th percentile; hereafter this statistic is referred to as the *Gaussian median*. The *Gaussian mode* is the color value at which the color distribution is at its maximum (Hopkins et al., 2004). (In Section B.4.8, we discuss the effects of including correlation between SDSS magnitude bands.) Figure B.4 shows a comparison of CZRs using the mean, Gaussian median, and Gaussian mode statistic.

Tables C.4 (C.5, C.6) and C.7 (C.8, C.9) can be compared to Table C.1 (C.2, C.3) to show the results using different statistics to calculate the CZR. We find that using a mean statistic does slightly better than gmedian or gmode, with gmode giving the worst results.

The idea behind using a CZR to predict redshifts is that in a small enough redshift interval, we will have quasars that are very similar to each other. From those quasars, we choose the colors that best represent that small sample of quasars as the “ideal”. However, as can be seen in Figure B.2, even when the reddened quasars are removed, there is still a noticeable spread in the colors at each redshift. If the distribution of colors is non-trivial (for instance, the distribution is double-peaked or flat), simply using a median or mode may not be enough to characterize the quasars in that bin. The mean statistic gives equal weight to each quasar that contributes to the bin, and therefore most consistently gives the best characterization.

B.4.3 Magnitude Type

SDSS measures four different types of magnitudes: fiber, model, Petrosian, and point-spread function (PSF) for each object. We investigate how using different magnitude types to create CZRs could improve the photometric redshift estimates. Below, for completeness, we give a brief discussion of the SDSS magnitude types.

- *Point-spread function (psf) magnitudes:* A point-spread function model is fit to the object to determine the best measure of the total flux. This magnitude measure is best for isolated point sources. These sources are unresolved, and the PSF magnitude is unbiased because the image is consistent with a point-spread function.
- *Fiber magnitudes:* Fiber magnitudes are calculated from the flux in each band contained within the three arcsecond aperture of a spectroscopic fiber of the SDSS telescope.
- *Model magnitudes:* Two models, a pure deVaucouleurs profile and a pure exponential profile, are fit to the two-dimensional image of the object in each band. In the r -band, the best-fit model is chosen and applied to the other bands to determine the model magnitudes. Because the same aperture is used in all bands, the flux measurements are appropriate for determining colors, especially for extended sources such as galaxies.
- *Petrosian magnitudes:* Petrosian magnitudes are typically used for galaxy photometry. From the azimuthally averaged light profile of the galaxy, a radius is determined for a circular aperture in which galaxy fluxes are measured. The r -band profile of the galaxy determines the radius used in all bands to calculate the aperture in which the fluxes are measured.

Tables C.1 through C.9 also compare the photometric redshift estimation results using the different magnitude types. Using other magnitudes (than PSF) singly usually does worse, but in some cases can do only slightly better. . It is not surprising that the PSF magnitude CZRs give the most accurate redshift estimates, because this magnitude is optimized for measurement of point sources, which most of the quasars are. The other magnitude types, especially the fiber magnitude, which measure flux in fixed apertures, may not give as accurate of flux measurements if extraneous flux is allowed through the aperture.

Multiple PDFs

In addition to using different magnitude types separately, we convolve PDFs generated from two, three, and four magnitude types to create a composite PDF from which we estimate a photometric redshift. Each PDF is weighted equally in the convolution, but giving certain PDFs, such as the PDF generated from PSF magnitudes because it is the most successful alone, greater weight in future work may improve results.

Tables C.10 through C.12 show that combining 2, 3, and 4 PDFs from different magnitude types does slightly better than the Weinstein standard: by combining the information from several magnitude types, we find that our characterization of quasar colors is improved.

B.4.4 Reddened Quasars

In following the W04 algorithm, we remove quasars that we have classified as “reddened,” but we also investigate the effect on photometric redshifts if these reddened quasars are not removed from the sample used to calculate the CZR. Richards et al. (2001a) studied the nature of the outliers and found that the scatter is more pronounced on the red end of the distribution and increases for fainter magnitudes. It was also observed that this reddening effect is independent of redshift, and therefore

thought to be due to processes intrinsic to the quasar itself, rather than contamination from the host galaxy or intergalactic extinction.

By comparing the results shown in Tables C.13 through C.21, it is evident that removing reddened quasars gives slightly better results than leaving reddened quasars in the sample, confirming the method used by W04. Future work could include a new definition for reddened quasars.

B.4.5 Magnitude and Magnitude Error Limits

We hypothesize that by restricting the CZR training data to bright objects by imposing magnitude limits, or to objects with good photometry by imposing magnitude error limits, we can improve our estimates. Tables C.22 through C.24 summarize the results using magnitude error limits, while Tables C.25 through C.27 summarize the results using magnitude limits.

We apply magnitude error limits (in all bands) of 1.0, 0.5, 0.2, and 0.1 to the CZR training quasars and found that the limits made essentially no difference in the photometric estimate results, whether or not the same error limits were imposed on the quasars for which photoZs were calculated. The spread in quasar colors in each redshift interval is much larger than the spread due to including objects with less precise photometry, therefore it is not surprising that we see no effect.

We also imposed magnitude limits (in all bands) of 25.0, 21.0, and 20.0 to build CZRs. When the same magnitude limits were imposed on the quasars for which photoZs were calculated, a magnitude limit of 20.0 gave a several-percent improvement compared to our recreation of the Weinstein results. Brighter quasars will have more consistent colors, whereas dimmer quasars are likely to be reddened (though not enough to be removed with the reddening cut described above) and have colors that differ more from the mean colors. However, if the magnitude limit was not applied to the photoZ data, a CZR-data magnitude limit of 25.0 gave the best results, which were slightly better than the results for the W04 recreation. A CZR calculated from bright quasars will be a more accurate representation for the bright subset of objects for which photometric redshifts are to be calculated, but the dimmer quasars, with their more anomalous colors, will not fit the bright model as well.

B.4.6 Adding additional bands

Simulation with SDSS colors

All of the work thus far has been done using the five SDSS bands (u, g, r, i, z) and four colors derived by comparing the flux in consecutive bands. In order to simulate whether there would be an improvement in photometric redshift estimation, we generate CZRs and photometric redshifts using only combinations of three consecutive SDSS bands (two colors) and four consecutive SDSS bands (three colors). We also investigate whether there is an improvement in photometric redshift estimates if non-consecutive bands are used to calculate 3 colors, i.e., $u - r, g - i, r - z$.

Note that for the work in this section, reddened quasars were not removed: since the red limits are only defined in $u - g$ and $g - r$, and these colors are not always used in the CZRs calculated from fewer bands. Therefore, reported results may look worse, so the second row in the table shows results using the W04 parameters without removing reddened quasars, for a more accurate comparison.

From the “simulation” of adding additional bands (results are summarized in Tables C.28 - C.30), it is clear that using additional colors improves the photometric redshift estimates. Using non-

adjacent colors yields worse results than the W04 method.

Verification with GALEX data

We continue to verify that redshift estimates are improved when additional bands are included in the CZR by using ultraviolet data from GALEX that is matched to SDSS objects. Using a dataset of 7,642 SDSS DR5 quasars that have matches in GALEX, we calculated the mean CZRs and corresponding covariance matrices with 4 SDSS (psf magnitude) colors + 1 GALEX color. We continue to use the same redshift binning scheme as W04 without removing reddened quasars. The PDF for photometric redshift estimation is weighted according to a $N(z)$ weighting scheme based on the input sample. Tables C.31 - C.33 compare the results of using just the 4 colors for this dataset to using 5 colors. It is obvious that using an additional color improves the redshift estimates by at least 1%. We also performed N-fold testing on these results to ensure that we were not overfitting since we have a smaller sample, and find that there is no overfitting. We caution that some of the improvement may be due to the fact that only bright quasars will have GALEX matches, and we showed in Section B.4.5 that redshift estimates are more accurate for brighter objects. However, because of our “simulation” above, we conclude that the addition of more colors will be the main factor that improves photometric redshift estimates.

B.4.7 Weighting Functions

As stated above, have been using a simple $N(z)$ weighting function in which each redshift bin is weighted by the fraction of the total quasars in the training sample within that bin (Weinstein et al., 2004). When we use no weighting function (i.e., W_i in equation B.9 is always equal to $1/N$, where N is the number of redshift bins), we see that the results are typically worse (see Tables C.34 - C.51, which summarize the results when no weighting function is used and binning, magnitude, and statistic are varied with red quasars removed and not removed). Therefore, we conclude that a weighting function is an effective way to improve the photometric redshift estimates and explore the use of others.

Apparent Magnitude Weighting Function

We create an apparent magnitude weighting function $N(m, z)$ by dividing the entire training sample (the sample used to create the CZR) into bins by apparent magnitude. We then subdivide each of these magnitude bins into bins by spectroscopic redshift, thus defining the boundaries for an apparent magnitude weight function “matrix.” We count the number of objects in each cell of this matrix and normalize them by the total number of objects $N(m)$ within that cell’s magnitude shell. The weighting function $N(m, z)$ used for a given quasar is the matrix row corresponding to the apparent magnitude bin in which that quasar falls.

The redshift binning corresponds to the redshift binning for the CZR (for obvious reasons when calculating photometric redshifts). The CZR code allows the user to input the magnitude binning. The user either gives a set apparent magnitude ranges for each bin, or chooses from a set of lists of magnitude-bin minima– which enables the use of non-uniform width magnitude bins.

Absolute Magnitude Weighting Function

From the original training dataset, we bin quasars by absolute magnitude, and create an $N(M)$ weighting function in which each absolute magnitude bin is weighted by the fraction of the total quasars within that bin. The weighting function for an individual quasar is calculated by converting absolute magnitude bin edges to redshift via the distance modulus. The distance modulus is calculated from the difference between the quasar’s apparent magnitude and the absolute magnitude of the bin edge. Since the distance modulus depends only on redshift and not on magnitude, we take the redshift value corresponding to the distance modulus as the bin redshift. We use the resulting interpolated $N(z)$ as the weighting function.

Luminosity-based Weighting Functions

We also have developed weighting functions based on the DR3 Quasar Luminosity Function (Richards et al., 2006):

$$\Phi(M, z) = \Phi^* 10^{A_1 \mu} \quad (\text{B.13})$$

where

$$\mu = M - (M^* + B_1 \xi + B_2 \xi^2 + B_3 \xi^3) \quad (\text{B.14})$$

and

$$\xi = \log \frac{1+z}{1+z_{ref}} \quad (\text{B.15})$$

The fitting parameters for the luminosity function determined by Richards et al. (2006) used in the above equations are listed in Table B.3.

We have created a set of weighting functions based on this luminosity function by first defining the boundaries for a luminosity weightfunction “matrix” L by dividing the absolute magnitude range of the sample into bins, then dividing each absolute magnitude bin into redshift bins over the redshift range of the sample. In each cell of this matrix, we evaluate the value of the luminosity function as

$$L_{M,z} = \int_{M_{min}}^{M_{max}} \int_{z_{min}}^{z_{max}} \Phi(M, z) dV_c dM \quad (\text{B.16})$$

where Φ is given by Equation B.13 with apparent magnitude substituted for absolute magnitude using the relation

$$M = m - K_2 - \frac{c}{H_o} 5 \log \left[(1+z) \int_0^z \frac{dz'}{\sqrt{\Omega_M (1+z')^3 + \Omega_\Lambda}} \right] + 25 \quad (\text{B.17})$$

K_2 is the two-parameter K -correction as defined by Wisotzki (2000):

$$K_2(z) = K(0) - 2.5(1+\alpha) \log(1+z) \quad (\text{B.18})$$

where $K(0)$ is given as -0.42 and α is given as -0.45.

The comoving volume element is given by (Hogg, 2000)

$$dV_c = 4\pi \frac{c}{H_o} \frac{(1+z)^2 D_A^2}{\sqrt{\Omega_M (1+z)^3 + \Omega_\Lambda}} dz \quad (\text{B.19})$$

and D_A is the angular diameter distance from now until redshift z given by Hogg (2000)

$$D_A = \frac{c}{H_o(1+z)} \int_0^z \frac{dz'}{\sqrt{\Omega_M(1+z')^3 + \Omega_\Lambda}} \quad (\text{B.20})$$

The matrix cell values are normalized by the probability of finding a quasar from the training set in the bin (M, z) of the matrix: $(N_{M,z})/N$. The *collapsed matrix* $N(z)$ weight function is calculated by summing the matrix along the magnitude axis. The *matrix* $N(z)$ weight function is calculated for an individual quasar by using its apparent magnitude to calculating the corresponding absolute magnitude at the center of each redshift bin so that the i th value of $N(z)$ corresponds to the (M_i, z_i) element of the matrix.

Tables C.52 - C.54 show a comparison of photometric redshift estimation results using each of the above weighting functions. Using an $N(z)$ weighting function does better than no weighting function by about 1%. The apparent magnitude weighting function improves redshift estimates up to about 1%. We conclude that a weighting function adds additional information about the training data to the information already contained in the CZR and is necessary for accurate photometric redshift estimates.

B.4.8 Covariance between SDSS magnitude bands

Scranton et al. (2005) has shown that photometry in the five bands of the SDSS can be highly correlated; therefore covariance between the bands is non-negligible and should be taken into account when calculating the color error. The color error for an individual quasar is then expressed as

$$\delta(m_i - m_j)^2 \equiv (\delta m_i)^2 + (\delta m_j)^2 - 2c_{ij}\delta m_i\delta m_j \quad (\text{B.21})$$

where c_{ij} is the correlation coefficient between the two bands, as determined by Scranton et al. (2005). Table B.4 gives a list of correlation coefficient values used. The quasar's color covariance matrix then becomes:

$$V_o = \begin{pmatrix} \sigma_u^2 + \sigma_g^2 - c_{ug}\sigma_u\sigma_g & uggr & ugr i & ugi z \\ uggr & \sigma_g^2 + \sigma_r^2 - c_{gr}\sigma_g\sigma_r & grr i & gri z \\ ugr i & grr i & \sigma_r^2 + \sigma_i^2 - c_{ri}\sigma_r\sigma_i & ri i z \\ ugi z & gri z & ri i z & \sigma_i^2 + \sigma_z^2 - c_{iz}\sigma_i\sigma_z \end{pmatrix} \quad (\text{B.22})$$

where

$$uggr = -\sigma_g^2 + c_{ug}\sigma_u\sigma_g + c_{gr}\sigma_g\sigma_r - c_{ur}\sigma_u\sigma_r \quad (\text{B.23})$$

$$ugr i = c_{ur}\sigma_u\sigma_r + c_{gi}\sigma_g\sigma_i - c_{ui}\sigma_u\sigma_i - c_{gr}\sigma_g\sigma_r \quad (\text{B.24})$$

$$ugi z = c_{ui}\sigma_u\sigma_z + c_{gz}\sigma_g\sigma_z - c_{gi}\sigma_g\sigma_i - c_{uz}\sigma_u\sigma_z \quad (\text{B.25})$$

$$grr i = -\sigma_r^2 + c_{gr}\sigma_g\sigma_r + c_{ri}\sigma_r\sigma_i - c_{gi}\sigma_g\sigma_i \quad (\text{B.26})$$

$$griiz = c_{gi}\sigma_g\sigma_i + c_{rz}\sigma_r\sigma_z - c_{ri}\sigma_r\sigma_i - c_{gz}\sigma_g\sigma_z \quad (\text{B.27})$$

$$riiz = -\sigma_i^2 + c_{ri}\sigma_r\sigma_i + c_{rz}\sigma_r\sigma_z - c_{iz}\sigma_i\sigma_z \quad (\text{B.28})$$

When the correlation coefficients are included, the changes to the CZRs are small (Figure B.5). The redshift estimate results in Tables C.55- C.57 also show that the contribution of correlation coefficients gives only negligible improvement.

B.4.9 CZRs from SDSS DR3 Quasar Subpopulations

The CZR technique can be applied to subsets of data from the training sample used above. We isolated DR3 quasars classified as extended objects, quasars with multiwavelength measurements (e.g. radio, IR, X-ray), or quasars with broad absorption features to generate CZRs for these subpopulations (see Figure B.6). Tables C.58- C.60 show results when these CZRs are applied to the subsets to estimate photometric redshifts. The colors of a subpopulation (especially one based on multiwavelength properties) are more likely to be similar, which will result in a CZR that more accurately characterizes the subpopulation. When calculating a photometric redshift for an object with a particular attribute, it may improve the estimate to convolve the PDF from the subpopulation CZR with the more general PDF.

B.5 CATASTROPHIC FAILURE ANALYSIS

A catastrophic failure is defined to be a photometric redshift estimate for which $|z_{spec} - z_{phot}| \geq 0.5$. This section details the analysis of the 6,821 catastrophic failure objects that occurred in the recreation of the algorithm developed by Weinstein et al. (2004). By analyzing the properties of the objects that failed and searching for similarities and patterns, we hope improve our algorithm to better estimate photometric redshifts.

It is evident from the z_{phot} vs. z_{spec} plot in Figure B.7 that the catastrophic failure objects can be separated into sections, and we have investigated four distinct sections of catastrophic failures. The sections are described in Table B.5. In Section B.5.1 we investigate whether a color cut may be used to identify catastrophic failure objects, and in Sections B.5.2 and B.5.3 we give the details from our inspection of the spectra and PDFs for the catastrophic failures, respectively.

B.5.1 Colors of catastrophic failure objects

In general, it is impossible to separate all catastrophic failure-type objects from non-catastrophic failure objects by a simple color cut, as can be seen in the color-color plots of all catastrophic failures superimposed on the color-color plot for the entire quasar sample in Figure B.8. However, by looking at the color-color plots for each of the four sections of catastrophic failures (Figures B.9 to B.12), we see that objects in Section 1 have noticeably redder colors than the main sample of quasars.

Reddened quasars

Another possible source of catastrophic failures is the set of “reddened” quasars that were excluded from the sample used to generate the CZR. As discussed in Section B.3.1, these quasars are defined as “red” by a color cut in each (spectroscopic) redshift bin. A color-color plot superimposing the reddened quasars over the whole sample is shown in Figure B.13. When calculating photometric redshifts for the same quasars as were included in the original training data, we find that 1,320 of the 2,771 (47.6%) of the reddened quasars are catastrophic failures and 98 of the 143 (68.5%) Section 1 objects are considered “reddened” quasars.

We generated a CZR from the sample of “reddened” quasars, and calculated the photometric redshifts for the Section1 quasars. However, the results are poor. A rough color cut for “red” quasars cuts far too many quasars out of the main sample (over 3 times the number of red quasars as eliminated by the algorithm in Section B.3.1, and this “red” CZR is unsuccessful at estimating photometric redshifts.

B.5.2 Spectra of catastrophic failure objects

We hand-inspected the spectra of the 6,821 catastrophic failures that occurred in the recreation of the results given in Weinstein et al. (2004) to identify trends that might cause catastrophic failures.

Broad absorption line quasars

We also have found that a larger-than-average fraction of the catastrophically failing objects are broad absorption line quasars (BALQSOs; Weymann et al., 1991). BALQSOs typically constitute about 15% of all quasars (see, e.g., Hall, et al., 2000), but we have found that about 34% of the catastrophic failure objects are BALQSOs. We suspect that the wide absorption troughs that are seen in BALQSO spectra affect the broadband flux enough that the colors for these objects deviate from the colors seen for normal quasars at the same redshift, giving faulty photometric redshift estimates. However, we don’t see significant color differences of BALQSOs compared to the main sample (see Figure B.14). Therefore, isolating BALQSOs using a simple color cut is not a reasonable way to improve their CZR-based photometric redshift estimates.

Quasars with unusual spectra

A small subsample of the catastrophic failures (3.2%) have spectra where the continuum spectrum increases with wavelength. Therefore, these objects are found to be unusually red compared to normal quasars at the same redshift. 189 of the 219 (86.3%) objects with increasing continuum are considered “reddened” quasars by our definition.

B.5.3 PDFs of catastrophic failure objects

Finally, I have visually inspected the shapes of the PDFs of the objects that have catastrophically failed. In over 60% of the PDFs for objects in the extreme failure range, there is no peak at all at the location of the spectroscopic redshift. However, in CF sections 3 and 4, an overwhelming majority of the PDFs have a peak at the position of the spectroscopic redshift, but a larger peak is present at a different redshift position and therefore being selected by the W04 algorithm (see Figure B.15

for example PDFs). Therefore, changing the weighting used in the calculation of the PDF and/or convolving multiple PDFs may result in selection of the correct peak in the PDF: this could be one of the reasons our variations are improving photometric redshift estimates.

B.6 CONCLUSIONS

Very briefly, when all other things are held constant except the variation being discussed unless otherwise noted, and compared to the Weinstein standard:

- A non-overlapping binning scheme does only slightly better than the O2 binning scheme.
- Using other magnitudes (than PSF) singly usually gives worse results than the W04 scheme, but in some cases can do only slightly better. Combining 2, 3, and 4 PDFs from different magnitude types (CZRs generated without removing reddened quasars) does slightly better than the Weinstein standard.
- Using a mean statistic does slightly better than gmedian or gmode, with gmode giving the worst results.
- Removing reddened quasars gives slightly better results than leaving reddened quasars in the sample.
- We applied magnitude error limits (for all bands) on the training data used to build CZRs and found that they made little-to-no difference in the photometric estimate results, whether or not the same error limits were imposed on the test data for which photometric redshifts were calculated.
- We imposed magnitude limits (in all bands) of increasing brightness to the training data used to build CZRs. When the same magnitude limits were imposed on the test dataset, it is not surprising that a magnitude limit of 20.0 gave a several-percent improvement compared to my recreation of the Weinstein results. However, if the magnitude limit was not applied to the test data, a CZR-data magnitude limit of 25.0 gave the best results, which were slightly better than the results for my Weinstein recreation.
- Using an $N(z)$ weighting function does better than no weighting function by about 1%. The apparent magnitude weighting function improves redshift estimates by about 1%.
- From the “simulation” of adding additional bands, it is clear that using additional colors improves the photometric redshift estimates, though using non-adjacent colors yields worse results than the W04 method. When we use additional non-optical bands to increase the number of CZRs, the photometric redshift estimation success rate increases, but this may be due to the fact that only the brightest quasars with good photometry are present in the non-optical sample, which as we have shown yields a better CZR.

Table C.61 gives the mean statistics for a few of the best photometric redshift estimation techniques. The best photometric redshift estimates are made when the most parameters are included (i.e., as many bands as possible used to create the CZR, and results from multiple CZRs convolved to calculate

the PDF). We have applied extensive modifications to the W04 CZR algorithm, but found that there is no simple way to meaningfully improve the current success rate with the CZR technique; even the most effective modifications give only marginal improvements on the redshift estimate success rate. A parallel photometric redshift technique using machine learning algorithms has been developed within our group (Ball et al., 2007, 2008) with promising results.

Table B.1: Summary of CZR and Photometric Redshift Algorithm Variations

Parameter	Possible Variations
Binning	<i>overlapping</i> non-overlapping
Statistic	<i>mean</i> discrete median Gaussian median discrete mode Gaussian mode
SDSS Magnitude Type	<i>PSF</i> model fiber Petrosian convolve PDFs for multiple magnitude types
Treatment of Reddened Quasars	<i>removed</i> not removed redefined(?)
Error and Magnitude Limits	<i>not explicitly imposed</i> impose magnitude limits impose error limits impose combination of limits
PDF Weighting	no weight function <i>simple $N(z)$</i> apparent magnitude $N(m, z)$ luminosity function
Additional Bands	...

NOTE. – The parameter variation used by W04 is shown in italics.

Table B.2: Redshift binning schemes.

Variation	Divisions		z -bin Width		
	division1	division2	$z \leq \text{division1}$	division1 < $z \leq$ division2	$z > \text{division2}$
A	0.0	2.1	...	0.05	0.2
B	0.0	2.1	...	0.05	0.1
C	0.0	2.25	...	0.05	0.2
D	0.0	2.25	...	0.05	0.1
E	0.1	2.25	0.05	0.025	0.2
F	0.1	2.25	0.05	0.025	0.1
G	0.1	2.25	0.05	0.0125	0.2
H	0.1	2.25	0.05	0.0125	0.1

NOTE. – The (non-overlapping) bin schemes listed in the table above are based on what is referred to in this paper as the O2 (overlapping) binscheme. This scheme is used by Richards et al. (2001b) and Weinstein et al. (2004): bins are centered at intervals in redshift of 0.05; bins with centers $z \leq 2.15$ have width 0.075, bins with centers at $2.15 < z \leq 2.5$ have width 0.2, and bins with centers at $z > 2.5$ have width 0.5.

Table B.3: Parameters for Luminosity Function.

Fitting Parameter	Value
A_1	0.78
B_1	0.10
B_2	27.35
B_3	19.27
M^*	-26
z_{ref}	2.45
$\log(\Phi^*)$	-5.75

NOTE. – The values of these parameters are from Richards et al. (2006) using the “Fixed Power Law” form of the luminosity function they derived. Φ^* has units $\text{Mpc}^{-3}\text{mag}^{-1}$

Table B.4: Correlation coefficients between SDSS filter bands.

Bands	c_{ij}
c_{ug}	0.3
c_{ur}	0.2
c_{ui}	0.1
c_{uz}	0.05
c_{gr}	0.3
c_{gi}	0.2
c_{gz}	0.05
c_{ri}	0.3
c_{rz}	0.05
c_{iz}	0.05

NOTE. – The values in this table are estimated from Figure 7 in Scranton et al. (2005)

Table B.5: Catastrophic Failure Sections for Analysis.

Section	Range	# CF objects	# BALQSOs	% of section
1	$z_{phot} > 4.0$ and $z_{phot} > z_{spec}$	143	45	31.5
2	$2.4 < z_{phot} < 4.0$ and $z_{phot} > z_{spec}$	1078	396	36.7
2a	$2.4 < z_{phot} < 4.0$ and $z_{phot} < z_{spec}$	5	1	20.0
3	$z_{phot} < 2.4$ and $z_{phot} > z_{spec}$	3374	586	17.4
4	$z_{phot} < 2.4$ and $z_{phot} < z_{spec}$	2221	1273	57.4

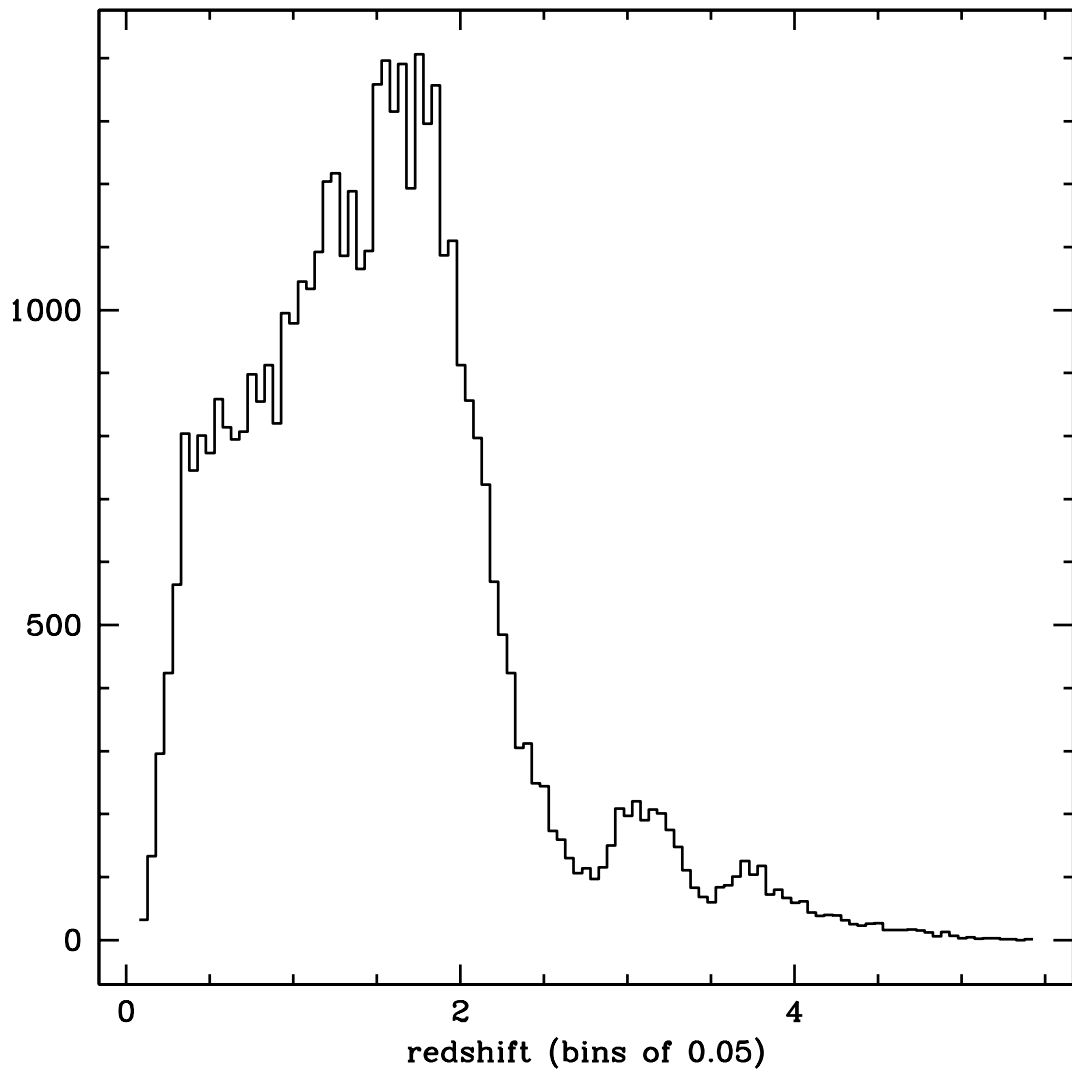


Figure B.1— Redshift distribution of the SDSS DR3 quasar sample.

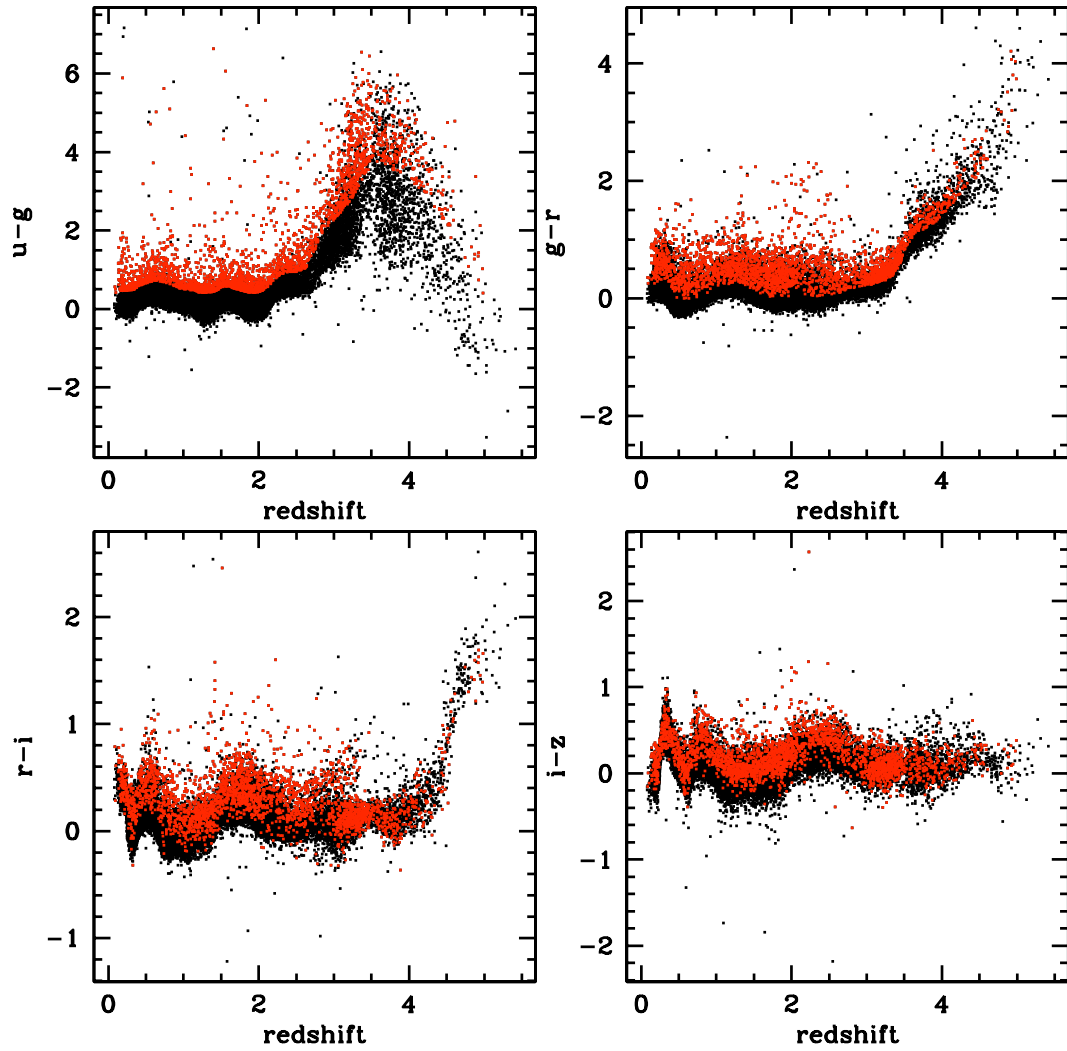


Figure B.2— Colors of SDSS DR3 quasars plotted as a function of redshift. The red points are those quasars that are considered reddened according to the scheme presented in Section B.3.1 (using the O2 binning scheme) and removed from the training set for the CZR (black points).

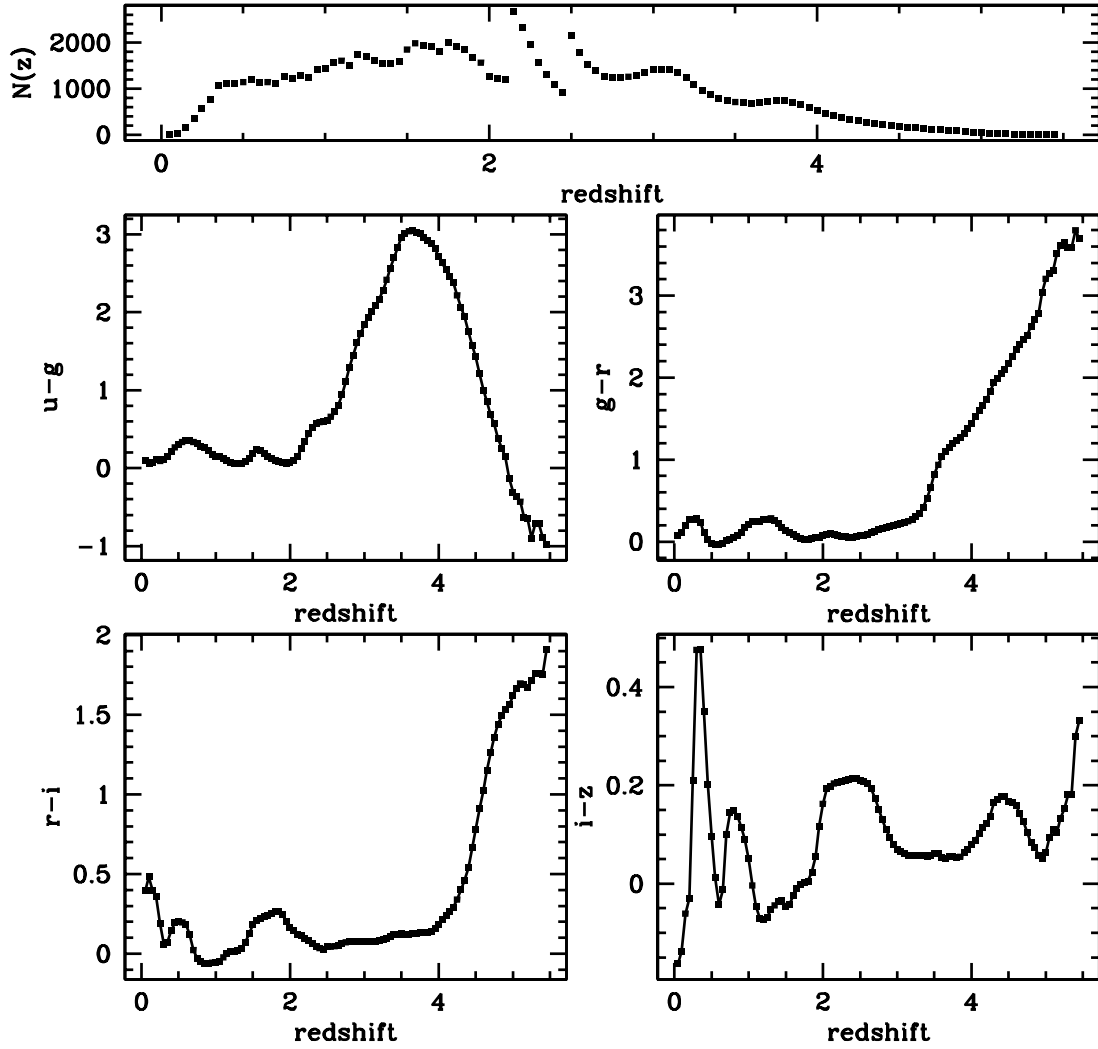


Figure B.3— Color-redshift relation (CZR) for the SDSS DR3 quasars according to the W04 scheme. The top panel shows the number distribution of quasars as a function of redshift.

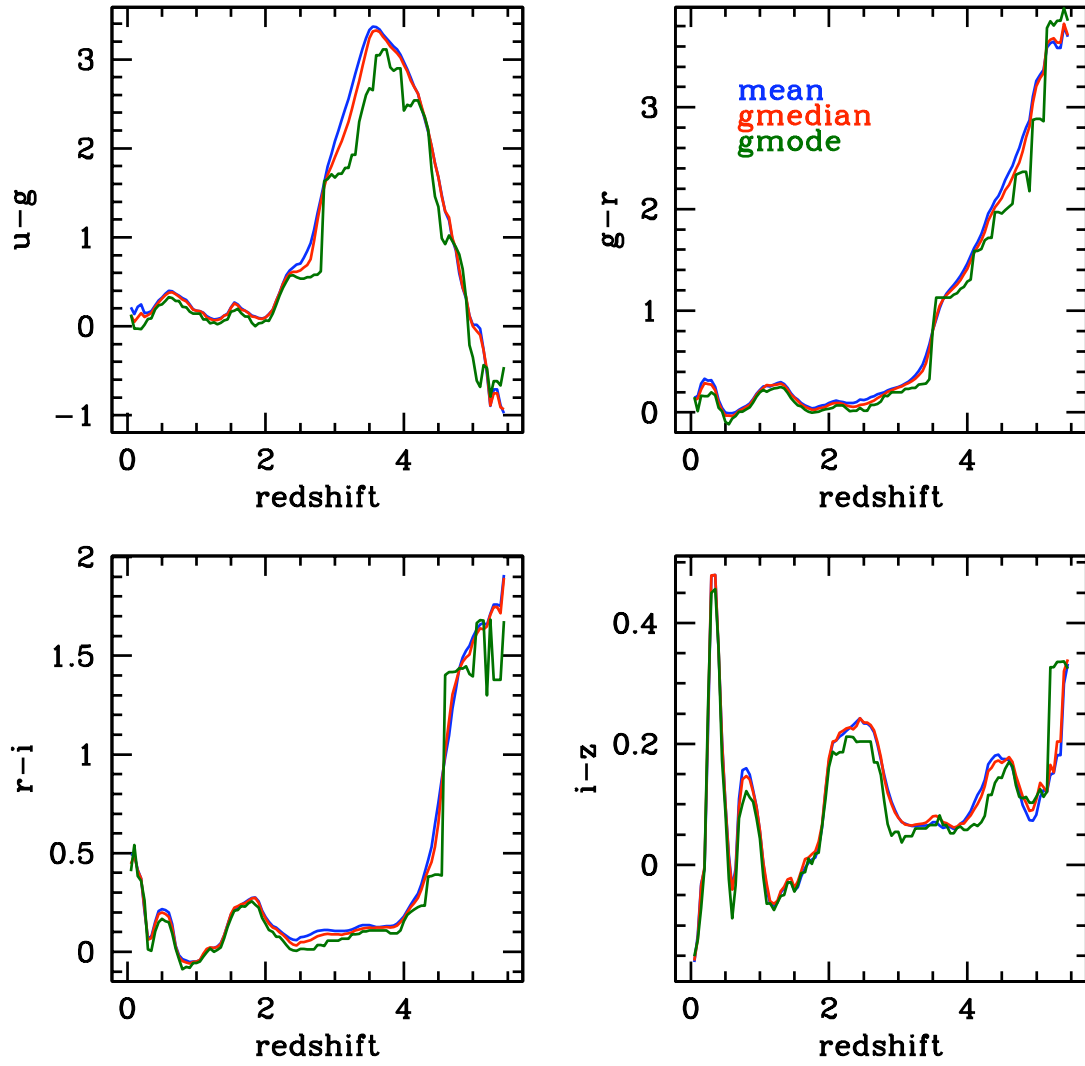


Figure B.4— Comparison of mean, gmedian, and gmode CZRs for the SDSS DR3 quasars using O2 binning.

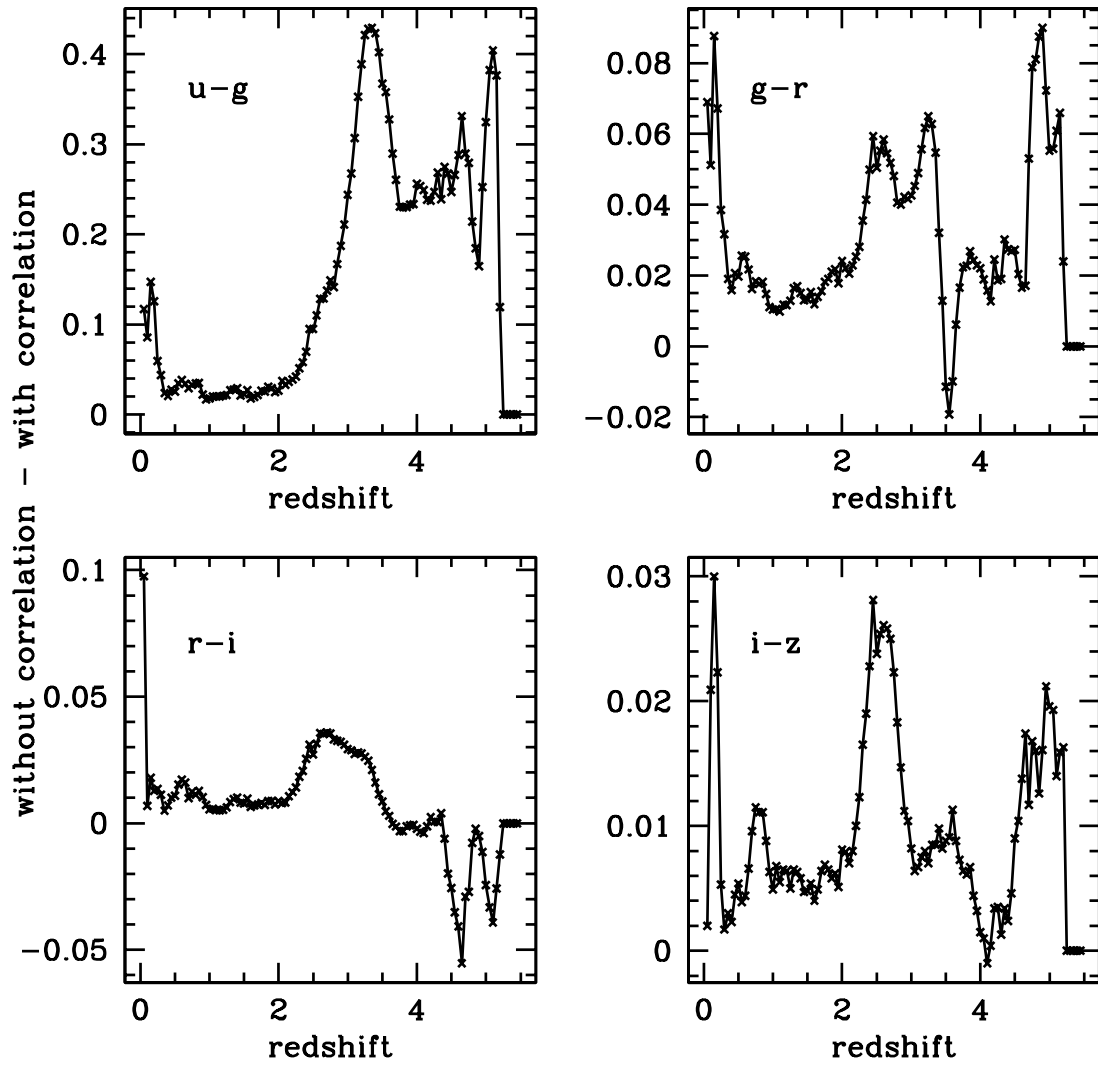


Figure B.5— The difference between mean CZRs that do and do not include covariance between the SDSS magnitude bands for the four SDSS colors (O2 binning).

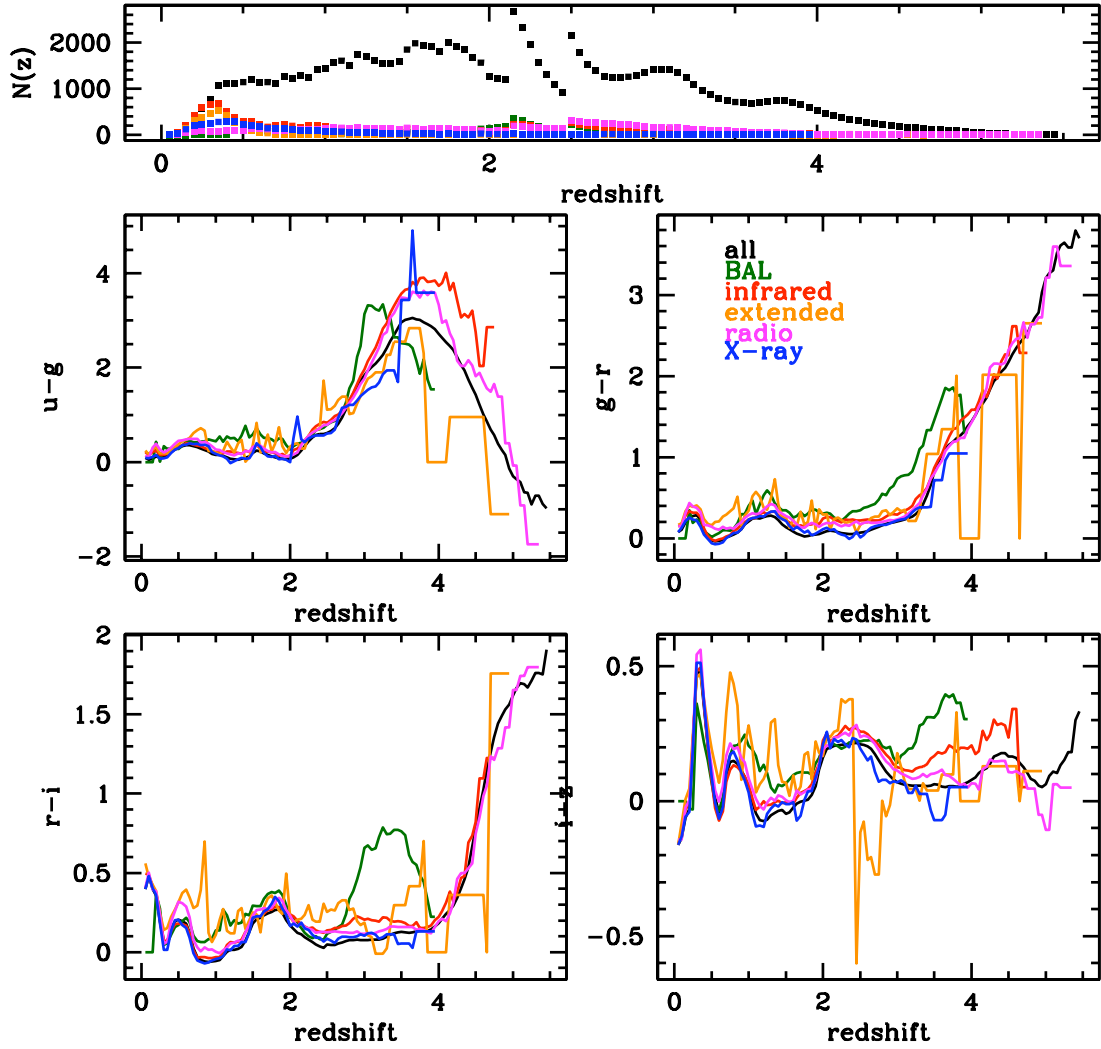


Figure B.6— Comparison of CZRs calculated according to the W04 scheme. The top panel shows the number distribution of quasars in each subsample as a function of redshift.

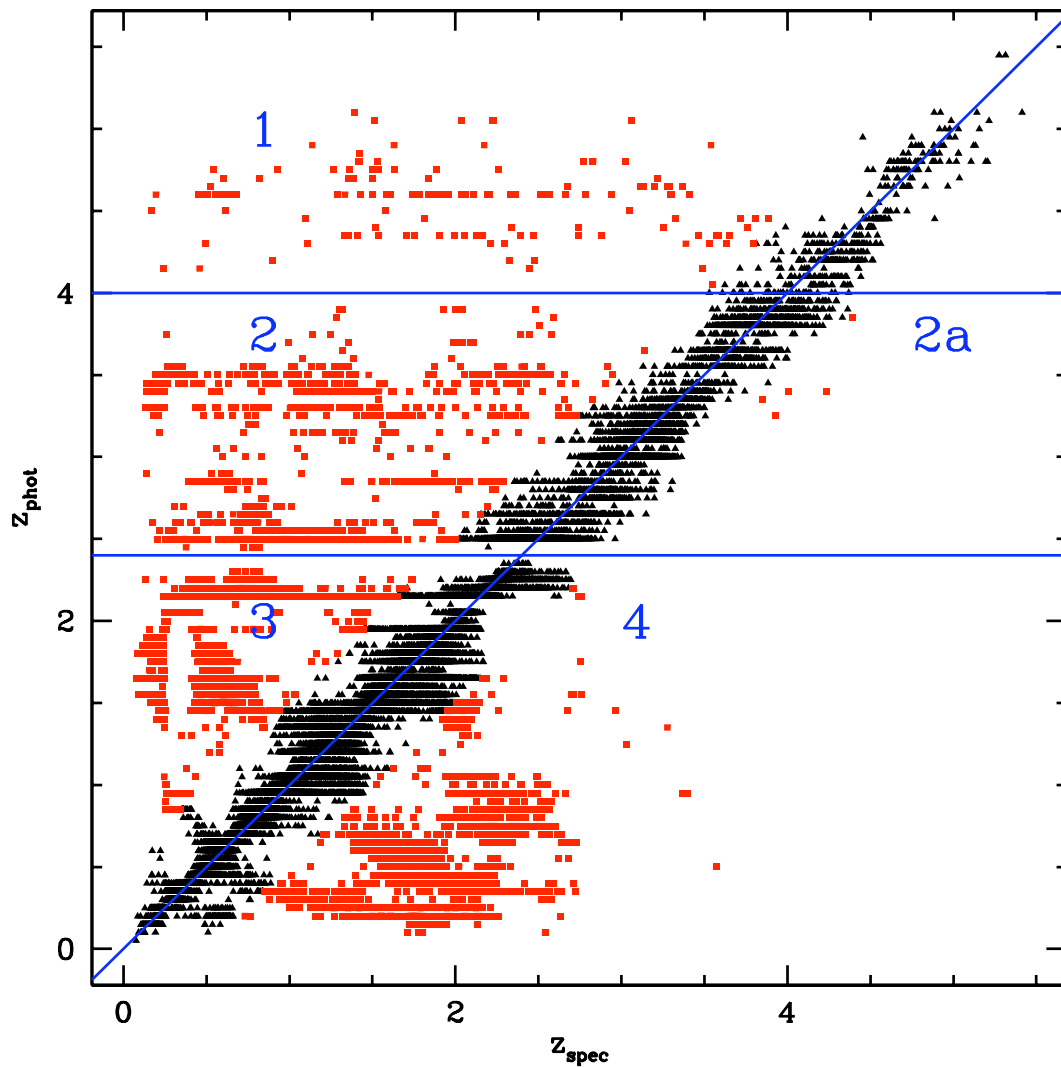


Figure B.7— Photometric redshift estimates are plotted against SDSS spectroscopic redshift for recreation of W04 algorithm. Catastrophic failures, where $|z_{\text{spec}} - z_{\text{phot}}| \geq 0.5$, are shown in red. Black points have $|z_{\text{spec}} - z_{\text{phot}}| < 0.5$. Divisions for the four catastrophic failure sections (in z_{phot}) are shown in blue.

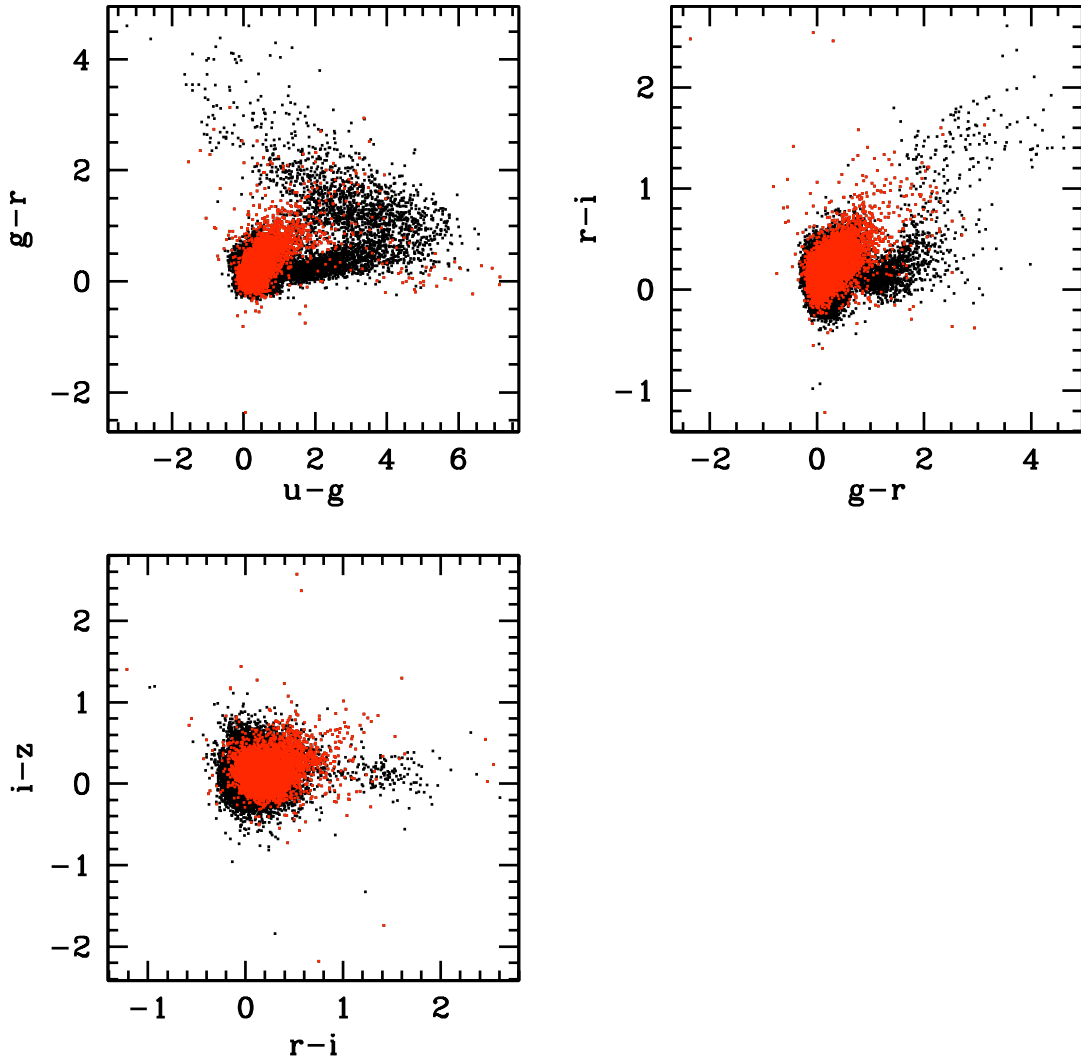


Figure B.8— Color-color plots for all 6,821 catastrophic failures (red points) superimposed on the entire quasar sample (black points)

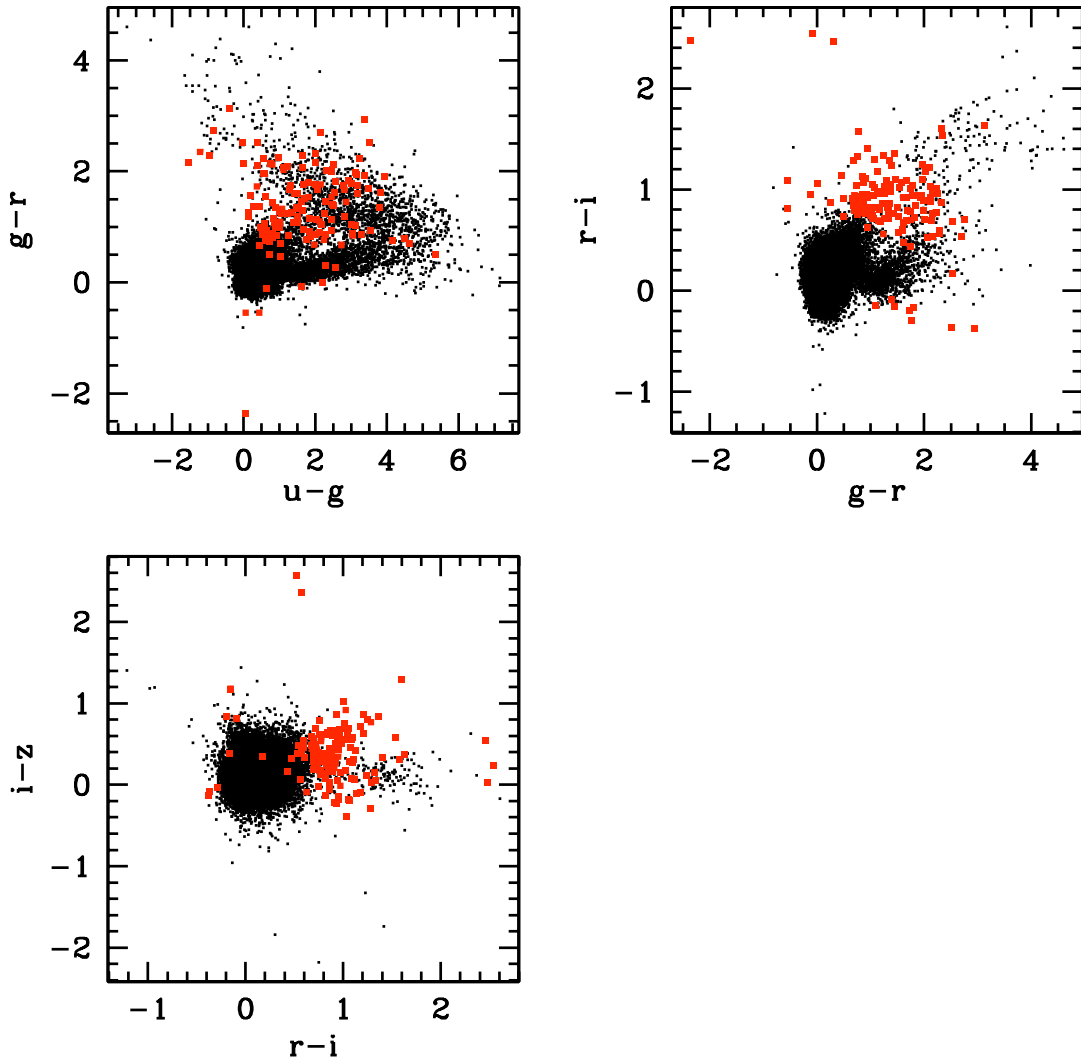


Figure B.9— Color-color plots for 143 quasars in catastrophic failure section 1 (red points). Since there are so few points in this section, the points have been enlarged for easy viewing. Black points show all quasars in the sample (including other catastrophic failures).

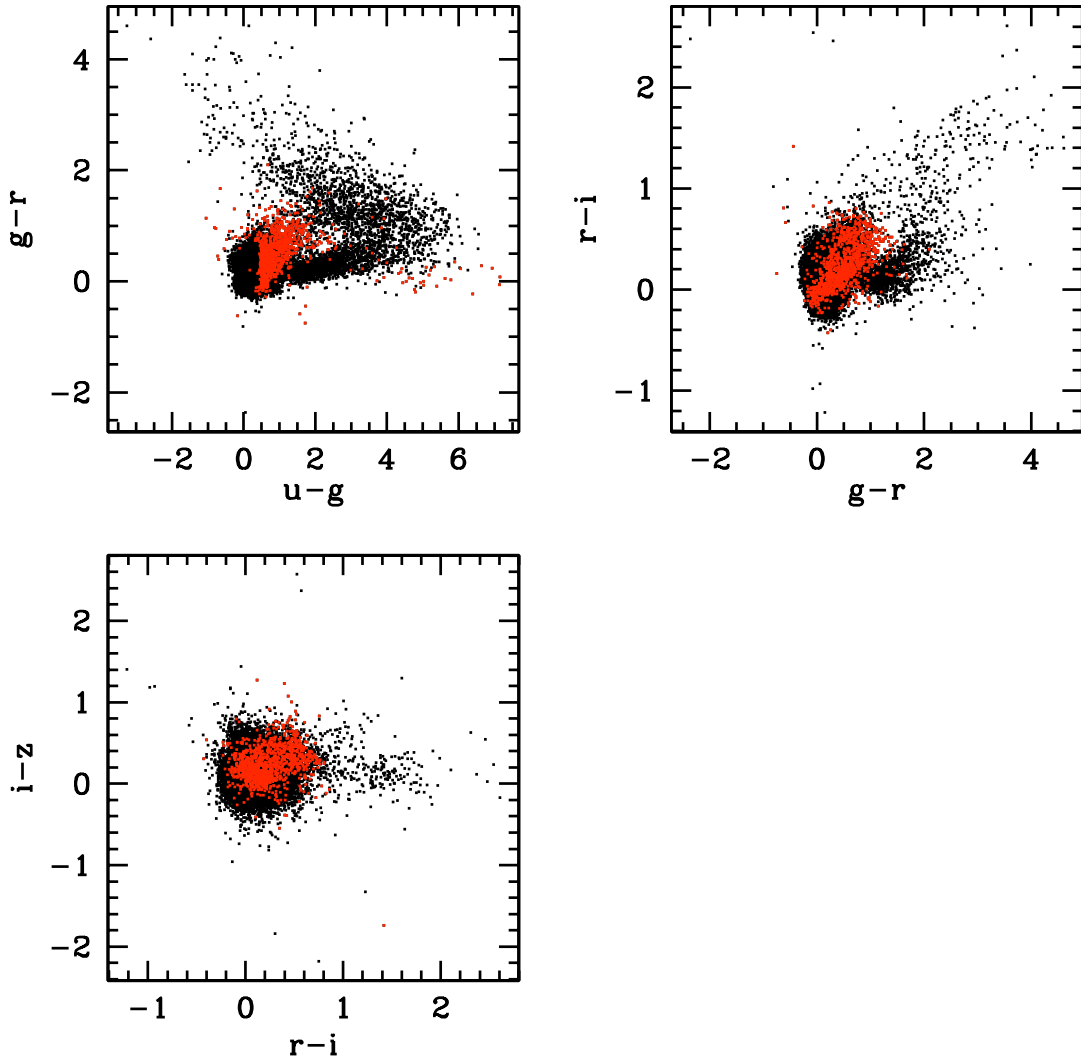


Figure B.10— Color-color plots for 1,078 quasars in catastrophic failure section 2 (red points). Black points show all quasars in the sample (including other catastrophic failures).

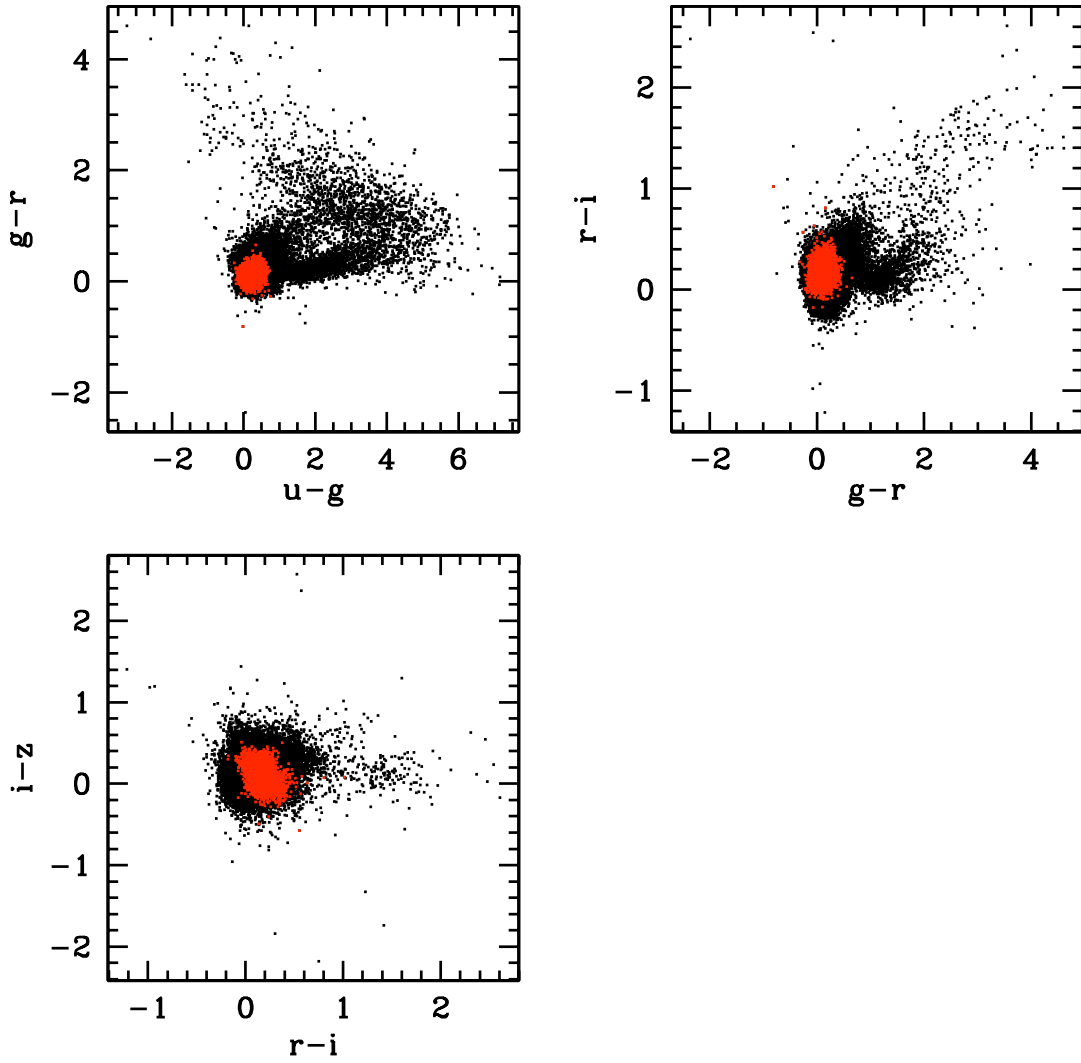


Figure B.11— Color-color plots for 3,374 quasars in catastrophic failure section 3 (red points). Black points show all quasars in the sample (including other catastrophic failures).

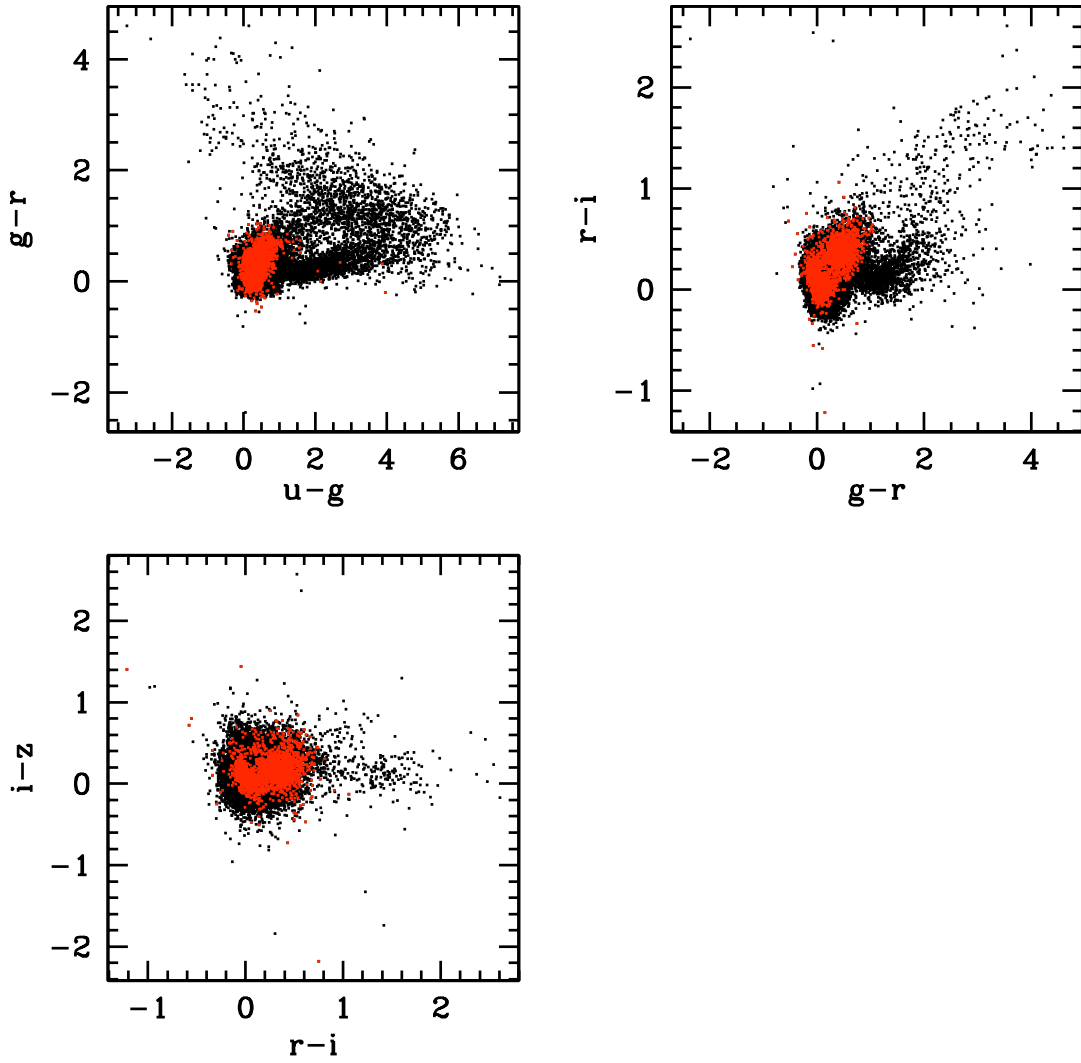


Figure B.12— Color-color plots for 2,221 quasars in catastrophic failure section 4 (red points). Black points show all quasars in the sample (including other catastrophic failures).

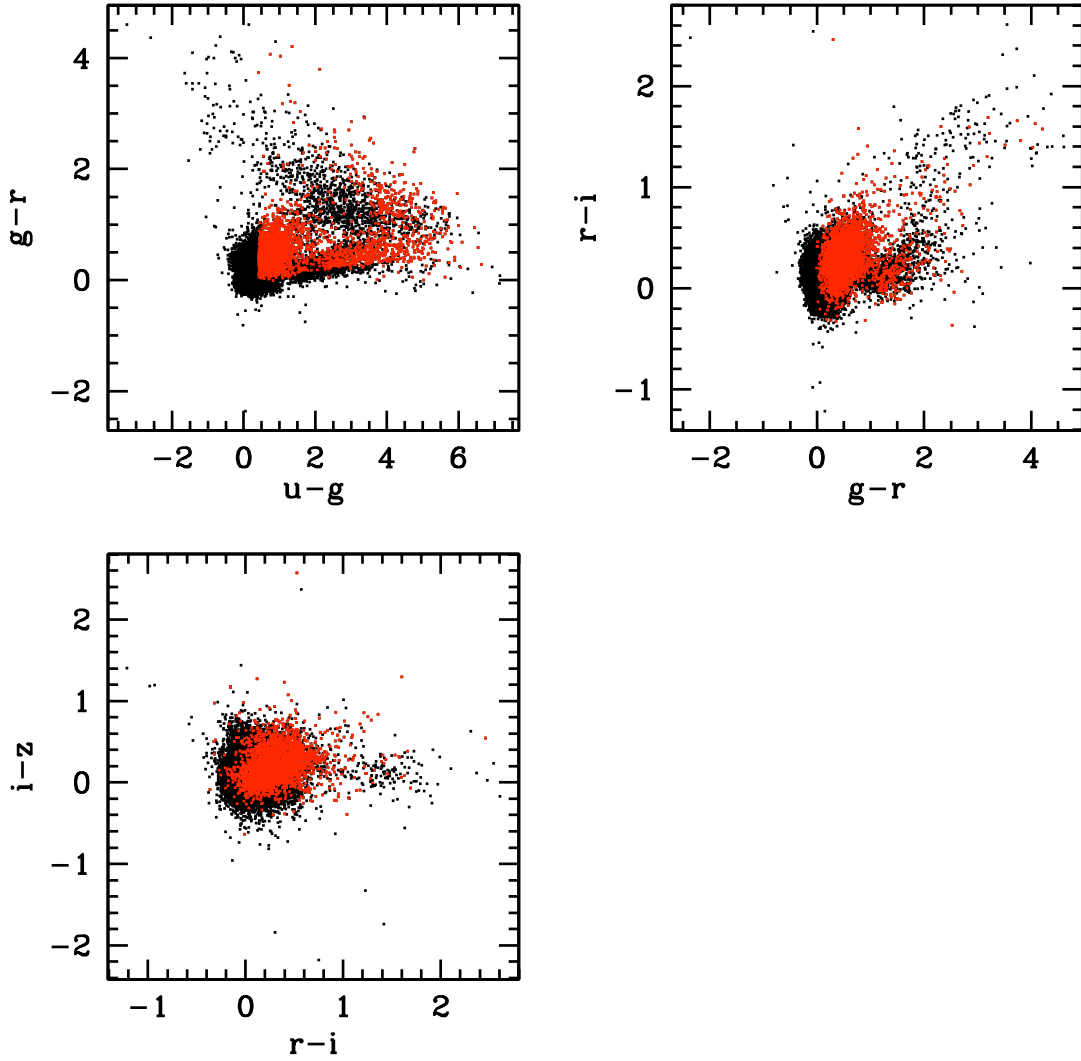


Figure B.13— Color-color plots for 2,771 reddened quasars classified according to the W04 algorithm. Black points show all quasars in the sample.

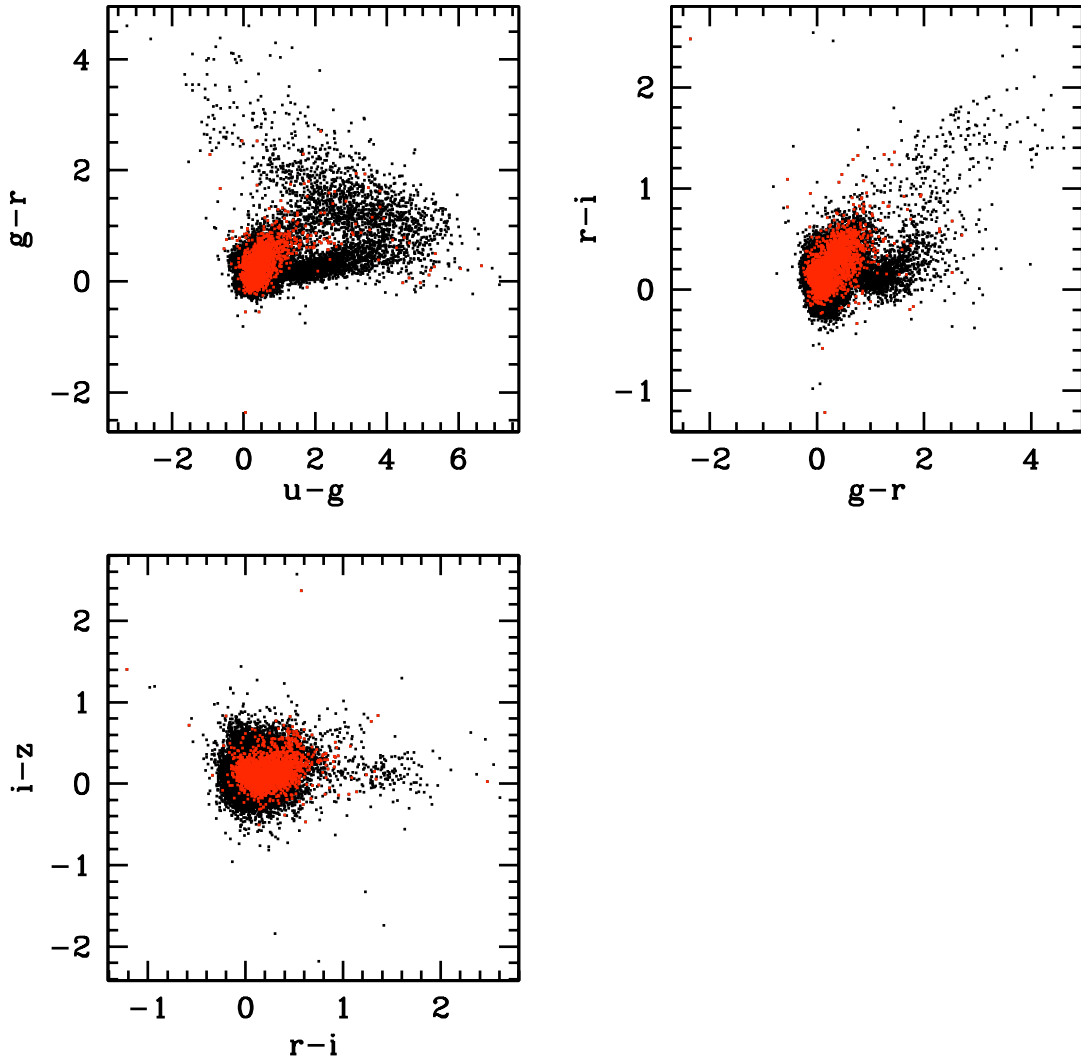


Figure B.14— Color-color plots for 2,302 BALQSOs that are catastrophic failures (red points). Black points show all other quasars in the sample (including other catastrophic failures).

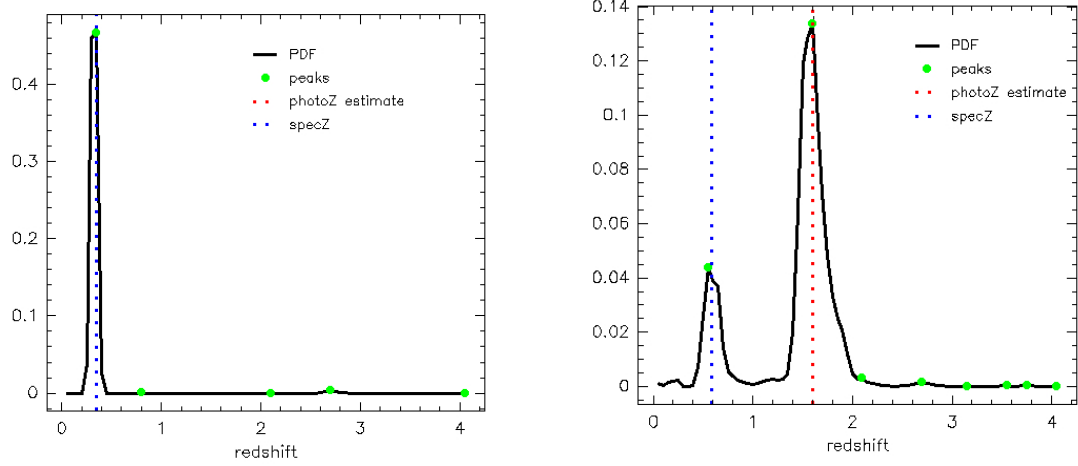


Figure B.15— *Left*: PDF in which the peak corresponds to the correct redshift. *Right*: PDF in which the second-highest peak corresponds to the correct redshift.

Appendix C

Tables of Results for CZR Based Photometric Redshift Estimator

Table C.1: PDF Photometric Redshift Estimates using mean, Simple Weighting Function and removing reddened quasars.

Mag	Bins	Stat	Red?	Weighting	CZR Parameters										Catastrophic Failures		not CF ⁴
					< 0.05	< 0.1	< 0.2	$ z_{spec} - z_{phot} ^1$	< 0.3	CF	% CF	Common ²	%	Diff ³	%		
psf	O2	mean	yes	SimpleWF	0.3835	0.5889	0.7612	0.8232	0.8232	6821	0.1469		
psf	A	mean	yes	SimpleWF	0.3878	0.5933	0.7612	0.8192	0.8192	6822	0.1470	5645	0.8275	693	0.1016	1176	
psf	C	mean	yes	SimpleWF	0.3975	0.6072	0.7700	0.8258	0.8258	6524	0.1405	5189	0.7954	875	0.1341	1632	
psf	E	mean	yes	SimpleWF	0.3967	0.5983	0.7671	0.8265	0.8265	6503	0.1401	5093	0.7832	942	0.1449	1728	
psf	G	mean	yes	SimpleWF	0.3930	0.5905	0.7569	0.8175	0.8175	6872	0.1480	4926	0.7168	1459	0.2123	1895	
model	O2	mean	yes	SimpleWF	0.3940	0.5988	0.7697	0.8271	0.8271	6690	0.1443	5533	0.8271	689	0.1030	1288	
model	A	mean	yes	SimpleWF	0.3948	0.5978	0.7619	0.8179	0.8179	6921	0.1493	5255	0.7593	1187	0.1715	1566	
model	C	mean	yes	SimpleWF	0.4086	0.6151	0.7750	0.8290	0.8290	6418	0.1384	4837	0.7537	1132	0.1764	1984	
model	E	mean	yes	SimpleWF	0.4123	0.6104	0.7714	0.8305	0.8305	6360	0.1372	4747	0.7464	1174	0.1846	2074	
model	G	mean	yes	SimpleWF	0.4083	0.6007	0.7636	0.8238	0.8238	6673	0.1439	4682	0.7016	1522	0.2281	2139	
fiber	O2	mean	yes	SimpleWF	0.3753	0.5755	0.7533	0.8132	0.8132	7228	0.1559	5074	0.7020	1622	0.2244	1747	
fiber	A	mean	yes	SimpleWF	0.3752	0.5711	0.7363	0.7925	0.7925	7973	0.1720	5006	0.6279	2386	0.2993	1815	
fiber	C	mean	yes	SimpleWF	0.3908	0.5932	0.7583	0.8138	0.8138	6935	0.1496	4660	0.6720	1767	0.2548	2161	
fiber	E	mean	yes	SimpleWF	0.3941	0.5903	0.7555	0.8150	0.8150	6878	0.1484	4594	0.6679	1782	0.2591	2227	
fiber	G	mean	yes	SimpleWF	0.3859	0.5807	0.7494	0.8092	0.8092	7160	0.1544	4474	0.6249	2156	0.3011	2347	
petro	O2	mean	yes	SimpleWF	0.3159	0.5018	0.6883	0.7616	0.7616	8701	0.1877	4659	0.5355	3453	0.3969	2162	
petro	A	mean	yes	SimpleWF	0.3223	0.5082	0.6794	0.7476	0.7476	9306	0.2007	4557	0.4897	4113	0.4420	2264	
petro	C	mean	yes	SimpleWF	0.3351	0.5276	0.7005	0.7666	0.7666	8449	0.1823	4200	0.4971	3678	0.4353	2621	
petro	E	mean	yes	SimpleWF	0.3410	0.5244	0.6933	0.7656	0.7656	8362	0.1804	4246	0.5078	3525	0.4215	2575	
petro	G	mean	yes	SimpleWF	0.3307	0.5154	0.6866	0.7576	0.7576	8810	0.1900	4244	0.4817	3958	0.4493	2577	

¹ These columns give the fraction of objects that have $|z_{spec} - z_{phot}|$ less than the value at the column header.

² Number of CF objects that are also classified as CF objects when the W04 algorithm generates their photometric redshifts.

³ Number of CF objects that were not classified as CF objects when the W04 algorithm generates their photometric redshifts.

⁴ Objects that are classified as CF objects when the W04 algorithm generates their photometric redshifts, but not in the current algorithm.

Table C.2: PDF Photometric Redshift Estimates for low-redshift quasars using mean, Simple Weighting Function and removing reddened quasars.

CZR Parameters					$z_{spec} \leq \text{division2}$			
Mag	Bins	Stat	Red?	Weighting	< 0.05	< 0.1	< 0.2	< 0.3
psf	O2	mean	yes	SimpleWF	0.3947	0.6036	0.7689	0.8196
psf	A	mean	yes	SimpleWF	0.4065	0.6063	0.7648	0.8155
psf	C	mean	yes	SimpleWF	0.4177	0.6222	0.7748	0.8215
psf	E	mean	yes	SimpleWF	0.4153	0.6076	0.7660	0.8165
psf	G	mean	yes	SimpleWF	0.4102	0.5969	0.7520	0.8039
model	O2	mean	yes	SimpleWF	0.4066	0.6152	0.7761	0.8252
model	A	mean	yes	SimpleWF	0.4148	0.6121	0.7667	0.8148
model	C	mean	yes	SimpleWF	0.4302	0.6314	0.7807	0.8250
model	E	mean	yes	SimpleWF	0.4331	0.6219	0.7712	0.8212
model	G	mean	yes	SimpleWF	0.4278	0.6090	0.7603	0.8112
fiber	O2	mean	yes	SimpleWF	0.3891	0.5935	0.7588	0.8086
fiber	A	mean	yes	SimpleWF	0.3911	0.5809	0.7369	0.7868
fiber	C	mean	yes	SimpleWF	0.4097	0.6055	0.7610	0.8081
fiber	E	mean	yes	SimpleWF	0.4119	0.5982	0.7523	0.8032
fiber	G	mean	yes	SimpleWF	0.4018	0.5855	0.7432	0.7942
petro	O2	mean	yes	SimpleWF	0.3275	0.5184	0.6956	0.7586
petro	A	mean	yes	SimpleWF	0.3351	0.5180	0.6839	0.7439
petro	C	mean	yes	SimpleWF	0.3498	0.5377	0.7043	0.7626
petro	E	mean	yes	SimpleWF	0.3547	0.5286	0.6885	0.7532
petro	G	mean	yes	SimpleWF	0.3418	0.5155	0.6773	0.7400

Table C.3: PDF Photometric Redshift Estimates for high-redshift quasars using mean, Simple Weighting Function and removing reddened quasars.

CZR Parameters					$z_{spec} > \text{division2}$			
Mag	Bins	Stat	Red?	Weighting	< 0.05	< 0.1	< 0.2	< 0.3
psf	O2	mean	yes	SimpleWF	0.3303	0.5189	0.7458	0.8403
psf	A	mean	yes	SimpleWF	0.2990	0.5318	0.7438	0.8369
psf	C	mean	yes	SimpleWF	0.2642	0.5079	0.7382	0.8544
psf	E	mean	yes	SimpleWF	0.2740	0.5368	0.7741	0.8927
psf	G	mean	yes	SimpleWF	0.2791	0.5482	0.7887	0.9076
model	O2	mean	yes	SimpleWF	0.3343	0.5208	0.7389	0.8359
model	A	mean	yes	SimpleWF	0.3000	0.5295	0.7388	0.8327
model	C	mean	yes	SimpleWF	0.2656	0.5075	0.7373	0.8553
model	E	mean	yes	SimpleWF	0.2743	0.5349	0.7723	0.8925
model	G	mean	yes	SimpleWF	0.2792	0.5454	0.7856	0.9066
fiber	O2	mean	yes	SimpleWF	0.3098	0.4901	0.7272	0.8348
fiber	A	mean	yes	SimpleWF	0.2998	0.5243	0.7334	0.8199
fiber	C	mean	yes	SimpleWF	0.2656	0.5117	0.7400	0.8516
fiber	E	mean	yes	SimpleWF	0.2765	0.5387	0.7768	0.8932
fiber	G	mean	yes	SimpleWF	0.2808	0.5488	0.7909	0.9083
petro	O2	mean	yes	SimpleWF	0.2605	0.4233	0.6536	0.7760
petro	A	mean	yes	SimpleWF	0.2611	0.4619	0.6582	0.7653
petro	C	mean	yes	SimpleWF	0.2379	0.4613	0.6759	0.7931
petro	E	mean	yes	SimpleWF	0.2510	0.4961	0.7245	0.8476
petro	G	mean	yes	SimpleWF	0.2576	0.5149	0.7480	0.8741

Table C.4: PDF Photometric Redshift Estimates using gmedian, Simple Weighting Function and removing reddened quasars.

Mag	Bins	CZR Parameters			$ z_{spec} - z_{phot} $				Catastrophic Failures				not CF	
		Stat	Red?	Weighting	< 0.05	< 0.1	< 0.2	< 0.3	CF	% CF	Common	%		Diff
psf	O2	mean	yes	SimpleWF	0.3835	0.5889	0.7648	0.8232	6821	0.1469
psf	O2	gmedian	yes	SimpleWF	0.3787	0.5840	0.7577	0.8193	6933	0.1494	6062	0.8744	382	0.0551
psf	A	gmedian	yes	SimpleWF	0.3857	0.5892	0.7576	0.8172	6856	0.1477	5636	0.8221	727	0.1060
psf	C	gmedian	yes	SimpleWF	0.3950	0.6023	0.7661	0.8235	6600	0.1422	5247	0.7950	885	0.1341
psf	E	gmedian	yes	SimpleWF	0.3958	0.5962	0.7632	0.8228	6634	0.1429	5127	0.7728	1038	0.1565
psf	G	gmedian	yes	SimpleWF	0.3906	0.5879	0.7535	0.8149	6961	0.1500	4927	0.7078	1537	0.2208
model	O2	gmedian	yes	SimpleWF	0.3871	0.5898	0.7592	0.8190	6944	0.1498	5495	0.7913	958	0.1380
model	A	gmedian	yes	SimpleWF	0.3969	0.5991	0.7612	0.8184	6788	0.1464	5238	0.7717	1078	0.1588
model	C	gmedian	yes	SimpleWF	0.4064	0.6107	0.7691	0.8246	6513	0.1405	4896	0.7517	1166	0.1790
model	E	gmedian	yes	SimpleWF	0.4124	0.6079	0.7676	0.8264	6494	0.1401	4761	0.7331	1275	0.1963
model	G	gmedian	yes	SimpleWF	0.4056	0.5979	0.7596	0.8202	6764	0.1459	4643	0.6864	1638	0.2422
fiber	O2	gmedian	yes	SimpleWF	0.3750	0.5725	0.7491	0.8117	7235	0.1561	5108	0.7060	1603	0.2216
fiber	A	gmedian	yes	SimpleWF	0.3750	0.5699	0.7357	0.7927	7866	0.1697	5013	0.6373	2276	0.2893
fiber	C	gmedian	yes	SimpleWF	0.3881	0.5886	0.7537	0.8104	6990	0.1508	4695	0.6717	1780	0.2546
fiber	E	gmedian	yes	SimpleWF	0.3920	0.5888	0.7518	0.8123	6934	0.1496	4610	0.6648	1811	0.2612
fiber	G	gmedian	yes	SimpleWF	0.3860	0.5799	0.7464	0.8064	7214	0.1556	4485	0.6217	2193	0.3040
petro	O2	gmedian	yes	SimpleWF	0.3134	0.4972	0.6815	0.7568	8842	0.1907	4696	0.5311	3538	0.4001
petro	A	gmedian	yes	SimpleWF	0.3233	0.5083	0.6816	0.7506	9026	0.1947	4560	0.5052	3846	0.4261
petro	C	gmedian	yes	SimpleWF	0.3280	0.5173	0.6920	0.7585	8717	0.1880	4305	0.4939	3825	0.4388
petro	E	gmedian	yes	SimpleWF	0.3370	0.5192	0.6880	0.7604	8549	0.1844	4308	0.5039	3642	0.4260
petro	G	gmedian	yes	SimpleWF	0.3297	0.5105	0.6824	0.7548	8884	0.1916	4294	0.4833	3972	0.4471

Table C.5: PDF Photometric Redshift Estimates for low-redshift quasars using gmedian, Simple Weighting Function and removing reddened quasars.

CZR Parameters					$z_{spec} \leq \text{division2}$			
Mag	Bins	Stat	Red?	Weighting	< 0.05	< 0.1	< 0.2	< 0.3
psf	O2	mean	yes	SimpleWF	0.3947	0.6036	0.7689	0.8196
psf	O2	gmedian	yes	SimpleWF	0.3899	0.5982	0.7614	0.8157
psf	A	gmedian	yes	SimpleWF	0.4043	0.6019	0.7610	0.8136
psf	C	gmedian	yes	SimpleWF	0.4147	0.6160	0.7694	0.8184
psf	E	gmedian	yes	SimpleWF	0.4141	0.6048	0.7609	0.8120
psf	G	gmedian	yes	SimpleWF	0.4075	0.5937	0.7479	0.8009
model	O2	gmedian	yes	SimpleWF	0.3989	0.6045	0.7646	0.8167
model	A	gmedian	yes	SimpleWF	0.4172	0.6137	0.7660	0.8156
model	C	gmedian	yes	SimpleWF	0.4277	0.6263	0.7736	0.8198
model	E	gmedian	yes	SimpleWF	0.4333	0.6192	0.7670	0.8166
model	G	gmedian	yes	SimpleWF	0.4248	0.6060	0.7555	0.8072
fiber	O2	gmedian	yes	SimpleWF	0.3884	0.5884	0.7533	0.8068
fiber	A	gmedian	yes	SimpleWF	0.3913	0.5802	0.7366	0.7875
fiber	C	gmedian	yes	SimpleWF	0.4070	0.6004	0.7559	0.8041
fiber	E	gmedian	yes	SimpleWF	0.4101	0.5968	0.7487	0.8005
fiber	G	gmedian	yes	SimpleWF	0.4025	0.5851	0.7404	0.7916
petro	O2	gmedian	yes	SimpleWF	0.3249	0.5126	0.6879	0.7543
petro	A	gmedian	yes	SimpleWF	0.3378	0.5210	0.6894	0.7498
petro	C	gmedian	yes	SimpleWF	0.3418	0.5262	0.6940	0.7526
petro	E	gmedian	yes	SimpleWF	0.3504	0.5231	0.6822	0.7468
petro	G	gmedian	yes	SimpleWF	0.3410	0.5104	0.6723	0.7364

Table C.6: PDF Photometric Redshift Estimates for high-redshift quasars using gmedian, Simple Weighting Function and removing reddened quasars.

CZR Parameters					$z_{spec} > \text{division2}$			
Mag	Bins	Stat	Red?	Weighting	< 0.05	< 0.1	< 0.2	< 0.3
psf	O2	mean	yes	SimpleWF	0.3303	0.5189	0.7458	0.8403
psf	O2	gmedian	yes	SimpleWF	0.3255	0.5165	0.7399	0.8367
psf	A	gmedian	yes	SimpleWF	0.2974	0.5286	0.7412	0.8345
psf	C	gmedian	yes	SimpleWF	0.2652	0.5115	0.7441	0.8575
psf	E	gmedian	yes	SimpleWF	0.2752	0.5397	0.7785	0.8939
psf	G	gmedian	yes	SimpleWF	0.2796	0.5495	0.7910	0.9071
model	O2	gmedian	yes	SimpleWF	0.3310	0.5204	0.7337	0.8301
model	A	gmedian	yes	SimpleWF	0.3001	0.5300	0.7383	0.8318
model	C	gmedian	yes	SimpleWF	0.2661	0.5078	0.7393	0.8561
model	E	gmedian	yes	SimpleWF	0.2743	0.5331	0.7718	0.8907
model	G	gmedian	yes	SimpleWF	0.2786	0.5445	0.7867	0.9066
fiber	O2	gmedian	yes	SimpleWF	0.3113	0.4965	0.7291	0.8348
fiber	A	gmedian	yes	SimpleWF	0.2978	0.5212	0.7315	0.8172
fiber	C	gmedian	yes	SimpleWF	0.2631	0.5106	0.7390	0.8523
fiber	E	gmedian	yes	SimpleWF	0.2724	0.5359	0.7727	0.8900
fiber	G	gmedian	yes	SimpleWF	0.2765	0.5454	0.7861	0.9045
petro	O2	gmedian	yes	SimpleWF	0.2590	0.4235	0.6510	0.7689
petro	A	gmedian	yes	SimpleWF	0.2548	0.4479	0.6446	0.7544
petro	C	gmedian	yes	SimpleWF	0.2364	0.4589	0.6790	0.7972
petro	E	gmedian	yes	SimpleWF	0.2484	0.4930	0.7260	0.8501
petro	G	gmedian	yes	SimpleWF	0.2553	0.5114	0.7496	0.8764

Table C.7: PDF Photometric Redshift Estimates using gmode, Simple Weighting Function and removing reddened quasars.

Mag		Bins		Stat		Red?		Weighting		$ z_{spec} - z_{phot} $			CF		% CF		Common		Diff		% Diff		not CF	
psf	O2	mean	yes	SimpleWF	< 0.05	< 0.1	< 0.2	< 0.3	CF	% CF	Common	%	Diff	%	
psf	O2	gmode	yes	SimpleWF	0.3835	0.5889	0.7648	0.8232	6821	0.1469	
psf	O2	gmode	yes	SimpleWF	0.3675	0.5696	0.7451	0.8105	7224	0.1556	5795	0.8022	924	0.1279	1026									
psf	A	gmode	yes	SimpleWF	0.3745	0.5743	0.7434	0.8058	7214	0.1554	5489	0.7609	1209	0.1676	1332									
psf	C	gmode	yes	SimpleWF	0.3866	0.5924	0.7586	0.8181	6722	0.1448	5283	0.7859	955	0.1421	1538									
psf	E	gmode	yes	SimpleWF	0.3831	0.5824	0.7526	0.8144	6984	0.1505	5113	0.7321	1374	0.1967	1708									
psf	G	gmode	yes	SimpleWF	0.3725	0.5706	0.7428	0.8043	7388	0.1592	4933	0.6677	1920	0.2599	1888									
model	O2	gmode	yes	SimpleWF	0.3743	0.5731	0.7436	0.8066	7379	0.1592	5361	0.7265	1500	0.2033	1460									
model	A	gmode	yes	SimpleWF	0.3766	0.5734	0.7376	0.7977	7544	0.1627	5118	0.6784	1891	0.2507	1703									
model	C	gmode	yes	SimpleWF	0.3916	0.5961	0.7598	0.8188	6664	0.1437	4917	0.7378	1262	0.1894	1904									
model	E	gmode	yes	SimpleWF	0.3910	0.5894	0.7583	0.8190	6785	0.1464	4758	0.7013	1541	0.2271	2063									
model	G	gmode	yes	SimpleWF	0.3766	0.5721	0.7434	0.8054	7353	0.1586	4662	0.6340	2163	0.2942	2159									
fiber	O2	gmode	yes	SimpleWF	0.3589	0.5549	0.7329	0.7971	7696	0.1660	4971	0.6459	2173	0.2824	1850									
fiber	A	gmode	yes	SimpleWF	0.3596	0.5570	0.7288	0.7927	7669	0.1654	4885	0.6370	2222	0.2897	1936									
fiber	C	gmode	yes	SimpleWF	0.3650	0.5658	0.7373	0.7992	7432	0.1603	4716	0.6346	2162	0.2909	2105									
fiber	E	gmode	yes	SimpleWF	0.3659	0.5635	0.7332	0.7967	7631	0.1646	4669	0.6118	2389	0.3131	2152									
fiber	G	gmode	yes	SimpleWF	0.3515	0.5437	0.7213	0.7854	8194	0.1767	4584	0.5594	2999	0.3660	2237									
petro	O2	gmode	yes	SimpleWF	0.3008	0.4788	0.6616	0.7450	9025	0.1947	4647	0.5149	3759	0.4165	2174									
petro	A	gmode	yes	SimpleWF	0.3047	0.4852	0.6574	0.7342	9634	0.2078	4573	0.4747	4396	0.4563	2248									
petro	C	gmode	yes	SimpleWF	0.3133	0.5010	0.6764	0.7510	8885	0.1917	4348	0.4894	3940	0.4434	2473									
petro	E	gmode	yes	SimpleWF	0.3156	0.4964	0.6741	0.7497	8980	0.1937	4351	0.4845	4011	0.4467	2470									
petro	G	gmode	yes	SimpleWF	0.2978	0.4776	0.6551	0.7296	9976	0.2152	4373	0.4384	4897	0.4909	2448									

Table C.8: PDF Photometric Redshift Estimates for low-redshift quasars using gmode, Simple Weighting Function and removing reddened quasars.

CZR Parameters					$z_{spec} \leq \text{division2}$			
Mag	Bins	Stat	Red?	Weighting	< 0.05	< 0.1	< 0.2	< 0.3
psf	O2	mean	yes	SimpleWF	0.3947	0.6036	0.7689	0.8196
psf	O2	gmode	yes	SimpleWF	0.3745	0.5808	0.7469	0.8026
psf	A	gmode	yes	SimpleWF	0.3910	0.5852	0.7435	0.7975
psf	C	gmode	yes	SimpleWF	0.4045	0.6035	0.7589	0.8094
psf	E	gmode	yes	SimpleWF	0.3995	0.5893	0.7492	0.8023
psf	G	gmode	yes	SimpleWF	0.3869	0.5746	0.7363	0.7890
model	O2	gmode	yes	SimpleWF	0.3838	0.5868	0.7460	0.7988
model	A	gmode	yes	SimpleWF	0.3932	0.5846	0.7381	0.7890
model	C	gmode	yes	SimpleWF	0.4104	0.6078	0.7606	0.8100
model	E	gmode	yes	SimpleWF	0.4091	0.5974	0.7556	0.8069
model	G	gmode	yes	SimpleWF	0.3921	0.5769	0.7377	0.7901
fiber	O2	gmode	yes	SimpleWF	0.3686	0.5680	0.7327	0.7868
fiber	A	gmode	yes	SimpleWF	0.3748	0.5677	0.7297	0.7859
fiber	C	gmode	yes	SimpleWF	0.3806	0.5737	0.7356	0.7890
fiber	E	gmode	yes	SimpleWF	0.3809	0.5686	0.7278	0.7826
fiber	G	gmode	yes	SimpleWF	0.3638	0.5448	0.7128	0.7683
petro	O2	gmode	yes	SimpleWF	0.3074	0.4884	0.6619	0.7366
petro	A	gmode	yes	SimpleWF	0.3137	0.4909	0.6572	0.7266
petro	C	gmode	yes	SimpleWF	0.3239	0.5043	0.6722	0.7403
petro	E	gmode	yes	SimpleWF	0.3251	0.4951	0.6643	0.7331
petro	G	gmode	yes	SimpleWF	0.3038	0.4718	0.6405	0.7076

Table C.9: PDF Photometric Redshift Estimates for high-redshift quasars using gmode, Simple Weighting Function and removing reddened quasars.

CZR Parameters					$z_{spec} > \text{division2}$			
Mag	Bins	Stat	Red?	Weighting	< 0.05	< 0.1	< 0.2	< 0.3
psf	O2	mean	yes	SimpleWF	0.3303	0.5189	0.7458	0.8403
psf	O2	gmode	yes	SimpleWF	0.3342	0.5167	0.7367	0.8482
psf	A	gmode	yes	SimpleWF	0.2961	0.5226	0.7427	0.8451
psf	C	gmode	yes	SimpleWF	0.2685	0.5188	0.7571	0.8750
psf	E	gmode	yes	SimpleWF	0.2750	0.5368	0.7753	0.8943
psf	G	gmode	yes	SimpleWF	0.2778	0.5443	0.7854	0.9060
model	O2	gmode	yes	SimpleWF	0.3292	0.5081	0.7321	0.8435
model	A	gmode	yes	SimpleWF	0.2980	0.5204	0.7353	0.8389
model	C	gmode	yes	SimpleWF	0.2676	0.5183	0.7547	0.8774
model	E	gmode	yes	SimpleWF	0.2717	0.5368	0.7760	0.8989
model	G	gmode	yes	SimpleWF	0.2738	0.5408	0.7816	0.9062
fiber	O2	gmode	yes	SimpleWF	0.3127	0.4928	0.7335	0.8461
fiber	A	gmode	yes	SimpleWF	0.2872	0.5065	0.7244	0.8250
fiber	C	gmode	yes	SimpleWF	0.2621	0.5135	0.7482	0.8661
fiber	E	gmode	yes	SimpleWF	0.2669	0.5304	0.7694	0.8897
fiber	G	gmode	yes	SimpleWF	0.2701	0.5364	0.7770	0.8986
petro	O2	gmode	yes	SimpleWF	0.2691	0.4331	0.6602	0.7850
petro	A	gmode	yes	SimpleWF	0.2616	0.4580	0.6582	0.7703
petro	C	gmode	yes	SimpleWF	0.2431	0.4791	0.7045	0.8219
petro	E	gmode	yes	SimpleWF	0.2533	0.5050	0.7383	0.8595
petro	G	gmode	yes	SimpleWF	0.2578	0.5157	0.7513	0.8746

Table C.10: PDF Photometric Redshift Estimates using combinations of PDFs from different magnitudes without removing reddened quasars.

Mag	CZR Parameters		$ z_{\text{spec}} - z_{\text{phot}} $												
	Bins	Stat	Red?	Weighting	< 0.05	< 0.1	< 0.2	< 0.3	# CF	% CF	# Common	%	# Diff	%	# not CF
psf	O2	mean	yes	Simple WF	0.3835	0.5889	0.7648	0.8232	6821	0.1469
psfmodel	O2	mean	no	Simple WF	0.3691	0.5775	0.7693	0.8273	6699	0.1445	4832	0.7213	1411	0.2106	1989
psffiber	O2	mean	no	Simple WF	0.3688	0.5769	0.7697	0.8272	6744	0.1455	4780	0.7088	1495	0.2217	2041
psfpetro	O2	mean	no	Simple WF	0.3444	0.5469	0.7495	0.8148	7094	0.1530	4646	0.6549	1972	0.2780	2175
modelfiber	O2	mean	no	Simple WF	0.3689	0.5755	0.7693	0.8273	6759	0.1458	4694	0.6945	1603	0.2372	2127
modelpetro	O2	mean	no	Simple WF	0.3425	0.5437	0.7457	0.8114	7255	0.1565	4616	0.6363	2176	0.2999	2205
fiberpetro	O2	mean	no	Simple WF	0.3303	0.5278	0.7303	0.7994	7619	0.1644	4511	0.5921	2596	0.3407	2310
psfmodelfiber	O2	mean	no	Simple WF	0.3707	0.5789	0.7712	0.8286	6689	0.1443	4790	0.7161	1439	0.2151	2031
psfmodelpetro	O2	mean	no	Simple WF	0.3579	0.5615	0.7594	0.8215	6919	0.1493	4691	0.6780	1763	0.2548	2130
psffiberpetro	O2	mean	no	Simple WF	0.3539	0.5564	0.7564	0.8193	6968	0.1503	4634	0.6650	1866	0.2678	2187
modelfiberpetro	O2	mean	no	Simple WF	0.3530	0.5540	0.7537	0.8176	7068	0.1525	4602	0.6511	2001	0.2831	2219
allmags	O2	mean	no	Simple WF	0.3612	0.5644	0.7621	0.8236	6855	0.1479	4679	0.6826	1714	0.2500	2142
allmags	O2	mean	no	No WF	0.3752	0.5752	0.7507	0.8089	7448	0.1607	4021	0.5399	2944	0.3953	2800

Table C.11: PDF Photometric Redshift Estimates for low-redshift quasars using combinations of PDFs from different magnitudes without removing reddened quasars.

Mag	CZR Parameters				$z_{spec} \leq \text{division2}$			
	Bins	Stat	Red?	Weighting	< 0.05	< 0.1	< 0.2	< 0.3
psf	O2	mean	yes	SimpleWF	0.3947	0.6036	0.7689	0.8196
psfmodel	O2	mean	no	SimpleWF	0.3843	0.6006	0.7861	0.8387
psffiber	O2	mean	no	SimpleWF	0.3844	0.5988	0.7845	0.8362
psfpetro	O2	mean	no	SimpleWF	0.3580	0.5668	0.7646	0.8238
modelfiber	O2	mean	no	SimpleWF	0.3840	0.5968	0.7842	0.8365
modelpetro	O2	mean	no	SimpleWF	0.3559	0.5631	0.7607	0.8206
fiberpetro	O2	mean	no	SimpleWF	0.3427	0.5460	0.7434	0.8061
psfmodelfiber	O2	mean	no	SimpleWF	0.3858	0.6003	0.7860	0.8378
psfmodelpetro	O2	mean	no	SimpleWF	0.3717	0.5819	0.7747	0.8308
psffiberpetro	O2	mean	no	SimpleWF	0.3675	0.5755	0.7698	0.8269
modelfiberpetro	O2	mean	no	SimpleWF	0.3665	0.5731	0.7675	0.8255
allmags	O2	mean	no	SimpleWF	0.3756	0.5848	0.7768	0.8322
allmags	O2	mean	no	NoWF	0.4104	0.6189	0.7918	0.8465

Table C.12: PDF Photometric Redshift Estimates for high-redshift quasars using combinations of PDFs from different magnitudes without removing reddened quasars.

Mag	CZR Parameters				$z_{spec} > \text{division2}$			
	Bins	Stat	Red?	Weighting	< 0.05	< 0.1	< 0.2	< 0.3
psf	O2	mean	yes	SimpleWF	0.3947	0.6036	0.7689	0.8196
psfmodel	O2	mean	no	SimpleWF	0.2966	0.4681	0.6890	0.7729
psffiber	O2	mean	no	SimpleWF	0.2944	0.4727	0.6990	0.7844
psfpetro	O2	mean	no	SimpleWF	0.2797	0.4522	0.6777	0.7718
modelfiber	O2	mean	no	SimpleWF	0.2972	0.4738	0.6987	0.7831
modelpetro	O2	mean	no	SimpleWF	0.2790	0.4512	0.6744	0.7681
fiberpetro	O2	mean	no	SimpleWF	0.2715	0.4415	0.6677	0.7675
psfmodelfiber	O2	mean	no	SimpleWF	0.2990	0.4774	0.7010	0.7850
psfmodelpetro	O2	mean	no	SimpleWF	0.2922	0.4649	0.6870	0.7774
psffiberpetro	O2	mean	no	SimpleWF	0.2890	0.4653	0.6924	0.7828
modelfiberpetro	O2	mean	no	SimpleWF	0.2890	0.4634	0.6879	0.7801
allmags	O2	mean	no	SimpleWF	0.2926	0.4672	0.6923	0.7829
allmags	O2	mean	no	NoWF	0.2076	0.3672	0.5553	0.6303

Table C.13: PDF Photometric Redshift Estimates using mean, Simple Weighting Function, without removing reddened quasars.

Mag	Bins	Stat	Red?	Weighting	CZR Parameters					Catastrophic Failures					
					mean	yes	SimpleWF	< 0.05	$ z_{spec} - z_{phot} < 0.1$	< 0.2	< 0.3	CF	% CF	Common	%
psf	O2	mean	no	SimpleWF	0.3835	0.5889	0.7648	0.8232	6821	0.1469
psf	O2	mean	no	SimpleWF	0.3648	0.5736	0.7660	0.8242	6800	0.1465	4883	0.7181	1446	0.2126	1938
psf	A	mean	no	SimpleWF	0.3596	0.5638	0.7580	0.8198	6815	0.1468	4905	0.7197	1445	0.2120	1916
psf	C	mean	no	SimpleWF	0.3669	0.5737	0.7593	0.8168	6959	0.1499	4195	0.6028	2303	0.3309	2626
psf	E	mean	no	SimpleWF	0.3736	0.5799	0.7683	0.8284	6372	0.1373	4354	0.6833	1565	0.2456	2467
psf	G	mean	no	SimpleWF	0.3828	0.5890	0.7667	0.8274	6410	0.1381	4445	0.6934	1518	0.2368	2376
model	O2	mean	no	SimpleWF	0.3703	0.5769	0.7687	0.8269	6729	0.1451	4748	0.7056	1531	0.2275	2073
model	A	mean	no	SimpleWF	0.3624	0.5640	0.7548	0.8164	7010	0.1512	4737	0.6757	1813	0.2586	2084
model	C	mean	no	SimpleWF	0.3729	0.5776	0.7604	0.8174	6982	0.1506	4108	0.5884	2408	0.3449	2713
model	E	mean	no	SimpleWF	0.3807	0.5844	0.7693	0.8298	6389	0.1378	4195	0.6566	1758	0.2752	2626
model	G	mean	no	SimpleWF	0.3956	0.5982	0.7722	0.8332	6199	0.1337	4221	0.6809	1553	0.2505	2600
fiber	O2	mean	no	SimpleWF	0.3585	0.5622	0.7570	0.8180	7067	0.1524	4568	0.6464	2007	0.2840	2253
fiber	A	mean	no	SimpleWF	0.3487	0.5453	0.7332	0.7955	7862	0.1696	4578	0.5823	2731	0.3474	2243
fiber	C	mean	no	SimpleWF	0.3653	0.5681	0.7518	0.8095	7246	0.1563	4019	0.5547	2720	0.3754	2802
fiber	E	mean	no	SimpleWF	0.3727	0.5765	0.7585	0.8190	6696	0.1444	4109	0.6136	2118	0.3163	2712
fiber	G	mean	no	SimpleWF	0.3765	0.5797	0.7564	0.8182	6747	0.1455	4082	0.6050	2187	0.3241	2739
petro	O2	mean	no	SimpleWF	0.2777	0.4594	0.6645	0.7455	9272	0.2000	4388	0.4733	4272	0.4607	2433
petro	A	mean	no	SimpleWF	0.2812	0.4628	0.6573	0.7366	9569	0.2064	4410	0.4609	4518	0.4721	2411
petro	C	mean	no	SimpleWF	0.2956	0.4846	0.6749	0.7483	9094	0.1962	3963	0.4358	4532	0.4984	2858
petro	E	mean	no	SimpleWF	0.3089	0.4958	0.6819	0.7562	8709	0.1879	4010	0.4604	4098	0.4705	2811
petro	G	mean	no	SimpleWF	0.3187	0.5105	0.6902	0.7616	8450	0.1823	4015	0.4751	3857	0.4564	2806

Table C.14: PDF Photometric Redshift Estimates for low-redshift quasars using mean, Simple Weighting Function without removing reddened quasars.

CZR Parameters					$z_{spec} \leq \text{division2}$			
Mag	Bins	Stat	Red?	Weighting	< 0.05	< 0.1	< 0.2	< 0.3
psf	O2	mean	yes	SimpleWF	0.3947	0.6036	0.7689	0.8196
psf	O2	mean	no	SimpleWF	0.3808	0.5970	0.7830	0.8359
psf	A	mean	no	SimpleWF	0.3794	0.5823	0.7729	0.8284
psf	C	mean	no	SimpleWF	0.3852	0.5885	0.7696	0.8198
psf	E	mean	no	SimpleWF	0.3901	0.5895	0.7710	0.8229
psf	G	mean	no	SimpleWF	0.3993	0.5962	0.7646	0.8164
model	O2	mean	no	SimpleWF	0.3849	0.5992	0.7853	0.8383
model	A	mean	no	SimpleWF	0.3832	0.5824	0.7700	0.8252
model	C	mean	no	SimpleWF	0.3918	0.5928	0.7704	0.8201
model	E	mean	no	SimpleWF	0.3984	0.5951	0.7730	0.8253
model	G	mean	no	SimpleWF	0.4141	0.6072	0.7713	0.8237
fiber	O2	mean	no	SimpleWF	0.3731	0.5832	0.7703	0.8254
fiber	A	mean	no	SimpleWF	0.3664	0.5603	0.7439	0.7993
fiber	C	mean	no	SimpleWF	0.3831	0.5824	0.7605	0.8113
fiber	E	mean	no	SimpleWF	0.3886	0.5850	0.7587	0.8112
fiber	G	mean	no	SimpleWF	0.3920	0.5858	0.7524	0.8059
petro	O2	mean	no	SimpleWF	0.2884	0.4756	0.6790	0.7547
petro	A	mean	no	SimpleWF	0.2955	0.4784	0.6745	0.7467
petro	C	mean	no	SimpleWF	0.3088	0.4963	0.6856	0.7541
petro	E	mean	no	SimpleWF	0.3205	0.5018	0.6836	0.7514
petro	G	mean	no	SimpleWF	0.3299	0.5135	0.6860	0.7495

Table C.15: PDF Photometric Redshift Estimates for high-redshift quasars using mean, Simple Weighting Function without removing reddened quasars.

CZR Parameters					$z_{spec} > \text{division2}$			
Mag	Bins	Stat	Red?	Weighting	< 0.05	< 0.1	< 0.2	< 0.3
psf	O2	mean	yes	SimpleWF	0.3303	0.5189	0.7458	0.8403
psf	O2	mean	no	SimpleWF	0.2887	0.4624	0.6848	0.7687
psf	A	mean	no	SimpleWF	0.2655	0.4758	0.6869	0.7790
psf	C	mean	no	SimpleWF	0.2462	0.4760	0.6907	0.7967
psf	E	mean	no	SimpleWF	0.2644	0.5170	0.7499	0.8650
psf	G	mean	no	SimpleWF	0.2744	0.5414	0.7807	0.8999
model	O2	mean	no	SimpleWF	0.3008	0.4711	0.6894	0.7730
model	A	mean	no	SimpleWF	0.2636	0.4763	0.6822	0.7749
model	C	mean	no	SimpleWF	0.2482	0.4773	0.6947	0.7997
model	E	mean	no	SimpleWF	0.2643	0.5140	0.7454	0.8600
model	G	mean	no	SimpleWF	0.2735	0.5385	0.7780	0.8965
fiber	O2	mean	no	SimpleWF	0.2892	0.4628	0.6934	0.7825
fiber	A	mean	no	SimpleWF	0.2648	0.4741	0.6821	0.7771
fiber	C	mean	no	SimpleWF	0.2478	0.4737	0.6942	0.7978
fiber	E	mean	no	SimpleWF	0.2678	0.5204	0.7571	0.8705
fiber	G	mean	no	SimpleWF	0.2738	0.5395	0.7830	0.8992
petro	O2	mean	no	SimpleWF	0.2268	0.3823	0.5957	0.7016
petro	A	mean	no	SimpleWF	0.2131	0.3883	0.5754	0.6886
petro	C	mean	no	SimpleWF	0.2088	0.4068	0.6038	0.7097
petro	E	mean	no	SimpleWF	0.2321	0.4562	0.6705	0.7884
petro	G	mean	no	SimpleWF	0.2443	0.4901	0.7181	0.8414

Table C.16: PDF Photometric Redshift Estimates using gmedian, Simple Weighting Function, without removing reddened quasars.

Mag	Bins	CZR Parameters		Weighting	$ z_{spec} - z_{phot} $				Catastrophic Failures				not CF		
		Stat	Red?		< 0.05	< 0.1	< 0.2	< 0.3	CF	% CF	Common	%		Diff	%
psf	O2	mean	yes	SimpleWF	0.3835	0.5889	0.7648	0.8232	6821	0.1469	
psf	O2	gmedian	no	SimpleWF	0.3633	0.5702	0.7601	0.8212	6917	0.1490	4854	0.7017	1580	0.2284	1967
psf	A	gmedian	no	SimpleWF	0.3580	0.5593	0.7518	0.8164	6897	0.1486	4841	0.7019	1585	0.2298	1980
psf	C	gmedian	no	SimpleWF	0.3646	0.5684	0.7545	0.8149	7003	0.1509	4214	0.6017	2315	0.3306	2607
psf	E	gmedian	no	SimpleWF	0.3730	0.5762	0.7635	0.8253	6516	0.1404	4382	0.6725	1679	0.2577	2439
psf	G	gmedian	no	SimpleWF	0.3816	0.5837	0.7613	0.8231	6558	0.1413	4439	0.6769	1670	0.2547	2382
model	O2	gmedian	no	SimpleWF	0.3684	0.5734	0.7616	0.8232	6859	0.1480	4737	0.6906	1665	0.2427	2084
model	A	gmedian	no	SimpleWF	0.3614	0.5626	0.7525	0.8153	6970	0.1503	4694	0.6735	1811	0.2598	2127
model	C	gmedian	no	SimpleWF	0.3686	0.5729	0.7555	0.8140	7090	0.1529	4145	0.5846	2474	0.3489	2676
model	E	gmedian	no	SimpleWF	0.3790	0.5811	0.7652	0.8275	6489	0.1400	4181	0.6443	1867	0.2877	2640
model	G	gmedian	no	SimpleWF	0.3933	0.5925	0.7660	0.8286	6374	0.1375	4198	0.6586	1738	0.2727	2623
fiber	O2	gmedian	no	SimpleWF	0.3570	0.5582	0.7514	0.8154	7131	0.1538	4581	0.6424	2044	0.2866	2240
fiber	A	gmedian	no	SimpleWF	0.3468	0.5439	0.7297	0.7930	7870	0.1698	4577	0.5816	2744	0.3487	2244
fiber	C	gmedian	no	SimpleWF	0.3613	0.5638	0.7460	0.8053	7344	0.1584	4087	0.5565	2754	0.3750	2734
fiber	E	gmedian	no	SimpleWF	0.3708	0.5714	0.7527	0.8157	6787	0.1464	4095	0.6034	2208	0.3253	2726
fiber	G	gmedian	no	SimpleWF	0.3728	0.5718	0.7488	0.8127	6891	0.1486	4100	0.5950	2305	0.3345	2721
petro	O2	gmedian	no	SimpleWF	0.2746	0.4547	0.6558	0.7383	9548	0.2060	4409	0.4618	4496	0.4709	2412
petro	A	gmedian	no	SimpleWF	0.2841	0.4666	0.6568	0.7374	9358	0.2019	4401	0.4703	4328	0.4625	2420
petro	C	gmedian	no	SimpleWF	0.2909	0.4777	0.6629	0.7380	9458	0.2040	4035	0.4266	4790	0.5064	2786
petro	E	gmedian	no	SimpleWF	0.3040	0.4860	0.6701	0.7476	8962	0.1933	4049	0.4518	4305	0.4804	2772
petro	G	gmedian	no	SimpleWF	0.3152	0.5034	0.6819	0.7557	8609	0.1857	4067	0.4724	3970	0.4611	2754

Table C.17: PDF Photometric Redshift Estimates for low-redshift quasars using gmedian, Simple Weighting Function without removing reddened quasars.

CZR Parameters					$z_{spec} \leq \text{division2}$			
Mag	Bins	Stat	Red?	Weighting	< 0.05	< 0.1	< 0.2	< 0.3
psf	O2	mean	yes	SimpleWF	0.3947	0.6036	0.7689	0.8196
psf	O2	gmedian	no	SimpleWF	0.3789	0.5912	0.7745	0.8309
psf	A	gmedian	no	SimpleWF	0.3772	0.5763	0.7648	0.8236
psf	C	gmedian	no	SimpleWF	0.3815	0.5810	0.7618	0.8158
psf	E	gmedian	no	SimpleWF	0.3887	0.5841	0.7636	0.8180
psf	G	gmedian	no	SimpleWF	0.3973	0.5892	0.7570	0.8108
model	O2	gmedian	no	SimpleWF	0.3836	0.5943	0.7761	0.8330
model	A	gmedian	no	SimpleWF	0.3813	0.5807	0.7668	0.8235
model	C	gmedian	no	SimpleWF	0.3861	0.5860	0.7626	0.8143
model	E	gmedian	no	SimpleWF	0.3955	0.5898	0.7660	0.8206
model	G	gmedian	no	SimpleWF	0.4108	0.5997	0.7627	0.8173
fiber	O2	gmedian	no	SimpleWF	0.3709	0.5756	0.7617	0.8208
fiber	A	gmedian	no	SimpleWF	0.3640	0.5580	0.7395	0.7961
fiber	C	gmedian	no	SimpleWF	0.3777	0.5759	0.7522	0.8049
fiber	E	gmedian	no	SimpleWF	0.3858	0.5778	0.7506	0.8061
fiber	G	gmedian	no	SimpleWF	0.3873	0.5759	0.7427	0.7990
petro	O2	gmedian	no	SimpleWF	0.2849	0.4700	0.6694	0.7480
petro	A	gmedian	no	SimpleWF	0.2985	0.4833	0.6738	0.7481
petro	C	gmedian	no	SimpleWF	0.3027	0.4878	0.6709	0.7416
petro	E	gmedian	no	SimpleWF	0.3139	0.4885	0.6670	0.7387
petro	G	gmedian	no	SimpleWF	0.3252	0.5041	0.6745	0.7411

Table C.18: PDF Photometric Redshift Estimates for high-redshift quasars using gmedian, Simple Weighting Function without removing reddened quasars.

CZR Parameters					$z_{spec} > \text{division2}$			
Mag	Bins	Stat	Red?	Weighting	< 0.05	< 0.1	< 0.2	< 0.3
psf	O2	mean	yes	SimpleWF	0.3303	0.5189	0.7458	0.8403
psf	O2	gmedian	no	SimpleWF	0.2892	0.4704	0.6917	0.7750
psf	A	gmedian	no	SimpleWF	0.2670	0.4784	0.6900	0.7818
psf	C	gmedian	no	SimpleWF	0.2526	0.4855	0.7060	0.8088
psf	E	gmedian	no	SimpleWF	0.2690	0.5242	0.7625	0.8735
psf	G	gmedian	no	SimpleWF	0.2781	0.5469	0.7897	0.9047
model	O2	gmedian	no	SimpleWF	0.2962	0.4739	0.6927	0.7764
model	A	gmedian	no	SimpleWF	0.2668	0.4763	0.6849	0.7765
model	C	gmedian	no	SimpleWF	0.2532	0.4863	0.7086	0.8118
model	E	gmedian	no	SimpleWF	0.2697	0.5234	0.7600	0.8728
model	G	gmedian	no	SimpleWF	0.2778	0.5449	0.7879	0.9034
fiber	O2	gmedian	no	SimpleWF	0.2907	0.4755	0.7026	0.7898
fiber	A	gmedian	no	SimpleWF	0.2651	0.4769	0.6836	0.7784
fiber	C	gmedian	no	SimpleWF	0.2526	0.4838	0.7052	0.8085
fiber	E	gmedian	no	SimpleWF	0.2713	0.5293	0.7669	0.8785
fiber	G	gmedian	no	SimpleWF	0.2772	0.5449	0.7886	0.9033
petro	O2	gmedian	no	SimpleWF	0.2252	0.3819	0.5910	0.6922
petro	A	gmedian	no	SimpleWF	0.2155	0.3870	0.5762	0.6864
petro	C	gmedian	no	SimpleWF	0.2129	0.4108	0.6102	0.7142
petro	E	gmedian	no	SimpleWF	0.2385	0.4694	0.6904	0.8068
petro	G	gmedian	no	SimpleWF	0.2486	0.4988	0.7309	0.8519

Table C.19: PDF Photometric Redshift Estimates using gmode, Simple Weighting Function, without removing reddened quasars.

Mag		Bins		Stat		Red?		Weighting		$ z_{spec} - z_{phot} $				Catastrophic Failures		not CF	
psf	O2	mean	yes	gmode	no	SimpleWF	SimpleWF	< 0.05	< 0.1	< 0.2	< 0.3	CF	% CF	Common	%	Diff	%
psf	O2	gmode	no	SimpleWF	SimpleWF	0.3835	0.5889	0.7648	0.8232	6821	0.1469	4821	0.6997	1576	0.2287	2000	
psf	A	gmode	no	SimpleWF	SimpleWF	0.3546	0.5597	0.7510	0.8184	6890	0.1484	4775	0.6690	1871	0.2621	2046	
psf	C	gmode	no	SimpleWF	SimpleWF	0.3502	0.5502	0.7391	0.8070	7138	0.1538	4239	0.6143	2192	0.3176	2582	
psf	E	gmode	no	SimpleWF	SimpleWF	0.3607	0.5655	0.7507	0.8138	6901	0.1487	4343	0.6420	1947	0.2878	2478	
psf	G	gmode	no	SimpleWF	SimpleWF	0.3646	0.5692	0.7538	0.8174	6765	0.1457	4398	0.6313	2085	0.2993	2423	
model	O2	gmode	no	SimpleWF	SimpleWF	0.3650	0.5673	0.7474	0.8117	6967	0.1501	4765	0.6598	1972	0.2731	2056	
model	A	gmode	no	SimpleWF	SimpleWF	0.3492	0.5516	0.7409	0.8103	7222	0.1558	4615	0.6041	2498	0.3270	2206	
model	C	gmode	no	SimpleWF	SimpleWF	0.3438	0.5408	0.7306	0.7967	7639	0.1648	4204	0.5877	2460	0.3439	2617	
model	E	gmode	no	SimpleWF	SimpleWF	0.3593	0.5634	0.7503	0.8105	7153	0.1543	4204	0.6203	2109	0.3112	2617	
model	G	gmode	no	SimpleWF	SimpleWF	0.3624	0.5679	0.7577	0.8208	6777	0.1462	4232	0.6256	2052	0.3033	2589	
fiber	O2	gmode	no	SimpleWF	SimpleWF	0.3681	0.5684	0.7516	0.8180	6765	0.1459	4506	0.6213	2232	0.3078	2315	
fiber	A	gmode	no	SimpleWF	SimpleWF	0.3438	0.5461	0.7399	0.8073	7252	0.1564	4473	0.5887	2591	0.3410	2348	
fiber	C	gmode	no	SimpleWF	SimpleWF	0.3364	0.5358	0.7250	0.7948	7598	0.1639	4202	0.5526	2869	0.3773	2619	
fiber	E	gmode	no	SimpleWF	SimpleWF	0.3432	0.5480	0.7337	0.7980	7604	0.1640	4219	0.5764	2568	0.3509	2602	
fiber	G	gmode	no	SimpleWF	SimpleWF	0.3479	0.5486	0.7376	0.8032	7319	0.1579	4229	0.5489	2906	0.3772	2592	
petro	O2	gmode	no	SimpleWF	SimpleWF	0.3431	0.5409	0.7277	0.7929	7704	0.1662	4409	0.4818	4128	0.4510	2412	
petro	A	gmode	no	SimpleWF	SimpleWF	0.2644	0.4449	0.6483	0.7365	9152	0.1974	4368	0.4593	4505	0.4737	2453	
petro	C	gmode	no	SimpleWF	SimpleWF	0.2724	0.4504	0.6418	0.7306	9511	0.2052	4031	0.4374	4574	0.4964	2790	
petro	E	gmode	no	SimpleWF	SimpleWF	0.2821	0.4675	0.6571	0.7401	9215	0.1988	3993	0.4511	4255	0.4807	2828	
petro	G	gmode	no	SimpleWF	SimpleWF	0.2907	0.4717	0.6612	0.7449	8851	0.1909	4116	0.4504	4413	0.4829	2705	
petro	G	gmode	no	SimpleWF	SimpleWF	0.2964	0.4796	0.6620	0.7402	9138	0.1971						

Table C.20: PDF Photometric Redshift Estimates for low-redshift quasars using gmode, Simple Weighting Function without removing reddened quasars.

CZR Parameters					$z_{spec} \leq \text{division2}$			
Mag	Bins	Stat	Red?	Weighting	< 0.05	< 0.1	< 0.2	< 0.3
psf	O2	mean	yes	SimpleWF	0.3947	0.6036	0.7689	0.8196
psf	O2	gmode	no	SimpleWF	0.3681	0.5788	0.7618	0.8207
psf	A	gmode	no	SimpleWF	0.3657	0.5627	0.7448	0.8049
psf	C	gmode	no	SimpleWF	0.3757	0.5754	0.7547	0.8107
psf	E	gmode	no	SimpleWF	0.3782	0.5752	0.7520	0.8081
psf	G	gmode	no	SimpleWF	0.3779	0.5703	0.7416	0.7977
model	O2	gmode	no	SimpleWF	0.3607	0.5686	0.7484	0.8103
model	A	gmode	no	SimpleWF	0.3597	0.5538	0.7383	0.7951
model	C	gmode	no	SimpleWF	0.3739	0.5722	0.7533	0.8062
model	E	gmode	no	SimpleWF	0.3756	0.5727	0.7554	0.8103
model	G	gmode	no	SimpleWF	0.3813	0.5715	0.7460	0.8047
fiber	O2	gmode	no	SimpleWF	0.3535	0.5583	0.7415	0.8012
fiber	A	gmode	no	SimpleWF	0.3513	0.5498	0.7328	0.7947
fiber	C	gmode	no	SimpleWF	0.3561	0.5556	0.7352	0.7930
fiber	E	gmode	no	SimpleWF	0.3593	0.5507	0.7320	0.7905
fiber	G	gmode	no	SimpleWF	0.3531	0.5405	0.7188	0.7765
petro	O2	gmode	no	SimpleWF	0.2732	0.4561	0.6557	0.7387
petro	A	gmode	no	SimpleWF	0.2821	0.4598	0.6503	0.7328
petro	C	gmode	no	SimpleWF	0.2910	0.4727	0.6586	0.7376
petro	E	gmode	no	SimpleWF	0.2975	0.4693	0.6521	0.7301
petro	G	gmode	no	SimpleWF	0.3032	0.4760	0.6500	0.7214

Table C.21: PDF Photometric Redshift Estimates for high-redshift quasars using gmode, Simple Weighting Function without removing reddened quasars.

CZR Parameters					$z_{spec} > \text{division2}$			
Mag	Bins	Stat	Red?	Weighting	< 0.05	< 0.1	< 0.2	< 0.3
psf	O2	mean	yes	SimpleWF	0.3303	0.5189	0.7458	0.8403
psf	O2	gmode	no	SimpleWF	0.2901	0.4691	0.6995	0.8072
psf	A	gmode	no	SimpleWF	0.2768	0.4911	0.7119	0.8171
psf	C	gmode	no	SimpleWF	0.2613	0.5002	0.7238	0.8339
psf	E	gmode	no	SimpleWF	0.2749	0.5299	0.7654	0.8786
psf	G	gmode	no	SimpleWF	0.2799	0.5471	0.7859	0.9038
model	O2	gmode	no	SimpleWF	0.2942	0.4706	0.7050	0.8101
model	A	gmode	no	SimpleWF	0.2681	0.4792	0.6941	0.8042
model	C	gmode	no	SimpleWF	0.2627	0.5055	0.7304	0.8386
model	E	gmode	no	SimpleWF	0.2756	0.5365	0.7734	0.8901
model	G	gmode	no	SimpleWF	0.2809	0.5478	0.7880	0.9057
fiber	O2	gmode	no	SimpleWF	0.2975	0.4880	0.7319	0.8364
fiber	A	gmode	no	SimpleWF	0.2651	0.4696	0.6881	0.7954
fiber	C	gmode	no	SimpleWF	0.2583	0.4978	0.7241	0.8310
fiber	E	gmode	no	SimpleWF	0.2726	0.5350	0.7745	0.8872
fiber	G	gmode	no	SimpleWF	0.2767	0.5436	0.7865	0.9014
petro	O2	gmode	no	SimpleWF	0.2230	0.3919	0.6127	0.7260
petro	A	gmode	no	SimpleWF	0.2266	0.4060	0.6017	0.7199
petro	C	gmode	no	SimpleWF	0.2233	0.4334	0.6469	0.7567
petro	E	gmode	no	SimpleWF	0.2458	0.4878	0.7211	0.8424
petro	G	gmode	no	SimpleWF	0.2515	0.5035	0.7411	0.8647

Table C.22: PDF Photometric Redshift Estimates varying magnitude error limits and re-moving reddened quasars.

CZR Parameters										Catastrophic Failures									
Mag	Bins	Stat	Red?	Weighting	CZR errlim	z_{phot} errlim	$ z_{spec} - z_{phot} $					# CF	% CF	# Common	%	# Diff	%	# not CF	
psf	O2	mean	yes	SimpleWF	None	None	< 0.05	< 0.1	< 0.2	< 0.3	6821	0.1469		
psf	O2	mean	yes	SimpleWF	1.0	1.0	0.3982	0.5973	0.7646	0.8227	6774	0.1478	5847	0.8632	433	0.0639	974		
psf	O2	mean	yes	SimpleWF	0.5	0.5	0.4081	0.6049	0.7639	0.8164	6935	0.1564	5407	0.7797	1030	0.1485	1414		
psf	O2	mean	yes	SimpleWF	0.2	0.2	0.4125	0.6071	0.7629	0.8166	6743	0.1560	5123	0.7598	1133	0.1680	1698		
psf	O2	mean	yes	SimpleWF	0.1	0.1	0.4222	0.6167	0.7642	0.8157	6169	0.1588	4460	0.7230	1281	0.2077	2361		
psf	O2	mean	yes	SimpleWF	0.05	0.05	0.4460	0.6349	0.7741	0.8238	3881	0.1547	2635	0.6789	915	0.2358	4186		
psf	O2	mean	yes	SimpleWF	0.02	0.02	0.4987	0.6297	0.7481	0.7935	70	0.1763	43	0.6143	27	0.3857	6778		
psf	C	mean	yes	SimpleWF	1.0	1.0	0.4070	0.6099	0.7707	0.8255	6463	0.1410	4996	0.7730	1000	0.1547	1825		
psf	C	mean	yes	SimpleWF	0.5	0.5	0.4108	0.6093	0.7663	0.8187	6730	0.1517	4802	0.7135	1428	0.2122	2019		
psf	C	mean	yes	SimpleWF	0.2	0.2	0.4153	0.6134	0.7673	0.8188	6578	0.1522	4541	0.6903	1555	0.2364	2280		
psf	C	mean	yes	SimpleWF	0.1	0.1	0.4273	0.6252	0.7707	0.8211	5874	0.1512	3980	0.6776	1474	0.2509	2841		
psf	O2	mean	yes	SimpleWF	1.0	None	0.3964	0.5953	0.7642	0.8230	6838	0.1473	5903	0.8633	437	0.0639	918		
psf	O2	mean	yes	SimpleWF	0.5	None	0.4006	0.5980	0.7623	0.8175	7149	0.1540	5590	0.7819	1049	0.1467	1231		
psf	O2	mean	yes	SimpleWF	0.2	None	0.3971	0.5892	0.7496	0.8088	7390	0.1592	5533	0.7487	1325	0.1793	1288		
psf	O2	mean	yes	SimpleWF	0.1	None	0.3916	0.5807	0.7392	0.7994	7736	0.1667	5482	0.7086	1691	0.2186	1339		
psf	O2	mean	yes	SimpleWF	0.05	None	0.3856	0.5713	0.7253	0.7860	8276	0.1783	5414	0.6542	2246	0.2714	1407		
psf	O2	mean	yes	SimpleWF	0.02	None	0.3535	0.5311	0.6915	0.7578	9093	0.1959	5257	0.5781	3173	0.3489	1564		
psf	O2	mean	yes	SimpleWF	0.01	None	0.2439	0.4005	0.5702	0.6542	13250	0.2854	5055	0.3815	7290	0.5502	1766		
psf	C	mean	yes	SimpleWF	1.0	None	0.4052	0.6084	0.7701	0.8255	6527	0.1406	5049	0.7736	1008	0.1544	1772		
psf	C	mean	yes	SimpleWF	0.5	None	0.4036	0.6029	0.7641	0.8189	6965	0.1500	4980	0.7150	1472	0.2113	1841		
psf	C	mean	yes	SimpleWF	0.2	None	0.4006	0.5969	0.7562	0.8119	7192	0.1549	4945	0.6876	1721	0.2393	1876		
psf	C	mean	yes	SimpleWF	0.1	None	0.3983	0.5932	0.7513	0.8078	7315	0.1576	4941	0.6755	1832	0.2504	1880		

Table C.23: PDF Photometric Redshift Estimates for low-redshift quasars varying magnitude error limits and removing reddened quasars.

CZR Parameters							$z_{spec} \leq \text{division2}$			
Mag	Bins	Stat	Red?	Weighting	CZR errlim	z_{phot} errlim	< 0.05	< 0.1	< 0.2	< 0.3
psf	O2	mean	yes	SimpleWF	10.0	10.0	0.3947	0.6036	0.7689	0.8196
psf	O2	mean	yes	SimpleWF	1.0	1.0	0.4119	0.6131	0.7675	0.8178
psf	O2	mean	yes	SimpleWF	0.5	0.5	0.4169	0.6159	0.7660	0.8122
psf	O2	mean	yes	SimpleWF	0.2	0.2	0.4217	0.6197	0.7679	0.8143
psf	O2	mean	yes	SimpleWF	0.1	0.1	0.4300	0.6284	0.7698	0.8138
psf	O2	mean	yes	SimpleWF	0.05	0.05	0.4529	0.6454	0.7773	0.8180
psf	O2	mean	yes	SimpleWF	0.02	0.02	0.5013	0.6354	0.7453	0.7909
psf	C	mean	yes	SimpleWF	1.0	1.0	0.4262	0.6229	0.7734	0.8199
psf	C	mean	yes	SimpleWF	0.5	0.5	0.4261	0.6181	0.7664	0.8123
psf	C	mean	yes	SimpleWF	0.2	0.2	0.4287	0.6209	0.7684	0.8138
psf	C	mean	yes	SimpleWF	0.1	0.1	0.4384	0.6309	0.7719	0.8169
psf	O2	mean	yes	SimpleWF	1.0	None	0.4116	0.6126	0.7669	0.8172
psf	O2	mean	yes	SimpleWF	0.5	None	0.4158	0.6143	0.7640	0.8101
psf	O2	mean	yes	SimpleWF	0.2	None	0.4180	0.6144	0.7614	0.8076
psf	O2	mean	yes	SimpleWF	0.1	None	0.4161	0.6131	0.7578	0.8027
psf	O2	mean	yes	SimpleWF	0.05	None	0.4124	0.6073	0.7505	0.7960
psf	O2	mean	yes	SimpleWF	0.02	None	0.3854	0.5741	0.7269	0.7740
psf	O2	mean	yes	SimpleWF	0.01	None	0.2664	0.4386	0.6160	0.6931
psf	C	mean	yes	SimpleWF	1.0	None	0.4259	0.6223	0.7727	0.8191
psf	C	mean	yes	SimpleWF	0.5	None	0.4250	0.6164	0.7642	0.8101
psf	C	mean	yes	SimpleWF	0.2	None	0.4246	0.6151	0.7616	0.8069
psf	C	mean	yes	SimpleWF	0.1	None	0.4232	0.6139	0.7581	0.8038

Table C.24: PDF Photometric Redshift Estimates for high-redshift quasars varying magnitude error limits and removing reddened quasars.

CZR Parameters							$z_{spec} > \text{division2}$			
Mag	Bins	Stat	Red?	Weighting	CZR errlim	z_{phot} errlim	< 0.05	< 0.1	< 0.2	< 0.3
psf	O2	mean	yes	SimpleWF	10.0	10.0	0.3947	0.6036	0.7689	0.8196
psf	O2	mean	yes	SimpleWF	1.0	1.0	0.3284	0.5164	0.7496	0.8478
psf	O2	mean	yes	SimpleWF	0.5	0.5	0.3531	0.5361	0.7505	0.8426
psf	O2	mean	yes	SimpleWF	0.2	0.2	0.3468	0.5171	0.7276	0.8335
psf	O2	mean	yes	SimpleWF	0.1	0.1	0.3579	0.5190	0.7172	0.8317
psf	O2	mean	yes	SimpleWF	0.05	0.05	0.3881	0.5474	0.7468	0.8725
psf	O2	mean	yes	SimpleWF	0.02	0.02	0.4583	0.5417	0.7917	0.8333
psf	C	mean	yes	SimpleWF	1.0	1.0	0.2677	0.5159	0.7513	0.8655
psf	C	mean	yes	SimpleWF	0.5	0.5	0.2633	0.5247	0.7652	0.8799
psf	C	mean	yes	SimpleWF	0.2	0.2	0.2583	0.5251	0.7550	0.8781
psf	C	mean	yes	SimpleWF	0.1	0.1	0.2604	0.5405	0.7528	0.8830
psf	O2	mean	yes	SimpleWF	1.0	None	0.3242	0.5127	0.7516	0.8507
psf	O2	mean	yes	SimpleWF	0.5	None	0.3283	0.5205	0.7543	0.8531
psf	O2	mean	yes	SimpleWF	0.2	None	0.2979	0.4695	0.6935	0.8143
psf	O2	mean	yes	SimpleWF	0.1	None	0.2749	0.4270	0.6505	0.7835
psf	O2	mean	yes	SimpleWF	0.05	None	0.2582	0.4000	0.6056	0.7387
psf	O2	mean	yes	SimpleWF	0.02	None	0.2017	0.3265	0.5232	0.6808
psf	O2	mean	yes	SimpleWF	0.01	None	0.1368	0.2193	0.3529	0.4693
psf	C	mean	yes	SimpleWF	1.0	None	0.2691	0.5161	0.7535	0.8676
psf	C	mean	yes	SimpleWF	0.5	None	0.2627	0.5143	0.7636	0.8773
psf	C	mean	yes	SimpleWF	0.2	None	0.2416	0.4763	0.7202	0.8452
psf	C	mean	yes	SimpleWF	0.1	None	0.2334	0.4567	0.7063	0.8344

Table C.25: PDF Photometric Redshift Estimates varying magnitude limits and removing reddened quasars.

Mag	Bins	Stat	Stat	Red?	Weighting	CZR		$ z_{spec} - z_{phot} $					Catastrophic Failures				#	
						maglim	z_{phot} maglim	< 0.05	< 0.1	< 0.2	< 0.3	# CF	% CF	# Common	%	# Diff		%
psf	O2	mean	mean	yes	SimpleWF	None	None	0.3835	0.5889	0.7648	0.8232	6821	0.1469	
psf	O2	mean	mean	yes	SimpleWF	25.0	25.0	0.3898	0.5963	0.7687	0.8237	6830	0.1485	6055	0.8865	296	0.0433	766
psf	O2	mean	mean	yes	SimpleWF	21.0	21.0	0.4172	0.6075	0.7567	0.8127	6839	0.1619	4809	0.7032	1572	0.2299	2012
psf	O2	mean	mean	yes	SimpleWF	20.0	20.0	0.4545	0.6505	0.7945	0.8486	4471	0.1296	3148	0.7041	982	0.2196	3673
psf	C	mean	mean	yes	SimpleWF	25.0	25.0	0.3975	0.6074	0.7712	0.8260	6539	0.1422	5121	0.7831	952	0.1456	1700
psf	C	mean	mean	yes	SimpleWF	21.0	21.0	0.4263	0.6218	0.7735	0.8252	6228	0.1474	4239	0.6806	1556	0.2498	2582
psf	C	mean	mean	yes	SimpleWF	20.0	20.0	0.4615	0.6634	0.8050	0.8531	4287	0.1243	2852	0.6653	1108	0.2585	3969
psf	O2	mean	mean	yes	SimpleWF	25.0	None	0.3882	0.5948	0.7683	0.8243	6857	0.1477	6080	0.8867	296	0.0432	741
psf	O2	mean	mean	yes	SimpleWF	21.0	None	0.3890	0.5700	0.7222	0.7861	8227	0.1772	5371	0.6529	2252	0.2737	1450
psf	O2	mean	mean	yes	SimpleWF	20.0	None	0.3904	0.5719	0.7156	0.7754	8907	0.1919	5099	0.5725	3179	0.3569	1722
psf	C	mean	mean	yes	SimpleWF	25.0	None	0.3962	0.6064	0.7711	0.8265	6566	0.1415	5144	0.7834	954	0.1453	1677
psf	C	mean	mean	yes	SimpleWF	21.0	None	0.3971	0.5834	0.7375	0.7940	8082	0.1741	4770	0.5902	2717	0.3362	2051
psf	C	mean	mean	yes	SimpleWF	20.0	None	0.4007	0.5888	0.7336	0.7855	8596	0.1852	4705	0.5473	3288	0.3825	2116

Table C.26: PDF Photometric Redshift Estimates for low-redshift quasars varying magnitude limits and removing reddened quasars.

CZR Parameters							$z_{spec} \leq \text{division2}$			
Mag	Bins	Stat	Red?	Weighting	CZR maglim	z_{phot} maglim	< 0.05	< 0.1	< 0.2	< 0.3
psf	O2	mean	yes	SimpleWF	None	None	0.3947	0.6036	0.7689	0.8196
psf	O2	mean	yes	SimpleWF	25.0	25.0	0.3977	0.6068	0.7699	0.8181
psf	O2	mean	yes	SimpleWF	21.0	21.0	0.4287	0.6238	0.7670	0.8141
psf	O2	mean	yes	SimpleWF	20.0	20.0	0.4634	0.6636	0.8021	0.8482
psf	C	mean	yes	SimpleWF	25.0	25.0	0.4158	0.6191	0.7725	0.8189
psf	C	mean	yes	SimpleWF	21.0	21.0	0.4373	0.6267	0.7741	0.8218
psf	C	mean	yes	SimpleWF	20.0	20.0	0.4706	0.6666	0.8049	0.8501
psf	O2	mean	yes	SimpleWF	25.0	None	0.3976	0.6066	0.7697	0.8178
psf	O2	mean	yes	SimpleWF	21.0	None	0.4222	0.6144	0.7558	0.8026
psf	O2	mean	yes	SimpleWF	20.0	None	0.4286	0.6253	0.7656	0.8132
psf	C	mean	yes	SimpleWF	25.0	None	0.4156	0.6189	0.7722	0.8186
psf	C	mean	yes	SimpleWF	21.0	None	0.4306	0.6175	0.7633	0.8109
psf	C	mean	yes	SimpleWF	20.0	None	0.4348	0.6252	0.7654	0.8125

Table C.27: PDF Photometric Redshift Estimates for high-redshift quasars varying magnitude limits and removing reddened quasars.

CZR Parameters							$z_{spec} > \text{division2}$			
Mag	Bins	Stat	Red?	Weighting	CZR maglim	z_{phot} maglim	< 0.05	< 0.1	< 0.2	< 0.3
psf	O2	mean	yes	SimpleWF	None	None	0.3947	0.6036	0.7689	0.8196
psf	O2	mean	yes	SimpleWF	25.0	25.0	0.3502	0.5437	0.7625	0.8517
psf	O2	mean	yes	SimpleWF	21.0	21.0	0.3208	0.4715	0.6710	0.8011
psf	O2	mean	yes	SimpleWF	20.0	20.0	0.3669	0.5206	0.7189	0.8520
psf	C	mean	yes	SimpleWF	25.0	25.0	0.2679	0.5238	0.7627	0.8769
psf	C	mean	yes	SimpleWF	21.0	21.0	0.2598	0.5473	0.7648	0.8762
psf	C	mean	yes	SimpleWF	20.0	20.0	0.2873	0.6016	0.8073	0.9113
psf	O2	mean	yes	SimpleWF	25.0	None	0.3437	0.5385	0.7621	0.8549
psf	O2	mean	yes	SimpleWF	21.0	None	0.2310	0.3589	0.5626	0.7072
psf	O2	mean	yes	SimpleWF	20.0	None	0.2085	0.3182	0.4776	0.5956
psf	C	mean	yes	SimpleWF	25.0	None	0.2681	0.5238	0.7641	0.8785
psf	C	mean	yes	SimpleWF	21.0	None	0.1758	0.3577	0.5667	0.6822
psf	C	mean	yes	SimpleWF	20.0	None	0.1754	0.3487	0.5233	0.6066

Table C.28: PDF Photometric Redshift Estimates using fewer colors.

Mag	CZR Parameters		$ z_{spec} - z_{phot} $												
	Bins	Stat	Red?	Weighting	< 0.05	< 0.1	< 0.2	< 0.3	CF	% CF	Common	%	Diff	%	not CF
psf UGRIZ	O2	mean	yes	SimpleWF	0.3835	0.5889	0.7648	0.8232	6821	0.1469
psf UGRIZ	O2	mean	no	SimpleWF	0.3648	0.5736	0.7660	0.8242	6800	0.1465	4883	0.7181	1446	0.2126	1938
psf UGR	O2	mean	no	SimpleWF	0.1724	0.3130	0.5034	0.5918	14775	0.3183	4948	0.3349	8729	0.5908	1873
psf GRI	O2	mean	no	SimpleWF	0.2050	0.3548	0.5282	0.6050	15241	0.3283	4909	0.3221	9261	0.6076	1912
psf RIZ	O2	mean	no	SimpleWF	0.2209	0.3768	0.5702	0.6586	13532	0.2915	4711	0.3481	7879	0.5822	2110
psf UGRI	O2	mean	no	SimpleWF	0.2729	0.4577	0.6500	0.7195	10572	0.2278	4971	0.4702	4829	0.4568	1850
psf GRIZ	O2	mean	no	SimpleWF	0.3037	0.4844	0.6651	0.7271	10986	0.2367	4979	0.4532	5260	0.4788	1842
psf non-adj	O2	mean	no	SimpleWF	0.2573	0.4440	0.6438	0.7312	8585	0.1849	4680	0.5451	3904	0.4547	2142

Table C.29: PDF Photometric Redshift Estimates for low-redshift quasars using fewer colors.

Mag	CZR Parameters				$z_{spec} \leq \text{division2}$			
	Bins	Stat	Red?	Weighting	< 0.05	< 0.1	< 0.2	< 0.3
psf UGRIZ	O2	mean	yes	SimpleWF	0.3947	0.6036	0.7689	0.8196
psf UGRIZ	O2	mean	no	SimpleWF	0.3808	0.5970	0.7830	0.8359
psf UGR	O2	mean	no	SimpleWF	0.1712	0.3114	0.4943	0.5745
psf GRI	O2	mean	no	SimpleWF	0.2171	0.3809	0.5650	0.6453
psf RIZ	O2	mean	no	SimpleWF	0.2343	0.4095	0.6236	0.7185
psf UGRI	O2	mean	no	SimpleWF	0.2816	0.4719	0.6595	0.7248
psf GRIZ	O2	mean	no	SimpleWF	0.3283	0.5256	0.7128	0.7724
psf non-adj	O2	mean	no	SimpleWF	0.2528	0.4429	0.6395	0.7251

Table C.30: PDF Photometric Redshift Estimates for high-redshift quasars using fewer colors.

Mag	CZR Parameters				$z_{spec} \leq \text{division2}$			
	Bins	Stat	Red?	Weighting	< 0.05	< 0.1	< 0.2	< 0.3
psf	O2	mean	yes	SimpleWF	0.3303	0.5189	0.7458	0.8403
psf	O2	mean	no	SimpleWF	0.2887	0.4624	0.6848	0.7687
psf UGR	O2	mean	no	SimpleWF	0.1780	0.3209	0.5466	0.6739
psf GRI	O2	mean	no	SimpleWF	0.1479	0.2311	0.3534	0.4137
psf RIZ	O2	mean	no	SimpleWF	0.1575	0.2214	0.3164	0.3737
psf UGRI	O2	mean	no	SimpleWF	0.2314	0.3902	0.6045	0.6947
psf GRIZ	O2	mean	no	SimpleWF	0.1870	0.2888	0.4386	0.5118
psf non-adj	O2	mean	no	SimpleWF	0.2788	0.4489	0.6645	0.7605

Table C.31: Photometric Redshift Estimates: Comparison between using 4 colors and 5 colors for quasars with GALEX matches.

Mag	CZR Parameters				$ z_{spec} - z_{phot} $				CF	% CF
	Bins	Stat	Red?	Weighting	< 0.05	< 0.1	< 0.2	< 0.3		
psf	O2	mean	no	SimpleWF	0.5533	0.7429	0.8609	0.9004	1250	0.0818
psfgalex	O2	mean	no	SimpleWF	0.5752	0.7567	0.8731	0.9135	530	0.0694

Table C.32: Photometric Redshift Estimates for low-redshift quasars: Comparison between using 4 colors and 5 colors for quasars with GALEX matches.

Mag	CZR Parameters				$z_{spec} \leq 2.1$			
	Bins	Stat	Red?	Weighting	< 0.05	< 0.1	< 0.2	< 0.3
psf	O2	mean	no	SimpleWF	0.5647	0.7569	0.8767	0.9162
psfgalex	O2	mean	no	SimpleWF	0.5871	0.7700	0.8884	0.9284

Table C.33: Photometric Redshift Estimates for high-redshift quasars: Comparison between using 4 colors and 5 colors for quasars with GALEX matches.

Mag	CZR Parameters				$z_{spec} \leq 2.1$			
	Bins	Stat	Red?	Weighting	< 0.05	< 0.1	< 0.2	< 0.3
psf	O2	mean	no	SimpleWF	0.1834	0.2882	0.3493	0.3886
psfgalex	O2	mean	no	SimpleWF	0.1921	0.3275	0.3755	0.4323

Table C.34: PDF Photometric Redshift Estimates using mean, No Weighting Function and removing reddened quasars.

Mag	Bins	Stat	Red?	CZR Parameters		$ z_{spec} - z_{phot} $		CF	% CF	Catastrophic Failures		%	not CF
				Weighting	SimpleWF	< 0.05	< 0.1			< 0.2	< 0.3		
psf	O2	mean	yes	SimpleWF	0.3835	0.5889	0.7648	0.8232	6821	0.1469
psf	O2	mean	yes	NoWF	0.3871	0.5890	0.7502	0.8074	7481	0.1612	0.6458	2650	0.3542
psf	A	mean	yes	NoWF	0.3885	0.5888	0.7462	0.7988	7814	0.1683	0.5866	3230	0.4134
psf	C	mean	yes	NoWF	0.3908	0.5934	0.7481	0.8024	7607	0.1639	0.6522	2646	0.3478
psf	E	mean	yes	NoWF	0.3968	0.5905	0.7457	0.8015	7637	0.1645	0.6286	2836	0.3714
psf	G	mean	yes	NoWF	0.4030	0.5922	0.7435	0.8011	7690	0.1657	0.6120	2984	0.3880
model	O2	mean	yes	NoWF	0.3985	0.5981	0.7548	0.8100	7372	0.1590	0.6257	2248	0.3049
model	A	mean	yes	NoWF	0.3971	0.5968	0.7506	0.8023	7623	0.1644	0.5746	2724	0.3573
model	C	mean	yes	NoWF	0.4037	0.6072	0.7594	0.8135	7090	0.1529	0.6518	1982	0.2795
model	E	mean	yes	NoWF	0.4163	0.6071	0.7555	0.8131	7110	0.1534	0.6444	2055	0.2890
model	G	mean	yes	NoWF	0.4178	0.6066	0.7529	0.8111	7203	0.1554	0.6286	2189	0.3039
fiber	O2	mean	yes	NoWF	0.3751	0.5736	0.7397	0.7960	7879	0.1700	0.5431	3047	0.3867
fiber	A	mean	yes	NoWF	0.3710	0.5632	0.7200	0.7733	8856	0.1910	0.4828	3949	0.4459
fiber	C	mean	yes	NoWF	0.3832	0.5815	0.7383	0.7937	7927	0.1710	0.5689	2852	0.3598
fiber	E	mean	yes	NoWF	0.3942	0.5849	0.7344	0.7924	7955	0.1716	0.5586	2954	0.3713
fiber	G	mean	yes	NoWF	0.3966	0.5833	0.7358	0.7937	7869	0.1697	0.5491	3010	0.3825
petro	O2	mean	yes	NoWF	0.3184	0.5004	0.6753	0.7423	9619	0.2075	0.4071	5064	0.5265
petro	A	mean	yes	NoWF	0.3238	0.5031	0.6665	0.7290	10357	0.2234	0.3802	5747	0.5549
petro	C	mean	yes	NoWF	0.3308	0.5136	0.6771	0.7406	9778	0.2109	0.4095	5158	0.5275
petro	E	mean	yes	NoWF	0.3375	0.5135	0.6714	0.7403	9661	0.2084	0.4280	4907	0.5079
petro	G	mean	yes	NoWF	0.3370	0.5146	0.6710	0.7388	9796	0.2113	0.4124	5130	0.5237

Table C.35: PDF Photometric Redshift Estimates for low-redshift quasars using mean, No Weighting Function and removing reddened quasars.

CZR Parameters					$z_{spec} \leq \text{division2}$			
Mag	Bins	Stat	Red?	Weighting	< 0.05	< 0.1	< 0.2	< 0.3
psf	O2	mean	yes	SimpleWF	0.3947	0.6036	0.7689	0.8196
psf	O2	mean	yes	NoWF	0.4105	0.6142	0.7657	0.8173
psf	A	mean	yes	NoWF	0.4180	0.6196	0.7670	0.8151
psf	C	mean	yes	NoWF	0.4112	0.6096	0.7521	0.7973
psf	E	mean	yes	NoWF	0.4181	0.6072	0.7508	0.7974
psf	G	mean	yes	NoWF	0.4253	0.6102	0.7495	0.7983
model	O2	mean	yes	NoWF	0.4226	0.6245	0.7706	0.8204
model	A	mean	yes	NoWF	0.4271	0.6275	0.7712	0.8185
model	C	mean	yes	NoWF	0.4259	0.6249	0.7650	0.8099
model	E	mean	yes	NoWF	0.4403	0.6259	0.7617	0.8104
model	G	mean	yes	NoWF	0.4418	0.6263	0.7599	0.8091
fiber	O2	mean	yes	NoWF	0.4018	0.6028	0.7564	0.8070
fiber	A	mean	yes	NoWF	0.4012	0.5949	0.7420	0.7907
fiber	C	mean	yes	NoWF	0.4019	0.5949	0.7410	0.7881
fiber	E	mean	yes	NoWF	0.4145	0.5984	0.7357	0.7850
fiber	G	mean	yes	NoWF	0.4176	0.5985	0.7383	0.7869
petro	O2	mean	yes	NoWF	0.3440	0.5319	0.6983	0.7599
petro	A	mean	yes	NoWF	0.3533	0.5375	0.6960	0.7528
petro	C	mean	yes	NoWF	0.3471	0.5264	0.6800	0.7347
petro	E	mean	yes	NoWF	0.3552	0.5266	0.6734	0.7338
petro	G	mean	yes	NoWF	0.3545	0.5287	0.6733	0.7322

Table C.36: PDF Photometric Redshift Estimates for high-redshift quasars using mean, No Weighting Function and removing reddened quasars.

CZR Parameters					$z_{spec} > \text{division2}$			
Mag	Bins	Stat	Red?	Weighting	< 0.05	< 0.1	< 0.2	< 0.3
psf	O2	mean	yes	SimpleWF	0.3303	0.5189	0.7458	0.8403
psf	O2	mean	yes	NoWF	0.2762	0.4692	0.6767	0.7601
psf	A	mean	yes	NoWF	0.2484	0.4427	0.6476	0.7211
psf	C	mean	yes	NoWF	0.2559	0.4862	0.7217	0.8364
psf	E	mean	yes	NoWF	0.2565	0.4808	0.7124	0.8292
psf	G	mean	yes	NoWF	0.2557	0.4731	0.7037	0.8198
model	O2	mean	yes	NoWF	0.2841	0.4729	0.6796	0.7609
model	A	mean	yes	NoWF	0.2544	0.4510	0.6529	0.7250
model	C	mean	yes	NoWF	0.2573	0.4902	0.7222	0.8369
model	E	mean	yes	NoWF	0.2576	0.4833	0.7145	0.8307
model	G	mean	yes	NoWF	0.2591	0.4765	0.7068	0.8240
fiber	O2	mean	yes	NoWF	0.2484	0.4348	0.6604	0.7440
fiber	A	mean	yes	NoWF	0.2272	0.4129	0.6156	0.6903
fiber	C	mean	yes	NoWF	0.2600	0.4930	0.7208	0.8308
fiber	E	mean	yes	NoWF	0.2603	0.4958	0.7261	0.8415
fiber	G	mean	yes	NoWF	0.2577	0.4828	0.7190	0.8380
petro	O2	mean	yes	NoWF	0.1965	0.3508	0.5662	0.6591
petro	A	mean	yes	NoWF	0.1836	0.3395	0.5261	0.6156
petro	C	mean	yes	NoWF	0.2226	0.4290	0.6585	0.7797
petro	E	mean	yes	NoWF	0.2200	0.4270	0.6580	0.7831
petro	G	mean	yes	NoWF	0.2208	0.4218	0.6552	0.7825

Table C.37: PDF Photometric Redshift Estimates using gmedian, No Weighting Function and removing reddened quasars.

Mag	Bins	CZR Parameters		Weighting	< 0.05	$ z_{spec} - z_{phot} $		CF	% CF	Common	%	Diff	%	not CF
		Stat	Red?			< 0.1	< 0.2							
psf	O2	mean	yes	SimpleWF	0.3835	0.5889	0.7648	0.8232	0.1469
psf	O2	gmedian	yes	NoWF	0.3843	0.5848	0.7458	0.8045	0.1625	4910	0.6509	2633	0.3491	1911
psf	A	gmedian	yes	NoWF	0.3864	0.5857	0.7439	0.7971	0.1689	4650	0.5930	3191	0.4070	2171
psf	C	gmedian	yes	NoWF	0.3875	0.5889	0.7437	0.7994	0.1654	4986	0.6495	2691	0.3505	1835
psf	E	gmedian	yes	NoWF	0.3957	0.5875	0.7413	0.7982	0.1667	4834	0.6245	2906	0.3755	1987
psf	G	gmedian	yes	NoWF	0.4003	0.5904	0.7397	0.7977	0.1679	4752	0.6098	3041	0.3902	2069
model	O2	gmedian	yes	NoWF	0.3919	0.5893	0.7457	0.8031	0.1635	4681	0.6177	2362	0.3117	2140
model	A	gmedian	yes	NoWF	0.3985	0.5952	0.7516	0.8039	0.1610	4414	0.5915	2530	0.3391	2407
model	C	gmedian	yes	NoWF	0.4011	0.5995	0.7536	0.8085	0.1558	4667	0.6462	2051	0.2840	2154
model	E	gmedian	yes	NoWF	0.4139	0.6015	0.7508	0.8090	0.1565	4611	0.6355	2154	0.2969	2210
model	G	gmedian	yes	NoWF	0.4154	0.6002	0.7474	0.8060	0.1588	4535	0.6159	2322	0.3154	2286
fiber	O2	gmedian	yes	NoWF	0.3760	0.5734	0.7400	0.7970	0.1671	4368	0.5638	2846	0.3674	2453
fiber	A	gmedian	yes	NoWF	0.3703	0.5611	0.7193	0.7732	0.1894	4349	0.4953	3816	0.4346	2472
fiber	C	gmedian	yes	NoWF	0.3819	0.5774	0.7351	0.7911	0.1715	4524	0.5691	2859	0.3596	2297
fiber	E	gmedian	yes	NoWF	0.3915	0.5817	0.7298	0.7880	0.1747	4462	0.5510	3079	0.3802	2359
fiber	G	gmedian	yes	NoWF	0.3942	0.5806	0.7303	0.7889	0.1736	4334	0.5384	3166	0.3933	2487
petro	O2	gmedian	yes	NoWF	0.3134	0.4934	0.6700	0.7375	0.2097	3996	0.4110	5072	0.5217	2825
petro	A	gmedian	yes	NoWF	0.3259	0.5049	0.6703	0.7329	0.2173	3954	0.3926	5461	0.5422	2867
petro	C	gmedian	yes	NoWF	0.3275	0.5081	0.6734	0.7371	0.2134	4059	0.4102	5191	0.5247	2762
petro	E	gmedian	yes	NoWF	0.3347	0.5097	0.6657	0.7347	0.2142	4207	0.4237	5074	0.5110	2614
petro	G	gmedian	yes	NoWF	0.3331	0.5076	0.6618	0.7293	0.2199	4088	0.4011	5438	0.5336	2733

Table C.38: PDF Photometric Redshift Estimates for low-redshift quasars using gmedian, No Weighting Function and removing reddened quasars.

CZR Parameters					$z_{spec} \leq \text{division2}$			
Mag	Bins	Stat	Red?	Weighting	< 0.05	< 0.1	< 0.2	< 0.3
psf	O2	mean	yes	SimpleWF	0.3947	0.6036	0.7689	0.8196
psf	O2	gmedian	yes	NoWF	0.4081	0.6106	0.7621	0.8152
psf	A	gmedian	yes	NoWF	0.4144	0.6142	0.7619	0.8115
psf	C	gmedian	yes	NoWF	0.4078	0.6046	0.7471	0.7939
psf	E	gmedian	yes	NoWF	0.4170	0.6042	0.7459	0.7937
psf	G	gmedian	yes	NoWF	0.4228	0.6082	0.7447	0.7933
model	O2	gmedian	yes	NoWF	0.4148	0.6147	0.7617	0.8134
model	A	gmedian	yes	NoWF	0.4278	0.6240	0.7704	0.8186
model	C	gmedian	yes	NoWF	0.4234	0.6169	0.7585	0.8043
model	E	gmedian	yes	NoWF	0.4377	0.6201	0.7562	0.8055
model	G	gmedian	yes	NoWF	0.4395	0.6194	0.7531	0.8026
fiber	O2	gmedian	yes	NoWF	0.4020	0.6019	0.7567	0.8083
fiber	A	gmedian	yes	NoWF	0.3996	0.5914	0.7400	0.7899
fiber	C	gmedian	yes	NoWF	0.4003	0.5901	0.7373	0.7853
fiber	E	gmedian	yes	NoWF	0.4117	0.5950	0.7309	0.7803
fiber	G	gmedian	yes	NoWF	0.4150	0.5953	0.7319	0.7809
petro	O2	gmedian	yes	NoWF	0.3386	0.5237	0.6918	0.7548
petro	A	gmedian	yes	NoWF	0.3551	0.5385	0.7001	0.7575
petro	C	gmedian	yes	NoWF	0.3432	0.5202	0.6756	0.7305
petro	E	gmedian	yes	NoWF	0.3519	0.5220	0.6665	0.7270
petro	G	gmedian	yes	NoWF	0.3499	0.5203	0.6623	0.7208

Table C.39: PDF Photometric Redshift Estimates for high-redshift quasars using gmedian, No Weighting Function and removing reddened quasars.

CZR Parameters					$z_{spec} > \text{division2}$			
Mag	Bins	Stat	Red?	Weighting	< 0.05	< 0.1	< 0.2	< 0.3
psf	O2	mean	yes	SimpleWF	0.3303	0.5189	0.7458	0.8403
psf	O2	gmedian	yes	NoWF	0.2710	0.4623	0.6687	0.7536
psf	A	gmedian	yes	NoWF	0.2535	0.4506	0.6585	0.7289
psf	C	gmedian	yes	NoWF	0.2532	0.4848	0.7210	0.8357
psf	E	gmedian	yes	NoWF	0.2552	0.4773	0.7107	0.8280
psf	G	gmedian	yes	NoWF	0.2513	0.4724	0.7070	0.8262
model	O2	gmedian	yes	NoWF	0.2831	0.4690	0.6699	0.7542
model	A	gmedian	yes	NoWF	0.2594	0.4582	0.6623	0.7341
model	C	gmedian	yes	NoWF	0.2541	0.4845	0.7209	0.8361
model	E	gmedian	yes	NoWF	0.2563	0.4789	0.7152	0.8320
model	G	gmedian	yes	NoWF	0.2561	0.4737	0.7103	0.8285
fiber	O2	gmedian	yes	NoWF	0.2525	0.4376	0.6606	0.7432
fiber	A	gmedian	yes	NoWF	0.2310	0.4170	0.6210	0.6940
fiber	C	gmedian	yes	NoWF	0.2601	0.4937	0.7203	0.8298
fiber	E	gmedian	yes	NoWF	0.2575	0.4938	0.7225	0.8387
fiber	G	gmedian	yes	NoWF	0.2569	0.4832	0.7192	0.8413
petro	O2	gmedian	yes	NoWF	0.1936	0.3493	0.5667	0.6552
petro	A	gmedian	yes	NoWF	0.1874	0.3448	0.5287	0.6158
petro	C	gmedian	yes	NoWF	0.2236	0.4278	0.6590	0.7807
petro	E	gmedian	yes	NoWF	0.2213	0.4283	0.6603	0.7856
petro	G	gmedian	yes	NoWF	0.2216	0.4234	0.6582	0.7856

Table C.40: PDF Photometric Redshift Estimates using gmode, No Weighting Function and removing reddened quasars.

Mag	Bins	Stat	Red?	CZR Parameters		$ z_{spec} - z_{phot} $					Catastrophic Failures				
				Weighting	< 0.05	< 0.1	< 0.2	< 0.3	CF	% CF	Common	%	Diff	%	not CF
psf	O2	mean	yes	SimpleWF	0.3835	0.5889	0.7648	0.8232	6821	0.1469	
psf	O2	gmode	yes	NoWF	0.3757	0.5715	0.7356	0.7989	7717	0.1662	4925	0.6382	2792	0.3618	1896
psf	A	gmode	yes	NoWF	0.3719	0.5702	0.7301	0.7848	8297	0.1787	4796	0.5780	3501	0.4220	2025
psf	C	gmode	yes	NoWF	0.3723	0.5712	0.7272	0.7849	8248	0.1777	5022	0.6089	3226	0.3911	1799
psf	E	gmode	yes	NoWF	0.3774	0.5687	0.7235	0.7816	8492	0.1829	4936	0.5813	3556	0.4187	1885
psf	G	gmode	yes	NoWF	0.3785	0.5664	0.7216	0.7830	8354	0.1800	4799	0.5745	3555	0.4255	2022
model	O2	gmode	yes	NoWF	0.3766	0.5751	0.7335	0.7931	7963	0.1718	4742	0.5955	3221	0.4045	2079
model	A	gmode	yes	NoWF	0.3825	0.5764	0.7351	0.7879	8056	0.1738	4659	0.5783	2838	0.3523	2162
model	C	gmode	yes	NoWF	0.3849	0.5821	0.7394	0.7968	7601	0.1640	4738	0.6233	2863	0.3767	2083
model	E	gmode	yes	NoWF	0.3939	0.5868	0.7403	0.8009	7557	0.1630	4542	0.6010	2497	0.3304	2279
model	G	gmode	yes	NoWF	0.3851	0.5721	0.7291	0.7912	7835	0.1690	4496	0.5738	2795	0.3567	2325
fiber	O2	gmode	yes	NoWF	0.3663	0.5610	0.7290	0.7890	7968	0.1719	4348	0.5457	3064	0.3845	2473
fiber	A	gmode	yes	NoWF	0.3607	0.5564	0.7189	0.7772	8380	0.1808	4375	0.5221	3434	0.4098	2446
fiber	C	gmode	yes	NoWF	0.3584	0.5535	0.7132	0.7724	8645	0.1865	4608	0.5330	3434	0.3972	2213
fiber	E	gmode	yes	NoWF	0.3649	0.5558	0.7123	0.7723	8767	0.1891	4503	0.5136	3647	0.4160	2318
fiber	G	gmode	yes	NoWF	0.3653	0.5560	0.7112	0.7736	8705	0.1878	4440	0.5101	3655	0.4199	2381
petro	O2	gmode	yes	NoWF	0.2969	0.4699	0.6387	0.7115	10667	0.2301	3906	0.3662	6049	0.5671	2915
petro	A	gmode	yes	NoWF	0.3156	0.4971	0.6624	0.7308	10054	0.2169	4010	0.3988	5392	0.5363	2811
petro	C	gmode	yes	NoWF	0.3161	0.4971	0.6620	0.7335	9927	0.2141	4142	0.4172	5141	0.5179	2679
petro	E	gmode	yes	NoWF	0.3168	0.4917	0.6531	0.7251	10217	0.2204	4259	0.4169	5286	0.5174	2562
petro	G	gmode	yes	NoWF	0.3116	0.4898	0.6535	0.7236	10334	0.2229	4255	0.4117	5395	0.5221	2566

Table C.41: PDF Photometric Redshift Estimates for low-redshift quasars using gmode, No Weighting Function and removing reddened quasars.

CZR Parameters					$z_{spec} \leq \text{division2}$			
Mag	Bins	Stat	Red?	Weighting	< 0.05	< 0.1	< 0.2	< 0.3
psf	O2	mean	yes	SimpleWF	0.3947	0.6036	0.7689	0.8196
psf	O2	gmode	yes	NoWF	0.3964	0.5947	0.7482	0.8037
psf	A	gmode	yes	NoWF	0.3955	0.5928	0.7397	0.7890
psf	C	gmode	yes	NoWF	0.3918	0.5861	0.7281	0.7746
psf	E	gmode	yes	NoWF	0.3971	0.5838	0.7252	0.7727
psf	G	gmode	yes	NoWF	0.3998	0.5830	0.7238	0.7745
model	O2	gmode	yes	NoWF	0.3954	0.5970	0.7443	0.7968
model	A	gmode	yes	NoWF	0.4062	0.5985	0.7452	0.7930
model	C	gmode	yes	NoWF	0.4059	0.5979	0.7415	0.7880
model	E	gmode	yes	NoWF	0.4152	0.6029	0.7420	0.7927
model	G	gmode	yes	NoWF	0.4064	0.5883	0.7316	0.7834
fiber	O2	gmode	yes	NoWF	0.3895	0.5884	0.7435	0.7963
fiber	A	gmode	yes	NoWF	0.3856	0.5820	0.7337	0.7871
fiber	C	gmode	yes	NoWF	0.3736	0.5629	0.7110	0.7619
fiber	E	gmode	yes	NoWF	0.3820	0.5662	0.7104	0.7621
fiber	G	gmode	yes	NoWF	0.3827	0.5685	0.7102	0.7639
petro	O2	gmode	yes	NoWF	0.3169	0.4941	0.6518	0.7191
petro	A	gmode	yes	NoWF	0.3376	0.5209	0.6811	0.7461
petro	C	gmode	yes	NoWF	0.3299	0.5073	0.6613	0.7234
petro	E	gmode	yes	NoWF	0.3315	0.5010	0.6505	0.7131
petro	G	gmode	yes	NoWF	0.3255	0.5008	0.6537	0.7156

Table C.42: PDF Photometric Redshift Estimates for high-redshift quasars using gmode, No Weighting Function and removing reddened quasars.

CZR Parameters					$z_{spec} > \text{division2}$			
Mag	Bins	Stat	Red?	Weighting	< 0.05	< 0.1	< 0.2	< 0.3
psf	O2	mean	yes	SimpleWF	0.3303	0.5189	0.7458	0.8403
psf	O2	gmode	yes	NoWF	0.2775	0.4615	0.6759	0.7762
psf	A	gmode	yes	NoWF	0.2594	0.4628	0.6845	0.7648
psf	C	gmode	yes	NoWF	0.2437	0.4724	0.7212	0.8527
psf	E	gmode	yes	NoWF	0.2473	0.4688	0.7129	0.8408
psf	G	gmode	yes	NoWF	0.2382	0.4568	0.7073	0.8390
model	O2	gmode	yes	NoWF	0.2874	0.4710	0.6821	0.7759
model	A	gmode	yes	NoWF	0.2698	0.4715	0.6874	0.7638
model	C	gmode	yes	NoWF	0.2459	0.4774	0.7252	0.8551
model	E	gmode	yes	NoWF	0.2535	0.4811	0.7288	0.8550
model	G	gmode	yes	NoWF	0.2446	0.4651	0.7129	0.8425
fiber	O2	gmode	yes	NoWF	0.2561	0.4306	0.6600	0.7543
fiber	A	gmode	yes	NoWF	0.2426	0.4347	0.6487	0.7303
fiber	C	gmode	yes	NoWF	0.2578	0.4917	0.7277	0.8421
fiber	E	gmode	yes	NoWF	0.2521	0.4873	0.7253	0.8400
fiber	G	gmode	yes	NoWF	0.2500	0.4740	0.7177	0.8375
petro	O2	gmode	yes	NoWF	0.2016	0.3552	0.5767	0.6756
petro	A	gmode	yes	NoWF	0.2112	0.3837	0.5734	0.6581
petro	C	gmode	yes	NoWF	0.2244	0.4300	0.6670	0.7999
petro	E	gmode	yes	NoWF	0.2200	0.4303	0.6700	0.8043
petro	G	gmode	yes	NoWF	0.2195	0.4173	0.6521	0.7762

Table C.43: PDF Photometric Redshift Estimates using mean, No Weighting Function, without removing reddened quasars.

Mag	Bins	Stat	Red?	CZR Parameters		$ z_{spec} - z_{phot} $				Catastrophic Failures					
				Weighting	SimpleWF	< 0.05	< 0.1	< 0.2	< 0.3	CF	% CF	Common	%	Diff	%
psf	O2	mean	no	SimpleWF	0.3835	0.5889	0.7648	0.8232	6821	0.1469
psf	O2	mean	no	NoWF	0.3751	0.5784	0.7526	0.8091	7442	0.1603	4137	0.5559	2822	0.3792	2684
psf	A	mean	no	NoWF	0.3690	0.5703	0.7455	0.7999	7837	0.1688	4025	0.5136	3296	0.4206	2796
psf	C	mean	no	NoWF	0.3708	0.5753	0.7492	0.8044	7630	0.1644	4166	0.5460	2958	0.3877	2655
psf	E	mean	no	NoWF	0.3811	0.5813	0.7500	0.8045	7554	0.1627	4122	0.5457	2927	0.3875	2699
psf	G	mean	no	NoWF	0.3888	0.5891	0.7482	0.8045	7544	0.1625	4192	0.5557	2835	0.3758	2629
model	O2	mean	no	NoWF	0.3794	0.5792	0.7472	0.8027	7796	0.1682	4024	0.5162	3252	0.4171	2797
model	A	mean	no	NoWF	0.3710	0.5704	0.7446	0.7976	7966	0.1718	4004	0.5026	3431	0.4307	2817
model	C	mean	no	NoWF	0.3775	0.5801	0.7545	0.8088	7427	0.1602	4073	0.5484	2859	0.3849	2748
model	E	mean	no	NoWF	0.3900	0.5892	0.7564	0.8112	7272	0.1569	4022	0.5531	2769	0.3808	2799
model	G	mean	no	NoWF	0.4021	0.6026	0.7583	0.8149	7087	0.1529	4103	0.5789	2510	0.3542	2718
fiber	O2	mean	no	NoWF	0.3667	0.5630	0.7369	0.7937	8060	0.1739	3955	0.4907	3566	0.4424	2866
fiber	A	mean	no	NoWF	0.3543	0.5481	0.7188	0.7719	9073	0.1957	3986	0.4393	4465	0.4921	2835
fiber	C	mean	no	NoWF	0.3667	0.5660	0.7398	0.7947	8017	0.1729	4028	0.5024	3455	0.4310	2793
fiber	E	mean	no	NoWF	0.3805	0.5760	0.7390	0.7952	7906	0.1705	4000	0.5059	3388	0.4285	2821
fiber	G	mean	no	NoWF	0.3862	0.5814	0.7388	0.7966	7803	0.1683	4013	0.5143	3274	0.4196	2808
petro	O2	mean	no	NoWF	0.2864	0.4620	0.6419	0.7137	10803	0.2330	3844	0.3558	6258	0.5793	2977
petro	A	mean	no	NoWF	0.2940	0.4727	0.6485	0.7140	11087	0.2392	3744	0.3377	6648	0.5996	3077
petro	C	mean	no	NoWF	0.3014	0.4838	0.6607	0.7257	10505	0.2266	3742	0.3562	6112	0.5818	3079
petro	E	mean	no	NoWF	0.3115	0.4877	0.6587	0.7241	10494	0.2264	3713	0.3538	6134	0.5845	3108
petro	G	mean	no	NoWF	0.3206	0.5004	0.6631	0.7313	10098	0.2178	3834	0.3797	5628	0.5573	2987

Table C.44: PDF Photometric Redshift Estimates for low-redshift quasars using mean, No Weighting Function and without removing reddened quasars.

CZR Parameters					$z_{spec} \leq \text{division2}$			
Mag	Bins	Stat	Red?	Weighting	< 0.05	< 0.1	< 0.2	< 0.3
psf	O2	mean	yes	SimpleWF	0.3947	0.6036	0.7689	0.8196
psf	O2	mean	no	NoWF	0.4099	0.6230	0.7927	0.8454
psf	A	mean	no	NoWF	0.4057	0.6164	0.7892	0.8408
psf	C	mean	no	NoWF	0.3920	0.5962	0.7655	0.8146
psf	E	mean	no	NoWF	0.4044	0.6037	0.7668	0.8148
psf	G	mean	no	NoWF	0.4138	0.6128	0.7638	0.8140
model	O2	mean	no	NoWF	0.4124	0.6206	0.7832	0.8348
model	A	mean	no	NoWF	0.4073	0.6146	0.7867	0.8368
model	C	mean	no	NoWF	0.3994	0.6018	0.7711	0.8192
model	E	mean	no	NoWF	0.4142	0.6123	0.7736	0.8218
model	G	mean	no	NoWF	0.4289	0.6281	0.7748	0.8252
fiber	O2	mean	no	NoWF	0.3998	0.6042	0.7751	0.8288
fiber	A	mean	no	NoWF	0.3886	0.5903	0.7598	0.8101
fiber	C	mean	no	NoWF	0.3863	0.5851	0.7546	0.8038
fiber	E	mean	no	NoWF	0.4027	0.5968	0.7537	0.8041
fiber	G	mean	no	NoWF	0.4096	0.6028	0.7518	0.8032
petro	O2	mean	no	NoWF	0.3163	0.5033	0.6857	0.7548
petro	A	mean	no	NoWF	0.3263	0.5175	0.6976	0.7597
petro	C	mean	no	NoWF	0.3179	0.5031	0.6779	0.7380
petro	E	mean	no	NoWF	0.3305	0.5088	0.6763	0.7365
petro	G	mean	no	NoWF	0.3419	0.5235	0.6801	0.7427

Table C.45: PDF Photometric Redshift Estimates for high-redshift quasars using mean, No Weighting Function and without removing reddened quasars.

CZR Parameters					$z_{spec} > \text{division2}$			
Mag	Bins	Stat	Red?	Weighting	< 0.05	< 0.1	< 0.2	< 0.3
psf	O2	mean	yes	SimpleWF	0.3303	0.5189	0.7458	0.8403
psf	O2	mean	no	NoWF	0.2096	0.3662	0.5616	0.6366
psf	A	mean	no	NoWF	0.1943	0.3516	0.5380	0.6056
psf	C	mean	no	NoWF	0.2305	0.4372	0.6418	0.7371
psf	E	mean	no	NoWF	0.2267	0.4334	0.6390	0.7364
psf	G	mean	no	NoWF	0.2239	0.4328	0.6454	0.7419
model	O2	mean	no	NoWF	0.2225	0.3821	0.5761	0.6498
model	A	mean	no	NoWF	0.1984	0.3604	0.5444	0.6113
model	C	mean	no	NoWF	0.2325	0.4369	0.6451	0.7403
model	E	mean	no	NoWF	0.2307	0.4361	0.6427	0.7414
model	G	mean	no	NoWF	0.2253	0.4341	0.6492	0.7470
fiber	O2	mean	no	NoWF	0.2094	0.3672	0.5554	0.6266
fiber	A	mean	no	NoWF	0.1915	0.3476	0.5240	0.5902
fiber	C	mean	no	NoWF	0.2368	0.4397	0.6425	0.7349
fiber	E	mean	no	NoWF	0.2342	0.4389	0.6424	0.7364
fiber	G	mean	no	NoWF	0.2312	0.4405	0.6526	0.7527
petro	O2	mean	no	NoWF	0.1442	0.2657	0.4336	0.5185
petro	A	mean	no	NoWF	0.1403	0.2601	0.4152	0.4968
petro	C	mean	no	NoWF	0.1919	0.3561	0.5470	0.6444
petro	E	mean	no	NoWF	0.1858	0.3477	0.5421	0.6419
petro	G	mean	no	NoWF	0.1799	0.3476	0.5505	0.6554

Table C.46: PDF Photometric Redshift Estimates using gmedian, No Weighting Function, without removing reddened quasars.

CZR Parameters		$ z_{spec} - z_{phot} $										Catastrophic Failures			
Mag	Bins	Stat	Red?	Weighting	< 0.05	< 0.1	< 0.2	< 0.3	CF	% CF	Common	%	Diff	%	not CF
psf	O2	mean	yes	SimpleWF	0.3835	0.5889	0.7648	0.8232	6821	0.1469
psf	O2	gmedian	no	NoWF	0.3749	0.5776	0.7519	0.8098	7403	0.1595	4177	0.5642	2741	0.3703	2644
psf	A	gmedian	no	NoWF	0.3659	0.5663	0.7439	0.8000	7774	0.1675	4042	0.5199	3205	0.4123	2779
psf	C	gmedian	no	NoWF	0.3684	0.5714	0.7466	0.8037	7585	0.1634	4175	0.5504	2901	0.3825	2646
psf	E	gmedian	no	NoWF	0.3805	0.5810	0.7497	0.8057	7512	0.1618	4174	0.5556	3338	0.4444	2647
psf	G	gmedian	no	NoWF	0.3865	0.5855	0.7474	0.8067	7402	0.1595	4234	0.5720	2683	0.3625	2587
model	O2	gmedian	no	NoWF	0.3741	0.5732	0.7415	0.7990	7924	0.1709	4113	0.5191	3280	0.4139	2708
model	A	gmedian	no	NoWF	0.3689	0.5681	0.7435	0.7988	7838	0.1691	4009	0.5115	3312	0.4226	2812
model	C	gmedian	no	NoWF	0.3724	0.5725	0.7469	0.8032	7606	0.1641	4126	0.5425	2975	0.3911	2695
model	E	gmedian	no	NoWF	0.3900	0.5870	0.7542	0.8111	7283	0.1571	4068	0.5586	2735	0.3755	2753
model	G	gmedian	no	NoWF	0.4007	0.5972	0.7536	0.8134	7105	0.1533	4167	0.5865	2465	0.3469	2654
fiber	O2	gmedian	no	NoWF	0.3665	0.5635	0.7385	0.7969	7913	0.1707	3998	0.5052	3375	0.4265	2823
fiber	A	gmedian	no	NoWF	0.3538	0.5473	0.7183	0.7736	8926	0.1925	4033	0.4518	4282	0.4797	2788
fiber	C	gmedian	no	NoWF	0.3641	0.5629	0.7361	0.7931	8016	0.1729	4064	0.5070	3408	0.4251	2757
fiber	E	gmedian	no	NoWF	0.3803	0.5733	0.7374	0.7959	7829	0.1689	4038	0.5158	3275	0.4183	2783
fiber	G	gmedian	no	NoWF	0.3826	0.5774	0.7356	0.7962	7738	0.1669	4048	0.5231	3167	0.4093	2773
petro	O2	gmedian	no	NoWF	0.2837	0.4574	0.6336	0.7053	11163	0.2408	3931	0.3521	6519	0.5840	2890
petro	A	gmedian	no	NoWF	0.2930	0.4727	0.6481	0.7159	10864	0.2344	3749	0.3451	6431	0.5920	3072
petro	C	gmedian	no	NoWF	0.2950	0.4765	0.6514	0.7179	10727	0.2314	3791	0.3534	6262	0.5838	3030
petro	E	gmedian	no	NoWF	0.3088	0.4831	0.6531	0.7203	10583	0.2283	3778	0.3570	6136	0.5798	3043
petro	G	gmedian	no	NoWF	0.3187	0.4970	0.6605	0.7297	10125	0.2184	3906	0.3858	5569	0.5500	2915

Table C.47: PDF Photometric Redshift Estimates for low-redshift quasars using gmedian, No Weighting Function and without removing reddened quasars.

CZR Parameters					$z_{spec} \leq \text{division2}$			
Mag	Bins	Stat	Red?	Weighting	< 0.05	< 0.1	< 0.2	< 0.3
psf	O2	mean	yes	SimpleWF	0.3947	0.6036	0.7689	0.8196
psf	O2	gmedian	no	NoWF	0.4089	0.6192	0.7888	0.8434
psf	A	gmedian	no	NoWF	0.4010	0.6094	0.7840	0.8382
psf	C	gmedian	no	NoWF	0.3886	0.5905	0.7611	0.8128
psf	E	gmedian	no	NoWF	0.4029	0.6015	0.7643	0.8142
psf	G	gmedian	no	NoWF	0.4105	0.6065	0.7596	0.8123
model	O2	gmedian	no	NoWF	0.4047	0.6112	0.7742	0.8284
model	A	gmedian	no	NoWF	0.4038	0.6097	0.7822	0.8352
model	C	gmedian	no	NoWF	0.3932	0.5926	0.7614	0.8118
model	E	gmedian	no	NoWF	0.4138	0.6086	0.7689	0.8192
model	G	gmedian	no	NoWF	0.4270	0.6208	0.7667	0.8197
fiber	O2	gmedian	no	NoWF	0.3979	0.6015	0.7745	0.8304
fiber	A	gmedian	no	NoWF	0.3862	0.5869	0.7560	0.8095
fiber	C	gmedian	no	NoWF	0.3827	0.5802	0.7487	0.8008
fiber	E	gmedian	no	NoWF	0.4017	0.5918	0.7495	0.8029
fiber	G	gmedian	no	NoWF	0.4048	0.5956	0.7447	0.7985
petro	O2	gmedian	no	NoWF	0.3111	0.4952	0.6739	0.7445
petro	A	gmedian	no	NoWF	0.3239	0.5158	0.6953	0.7610
petro	C	gmedian	no	NoWF	0.3107	0.4942	0.6668	0.7294
petro	E	gmedian	no	NoWF	0.3268	0.5016	0.6678	0.7305
petro	G	gmedian	no	NoWF	0.3388	0.5168	0.6735	0.7368

Table C.48: PDF Photometric Redshift Estimates for high-redshift quasars using gmedian, No Weighting Function and without removing reddened quasars.

CZR Parameters					$z_{spec} > \text{division2}$			
Mag	Bins	Stat	Red?	Weighting	< 0.05	< 0.1	< 0.2	< 0.3
psf	O2	mean	yes	SimpleWF	0.3303	0.5189	0.7458	0.8403
psf	O2	gmedian	no	NoWF	0.2136	0.3799	0.5768	0.6500
psf	A	gmedian	no	NoWF	0.1991	0.3615	0.5538	0.6185
psf	C	gmedian	no	NoWF	0.2354	0.4450	0.6513	0.7438
psf	E	gmedian	no	NoWF	0.2321	0.4457	0.6536	0.7492
psf	G	gmedian	no	NoWF	0.2282	0.4464	0.6665	0.7692
model	O2	gmedian	no	NoWF	0.2286	0.3929	0.5861	0.6592
model	A	gmedian	no	NoWF	0.2030	0.3702	0.5597	0.6258
model	C	gmedian	no	NoWF	0.2348	0.4397	0.6509	0.7463
model	E	gmedian	no	NoWF	0.2328	0.4440	0.6571	0.7573
model	G	gmedian	no	NoWF	0.2269	0.4412	0.6671	0.7719
fiber	O2	gmedian	no	NoWF	0.2169	0.3826	0.5677	0.6377
fiber	A	gmedian	no	NoWF	0.1997	0.3589	0.5391	0.6029
fiber	C	gmedian	no	NoWF	0.2408	0.4485	0.6527	0.7425
fiber	E	gmedian	no	NoWF	0.2386	0.4510	0.6570	0.7500
fiber	G	gmedian	no	NoWF	0.2355	0.4566	0.6759	0.7807
petro	O2	gmedian	no	NoWF	0.1535	0.2780	0.4420	0.5191
petro	A	gmedian	no	NoWF	0.1459	0.2679	0.4235	0.5014
petro	C	gmedian	no	NoWF	0.1911	0.3600	0.5495	0.6419
petro	E	gmedian	no	NoWF	0.1904	0.3609	0.5561	0.6528
petro	G	gmedian	no	NoWF	0.1863	0.3663	0.5748	0.6835

Table C.49: PDF Photometric Redshift Estimates using gmode, No Weighting Function, without removing reddened quasars.

CZR Parameters		Weighting		$ z_{spec} - z_{phot} $		CF	% CF	Common	%	Diff	%	not CF				
Mag	Bins	Stat	Red?	SimpleWF	< 0.05	< 0.1	< 0.2	< 0.3	< 0.3	CF	% CF	Common	%	Diff	%	not CF
psf	O2	mean	yes	SimpleWF	0.3835	0.5889	0.7648	0.8232	0.8232	6821	0.1469
psf	O2	gmode	no	NoWF	0.3638	0.5638	0.7392	0.8046	0.8046	7487	0.1613	4204	0.5615	2795	0.3733	2617
psf	A	gmode	no	NoWF	0.3598	0.5616	0.7380	0.7978	0.7978	7688	0.1656	4179	0.5436	2989	0.3888	2642
psf	C	gmode	no	NoWF	0.3615	0.5658	0.7403	0.8019	0.8019	7485	0.1612	4367	0.5834	2611	0.3488	2454
psf	E	gmode	no	NoWF	0.3715	0.5717	0.7412	0.8010	0.8010	7597	0.1637	4376	0.5760	3221	0.4240	2445
psf	G	gmode	no	NoWF	0.3755	0.5728	0.7381	0.8040	0.8040	7330	0.1579	4364	0.5954	2966	0.4046	2457
model	O2	gmode	no	NoWF	0.3597	0.5602	0.7290	0.7950	0.7950	8002	0.1726	4281	0.5350	3187	0.3983	2540
model	A	gmode	no	NoWF	0.3557	0.5539	0.7336	0.7893	0.7893	8203	0.1769	4228	0.5154	3410	0.4157	2593
model	C	gmode	no	NoWF	0.3634	0.5642	0.7428	0.8004	0.8004	7612	0.1642	4274	0.5615	2834	0.3723	2547
model	E	gmode	no	NoWF	0.3765	0.5760	0.7478	0.8058	0.8058	7407	0.1598	4269	0.5763	2640	0.3564	2552
model	G	gmode	no	NoWF	0.3756	0.5704	0.7351	0.8046	0.8046	7255	0.1565	4244	0.5850	2521	0.3475	2577
fiber	O2	gmode	no	NoWF	0.3565	0.5526	0.7307	0.7957	0.7957	7743	0.1670	4067	0.5252	3139	0.4054	2754
fiber	A	gmode	no	NoWF	0.3463	0.5475	0.7227	0.7821	0.7821	8372	0.1806	4101	0.4898	3711	0.4433	2720
fiber	C	gmode	no	NoWF	0.3469	0.5480	0.7205	0.7806	0.7806	8452	0.1823	4266	0.5047	3610	0.4271	2555
fiber	E	gmode	no	NoWF	0.3622	0.5570	0.7221	0.7836	0.7836	8315	0.1794	4258	0.5121	3495	0.4203	2563
fiber	G	gmode	no	NoWF	0.3617	0.5551	0.7162	0.7791	0.7791	8425	0.1817	4222	0.5011	3625	0.4303	2599
petro	O2	gmode	no	NoWF	0.2655	0.4366	0.6122	0.6874	0.6874	11652	0.2514	3991	0.3425	6881	0.5905	2830
petro	A	gmode	no	NoWF	0.2850	0.4647	0.6384	0.7131	0.7131	10835	0.2337	3792	0.3500	6362	0.5872	3029
petro	C	gmode	no	NoWF	0.2876	0.4686	0.6421	0.7165	0.7165	10682	0.2304	3837	0.3592	6164	0.5770	2984
petro	E	gmode	no	NoWF	0.2966	0.4700	0.6407	0.7145	0.7145	10571	0.2280	3827	0.3620	6063	0.5736	2994
petro	G	gmode	no	NoWF	0.2983	0.4799	0.6536	0.7247	0.7247	10174	0.2195	4026	0.3957	5513	0.5419	2795

Table C.50: PDF Photometric Redshift Estimates for low-redshift quasars using gmode, No Weighting Function and without removing reddened quasars.

CZR Parameters					$z_{spec} \leq \text{division2}$			
Mag	Bins	Stat	Red?	Weighting	< 0.05	< 0.1	< 0.2	< 0.3
psf	O2	mean	yes	SimpleWF	0.3947	0.6036	0.7689	0.8196
psf	O2	gmode	no	NoWF	0.3961	0.6045	0.7750	0.8337
psf	A	gmode	no	NoWF	0.3913	0.6013	0.7722	0.8296
psf	C	gmode	no	NoWF	0.3814	0.5848	0.7519	0.8064
psf	E	gmode	no	NoWF	0.3938	0.5923	0.7539	0.8060
psf	G	gmode	no	NoWF	0.4002	0.5952	0.7495	0.8065
model	O2	gmode	no	NoWF	0.3853	0.5929	0.7548	0.8167
model	A	gmode	no	NoWF	0.3842	0.5872	0.7626	0.8152
model	C	gmode	no	NoWF	0.3826	0.5814	0.7538	0.8043
model	E	gmode	no	NoWF	0.3980	0.5947	0.7592	0.8092
model	G	gmode	no	NoWF	0.3990	0.5908	0.7446	0.8062
fiber	O2	gmode	no	NoWF	0.3856	0.5887	0.7609	0.8215
fiber	A	gmode	no	NoWF	0.3760	0.5839	0.7548	0.8124
fiber	C	gmode	no	NoWF	0.3618	0.5614	0.7281	0.7825
fiber	E	gmode	no	NoWF	0.3802	0.5720	0.7301	0.7857
fiber	G	gmode	no	NoWF	0.3819	0.5728	0.7240	0.7805
petro	O2	gmode	no	NoWF	0.2876	0.4679	0.6444	0.7170
petro	A	gmode	no	NoWF	0.3123	0.5016	0.6783	0.7523
petro	C	gmode	no	NoWF	0.3014	0.4830	0.6523	0.7229
petro	E	gmode	no	NoWF	0.3132	0.4864	0.6507	0.7194
petro	G	gmode	no	NoWF	0.3162	0.4985	0.6662	0.7315

Table C.51: PDF Photometric Redshift Estimates for high-redshift quasars using gmode, No Weighting Function and without removing reddened quasars.

CZR Parameters					$z_{spec} > \text{division2}$			
Mag	Bins	Stat	Red?	Weighting	< 0.05	< 0.1	< 0.2	< 0.3
psf	O2	mean	yes	SimpleWF	0.3303	0.5189	0.7458	0.8403
psf	O2	gmode	no	NoWF	0.2104	0.3702	0.5692	0.6660
psf	A	gmode	no	NoWF	0.2101	0.3731	0.5756	0.6468
psf	C	gmode	no	NoWF	0.2305	0.4410	0.6640	0.7720
psf	E	gmode	no	NoWF	0.2244	0.4354	0.6578	0.7677
psf	G	gmode	no	NoWF	0.2126	0.4254	0.6624	0.7876
model	O2	gmode	no	NoWF	0.2379	0.4048	0.6064	0.6916
model	A	gmode	no	NoWF	0.2207	0.3955	0.5953	0.6662
model	C	gmode	no	NoWF	0.2364	0.4505	0.6701	0.7741
model	E	gmode	no	NoWF	0.2345	0.4528	0.6724	0.7834
model	G	gmode	no	NoWF	0.2207	0.4358	0.6722	0.7941
fiber	O2	gmode	no	NoWF	0.2179	0.3810	0.5871	0.6733
fiber	A	gmode	no	NoWF	0.2051	0.3745	0.5701	0.6383
fiber	C	gmode	no	NoWF	0.2486	0.4594	0.6701	0.7676
fiber	E	gmode	no	NoWF	0.2432	0.4577	0.6693	0.7699
fiber	G	gmode	no	NoWF	0.2283	0.4377	0.6650	0.7694
petro	O2	gmode	no	NoWF	0.1605	0.2879	0.4592	0.5468
petro	A	gmode	no	NoWF	0.1552	0.2892	0.4486	0.5268
petro	C	gmode	no	NoWF	0.1967	0.3738	0.5751	0.6741
petro	E	gmode	no	NoWF	0.1867	0.3620	0.5748	0.6820
petro	G	gmode	no	NoWF	0.1801	0.3574	0.5700	0.6795

Table C.52: PDF Photometric Redshift Estimates using other weighting functions.

Mag	Bins	Stat	Red?	CZR Parameters		$ z_{spec} - z_{phot} $										Catastrophic Failures				# not CF
				Weighting	Mag Bins	< 0.05	< 0.1	< 0.2	< 0.3	# CF	% CF	# Common	%	# Diff	%					
psf	O2	mean	yes	SimpleWF	Mag Bins	0.3835	0.5889	0.7648	0.8232	6821	0.1469				
psf	O2	mean	yes	NoWF	Mag Bins	0.3871	0.5890	0.7502	0.8074	7481	0.1612				
psf	O2	mean	yes	apparMagWF	sdssdr3_1.0	0.3930	0.5970	0.7703	0.8297	6524	0.1405	5493	0.8420	574	0.0880	1328				
psf	O2	mean	yes	apparMagWF	sdssdr3_0.5	0.3973	0.5984	0.7720	0.8322	6401	0.1379	5367	0.8385	587	0.0917	1454				
psf	O2	mean	yes	apparMagWF	sdssdr3_5bins	0.3940	0.5957	0.7697	0.8301	6498	0.1400	5456	0.8396	579	0.0891	1365				
psf	O2	mean	yes	NoMfromfile	sdssdr3_abs0.5	0.3452	0.5436	0.7124	0.7758	8842	0.1905	4963	0.5613	3255	0.3681	1858				
psf	O2	mean	yes	collapsedmatrixNoFz	sdssdr3_abs0.5	0.2208	0.3606	0.5263	0.6038	16600	0.3576	5113	0.3080	10275	0.6190	1708				
psf	O2	mean	yes	matrixNoFz	sdssdr3_abs0.5	0.3628	0.5625	0.7397	0.8068	7255	0.1563	4144	0.5712	3111	0.4288	2677				

Table C.53: PDF Photometric Redshift Estimates for low-redshift quasars using other weighting functions.

CZR Parameters						$z_{spec} \leq \text{division2}$			
Mag	Bins	Stat	Red?	Weighting	Mag Bins	< 0.05	< 0.1	< 0.2	< 0.3
psf	O2	mean	yes	SimpleWF	...	0.3947	0.6036	0.7689	0.8196
psf	O2	mean	yes	NoWF	...	0.4105	0.6142	0.7657	0.8173
psf	O2	mean	yes	apparMagWF	sdssdr3_1.0	0.4058	0.6135	0.7757	0.8273
psf	O2	mean	yes	apparMagWF	sdssdr3_0.5	0.4099	0.6145	0.7777	0.8301
psf	O2	mean	yes	apparMagWF	sdssdr3_5bins	0.4065	0.6118	0.7753	0.8278
psf	O2	mean	yes	NofMfromfile	sdssdr3_abs0.5	0.3457	0.5408	0.6987	0.7550
psf	O2	mean	yes	collapsedmatrixNofz	sdssdr3_abs0.5	0.1991	0.3320	0.4807	0.5419
psf	O2	mean	yes	matrixNofz	sdssdr3_abs0.5	0.3941	0.6063	0.7769	0.8327

Table C.54: PDF Photometric Redshift Estimates for high-redshift quasars using other weighting functions.

CZR Parameters						$z_{spec} > \text{division2}$			
Mag	Bins	Stat	Red?	Weighting	Mag Bins	< 0.05	< 0.1	< 0.2	< 0.3
psf	O2	mean	yes	SimpleWF	...	0.3303	0.5189	0.7458	0.8403
psf	O2	mean	yes	NoWF	...	0.2762	0.4692	0.6767	0.7601
psf	O2	mean	yes	apparMagWF	sdssdr3_1.0	0.3322	0.5186	0.7450	0.8412
psf	O2	mean	yes	apparMagWF	sdssdr3_0.5	0.3370	0.5217	0.7450	0.8425
psf	O2	mean	yes	apparMagWF	sdssdr3_5bins	0.3349	0.5191	0.7433	0.8410
psf	O2	mean	yes	NofMfromfile	sdssdr3_0.5	0.3428	0.5571	0.7777	0.8744
psf	O2	mean	yes	collapsedmatrixNofz	sdssdr3_abs0.5	0.3239	0.4961	0.7427	0.8980
psf	O2	mean	yes	matrixNofz	sdssdr3_abs0.5	0.2142	0.3546	0.5628	0.6837

Table C.55: PDF Photometric Redshift Estimates for quasars in the SDSS DR3 Quasar Catalog including correlation.

Mag	Bins	CZR Parameters				$ z_{spec} - \hat{z}_{phot} $						Catastrophic Failures				
		Stat	Corr?	Red?	Weighting	< 0.05	< 0.1	< 0.2	< 0.3	CF	% CF	Common	%	Diff	%	not CF
psf	O2	mean	no	yes	SimpleWF	0.3835	0.5889	0.7648	0.8232	6821	0.1469
psf	O2	gmedian	no	yes	SimpleWF	0.3787	0.5840	0.7577	0.8193	6933	0.1494	6062	0.8744	382	0.0551	759
psf	O2	gmode	no	yes	SimpleWF	0.3675	0.5696	0.7451	0.8105	7224	0.1556	5795	0.8022	924	0.1279	1026
psf	O2	mean	yes	yes	SimpleWF	0.3837	0.5892	0.7650	0.8237	6784	0.1461	6258	0.9225	43	0.0063	563
psf	O2	gmedian	yes	yes	SimpleWF	0.3797	0.5848	0.7584	0.8197	6907	0.1488	6053	0.8764	369	0.0534	768
psf	O2	gmode	yes	yes	SimpleWF	0.3688	0.5684	0.7443	0.8098	7237	0.1559	5794	0.8006	934	0.1291	1027

Table C.56: Photometric Redshift Estimates for low-redshift quasars in the SDSS DR3 Quasar Catalog including correlation.

CZR Parameters						$z_{spec} \leq 2.1$			
Mag	Bins	Stat	Corr?	Red?	Weighting	< 0.05	< 0.1	< 0.2	< 0.3
psf	O2	mean	no	yes	SimpleWF	0.3947	0.6036	0.7689	0.8196
psf	O2	gmedian	no	yes	SimpleWF	0.3899	0.5982	0.7614	0.8157
psf	O2	gmode	no	yes	SimpleWF	0.3745	0.5808	0.7469	0.8026
psf	O2	mean	yes	yes	SimpleWF	0.3951	0.6040	0.7693	0.8205
psf	O2	gmedian	yes	yes	SimpleWF	0.3913	0.5995	0.7624	0.8165
psf	O2	gmode	yes	yes	SimpleWF	0.3772	0.5806	0.7465	0.8023

Table C.57: Photometric Redshift Estimates for high-redshift quasars in the SDSS DR3 Quasar Catalog including correlation.

CZR Parameters						$z_{spec} > 2.1$			
Mag	Bins	Stat	Corr?	Red?	Weighting	< 0.05	< 0.1	< 0.2	< 0.3
psf	O2	mean	no	yes	SimpleWF	0.3303	0.5189	0.7458	0.8403
psf	O2	gmedian	no	yes	SimpleWF	0.3255	0.5165	0.7399	0.8367
psf	O2	gmode	no	yes	SimpleWF	0.3342	0.5167	0.7367	0.8482
psf	O2	mean	yes	yes	SimpleWF	0.3296	0.5191	0.7445	0.8392
psf	O2	gmedian	yes	yes	SimpleWF	0.3245	0.5154	0.7394	0.8350
psf	O2	gmode	yes	yes	SimpleWF	0.3287	0.5105	0.7337	0.8454

Table C.58: Photometric Redshift Estimates for subpopulations in the SDSS DR3 Quasar Catalog.

Subpop	Mag	Bins	CZR Parameters		Weighting	< 0.05	< 0.1	$ z_{spec} - z_{phot} $ < 0.2	< 0.3	CF	% CF
			Stat	Red?							
extended	psf	O2	mean	no	NoWF	0.4295	0.5441	0.5778	0.5922	788	0.3794
radio	psf	O2	mean	no	NoWF	0.3301	0.5134	0.6678	0.7397	832	0.2215
IR	psf	O2	mean	no	NoWF	0.4850	0.6387	0.7523	0.7925	1158	0.1870
xray	psf	O2	mean	no	NoWF	0.5314	0.6849	0.7590	0.7844	525	0.1965
BALs	psf	O2	mean	no	NoWF	0.2121	0.3229	0.4455	0.5089	953	0.4142
extended	psf	O2	mean	no	SimpleWF	0.6769	0.8604	0.9100	0.9292	103	0.0496
radio	psf	O2	mean	no	SimpleWF	0.3261	0.5023	0.6753	0.7501	788	0.2097
IR	psf	O2	mean	no	SimpleWF	0.5276	0.6755	0.7784	0.8178	1021	0.1649
xray	psf	O2	mean	no	SimpleWF	0.6261	0.7897	0.8589	0.8870	230	0.0861
BALs	psf	O2	mean	no	SimpleWF	0.2399	0.3855	0.5554	0.6367	725	0.3151
red	psf	O2	mean	no	SimpleWF	0.2346	0.4009	0.6398	0.7257	641	0.2313

Table C.59: Photometric Redshift Estimates for low-redshift quasars in subpopulations in the SDSS DR3 Quasar Catalog.

Subpop	CZR Parameters					$z_{spec} \leq 2.1$			
	Mag	Bins	Stat	Red?	Weighting	< 0.05	< 0.1	< 0.2	< 0.3
extended	psf	O2	mean	no	NoWF	0.4332	0.5468	0.5780	0.5898
radio	psf	O2	mean	no	NoWF	0.3621	0.5477	0.6878	0.7585
IR	psf	O2	mean	no	NoWF	0.5246	0.6808	0.7875	0.8249
xray	psf	O2	mean	no	NoWF	0.5355	0.6883	0.7602	0.7830
BALs	psf	O2	mean	no	NoWF	0.2593	0.3882	0.5165	0.5834
extended	psf	O2	mean	no	SimpleWF	0.6839	0.8688	0.9171	0.9351
radio	psf	O2	mean	no	SimpleWF	0.3499	0.5273	0.6782	0.7397
IR	psf	O2	mean	no	SimpleWF	0.5741	0.7279	0.8218	0.8557
xray	psf	O2	mean	no	SimpleWF	0.6344	0.7986	0.8677	0.8951
BALs	psf	O2	mean	no	SimpleWF	0.2398	0.3859	0.5633	0.6392
red	psf	O2	mean	no	SimpleWF	0.2351	0.3663	0.5743	0.6590

Table C.60: Photometric Redshift Estimates for high-redshift quasars in subpopulations in the SDSS DR3 Quasar Catalog.

Subpop	CZR Parameters					$z_{spec} > 2.1$			
	Mag	Bins	Stat	Red?	Weighting	< 0.05	< 0.1	< 0.2	< 0.3
extended	psf	O2	mean	no	NoWF	0.1481	0.3333	0.5556	0.7778
radio	psf	O2	mean	no	NoWF	0.1973	0.3712	0.5849	0.6616
IR	psf	O2	mean	no	NoWF	0.1386	0.2709	0.4441	0.5087
xray	psf	O2	mean	no	NoWF	0.2683	0.4634	0.6829	0.8780
BALs	psf	O2	mean	no	NoWF	0.0453	0.0925	0.1949	0.2461
extended	psf	O2	mean	no	SimpleWF	0.1481	0.2222	0.3704	0.4815
radio	psf	O2	mean	no	SimpleWF	0.2274	0.3986	0.6630	0.7932
IR	psf	O2	mean	no	SimpleWF	0.1213	0.2173	0.3984	0.4866
xray	psf	O2	mean	no	SimpleWF	0.0976	0.2195	0.2927	0.3659
BALs	psf	O2	mean	no	SimpleWF	0.2402	0.3839	0.5276	0.6280
red	psf	O2	mean	no	SimpleWF	0.2338	0.4494	0.7316	0.8190

Table C.61: Mean Statistics for selected variations for calculating PDF PhotoZs.

Mag	Bins	CZR Parameters		Weighting	Δz	$\frac{ z_{spec} - z_{phot} }{\Delta z/(1+z)}$	no CF		$z_{spec} < 2.1$		$z_{spec} > 2.1$	
		Stat	Red?				Δz	$\Delta z/(1+z)$	Δz	$\Delta z/(1+z)$	Δz	$\Delta z/(1+z)$
psf	O2	mean	yes	SimpleWF	0.2830	0.1392	0.3466	0.0864	0.2859	0.1523	0.3567	0.2694
psf	C	mean	yes	SimpleWF	0.2686	0.1258	0.3176	0.0849	0.2720	0.1347	0.3278	0.2457
psf	E	mean	yes	SimpleWF	0.2695	0.1289	0.3188	0.0861	0.2824	0.1411	0.3456	0.1843
model	O2	mean	yes	SimpleWF	0.2755	0.1325	0.3334	0.0846	0.2757	0.1439	0.3385	0.2742
model	C	mean	yes	SimpleWF	0.2617	0.1199	0.3048	0.0832	0.2643	0.1281	0.3131	0.2445
model	E	mean	yes	SimpleWF	0.2607	0.1220	0.3028	0.0840	0.2722	0.1331	0.3268	0.1848
psf	O2	mean	no	SimpleWF	0.2774	0.1345	0.3190	0.0889	0.2561	0.1398	0.2839	0.3790
psf	C	mean	no	SimpleWF	0.2776	0.1251	0.3118	0.0894	0.2688	0.1300	0.2967	0.3359
model	G	mean	no	SimpleWF	0.2534	0.1204	0.2756	0.0866	0.2654	0.1318	0.2989	0.1738
												Δz^2
												0.2984
												0.2500
												0.1418
												0.3094
												0.2500
												0.1442
												0.4858
												0.4116
												0.1214

References

- Abazajian, K., et al. 2005, AJ, 126, 2081
- Abell, G. O. 1958, ApJS, 3, 211
- Adelberger, K. L. & Steidel, C. C. 2005, ApJ, 627, L1
- Adelberger, K. L. & Steidel, C. C. 2006, ApJ, 630, 50
- Adelman-McCarthy, J. K. et al. 2007, ApJS, 172, 634
- Aguerri, J. A. L., Sanchez-Janssen, R., & Munoz-Tunton, C. 2007, A&A, 471, 17
- Antonucci, R. 1993, ARA&A, 31, 473
- Bahcall, N. A. & Chokshi, A. 1991, ApJ, 308, L9
- Bahcall, J. N., Schmidt, M., & Gunn, J. E. 1969, AJ, 157, L77
- Ball, N. M. et al. 2007, ApJ, 663, 774
- Ball, N. M. et al. 2008, ApJ, 683, 12B
- Barr, J. M. et al. 2003, MNRAS, 346, 229
- Baum, W. A. 1962, in IAU Symp. 15: Problems of Extra-Galactic Research, 15, 390
- Best, P.N. 2004, MNRAS, 351, 70
- Blanton, M. et al. 2003, ApJ, 592, 819
- Blanton, M. et al. 2005, ApJ, 629, 143
- Blanton, M. et al. 2007, AJ, 133, 734 (kcorrect.v4.1.4)
- Brunner, R. J. et al. 1997, ApJ, 482, L21
- Budavari, T. et al. 2003, ApJ, 595, 59
- Cardelli, J. A., Clayton, G. C., & Mathis, J. S. 1989, ApJ, 345, 256
- Charlot, S. & Fall, S. M. 2000, ApJ, 539, 718
- Coldwell, G. V. et al. 2002, MNRAS, 336, 207
- Coldwell, G. V. & Lambas, D. G. 2003, MNRAS, 344, 156
- Coldwell, G. V. & Lambas, D. G. 2006, MNRAS, 371, 786
- Coleman G. D., Wu C.-C., & Weedman, D. W. 1980, ApJS, 43, 393 (CWW)
- Cooray, A. & Sheth, R. 2002, Phys. Rep., 372, 1

Connolly, A. J. et al. 1999, in ASP Conf Ser. 191: Photometric Redshifts and the Detection of High Redshift Galaxies, ed. R. J. Weymann, L. J. StorrieLombardi, & R. J. Brunner (San Francisco: ASP), 13

Croton, D. et al. 2006, MNRAS, 365, 11

Csabai, I. et al. 2003, AJ, 125, 580

da Angela, J. et al. 2008, MNRAS, 383, 565

Di Matteo, T. et al. 2005, Nature, 433, 604

Djorgovski, S. 1991 in ASP Conf. Ser. 21: The Space Distribution of Quasars, ed. D. Crampton (San Francisco: ASP), 349

Djorgovski, S. et al. 2007, ApJ, 662, L1

Dressler, A. et al. 1997, ApJ, 490, 577

Dressler, A. 1980, ApJ, 236, 351

Ellingson, E. et al. 1991, ApJ, 371, 49

Ellis, R. 1997, ARA&A, 35, 389

Elvis, M. 2000, ApJ, 545, 63

Fasano, G. et al. 2000, ApJ, 542, 673

Ferrara, A. 1998, ApJ, 499, L77

Ferrarese, L. & Merritt, D. 2000, ApJ, 539, L9

Fisher, K. B. et al. 1996, ApJ, 468, 469

Gehardt, K. et al. 2000, ApJ, 539, L13

Georgakakis, A. et al. 2007, ApJ, 660, L15

Hall, P. B., et al., 2002, ApJS, 141, 267

Hao, L. et al. 2005a, AJ, 129, 1783

Hao, L. et al. 2005b, AJ, 129, 1795

Hatziminaoglou, E. et al. 2000, A&A, 359, 9

Heckman, T. et al. 2004, ApJ, 613, 109

Heckman, T. et al. 2005, ApJ, 634, 161

Hennawi, J. et al. 2006, AJ, 131, 1

Hogg, D. W. 2000, preprint (astro-ph/9905116)

Hogg, D. W. et al. 2002, preprint (astro-ph/0210394v1)

Hogg, D. W. et al. 2003, ApJ, 585, L5

Hopkins, P. F. et al. 2004, AJ, 128, 1112

Hopkins, P. et al. 2005a, ApJ, 625, L71

Hopkins, P. et al. 2005b, ApJ, 630, 705

Hopkins, P. et al. 2005c, ApJ, 630, 716
Hopkins, P. et al. 2006, ApJS, 163, 1
Hopkins, P. & Hernquist, L. 2006, ApJS, 166, 1
Hopkins, P. et al. 2008, ApJS, 175, 356
Ivezic, Z. et al. 2002, AJ, 124, 2364
Kauffmann, G. & Haehnelt, M. G. 2002, MNRAS, 332, 529
Kauffmann, G. et al. 2003, MNRAS, 346, 1055
Kewley, L. J. et al. 2001, ApJ, 556, 121
Kochanek, C. S. et al. 1999, ApJ, 510, 590
Koo, D. C. 1985, AJ, 90, 418
Kormendy, J. & Richstone, D. ARA&A, 33, 581
Koulouridis, E. et al. 2006, ApJ, 639, 37
Lacey, C. & Cole, S. 1993, MNRAS, 262, 627
Li, C. et al. 2006, MNRAS, 373, 457
Li, C. et al. 2008, MNRAS, 385, 1915
Lidz, A. et al. 2006, ApJ, 641, 41
Loh, E. D. & Spillar, E. J. 1986, ApJ, 303, 154
Lupton, R. H. *Statistics in Theory and Practice*. Princeton: Princeton Univ. Press, 1993.
Lupton, R. H., Gunn, J. E., & Szalay, A. S. 1999, AJ, 118, 1406
Lynden-Bell, D. 1969, Nature, 223, 690
Madau, P. & Rees, M. 2001, ApJ, 551, L27
Maddox, S. et al. 1990, MNRAS, 242, 43
Magorrian, J. et al. 1998, AJ, 115, 2285
Marconi, A. & Hunt, L. 2003, ApJ, 549, 21
McLure, R. J. & Dunlop, J. S. 2001, MNRAS, 321, 515
Montero-Dorta, A. et al. 2008, MNRAS, 392, 125
Mortlock, D. J. et al. 1999, MNRAS, 309, 836
Myers, A. et al. 2006, ApJ, 638, 622
Myers, A. et al. 2007, ApJ, 658, 99
Myers, A. et al. 2008, ApJ, 678, 635
Norberg, P. et al. 2002, MNRAS, 332, 827
O'Donnell, J. E. 1994, ApJ, 422, 158
Padmanabhan, N. et al. 2008, preprint (astro-ph/0802.2105)

Pogson, N. R. MNRAS, 17, 12, 1856.

Porciani, C. & Norberg, P. 2006, MNRAS, 371, 1824

Reyes, R. et al. 2008, AJ, 136, 2373

Richards, G. T. et al. 2001a, AJ, 121, 2308

Richards, G. T. et al. 2001b, AJ, 122, 1151

Richards, G. T. et al. 2006, AJ, 131, 2766

Richstone, D. et al. 1998, Nature, 395, A14

Ross, A. et al. 2006, ApJ, 649, 48

Scannapieco, E. & Oh, S. P. 2003, ApJ, 608, 62

Schlegel, D. J., Finkbeiner, D. P., & Davis, M. 1998, ApJ, 500, 525

Schneider, D. P. et al. 2005, AJ, 130, 367S

Schneider, D. P. et al. 2007, AJ, 134, 102

Scranton, R. et al. 2002, ApJ, 579, 48

Scranton, R. et al. 2005, astro-ph/0508564

Serber, W. et al. 2006, ApJ, 643, 68

Shen, Y. et al. 2008, ApJ, 680, 169

Shields, G. A. et al. 2003, ApJ, 583, 124

Söchting, I. K. et al. 2004, MNRAS, 347, 1241

Spergel, D. N. et al. 2003, ApJS, 148, 175

Strand, N. E., Brunner, R. J., & Myers, A. D. 2008, ApJ, 688, 180 (Paper I)

Tremaine, S. et al. 2002, ApJ, 574, 740

Tremonti, C. et al. 2004, ApJ, 613, 898

Urry, M. & Padovani, P. 1995, PASP, 107, 803

Vignali, D. et al. 2003, AJ, 125, 2876

Voges, W. et al. 1999 A&A, 349, 389

Volonteri, M. et al. 2003, ApJ, 582, 559

Waskett, T. J. et al. 2005, MNRAS, 363, 801

Weinstein, M. A. 2002, *Photometric Redshifts of Quasars (A Sloan Digital Sky Survey Project)*, Diss. The Pennsylvania State University

Weinstein, M. A. et al., 2004, ApJS, 155, 243

Weymann et al. 1991, ApJ, 373, 23

White, M. & Padmanabhan, N. 2009, MNRAS, 395, 2381

White, S. D. M. & Rees, M. J. MNRAS, 183, 341

Wilhite, B. C. et al. 2008, MNRAS, 383, 1232
Willis, A. G. & Strom, R. G. 1978, *Å*, 62, 375
Willmer, C. N. A., da Costa, L. N., & Pellegrini, P. S., 1998, AJ, 115, 869
Wisotzki, L. A&A. 353. 861-866. 2000.
Wold, M. et al. 2000, MNRAS, 316, 267
Wold, M. et al. 2001, MNRAS, 323, 231
Wurtz, R. et al. 2007, ApJ, 480, 547
Yee, H. C. K. & Green, R. F. 1984, ApJ, 280, 79
York, D. G. et al. 2000, AJ, 120, 1579
Zakamska, N. et al. 2003, AJ, 126, 2125
Zehavi, I. et al. 2002, ApJ, 571, 172
Zehavi, I. et al. 2005, ApJ, 630, 1

Curriculum Vitae of Natalie Erin Strand

EDUCATION

- Ph. D. in Physics: University of Illinois at Urbana-Champaign, October 2009
Thesis Advisor: Professor Robert J. Brunner
Thesis Title: AGN Environments in the Sloan Digital Sky Survey
- M. S. in Physics: University of Illinois at Urbana-Champaign, October 2005
- B. S. in Physics & Minor in Mathematics, The Pennsylvania State University, May 2003
Honors in Physics; Thesis Advisor: Professor Lee Samuel Finn
Thesis Title: Wavelets for LIGO Data Analysis

TEACHING EXPERIENCE

- Graduate Teacher Certificate at the University of Illinois at Urbana Champaign: Spring 2006
- Discussion Teaching Assistant for PHYS 199M: Enrichment Mechanics, UIUC
Spring 2008**
- Discussion Teaching Assistant for PHYS 211: Introductory Mechanics, UIUC
Fall 2003
Spring 2004**
Spring 2005*
Fall 2006**
Fall 2007 (Mentor TA, no sections)
Spring 2008**
- Discussion Teaching Assistant for ASTR 122: Stars and Galaxies, UIUC
Fall 2004*

* Rated Excellent on List of Teachers Rated Excellent by their Students

** Rated Outstanding on List of Teachers Rated Excellent by Their Students

RESEARCH EXPERIENCE

- Summer 2004 to present: Cosmology with AGN
Advisor: Professor Robert J. Brunner
Investigation of active galactic nuclei environments using Sloan Digital Sky Survey (SDSS) data

Analysis of photometric redshift prediction techniques using optical colors of quasars in SDSS
Wrote software to search for quasar groups in SDSS data

Tools: C, Python, SuperMongo, use of NCSA TeraGrid resources

- Fall 2000 to Spring 2003: Penn State LIGO Data Analysis Research

Advisor: Professor Lee Samuel Finn

Wrote wavelet software package to be part of the LIGO Data Analysis System to search for burst gravitational wave signals in LIGO data

Tools: C++

PUBLICATIONS

Strand, N. E., Brunner, R. B. and Myers, A. D. AGN Environments in the Sloan Digital Sky Survey I: Dependence on Type, Redshift, and Luminosity. *The Astrophysical Journal* 688 (2008): 180

Ball, N. M. et al. Robust Machine Learning Applied to Astronomical Data Sets III: Probabilistic Photometric Redshifts for Galaxies and Quasars in the SDSS and GALEX. *The Astrophysical Journal* 683 (2008): 12

Myers, A. D. et al. Quasar Clustering at 25 h⁻¹ kpc from a Complete Sample of Binaries. *The Astrophysical Journal* 678 (2007): 635

Ball, N. M. et al. Robust Machine Learning Applied to Astronomical Data Sets II: Quantifying Photometric Redshifts for Quasars Using Instance-based Learning. *The Astrophysical Journal* 663 (2007): 774

Abbott, B. et al. Search for Gravitational Waves Associated with 39 Gamma-ray Bursts using Data from the Second, Third, and Fourth LIGO Runs. *Physical Review D* 77 (2008): 062004

Abbott, B. et al. Searches for Periodic Gravitational Waves from Unknown Isolated Sources and Scorpius X-1: Results from the Second LIGO Science Run. *Physical Review D* 76 (2007): 082001

Abbott, B. et al. Joint LIGO and TAMA300 search for gravitational waves from inspiralling neutron star binaries. *Physical Review D* 73 (2006): 102002

Abbot, B. et al. Search for gravitational waves from binary black hole inspirals in LIGO data. *Physical Review D* 73 (2006): 062001

Abbot, B. et al. Upper limits from the LIGO and TAMA detectors on the rate of gravitational-wave bursts. *Physical Review D* 72 (2005): 122004

Abbot, B. et al. First all-sky upper limits from LIGO on the strength of periodic gravitational waves using the Hough transform. *Physical Review D* 72 (2005): 102004

Abbot, B. et al. Search for gravitational waves from primordial black hole coalescences in the galactic halo. *Physical Review D* 72 (2005): 0282002

Abbot, B. et al. Search for gravitational waves from galactic and extra-galactic binary neutron stars. *Physical Review D* 72 (2005): 082001

Abbott, B. et al. Upper limits on gravitational wave bursts in LIGO's second science run. *Physical Review D* 72 (2005): 062001

Abbott, B. et al. Limits on Gravitational-Wave Emission from Selected Pulsars Using LIGO Data. *Physical Review Letters* 94 (2005): 181103

Abbott, B. et al. Setting upper limits on the strength of periodic gravitational waves from PSR J1939+2134 using the first science data from the GEO 600 and LIGO detectors. *Physical Review D* 69 (2004): 082004

Abbott, B. et al. Search for gravitational waves associated with the gamma ray burst GRB030329 using the LIGO detectors. *Physical Review D* 72 (2005): 042002

Abbott, B. et al. First upper limits from LIGO on gravitational wave bursts. *Physical Review D* 69 (2004): 102001

Abbott, B. et al. Analysis of LIGO data for gravitational waves from binary neutron stars. *Physical Review D* 69 (2004): 122001

Abbott, B. et al. Analysis of first LIGO science data for stochastic gravitational waves. *Physical Review D* 69 (2004): 122004

AWARDS

- Scott Anderson Award, University of Illinois Department of Physics (2009)
- Selected as GAANN Fellow 2007-2008 by the University of Illinois Department of Physics
- Phi Beta Kappa Thesis Award (May 2003)
- Langhorne H. Brickwedde Award for Excellence in Undergraduate Physics, The Pennsylvania State University Department of Physics (May 2003)
- Deans List, Pennsylvania State University (Spring 2000-Spring 2003)
- Bookstore Academic Excellence Scholarship, Schreyer Honors College, The Pennsylvania State University (Fall 1999-Spring 2003)
- John and Elizabeth Holmes Teas Scholarship, The Pennsylvania State University Department of Physics (Fall 2000-Spring 2003)

HONOR SOCIETY MEMBERSHIPS

- Phi Beta Kappa
- Sigma Pi Sigma